HARVARD
Kenneth C. Griffin

GRADUATE SCHOOL
OF ARTS AND SCIENCES

DISSERTATION ACCEPTANCE CERTIFICATE

The undersigned, appointed by the

Department of Physics

have examined a dissertation entitled

Emergent Quantum Phases of Electrons in Multilayer Graphene Heterostructures

presented by Zeyu Hao

candidate for the degree of Doctor of Philosophy and hereby certify that it is worthy of acceptance.

Signature _____

Typed name: Prof. Philip Kim

Signature _____

Typed name: Prof. Ashvin Vishwanath

Signature _____

Typed name: Prof. Suyang Xu

Signature _____

Typed name: Prof. Mikhail Lukin

Date: April 30, 2024

Emergent Quantum Phases of Electrons in Multilayer Graphene Heterostructures

A DISSERTATION PRESENTED
BY
ZEYU HAO
TO
THE DEPARTMENT OF PHYSICS

IN PARTIAL FULFILLMENT OF THE REQUIREMENTS
FOR THE DEGREE OF
DOCTOR OF PHILOSOPHY
IN THE SUBJECT OF
PHYSICS

HARVARD UNIVERSITY
CAMBRIDGE, MASSACHUSETTS
MAY 2024

Dissertation Advisor: Professor Philip Kim Zeyu Hao

Emergent Quantum Phases of Electrons in Multilayer Graphene Heterostructures

Abstract

The flexibility of two-dimensional materials allows for the creation of various structural configurations to engineer many-body electronic Hamiltonians and to explore new phases of matter. In this thesis, I will discuss two different classes of graphene heterostructures that have enabled our observation of novel quantum phases of electrons. The first utilizes small-angle twisting of 2D materials to create a moiré pattern, introducing a new length scale for electrons to move and interact. By twisting two layers of Bernal bilayer graphene, we have observed emergent correlated metallic and insulating states, along with their spin-polarization nature. By twisting three graphene layers with alternating twist angles of ±1.56 degrees, we have discovered displacement field-tunable superconductivity, which occurs in close conjunction with correlation-driven flavor polarization. The similar phenomenology can also be found in twisted quadrilayer graphene, with more intricate interplay between the superconducting phases and the single particle dispersion. I will also discuss two experimental efforts in investigating the nature of the superconducting paring symmetry: fabricating Josephson junctions between twisted trilayer graphene and an s-wave superconductor, and measuring superfluid stiffness using microwave reflectometry. The latter has indicated the nodal nature of the superconducting gap.

The second graphene heterostructure involves a graphene double-layer structure where two parallel graphene sheets are brought close to each other but remain separated. This enables Coulomb interactions to couple electrons across the two layers, leading to a variety of interlayer correlated states under strong magnetic fields, including exciton condensation, interlayer fractional quantum

Hall states, and exciton condensation formed by composite fermions. The exploration of novel material manipulation methods presented in this thesis not only reveals new phenomena and underlying physical principles, but also holds significant promise for future material design and device applications.

Contents

Previous publications and list of authors

Results in Chapter 2 were published in (* indicates equal contributions) :

Xiaomeng Liu*, Zeyu Hao*, Eslam Khalaf, Jong Yeon Lee, Yuval Ronen, Hyobin Yoo, Danial Haei Najafabadi, Kenji Watanabe, Takashi Taniguchi, Ashvin Vishwanath, Philip Kim. "Tunable spin-polarized correlated states in twisted double bilayer graphene", Nature 583, 221-225 (2020).

Results in Chapter 3 were published in:

Zeyu Hao*, Andrew Zimmerman*, Patrick Ledwith, Eslam Khalaf, Danial Haie Najafabadi, Kenji Watanabe, Takashi Taniguchi, Ashvin Vishwanath, Philip Kim. "Electric field–tunable superconductivity in alternating-twist magic-angle trilayer graphene", Science 371, 1133-1138 (2021).

The following authors contributed to the results presented in Chapter 4:

Zeyu Hao*, Andrew Zimmerman*, Kenji Watanabe, Takashi Taniguchi, and Philip Kim.

The following authors contributed to the results presented in Chapter 5:

Isabelle Y. Phinney*, Andrew Zimmerman*, Zeyu Hao*, Kenji Watanabe, Takashi Taniguchi, and Philip Kim.

The following authors contributed to the results presented in Chapter 6:

Abhishek Banerjee*, Zeyu Hao*, Mary Kreidel*, Isabelle Y. Phinney, Jeong Min Park, Patrick Ledwith, Andrew Zimmerman, Robert M. Westervelt, Pablo Jarillo Herrero, Pavel Volkov, Ashvin Vishwanath, Kin Chung Fong, Philip Kim.

The following authors contributed to the results presented in Chapter 7:

Zeyu Hao, Andrew Zimmerman, Kenji Watanabe, Takashi Taniguchi, and Philip Kim.

Dedicated to my parents and sister, Huaimei Cui, Zhiguo Hao and Ting Hao.

Acknowledgments

IT TAKES A VILLAGE. No man is an island, and I'm grateful that over my 7 Harvard years, I could interact with so many brilliant people. First and foremost, I want to thank my advisor Philip Kim. Gossiping about professors is a beloved activity among graduate students, and it always feels like a luxury to be able to proudly share how good my advisor is. How could I forget the first Thanksgiving into the COVID lockdown, he and his wife drove door to door, delivering Thanksgiving meals to each of the group member on a rainy day? Or the times my experiments kept failing and I became increasingly disheartened, he genuinely worried about me and gently pushed me to enjoy a vacation? Or how he still kindly offered me encouragement and freedom when I tried to pursue projects that intrigued me but had not yet convinced him? Or in recent year as I become more mature, how I can increasingly appreciate his advice and insights about experiments, his relentless pursuit of deep physics and his creativity and knowledge when it comes to finding the underlying physical pictures for experimental data. There is not doubt that he is a brilliant physicist and great human-being, and I could not have asked for a better advisor.

I also want to thank all my committee members. Ashvin Vishwanath, some of the papers I had or am going to have all have his name on it—he is basically my second PI at this point. I'm always impressed by his deep insights and broad knowledge in both theory and experiments. Mikhail Lukin, who taught the first course I took at Harvard—his AMO course—opened up the quantum world to me. Although my main focus has always been condensed matter, I never stopped learning and paying attention to the developments in quantum science, which formed my unique perspectives.

He emphasis on intuitive physical pictures also profoundly shaped how I thought about physics throughout my PhD. I have also benefited immensely from his advice during our annual meetings. Suyang Xu joined Harvard just before COVID, and I quickly asked him to be on my committee. I first knew his name from the discovery of Weyl fermion metals. Since then, he has always been a creative and productive young scientist, serving as a role model for me. I'm very glad to have him on my committee. We both had scientific discussion and discussions about career.

I want to thank the mentors that I worked closely with, although over time, the proportion of mentorship decreases, replaced by collaboration. I'm glad with all of them, we also formed great friendships. Xiaomeng Liu was my first mentor and had a big influence on me. Not only is he a physicist, but also a photographer. In my eyes, he can often find unique angles in research, and he approaches his work as if it were a piece of art, consistently producing high-quality work with remarkable focus. Yuval Ronen is the strongest person I know, both physically and mentally. He has a broad interest in physics and can command and lead many fronts of efforts. He is also deeply compassionate, and cares about others. Andrew Zimmerman is one of the most calm and caring individuals I know. Many times when experiments don't work I would get upset and anxious. But he can always remain composed and think through the problems and patiently finding the solution with me. There were also times when I was in emotional auguish. He was always sensitive enough to see it and went out of his way to offer support. Abhishek has an unique charisma and is often entertaining. I admire his constant confidence and optimism; even when things don't quite work as planned, he maintains strong hope and believes that everything will turn out well in the end, which it often does.

I want to thank other collaborators I have worked with over the years. I thank Daniel Haie Najafabadi, Xilin Zhou, Isabelle Phinney, Nao Sumi and Mary Kreidel, with whom I worked closely at different stages of my PhD. I learned so much from each of them. I thank Kin Chung Fong and Jane Park for collaboration on the kinetic inductance project, Seung Hwan Lee, Jiho Sung and Gio

Scuri for helping with our measurments in their cryostats, Wonjae Lee and Khanh Pham for the collaboration on the BN defect project. I thank my theory collobrators: Jong Yeon Lee, Eslam Khalaf, Patrick Ledwith, Pavel Volkov. All of them are from Ashvin's group and like him have deep insights and taught me so much. I want to thank Margarita Davydova, who is also a theorist but also an artist and helped us make the beautiful art illustration for the TTG paper. I also want to thank Atac Imamoglu for welcoming me to his group during the short visit, and many of his group members, in particular Alperen Tugen, Felix Helmrich, Natasha Kiper, Deepankur Thureja, Gian-Marco Schnüriger, Haydn Adlong, Martin Kroner.

I want to thank all the people I interacted with in the Kim group. Like I cannot think of having a better advisor, I also cannot think of having a better group. It's been so much fun to be working beside this amazing group of people, diverse in both expertise and nationalities. I learn not only different kinds of physics from them, but also different cultures and perspectives. I want to thank some of the past members: Laurel Anderson, Andy Joe, Mehdi Rezaee, Rebecca Engelke, Önder Gul, Antti Laitinen, Frank Zhao, Jonah Waissman, Jing Shi, Aterm Talanov, Hyobin Yoo, Luis Jauregui, Qi Yang, and Dapeng Ding. Also some of the current members: Tom Werkmeister, Zhongying Yan, Jonathan Zauberman, Andrés Valdivia, Alex Cui, James Ehrets, Joon Young Park, Thao Dinh, Athalia Meron, Jeffrey Kwan, Jue Wang, Sejoon Lim, Nadine Leisgang, Grace Chen, Terry Phang, Kierstin Torres, Christina Henzinger, Talieh Ghiasi, Tae-In Jeong. I want to particularly thank Laurel, Andy, Mehdi, Alex, Christina, Tae-In for being more than a colleague to me but also a personal friend.

I want to thank my housemates, Haoyu Guo, Ruolan Xue, Chenyuan Li, Deng Pan. We lived together for 4 plus years and have become a family now. I don't know I could have lived through covid without them. We cooked and ate meals together everyday, occasionally even hosted physics seminars in that unbearable 2020 summer. We witnessed each other's significant moments. We will stay on as a family.

I want to thank all my other friends. At the beginning of my PhD, I told myself that there are two things that can make me happy: pursue physics and build relationships with people. I'm lucky enough to make many wonderful friends over the years. Many of them are not only passionate about Science but also kind, offering my not only inspirations but also emotional support. Thank you, Yicheng Bao, you constant passion and optimism are truly attractive; thank you, Ruihua Fan, you are always a deep thinker and has a black humor; thank you, Muqing Xu, for your kindness and reliability; thank you, Yi Jia, for always being supportive and trustworthy; thank you, Ziyan Zhu, for sharing many personal traits and; thank you, Erik Knall, for Hengyun Zhou, Nikola Maksimovic, Clemens Kuhlenkamp, Jane Park, and many more Xirui Wang, Grace Zhang, Ian Davenport, Valentin Walther, Lukas Homeier, Thanh Nguyen, Yimu Bao, Eric Fell, Andrew Pierce, Sasha Zibrov, Elizabeth Park, Lingyang Wu, Helin Zhang, Pasha Stroganov... Friendship is the biggest resrouce.

Finally I want to thank my family—my parents and sister. This PhD is not only my own achievement, but also the culmination of my family's decade-long striving for a better life. Different from most at Harvard, I come from a coal mining town where my father works as a coal miner, and my mother did too until I was born. Both coming from remote villages in China and a background of extreme poverty, my parents moved to the town, which is closer to a big city, in hopes that hard work could change their destiny. When I was a child, my father used to tell me his childhood stories as jokes to make me laugh. He would talk about how, due to the lack of money and food, he was often too hungry to fall asleep at night. When he complained to his mother, her response was only a scolding: "Go to sleep quickly; you won't feel hungry when you are asleep." Or the time he needed to turn in his tuition and was given an egg to exchange for money. But his shoes, disproportionately large because they had been handed down from adults, caused him to trip and break the egg. These stories easily cracked me up as a naïve child, but brought me to tears when I grew up and understood the unimaginable hardships they represented. Equally unimaginable to me was how, given

such impoverished conditions, they obtained the strength and determination to venture into an unknown city to make a living, and the conviction that they must work hard and make life better. They took on all kinds of labor work just to survive. Then later, due to the previous extreme labor work, my father suffered from several years' illness, even nearing death at one point, and my mother carried the whole family on her shoulder.

However, despite all the difficulties and even disasters, I and my sister had generally happy childhood. There lacked money and toys, but never laugh and care. They also prioritized our education and started teach us math and reading from a very young age, despite that the higher education for them was elementary school for my father, and middle school for my mother. They are live examples for us to know that we must also work hard to make life better. I'm also thankful for the freedom they gave me. They never asked me to go for a money making job. I was luckily to be pursuing my interest from an unprivileged background.

I'm glad I have the best of my youth here. Looking back, I have grown so much and am a completely different person now from who I was 7 years ago. I looking forward the future adventures to keep pursuing physics and relationships with people.

1

Introduction

As opposed to a gas of non-interacting particles, condensed matter physics is a study of "condensed" systems, where a large number of particles interact with each other and give rise to emergent phenomena and new laws that are fundamentally different from those of each individual constituent particle. This is the well-known principle of "more is different" by Philip W. Anderson [1]. A typical many-body system of such kind is a solid state crystal, where atoms strongly bond with each other through their valence electrons and form a periodic lattice. These valence electrons are now not limited to their original localized atomic orbitals but can travel in some sense "freely" in the lattice characterized by a lattice momentum and their eigenenergies form an energy band. They further interact with each other through Coulomb interactions. The most general Hamiltonian of this system

can be written as

$$H = \sum_{\text{electron}} \left[\frac{\mathbf{p}_i^2}{2m_e} + V_{\text{e-e}}(\mathbf{r}_i - \mathbf{r}_j) + \sum_{\text{ion}} V_{\text{ion-e}}(\mathbf{R}_I - \mathbf{r}_i) \right] + \sum_{\text{ion}} \left[\frac{\mathbf{P}_I^2}{2M_{\text{ion}}} + V_{\text{ion-ion}}(\mathbf{R}_I - \mathbf{R}_J) \right]$$

where $\mathbf{p}_i$, $\mathbf{r}_i$ and m_e represent electrons' momentum, position and mass, respectively, $\mathbf{P}_I$, $\mathbf{R}_I$ and M_{ion} ions' momentum, position and mass, respectively, $V_{\text{e-e}}$, $V_{\text{ion-e}}$ and $V_{\text{ion-ion}}$ Coulomb interactions between electron-electron, ion-electron and ion-ion, respectively. This seemingly simple Hamiltonian is in fact incredibly hard to solve most of the time, yet it leads to a myriad of complex phenomena in materials and many associated technical applications. Because of the dramatic differences in mass between electrons and ions, we can often decouple the two and focus on the electronic degrees of freedom, which are responsible for some of the most interesting phases of matter. In some sense, a big bulk of condensed matter study is the study of the many-body system of electrons in the environment of crystal lattices.

Despite the myriad phases of matter, there are actually good principles that classify them and help us understand them. Originally it was understood that symmetry dictates phases of matter thanks to Landau and Ginzburg. The process of a system transitioning from a disordered state into a more ordered state is essentially the process of certain symmetry spontaneously breaking. For example, the paramagnet to ferromagnet transition corresponds to the breaking of spin $SU(2)$ symmetry. However it was found that there are obviously different states of matter that share the same symmetry, such as integer quantum Hall states at different integer fillings. In this new regime of phase transitions, not symmetry, but topology plays the key role. The topology here is related to band topology and and states of matter involved are still product states in the language of quantum information science. Later, it was realized that there is a third and even more exotic class of phases termed topological ordered states. They represent the most frontier of condensed matter physics. Theories capturing these states show that they are characterized by long-range quantum entan-

glement, fractional excitations and topological degeneracy, and they can be used for topological quantum computation. Distinct from the previous two classes, topological ordered states cannot be simply written as product states of the large number of constituent objects, which are strongly entangled with each other. There is no "order" in the traditional sense in fact there is a good analogy where topological ordered states are similar to a disordered liquid compared to ordered states but they are melted by quantum fluctuations instead of thermal ones. The lack of traditional order also makes it hard to study them because traditional condensed matter methods access primarily thermodynamical quantities or linear responses, which often provide only indirect information – or none at all – about their quantum nature. This fundamentally limits our ability of finding new physics and pursuing next-generation quantum materials. For example, one of the most exotic states of matter in condensed matter physics is the topological ordered states such as fractional Chern insulators and quantum spin liquids. But the lack of direct tools to probe their quantum aspects severely hinders their experimental realization and further application. New tools are needed to better study these classes of matter.

Notably, with the recent quantum evolution, many atomic systems have become new playgrounds for studying many body physics. Two of the most promising platforms are optical lattices and Rydberg atom arrays. See Table 1.1 for a comparison for these different systems. Although these systems are in a completely different environment and are controlled and measured using different schemes, they are in rough stroke the same as solid state system, where large number of identical objects interact with each and unique many-body states emerge. Whereas the solid state is a system of electrons, optical lattices are a system of certain atoms governed by a Hubbard Hamiltonian and Rydberg atom array is a system of spins (two-level systems) governed by a particular spin Hamiltonian. These atom systems have recently demonstrated their power in studying the topological ordered states given their unique capability to perform quantum state measurements and non-local entanglement measurements.

	solids	optical lattice [2]	atom array [3]
	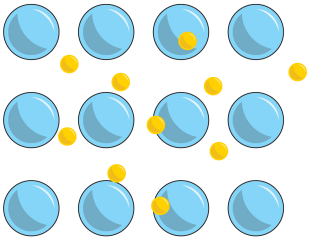	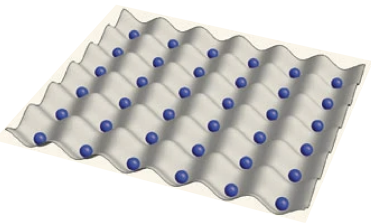	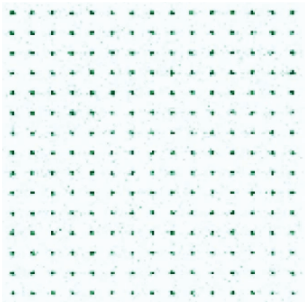
Interacting objects	electrons	atoms	spins (two-level systems)
Hamiltonians	$H_e = \sum_{\text{electron}}(\frac{p_i^2}{2m_e} + V_{e-e}(\mathbf{r}_i - \mathbf{r}_j) + \sum_{\text{ion}} V_{\text{ion}-e}(\mathbf{R}_I - \mathbf{r}_i))$	$H_{\text{Hubbard}} = -t\sum_{\langle i,j\rangle,\sigma} c^\dagger_{i,\sigma}c_{j,\sigma} + U\sum_i \frac{n_i(n_i-1)}{2} + \sum_{i,\sigma}\varepsilon_i n_{i,\sigma}$	$H_{\text{spin}} = \frac{\hbar\Omega}{2}\sum_i \sigma_x^i - \hbar\delta\sum_i n_i + \sum_{i<j} V_{ij}n_i n_j$
System size	1 μm^2 2D sample: $\sim 10^7$, moiré: $\sim 10^4$	$\sim 10^2 - 10^4$	$\sim 10^2 - 10^3$
Tuning knobs	chemical composition, doping, lattice, pressure, strain, magnetic/electric field, twisting(moiré)...	atomic species, lattice arrangement, Hamiltonian parameters, filling factor...	
Measurement	specific heat, density of states, electrical/thermal conductivity, optical response, scattering experiments, STM...	single-site imaging (allows for non-local operator measurement, entanglement entropy)	

Table 1.1: A comparison of different many-body physics platforms

The study of condensed matter physics can potentially learn methods in these systems and apply them to future material study. In fact, I believe the technologies developed in these fields can radically transform how we study materials. In the field of quantum science, the quantum states and quantum entanglement of qubits are measured and controlled on a regular basis. The methodology can be applied to probing the non-local quantum entanglement in condensed matter quantum states. For example, one could envision embedding a 2D material into a superconducting circuit or

a quantum-defect-hosting structure and coupling the material's states with the qubits. These platforms in fact already share to some extent similar workflow of on-chip device fabrication, characterization, and cryogenic measurements. By performing correlated measurements between two qubits, one can extract non-local information and obtain a picture of quantum entanglement within the target material. This would give us a completely new view of quantum materials, which may in turn illuminate how to utilize them for alternative quantum computing platforms.

In this thesis, I will mainly focus on the current 2D material system and methods used in more traditional condensed matter physics. I demonstrate how we engineer interaction drive physics and achieve new states of matter by creating novel use graphene heterostructrures, namely twisted structures and double layer structures of graphene.

1.1 Band structures of graphene and twisted graphene

As we have introduced above, the starting point of understanding the many-body system of electrons in a solid is to first understand how they move on a single-particle level, i.e., their non-interacting band structure. Here we give a quick review on the band structure calculation for monolayer graphene, Bernal bilayer graphene and twisted multilayer graphene.

We use tight-binding model to calculate the band structure of monolayer graphene[4,5]. The honey comb lattice of graphene is a triangular lattice with lattice vectors given by: $\mathbf{a}_1 = a(1/2, \sqrt{3}/2)$, $\mathbf{a}_2 = a(-1/2, \sqrt{3}/2)$ as shown in Fig 1.1, where a = 0.246 nm is the lattice constant and related to the nearest neighbour carbon atom distance $d = \frac{a}{\sqrt{3}}$= 0.142 nm. Each unit cell has two carbon sites $\alpha = A, B$ and we define an in-unit-cell vector for site B with respect to A: $\boldsymbol{\tau} = \frac{a}{\sqrt{3}}(0, 1)$. In fact we can define all three relative position vectors of the three nearest-neighbour B sites with respect to an A site: $\boldsymbol{\delta}_1 = \boldsymbol{\tau}, \boldsymbol{\delta}_2 = \boldsymbol{\tau} - \mathbf{a}_1, \boldsymbol{\delta}_3 = \boldsymbol{\tau} - \mathbf{a}_2$.The real space triangular lattice has a honeycomb reciprocal lattice in momentum space with the corresponding reciprocal lattice vector $\mathbf{b}_1 = \frac{4\pi}{\sqrt{3}a}(\sqrt{3}/2, 1/2)$,

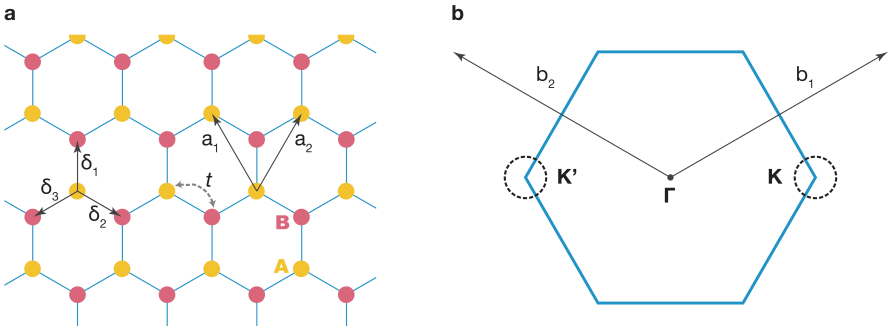

Figure 1.1: **a**, honeycomb lattice of graphene with A and B sublattice per unit cell. $\mathbf{a}_1$ and $\mathbf{a}_2$ are primitive lattice vector and $\boldsymbol{\delta}_{1,2,3}$ are position vectors for nearest neighbours. **b**, reciprocal lattice in Brillouin zone with two inequivalent valleys $\mathbf{K}, \mathbf{K}'$

.

$\mathbf{b}_2 = \frac{4\pi}{\sqrt{3}a}(-\sqrt{3}/2, 1/2)$. Under the single p_z orbital tight-binding model and considering only the nearest-neighbour hopping being $-t$, the Hamiltonian for monolayer graphene can be written as

$$
\begin{aligned}
H_{\text{mono}} &= -t \sum_{\mathbf{R},i=1,2,3} c_A^\dagger(\mathbf{R}) c_B(\mathbf{R}+\boldsymbol{\delta}_i) + \text{h.c.} \\
&= \sum_{\mathbf{k}} \begin{pmatrix} c_A^\dagger(\mathbf{k}) & c_B^\dagger(\mathbf{k}) \end{pmatrix} \begin{pmatrix} 0 & -tf(\mathbf{k}) \\ -tf^*(\mathbf{k}) & 0 \end{pmatrix} \begin{pmatrix} c_A(\mathbf{k}) \\ c_B(\mathbf{k}) \end{pmatrix} \\
f(\mathbf{k}) &= \sum_{i=1,2,3} e^{i\mathbf{k}\cdot\boldsymbol{\delta}_i}
\end{aligned}
$$

where the sum over $\mathbf{R}$ is over all the unit cells, $c_\alpha^\dagger(\mathbf{R}+\mathbf{r})$ and $c_\alpha(\mathbf{R}+\mathbf{r})$ are creation and annihilation operators for site α in localized Wannier wavefunction basis and they have corresponding Bloch wave function operators in the momentum space: $c_\alpha^\dagger(\mathbf{k}) = \frac{1}{\sqrt{N}} \sum_{\mathbf{R}} e^{i\mathbf{k}\cdot(\mathbf{R}+\mathbf{r})} c_\alpha^\dagger(\mathbf{R}+\mathbf{r})$, $c_\alpha(\mathbf{k}) = \frac{1}{\sqrt{N}} \sum_{\mathbf{R}} e^{-i\mathbf{k}\cdot(\mathbf{R}+\mathbf{r})} c_\alpha(\mathbf{R}+\mathbf{r})$. Solving for the eigenvalues of the Hamiltonian gives

$$
E(\mathbf{k}) = \pm t \sqrt{4\cos\left(\frac{1}{2}ak_x\right)\cos\left(\frac{\sqrt{3}}{2}ak_y\right) + 2\cos\left(ak_x\right) + 3}
$$

Near the two time-reversal symmetric points in momentum space $\mathbf{K} = \frac{4\pi}{3a}(1, 0)$ and $\mathbf{K}' = -\mathbf{K}$, the Hamiltonian reduces to a Dirac Hamiltonian

$$H^{\pm\mathbf{K}}_{\text{mono}}(\mathbf{q}) = \hbar v_F \begin{pmatrix} 0 & \pm q_x - iq_y \\ \pm q_x + iq_y & 0 \end{pmatrix} = \hbar v_F \mathbf{q} \cdot (\pm\sigma_x, \sigma_y), \quad \mathbf{q} = \mathbf{k} - (\pm\mathbf{K})$$

where the Fermi velocity $v_F = \frac{\sqrt{3}ta}{2\hbar}$. The *ab initio* calculations provide t = 2.97 eV, giving $v_F = 0.96 \times 10^6$ m/s.

In this low-energy limit, we may consider the annihilation operator for an electron near the $\mathbf{K}$ valley varying slowly in real space, with the slow modulation determined by a small momentum $\mathbf{q}$,

$$\chi^{\mathbf{K}}_{\alpha}(\mathbf{r}) = \int \frac{d\mathbf{k}}{(2\pi)^2} e^{i(\mathbf{k}-\mathbf{K})\cdot\mathbf{r}} c_{\alpha}(\mathbf{k}) = \int \frac{d\mathbf{q}}{(2\pi)^2} e^{i\mathbf{q}\cdot\mathbf{r}} c_{\alpha}(\mathbf{q})$$

Then we can obtain the corresponding real space Hamiltonian given that the total Hamiltonian being $H^{\mathbf{K}}_{\text{mono}} = \int \frac{d\mathbf{q}}{(2\pi)^2} H^{\mathbf{K}}_{\text{mono}}(\mathbf{q}) = \int d\mathbf{r} H^{\mathbf{K}}_{\text{mono}}(\mathbf{r})$

$$H^{\mathbf{K}}_{\text{mono}}(\mathbf{r}) = -i\hbar v_F \boldsymbol{\sigma} \cdot \nabla_{\mathbf{r}}$$

For Bernal bilayer graphene, the Hamiltonian is an extension of that of monolayer graphene with the addition of interlayer hopping terms $(\gamma_1, \gamma_3, \gamma_4) = (0.361, 0.283, 0.138)$ eV[6]. They correspond to the next order hopping terms with larger carbon-carbon distances.

$$
\begin{aligned}
H_{\mathrm{bi}} = & -t \sum_{\mathbf{R},i} c_{A,1}^{\dagger}(\mathbf{R}) c_{B,1}(\mathbf{R}+\boldsymbol{\delta}_i) + c_{A,2}^{\dagger}(\mathbf{R}-\boldsymbol{\delta}_i) c_{B,2}(\mathbf{R}) + \mathrm{h.c.} \\
& + \gamma_1 \sum_{\mathbf{R},i} c_{A,1}^{\dagger}(\mathbf{R}) c_{B,2}(\mathbf{R}) + \mathrm{h.c.} \\
& + \gamma_3 \sum_{\mathbf{R},i} c_{B,1}^{\dagger}(\mathbf{R}+\boldsymbol{\delta}_1) c_{A,2}(\mathbf{R}+\boldsymbol{\delta}_1+\boldsymbol{\delta}_i) + c_{A,2}^{\dagger}(\mathbf{R}-\boldsymbol{\delta}_1) c_{B,1}(\mathbf{R}-\boldsymbol{\delta}_1-\boldsymbol{\delta}_i) + \mathrm{h.c.} \\
& + \gamma_4 \sum_{\mathbf{R},i} c_{A,1}^{\dagger}(\mathbf{R}) c_{A,2}(\mathbf{R}-\boldsymbol{\delta}_i) + c_{B,2}^{\dagger}(\mathbf{R}) c_{B,1}(\mathbf{R}+\boldsymbol{\delta}_i) + \mathrm{h.c.} \\
& + U_1 \sum_{\mathbf{R},i} c_{A,1}^{\dagger}(\mathbf{R}) c_{A,1}(\mathbf{R}) + c_{A,1}^{\dagger}(\mathbf{R}+\boldsymbol{\delta}_i) c_{A,1}(\mathbf{R}+\boldsymbol{\delta}_i) \\
& + U_2 \sum_{\mathbf{R},i} c_{B,2}^{\dagger}(\mathbf{R}) c_{B,2}(\mathbf{R}) + c_{A,2}^{\dagger}(\mathbf{R}-\boldsymbol{\delta}_i) c_{A,2}(\mathbf{R}-\boldsymbol{\delta}_i) \\
= & \sum_{\mathbf{k}} \begin{pmatrix} c_{A,1}^{\dagger}(\mathbf{k}) \\ c_{B,1}^{\dagger}(\mathbf{k}) \\ c_{A,2}^{\dagger}(\mathbf{k}) \\ c_{B,2}^{\dagger}(\mathbf{k}) \end{pmatrix}^{T} \begin{pmatrix} U_1 & -tf(\mathbf{k}) & \gamma_4 f^{*}(\mathbf{k}) & \gamma_1 \\ -tf^{*}(\mathbf{k}) & U_1 & \gamma_3 f(\mathbf{k}) & \gamma_4 f^{*}(\mathbf{k}) \\ \gamma_4 f(\mathbf{k}) & \gamma_3 f^{*}(\mathbf{k}) & U_2 & -tf(\mathbf{k}) \\ \gamma_1 & \gamma_4 f(\mathbf{k}) & -tf^{*}(\mathbf{k}) & U_2 \end{pmatrix} \begin{pmatrix} c_{A,1}(\mathbf{k}) \\ c_{B,1}(\mathbf{k}) \\ c_{A,2}(\mathbf{k}) \\ c_{B,2}(\mathbf{k}) \end{pmatrix}
\end{aligned}
$$

Here all the terms are the same as the monolayer case and U_1 and U_2 are the electrostatic potentials for layer 1 and 2 respectively when the bilayer graphene is under an electric field.

The band structure of twisted bilayer graphene (TBG) with a twist angle θ can be calculated using the well-known "continuum theory"[7,8]. The general form of its Hamiltonian is

$$
H_{\mathrm{TBG}} = \sum_{\mathbf{R}_1,\mathbf{R}_2} \begin{pmatrix} H_1(\mathbf{R}_1) & T_{12}(\mathbf{R}_1,\mathbf{R}_2) \\ T_{12}^{\dagger}(\mathbf{R}_1,\mathbf{R}_2) & H_2(\mathbf{R}_2) \end{pmatrix}
$$

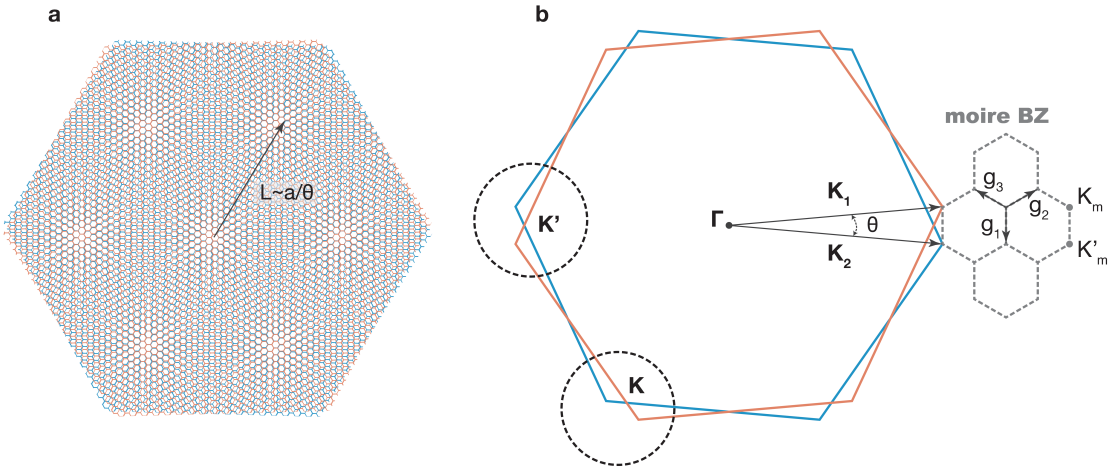

Figure 1.2: **a**, a illustration of moiré pattern formed by twisting two layers of graphene **b**, moiré Brillouin zones formed at each original graphene valley

.

where $\mathbf{R}_{l=1,2}$ are the positions in the two layers, $H_{l=1,2}(\mathbf{R})$ are the Hamiltonians for each graphene layer and in the low-energy limit, they are just the Dirac Hamiltonians that we have already solved for, but in rotated coordinates now. $T_{12}(\mathbf{R}_1, \mathbf{R}_2)$ is the hopping term between the two layers and the key term that results in many interesting new features of TBG.

A Dirac Hamiltonian rotated by an angle of $\theta_{l=1,2}$ (for TBG with a twist angle θ, we can have $\theta_{l=1,2} = \pm\frac{\theta}{2}$ or $\theta_{l=1,2} = \theta, 0$) can be derived using a rotation matrix in momentum space $R(\theta_l) = \begin{pmatrix} \cos\theta_l & -\sin\theta_l \\ \sin\theta_l & \cos\theta_l \end{pmatrix}$, which can be conveniently represented using which can be conviently represented using Pauli matrix σ_y as $R(\theta_l) = e^{-i\theta_l\sigma_y}$:

$$H_l^{\mathbf{K}}(\mathbf{q}) = \hbar v_F(R(\theta_l)\mathbf{q}) \cdot \boldsymbol{\sigma} = \hbar v_F \mathbf{q} \cdot (R(-\theta_l)\boldsymbol{\sigma}) = \hbar v_F \mathbf{q} \cdot \boldsymbol{\sigma}_{\theta_l}$$

where $\boldsymbol{\sigma} = (\sigma_x, \sigma_y)$, and $\boldsymbol{\sigma}_{\theta_l} = e^{i\sigma_z\frac{\theta_l}{2}}(\sigma_x, \sigma_y)e^{-i\sigma_z\frac{\theta_l}{2}}$. Here we have used the relation between rotation

in real space and rotation in spin space. Similarly for $\mathbf{K}' = -\mathbf{K}$

$$H_l^{\mathbf{K}'}(\mathbf{q}) = \hbar v_F \mathbf{q} \cdot \bar{\boldsymbol{\sigma}}_{\theta_l}, \quad \text{with } \bar{\boldsymbol{\sigma}}_{\theta_l} = e^{i\sigma_z \frac{\theta_l}{2}}(-\sigma_x, \sigma_y) e^{-i\sigma_z \frac{\theta_l}{2}}$$

From now on, we mainly focus on the $\mathbf{K}$ valley and $\mathbf{K}'$ can always be similarly derived. Similar to the monolayer graphene case, we can write a real space Hamiltonian for low energy electrons near $\mathbf{K}$,

$$H_l^{\mathbf{K}}(\mathbf{r}) = -i\hbar v_F \boldsymbol{\sigma}_{\theta_l} \cdot \nabla_{\mathbf{r}}$$

Now we try to calculate the more difficult hopping term. The general form of the hopping term is

$$V_{12}(\mathbf{R}_1, \mathbf{R}_2) = \sum_{\mathbf{R}_1,\alpha,\mathbf{R}_2,\beta} c^\dagger_{\alpha,1}(\mathbf{R}_1) T_{12}^{\alpha,\beta}(\mathbf{R}_1, \mathbf{R}_2) c_{\beta,2}(\mathbf{R}_2)$$

α, β are the sublattice index in layer 1 and 2 respectively, and $T_{12}^{\alpha\beta}(\mathbf{R}_1, \mathbf{R}_2)$ is the position dependent. We can reasonably assume this term is only determined by distance so that $T_{12}^{\alpha\beta}(\mathbf{R}_1, \mathbf{R}_2) = T_{12}^{\alpha\beta}(\mathbf{R}_1 + \boldsymbol{\tau}_{1,\alpha} - \mathbf{R}_2 - \boldsymbol{\tau}_{2,\beta})$, with a 2D Fourier transform $T_{12}^{\alpha\beta}(\mathbf{r}) = \int \frac{d^2\mathbf{p}}{(2\pi)^2} e^{i\mathbf{p}\cdot\mathbf{r}} T_{12}^{\alpha\beta}(\mathbf{p})$. This translation symmetry leads to an interlayer momentum (mod (lattice momentum)) conservation condition, i.e., an Umklapp condition between the two layers. More specifically, when we consider the hopping term in momentum space

$$\begin{aligned}
T_{12}^{\alpha\beta}(\mathbf{k}_1, \mathbf{k}_2) &= \frac{1}{N} \sum_{\mathbf{R}_1,\mathbf{R}_2} e^{-i\mathbf{k}_1\cdot(\mathbf{R}_1+\boldsymbol{\tau}_{1,\alpha})} T_{12}^{\alpha\beta}(\mathbf{R}_1, \mathbf{R}_2) e^{i\mathbf{k}_2\cdot(\mathbf{R}_2+\boldsymbol{\tau}_{2,\beta})} \\
&= \frac{1}{N} \sum_{\mathbf{R}_1,\mathbf{R}_2} e^{-i\mathbf{k}_1\cdot(\mathbf{R}_1+\boldsymbol{\tau}_{1,\alpha})} e^{i\mathbf{k}_2\cdot(\mathbf{R}_2+\boldsymbol{\tau}_{2,\beta})} \int \frac{d^2\mathbf{p}}{(2\pi)^2} e^{i\mathbf{p}\cdot(\mathbf{R}_1+\boldsymbol{\tau}_{1,\alpha}-\mathbf{R}_2-\boldsymbol{\tau}_{2,\beta})} T_{12}^{\alpha\beta}(\mathbf{p}) \\
&= N \sum_{\mathbf{G}_1,\mathbf{G}_2} e^{-i\mathbf{G}_1\cdot\boldsymbol{\tau}_{1,\alpha}} e^{i\mathbf{G}_2\cdot\boldsymbol{\tau}_{2,\beta}} \int \frac{d^2\mathbf{p}}{(2\pi)^2} T_{12}^{\alpha\beta}(\mathbf{p}) \delta_{\mathbf{G}_1,\mathbf{k}_1-p} \delta_{\mathbf{G}_2,\mathbf{k}_2-p}
\end{aligned}$$

where we have used $\sum_{\mathbf{R}} e^{i\mathbf{k}\cdot\mathbf{R}} = N\sum_G \delta_{\mathbf{k},\mathbf{G}}$. We further use $\delta_{\mathbf{k},\mathbf{k}'} = \frac{(2\pi)^2}{A}\delta(\mathbf{k}-\mathbf{k}')$, where A is the system's total area, then we obtain

$$T_{12}^{\alpha\beta}(\mathbf{k}_1,\mathbf{k}_2) = \frac{N}{A}\sum_{\mathbf{G}_1,\mathbf{G}_2} e^{-i\mathbf{G}_1\cdot\boldsymbol{\tau}_{1,\alpha}} e^{i\mathbf{G}_2\cdot\boldsymbol{\tau}_{2,\beta}} T_{12}^{\alpha\beta}(\mathbf{k}_1-\mathbf{G}_1)\delta_{\mathbf{k}_1-\mathbf{G}_1,\mathbf{k}_2-\mathbf{G}_2}$$

This is saying that during the interlayer hopping process, the momentum change can only be mini-Brillouin zone lattice momentum $\mathbf{k}_1-\mathbf{k}_2 = \mathbf{G}_1-\mathbf{G}_2$. Given that the interlayer distance is $\sqrt{d_\perp^2+r^2}$ where $d_\perp$ is the interlayer distance, $t(q)$ decays rapidly when $qd_\perp > 1$. Therefore in the expression of $T_{12}^{\alpha\beta}(\mathbf{k}_1,\mathbf{k}_2)$ where $\mathbf{k}_1,\mathbf{k}_2$ are close to the $\mathbf{K}$ point so that $\mathbf{k}_1 = \mathbf{K}_1+\mathbf{q}_1$ and $T_{12}^{\alpha\beta}(\mathbf{K}_1+\mathbf{q}_1-\mathbf{G}_1) \approx t_\perp(|\mathbf{K}_1-\mathbf{G}_1|)$, we only need to keep the three terms that give the smallest and the same $|\mathbf{K}_1-\mathbf{G}_1|$, corresponding to $\mathbf{G}_1 = 0, \mathbf{b}_{1,1}, -\mathbf{b}_{1,2}$, where the first subscript index denotes the layer index and the second one denotes the two reciprocal lattice vectors. Then we have

$$T_{12}^{\alpha\beta}(\mathbf{q}_1,\mathbf{q}_2) = \frac{t_\perp(|\mathbf{K}|)}{A_{\text{unit}}}\left(\begin{pmatrix}1&1\\1&1\end{pmatrix}\delta_{\mathbf{q}_1-\mathbf{q}_2,\mathbf{g}_1} + \begin{pmatrix}1&e^{i\frac{2\pi}{3}}\\e^{-i\frac{2\pi}{3}}&1\end{pmatrix}\delta_{\mathbf{q}_1-\mathbf{q}_2,\mathbf{g}_2} + \begin{pmatrix}1&e^{-i\frac{2\pi}{3}}\\e^{i\frac{2\pi}{3}}&1\end{pmatrix}\delta_{\mathbf{q}_1-\mathbf{q}_2,\mathbf{g}_3}\right)$$

where we have used $\mathbf{b}_{l,1}\cdot\boldsymbol{\tau}_{l,B} = \frac{2\pi}{3}, \mathbf{b}_{l,2}\cdot\boldsymbol{\tau}_{l,B} = -\frac{2\pi}{3}$ for our choice of these vectors, B denotes the sublattice site B. And we defined the three small reciprocal lattice vectors in the mini-Brillioun zone,

$$\begin{aligned}
\mathbf{g}_1 &= \mathbf{K}_1-\mathbf{K}_2 = 2|\mathbf{K}|\sin(\theta/2)(0,-1)\\
\mathbf{g}_2 &= \mathbf{K}_1-\mathbf{K}_2+\mathbf{b}_{1,1}-\mathbf{b}_{2,1} = 2|\mathbf{K}|\sin(\theta/2)(\frac{\sqrt{3}}{2},\frac{1}{2})\\
\mathbf{g}_3 &= \mathbf{K}_1-\mathbf{K}_2+\mathbf{b}_{1,2}-\mathbf{b}_{2,2} = 2|\mathbf{K}|\sin(\theta/2)(-\frac{\sqrt{3}}{2},\frac{1}{2})
\end{aligned}$$

This is assuming we have $\theta_{l=1,2} = \pm\frac{\theta}{2}$, more generally we have

$$g_1 = 2|\mathbf{K}|\sin(\theta_{12}/2)R(\varphi_{12})(0,-1), \quad g_{2,3} = R(\pm\frac{2\pi}{3})\mathbf{q}_1, \quad \text{where } \theta_{12} = \theta_1-\theta_2, \quad \varphi_{12} = (\theta_1+\theta_2)/2$$

Having solved for all the terms of the TBG Hamiltonian, now we can try to get a more intuitive picture. In fact, we can understand the calculation of TBG bands effectively as a tight-binding model in k-space. For calculating energy at a particular $\mathbf{q}$ point, we create a honeycomb lattice using this $\mathbf{q}$ point as a lattice site A' and $\mathbf{g}_{1,2,3}$ as the relative position vectors for the nearest-neighbour sites B' similar to the real space vector $\boldsymbol{\tau}_{1,2,3}$. Then the onsite energy of this k-sapce lattice is given by $H_1(\mathbf{q})$ or $H_2(\mathbf{q})$ depending on A' or B' site, and the "hopping" is given by $T_{12}^{\alpha\beta}(\mathbf{q}_1, \mathbf{q}_2)$ which is strictly limited to nearest neighbours.The original continuum mode obtained magic angle by calculating Fermi velocity v_F.

Again by using

$$\int \frac{d\mathbf{q}_1}{(2\pi)^2}\frac{d\mathbf{q}_2}{(2\pi)^2} c^\dagger_{\alpha,1}(\mathbf{q}_1) T_{12}^{\alpha\beta}(\mathbf{q}_1, \mathbf{q}_2) c_{\beta,2}(\mathbf{q}_2) = \int d\mathbf{r}_1 d\mathbf{r}_2 c^\dagger_{\alpha,1}(\mathbf{r}_1) T_{12}^{\alpha\beta}(\mathbf{r}_1, \mathbf{r}_2) c_{\beta,2}(\mathbf{r}_2)$$

in real space, we have

$$T_{12}^{\alpha\beta}(\mathbf{r}) = \frac{t_\perp(|\mathbf{K}|)}{A_{\text{unit}}} \begin{pmatrix} U_0(\mathbf{r}) & U_1(\mathbf{r}) \\ U_1^*(-\mathbf{r}) & U_0(\mathbf{r}) \end{pmatrix}, \quad U_0(\mathbf{r}) = \sum_{n=1}^{3} e^{-i\mathbf{g}_n\cdot\mathbf{r}}, \quad U_1(\mathbf{r}) = \sum_{n=1}^{3} e^{im(n-1)\frac{2\pi}{3}} e^{-i\mathbf{g}_n\cdot\mathbf{r}}$$

In the ideal moiré pattern of two rigid honeycomb lattices, the local atomic configuration between the two layers is a continuous distribution from AA (A sites of the two layers are aligned) to AB (top A sites is aligned with bottom B site) or BA. However in real materials of TBG, there are strong relaxation effects for AB and BA have lower configuration energy than AA, making small twist angle TBG a pattern of periodically distributed large AB and BA regions separated by narrow AA boundaries[9]. This effect can be taken into account simply by including two factors $w_{AA} < w_{AB}$ for the larger AB regions contributing more interlayer coupling.

$$T_{12}^{\alpha\beta}(\mathbf{r}) = \begin{pmatrix} w_{AA}U_0(\mathbf{r}) & w_{AB}U_1(\mathbf{r}) \\ w_{AB}U_1^*(-\mathbf{r}) & w_{AA}U_0(\mathbf{r}) \end{pmatrix}$$

The final real space TBG Hamiltonian can be written as

$$H_{\mathrm{TBG}}(\mathbf{r}) = \begin{pmatrix} -i\hbar v_F \sigma_{\theta_1} \cdot \nabla_{\mathbf{r}} & T_{12}(\mathbf{r}) \\ T_{12}^{\dagger}(\mathbf{r}) & -i\hbar v_F \sigma_{\theta_2} \cdot \nabla_{\mathbf{r}} \end{pmatrix}$$

Clearly one can easily generate to multilayer twisted graphene with alternating twist angles [10].

$$H_{\mathrm{TNG}}(\mathbf{r}) = \begin{pmatrix} -i\hbar v_F \sigma_{\theta_1} \cdot \nabla_{\mathbf{r}} & T_{12}(\mathbf{r}) & 0 & \dots & 0 \\ T_{12}^{\dagger}(\mathbf{r}) & -i\hbar v_F \sigma_{\theta_2} \cdot \nabla_{\mathbf{r}} & T_{23}(\mathbf{r}) & \dots & 0 \\ 0 & T_{23}^{\dagger}(\mathbf{r}) & -i\hbar v_F \sigma_{\theta_3} \cdot \nabla_{\mathbf{r}} & \dots & 0 \\ \dots & \dots & \dots & \dots & T_{n-1,n}(\mathbf{r}) \\ 0 & 0 & 0 & T_{n-1,n}^{\dagger}(\mathbf{r}) & -i\hbar v_F \sigma_{\theta_n} \cdot \nabla_{\mathbf{r}} \end{pmatrix}$$

This system forms a hierarchy of twisted angles. In particular, for twisted trilayer graphene, the band structure can be effectively decomposed into that of a twisted bilayer graphene and monolayer graphene.

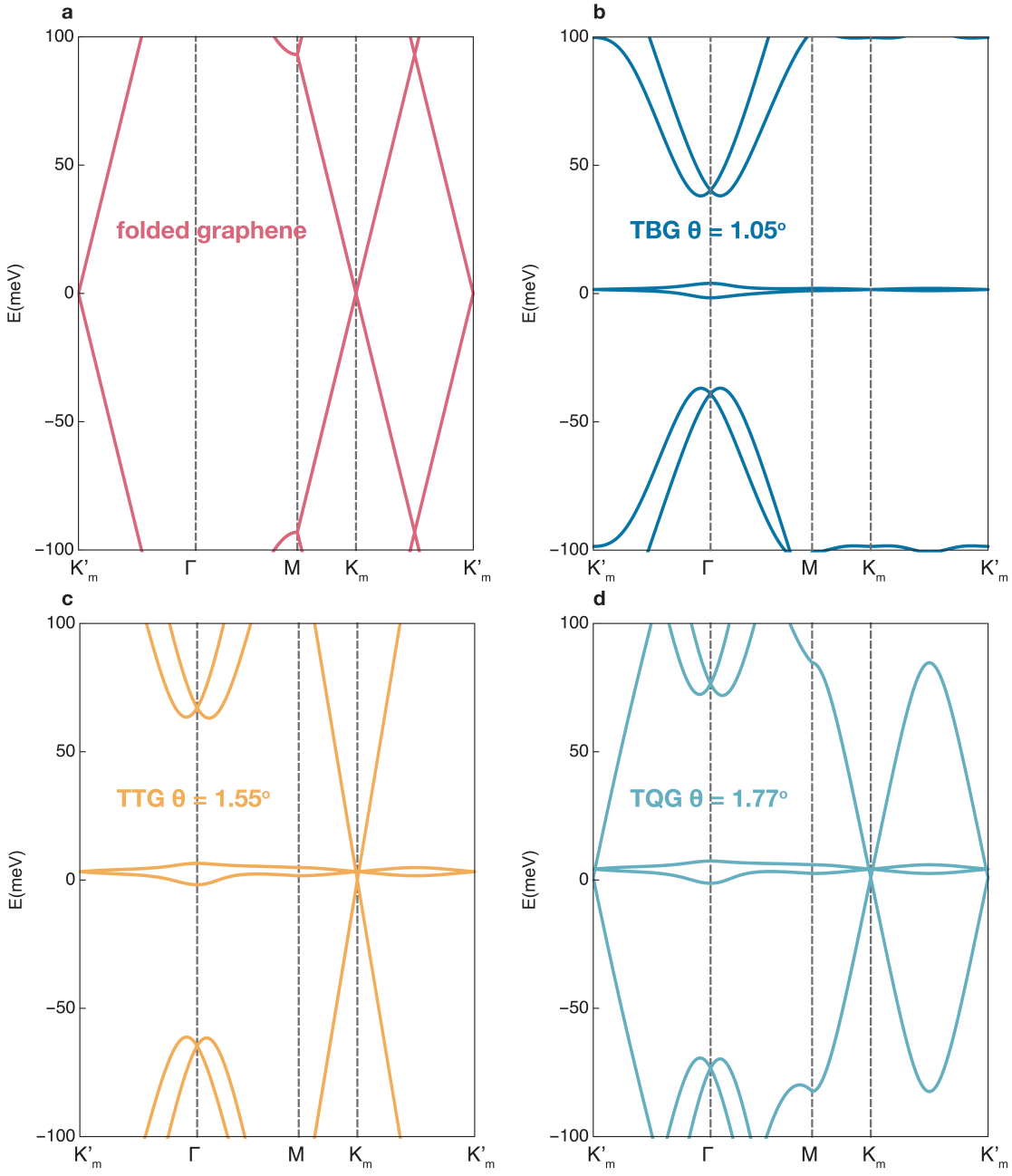

Figure 1.3: **a**, calculated energy bands of two layers of graphene rotated without interlayer hopping. **b**, magic angle TBG bands. **c**, magic angle TTG bands. **b**, magic angle TQG bands.

.

$$H_{\mathrm{TTG}}(\mathbf{r}) = \begin{pmatrix} -i\hbar v_F \sigma_{\theta_1} \cdot \nabla_{\mathbf{r}} & T(\mathbf{r}) & 0 \\ T^{\dagger}(\mathbf{r}) & -i\hbar v_F \sigma_{\theta_2} \cdot \nabla_{\mathbf{r}} & T(\mathbf{r}) \\ 0 & T^{\dagger}(\mathbf{r}) & -i\hbar v_F \sigma_{\theta_3} \cdot \nabla_{\mathbf{r}} \end{pmatrix}$$

$$\rightarrow VH_{\mathrm{TTG}}(\mathbf{r})V^{\dagger} = \begin{pmatrix} -i\hbar v_F \sigma_{\theta_1} \cdot \nabla_{\mathbf{r}} & \sqrt{2}T(\mathbf{r}) & 0 \\ \sqrt{2}T^{\dagger}(\mathbf{r}) & -i\hbar v_F \sigma_{\theta_2} \cdot \nabla_{\mathbf{r}} & 0 \\ 0 & 0 & -i\hbar v_F \sigma_{\theta_3} \cdot \nabla_{\mathbf{r}} \end{pmatrix}$$

In Figure 1.3 we show the calculated energy bands for twisted multilayer graphene up to 4 layers as well as two graphene twisted but without any coupling to compare.

1.2 Symmetry and topology in graphene and twisted graphene

Symmetry is important for understanding many condensed matter systems. The most salient feature of monolayer graphene, its Dirac dispersions, are indeed protected by the symmetries in the system, which include time reversal ($\mathcal{T}$) symmetry, spin $SU(2)$ symmetry (because spin-orbit coupling is very weak), C_3 rotation symmetry, C_2 inversion symmetry (note in 2D, inversion is the same as C_2 rotation around honeycomb center, so this combined with C_3 gives C_6 rotation symmetry), translational symmetry , mirror symmetry etc. The lecture notes by Leon Balents give a good argument for how these symmetries can stabilize the Dirac cones [11].

Rewriting the Dirac Hamiltonian that we have derived by now include both $\mathbf{K}$ and $\mathbf{K}'$ valley:

$$H(\mathbf{q}) = \hbar v_F(\mu_z \sigma_x q_x + \sigma_y q_y)$$

where σ_x and σ_y are still Pauli matrices in sublattice space but $\mu_z = \begin{pmatrix} 1 & 0 \\ 0 & -1 \end{pmatrix}$ is the Pauli matrix in $\mathbf{K}$ and $\mathbf{K}'$ valley space. In order to gap out Dirac cones, one needs to add a mass term proportional to $M\sigma_z$ to the Hamiltonian. $SU(2)$ spin symmetry requires that this term cannot contain any terms other than identity $\mathbf{I}$ in spin space. Translation symmetry ensures momentum conservation up to a lattice momentum so two valleys cannot be scattered into each other, excluding $\mu_{x,y}$ in the term. Then the available terms can then be $M\sigma_z$ which adds the same Mass to both valleys or $M\sigma_z\mu_z$ which adds opposite mass to the two valleys. However, time reversal changes the sign of K and swap valleys, $\mu_z \to -\mu_z$. So time reversal symmetry eliminates $M\sigma_z$. Finally inversion operation swaps sublattice so inversion symmetry eliminates $M\sigma_z$. This argument illustrates the power and importance of symmetry.

Another important element in graphene's Dirac dispersion is its band topology. In fact we can see how the Dirac crossings can stable due to the band topology which is enabled by time reversal symmetry and inversion symmetry. The graphene wavefunction near $\mathbf{K}$ valley satisfies similar Schödinger equation as a spin Zeeman Hamiltonian $\mathbf{B} \propto \hbar v_F \mathbf{q}$

$$\hbar v_F \mathbf{q} \cdot \boldsymbol{\sigma} \left|\varphi_{n,\mathbf{q}}\right\rangle = \varepsilon_n \left|\varphi_{n,\mathbf{q}}\right\rangle, \quad \left|\varphi_{n=\pm,\mathbf{q}}\right\rangle = \frac{1}{\sqrt{2}}(1, e^{\pm i\theta_{\mathbf{q}}})^T, \quad \theta_{\mathbf{q}} = \arctan\left(q_y/q_x\right)$$

Here $n = \pm$ correspond to conduction and valence bands. By calculating the Berry connection $\mathcal{A}_{n,\mathbf{q}} = \mathrm{Im}\left[\left\langle\varphi_{n,\mathbf{q}}\right| \nabla_{\mathbf{q}} \left|\varphi_{n,\mathbf{q}}\right\rangle\right]$ and we can obtain the Berry phase around $\mathbf{K}$ point $\Theta_{\mathbf{K}} = \oint_{\mathbf{K}} d\mathbf{q}\mathcal{A}_{n,\mathbf{q}} = \pi$. Similary we could obtain a Berry phase near $\mathbf{K}'$: $\Theta_{\mathbf{K}'} = -\pi$. Now let's argue by contradiction that adding any perturbations that preserve time reversal and inversion symmetry cannot gap out the Dirac points. First of all, the perturbations don not change the wavefunction $\left|\varphi_{n,\mathbf{q}}\right\rangle$ by much therefore the integral $\oint_{\mathbf{K}} d\mathbf{q}\mathcal{A}_{n,\mathbf{q}} = \pi$ shouldn't change much either. However, we can use another method to calculate the Berry phase $\Theta = \iint_{\mathrm{BZ}} d^2\mathbf{q} \cdot \mathcal{B}$ where Berry curva-

ture is defined $\mathcal{B}(\mathbf{q}) = \nabla \times \mathcal{A}$. Under time reversal $\mathcal{B}(\mathbf{q}) \to -\mathcal{B}(-\mathbf{q})$ and under inversion $\mathcal{B}(\mathbf{q}) \to \mathcal{B}(-\mathbf{q})$, therefore in a system with time reversal symmetry and inversion symmetry we expect $\mathcal{B}(\mathbf{q}) = 0$ as long as the wavefunction is analytic at $\mathbf{q}$. If the perturbations indeed gapped out the Dirac points, we would have $\Theta = 0$, which would contradict the result of Θ shouldn't change much from π that's calculated using $\mathcal{A}$. In fact, given that the physical quantity for Berry phase is $\omega(C) = e^{\oint_C d\mathbf{q}\cdot\mathcal{A}_{n,\mathbf{q}}}$, and under $\mathcal{T}$, $\omega(C) \to \omega^*(-C)$ and under inversion C_2, $\omega(C) \to \omega(-C)$, a system with time reversal and inversion symmetry must then have $\omega(C) = \pm 1$, with 1 being trivial and -1 meaning the loop C encircles a degeneracy point [12].

It's also easy to see that the Dirac Hamiltonian has a chiral symmetry: $\{H(\mathbf{q}), \sigma_z\} = 0$ because $H(\mathbf{q})$ is only composed of σ_x and σ_y. This means that for every eigenstate that satisfies $H(\mathbf{q})\,|\psi(q)\rangle = E(\mathbf{q})\,|\psi(\mathbf{q})\rangle$, $\sigma_z\,|\psi(\mathbf{q})\rangle$ is also an eigenstate with energy $-E(\mathbf{q})$. More intuitively, the negative-energy eigenstate of the pseudo-spin Hamiltonian corresponds to the pesudo-spin being aligned with the "magnetic field" proportional to $v_F\mathbf{q}$, then σ_z simply rotates the spin by 180° and gives the positive-energy eigenstate. At $\mathbf{K}$ where $E(0) = 0$, there are two degenerate zero modes with opposite eigenvalues of σ_z.

The continuum model of TBG has essentially all the same symmetries as monolayer graphene except that now the translation symmetry is that of a moiré lattice [13,14]. These symmetries are in fact also good approximations in real TBG systems. A key difference, however, is that in TBG near charge neutrality there are isolated electron bands (with single particle gaps) in each valley, and the small mini Brillouin zone lattice constant decouples the electronic states at the original $\mathbf{K}$ and $\mathbf{K}'$, leading to a separate charge conservation within each valley (valley "charge" conservation) and the corresponding $U(1)$ symmetry for each valley. Given this, we should now consider the role of valley in TBG as completely the same as that of spin. Note that although each valley breaks $\mathcal{T}$ symmetry but preserves $C_2\mathcal{T}$ symmetry. Similar to the robustness of Dirac points in monolayer graphene, the combination of $C_2\mathcal{T}$ symmetry also protects the Dirac points in TBG. There are now two Dirac

points at charge neutrality for each valley coming from the two graphene monolayers and both Dirac points have the same chirality. This non-trivial topology makes it impossible to construct a simple two-band tight-binding model using localized Wannier functions, which would give Dirac points with net zero chirality like in monolayer graphene.

In fact, the topological properties of TBG bands are more easily seen in the wavefunction written in sublattice basis and in the limit of $\kappa = w_{AA}/w_{AB} = 0$. These properties persist even after we recover κ to more realistic value of ~ 0.7. The $\kappa = 0$ limit is called chiral limit because now the Hamiltonian again has a chiral symmetry $\sigma_z H_{\text{TBG}} \sigma_z = -H_{\text{TBG}}$, where $\sigma_z = \text{diag}(1, -1, 1, -1)$ in the basis of $(\psi_{A,1}, \psi_{B,1}, \psi_{A,2}, \psi_{B,2})^T$, where once again A, B denotes sublattice and $l = 1, 2$ denotes the layer index. To get rid of the angle dependence in the Dirac part of the Hamiltonian, we write it in a new basis where the spinor in each layer is rotated by $\pm\theta/2$: $(\chi_{A,1}, \chi_{B,1}, \chi_{A,2}, \chi_{B,2})^T = (e^{i\sigma_z \frac{\theta}{4}}(\psi_{A,1}, \psi_{B,1})^T, (e^{-i\sigma_z \frac{\theta}{4}}(\psi_{A,2}, \psi_{B,2})^T)^T$ so that now we have

$$H_{\text{TBG}}(\mathbf{r}) = \hbar v_F |\mathbf{K}| \theta \begin{pmatrix} 0 & -i(\partial_x - i\partial_y) & 0 & \alpha U_1(\mathbf{r}) \\ -i(\partial_x + i\partial_y) & 0 & \alpha U_1^*(-\mathbf{r}) & 0 \\ 0 & \alpha U_1(-\mathbf{r}) & 0 & -i(\partial_x - i\partial_y) \\ \alpha U_1^*(\mathbf{r}) & 0 & -i(\partial_x + i\partial_y) & 0 \end{pmatrix}, \quad \alpha = \frac{w_{AB}}{\hbar v_F |\mathbf{K}| \theta}$$

Note that the layer dependent rotation doesn't change the form of the hopping matrices because of the opposite rotation angles. To write this more compactly, we shuffle the basis to $(\chi_{A,1}, \chi_{A,2}, \chi_{B,1}, \chi_{B,2})^T$ so that

$$H_{\text{TBG}}(\mathbf{r}) = \hbar v_F |\mathbf{K}| \theta \begin{pmatrix} 0 & D^*(-\mathbf{r}) \\ D(\mathbf{r}) & 0 \end{pmatrix}, \quad D(\mathbf{r}) = \begin{pmatrix} -2i\bar{\partial} & \alpha U_1^*(\mathbf{r}) \\ \alpha U_1^*(-\mathbf{r}) & -2i\bar{\partial} \end{pmatrix}, \quad \bar{\partial} = \frac{1}{2}(\partial_x + i\partial_y)$$

It was found that at certain angles corresponding to certain values of α, the chiral TBG Hamiltonian

has perfectly flat bands with zero energy at all momenta. This means $D(\mathbf{r})\psi_{\mathbf{k}}(\mathbf{r}) = 0$ has solutions at all $\mathbf{k}$. We already know the Bloch wavefunction at $\mathbf{K}$ is a zero-energy solution $D(\mathbf{r})\psi_{\mathbf{K}}(\mathbf{r}) = 0$ because that's where the Dirac point is at $\alpha = 0$ and at finite α it remains a zero mode because time reversal, inversion and C_3 rotation symmetry are still respected. The solution at other momenta is constructed by multiplying $\psi_{\mathbf{K}}(\mathbf{r})$ by a meromorphic function $F_{\mathbf{k}}(z)$ that's Bloch periodic where $z = x + iy$. First of all the zero mode at $\mathbf{K}$ still maintains $D(\mathbf{r})(F_{\mathbf{K}}(z)\psi_{\mathbf{K}}(\mathbf{r})) = F_{\mathbf{K}}(z)D(\mathbf{r})\psi_{\mathbf{K}}(\mathbf{r}) = 0$. However meromorphic function $F(z)$ has poles. Importantly, at magic angles, $\psi_{\mathbf{K}}(\mathbf{r}_0) = 0$ with $r_0 = \frac{1}{3}(\mathbf{a}_1 - \mathbf{a}_2)$. This is the key for cancelling the poles and obtaining flat bands. We omit the details for detailed procedure described in the reference [15] and only give the final wavefunction

$$\psi_{\mathbf{k}}(\mathbf{r}) = e^{i2\pi k_1 z/a_1}\frac{\theta(\frac{z-z_0}{a_1} - \frac{k}{b_2}|\omega)}{\theta(\frac{z-z_0}{a_1}|\omega)}\psi_{\mathbf{K}}(\mathbf{r}), \quad \theta(u|t) = -i\sum_{n=-\infty}^{\infty}(-1)^n e^{i\pi\tau(n+\frac{1}{2})^2 + i\pi(2n+1)u}$$

θ is the Jacobi theta function and $\omega = e^{i\frac{2}{3}\pi}$, z_0, k, a_1, b_2 are complex forms of $\mathbf{r}_0$, $\mathbf{k}$, $\mathbf{a}_1$, $\mathbf{b}_2$. Using this explict wavefunction, one can calculate the Chern number and obtain $C = 1$. Naturally the band related by C_2 or $\mathcal{T}$ has $C = -1$. With valley and spin, we have 4 perfect flat bands with $C = 1$ and 4 with $C = -1$.

1.3 Interactions effects in twisted graphene

Having established that on the single particle level, we can think of the TBG flat bands manifold as 8 degenerate flat bands labeled by their spin, valley and sublattice, now we can include the interaction effects. We follow closely to two references [16,17] for the following discussion. First we are reminded of quantum Hall ferromagnets, where electrons in Landau levels tend to polarize their spins due to interactions, following the similar principle to Hund rules. When the spins are aligned, the orbital part of the wavefunction is anti-symmetric, effectively reducing the electron wavefunction overlap and in turn minimizing the repulsion between electrons. Indeed experimentally, we see correlated

insulators at integer fillings, in some cases, Chern insulators, consistent with flavor polarization defined in 8-fold degenerate manifold of the flat bands.

A generic interacting Hamiltonian projected in the flat band manifold is

$$H = \sum_{\alpha,\mathbf{k}} c^\dagger_{\alpha,\mathbf{k}} h_{\alpha,\beta}(\mathbf{k}) c_{\beta,\mathbf{k}} + \frac{1}{2A}\sum_{\mathbf{q}} V_{\mathbf{q}} :\rho_{\mathbf{q}}\rho_{-\mathbf{q}}:, \quad V(\mathbf{q}) = \int d^2\mathbf{r} V(\mathbf{r}) e^{-i\mathbf{q}\cdot\mathbf{r}}$$

$$\rho_{\mathbf{q}} = \sum_{\alpha,\beta,\mathbf{k}} c^\dagger_{\alpha,\mathbf{k}} \Lambda^{\alpha,\beta}_{\mathbf{q}}(\mathbf{k}) c_{\beta,\mathbf{k}+\mathbf{q}}, \quad \Lambda^{\alpha,\beta}_{\mathbf{q}}(\mathbf{k}) = \left\langle u_{\alpha,\mathbf{k}} \middle| u_{\beta,\mathbf{k}+\mathbf{q}} \right\rangle$$

Here α,β are not just sublattice index, but include all 8 indices. The first term is the kinetic term and the second term is the interaction term. $\left|u_{\beta,\mathbf{k}+\mathbf{q}}\right\rangle$ is the periodic part of the Bloch wavefunctions and $\Lambda^{\alpha,\beta}_{\mathbf{q}}$ is the so-called form factor that includes the spatially varying wavefunciton magnitude and can be derived from the generic form of density $\rho(\mathbf{r}) = \int d^3\mathbf{r}\psi^*(\mathbf{r})\psi(\mathbf{r})$. The form factor is strongly affected by the symmetry of the system. For instance, given the system has chiral symmetry and $\sigma_z \left|u_{A/B,\mathbf{k}}\right\rangle = \pm \left|u_{A/B,\mathbf{k}}\right\rangle$, then

$$\left\langle u_{A,\mathbf{k}} \middle| u_{B,\mathbf{k}'} \right\rangle = \left\langle u_{A,\mathbf{k}} \right| \sigma_z^2 \left| u_{B,\mathbf{k}'} \right\rangle = -\left\langle u_{A,\mathbf{k}} \middle| u_{B,\mathbf{k}'} \right\rangle = 0$$

This says that the form factor $\Lambda^{\alpha,\beta}_{\mathbf{q}}$ is diagonal in the sublattice space, which means that the interaction is symmetric in terms of sublattice and won't mix different sublattice species during scattering processes. In fact, one can utilize all the symmetry in the chiral model and obtain $\Lambda_{\mathbf{q}} = F_{\mathbf{q}}(\mathbf{k}) e^{i\Phi_{\mathbf{q}}(\mathbf{k})\sigma_z\tau_z}$, where both $F_{\mathbf{q}}(\mathbf{k})$ and $\Phi_{\mathbf{q}}(\mathbf{k})$ are scalars. τ_z is the Pauli matrix in valley space. In fact $\sigma_z\tau_z$ corresponds to Chern number. This means that in terms of the interaction term, the 8 flat bands can be divided into two groups determined by Chern number 1 or -1 and within each group, the density operator is invariant under any unitary rotation, giving a $U(4) \times U(4)$ symmetry.

Knowing the form factor and ignoring the kinetic energy for now, we can obtain the ground state purely determined by the interaction term which should satisfy $\rho_{\mathbf{q}} \left|\Psi\right\rangle = 0$. The density operator

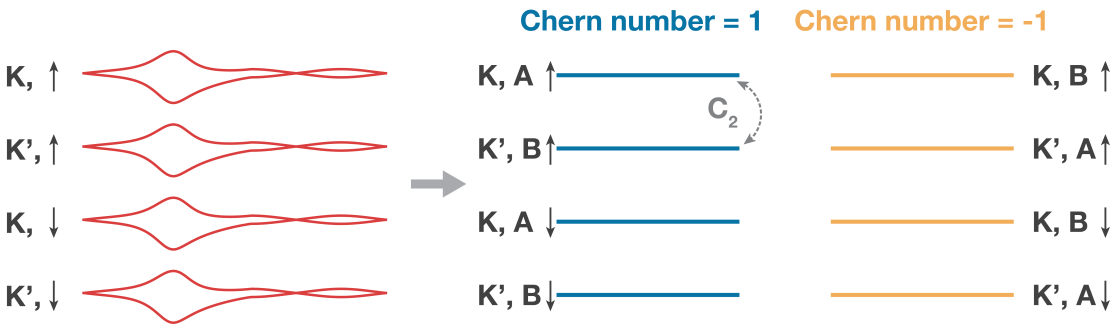

Figure 1.4: A illustration of basis change in the chiral model where the original conduction and valence flat bands are converted to the sublattice basis.

can be written explicitly

$$\rho_{\mathbf{q}} = \sum_{\mathbf{k}} F_{\mathbf{q}}(\mathbf{k})[e^{i\Phi_{\mathbf{q}}(\mathbf{k})}(c^{\dagger}_{A,K,\mathbf{k}}c_{A,K,\mathbf{k}+\mathbf{q}}+c^{\dagger}_{B,K',\mathbf{k}}c_{B,K',\mathbf{k}+\mathbf{q}})+e^{-i\Phi_{\mathbf{q}}(\mathbf{k})}(c^{\dagger}_{A,K',\mathbf{k}}c_{A,K',\mathbf{k}+\mathbf{q}}+c^{\dagger}_{B,K,\mathbf{k}}c_{B,K,\mathbf{k}+\mathbf{q}})]$$

We have omitted spin index for now since the system has full $SU(2)$ and the form factor is independent of spin. $\rho_{\mathbf{q}}$ consists of operators corresponding to momentum space hopping between $\mathbf{k}$ and $\mathbf{k}+\mathbf{q}$, therefore if a state with a combination fully filled or empty bands would be annihilated by the operator and therefore become the ground state. Indeed this is similar to a quantum Hall ferromagnet. For example, at half-filling, a ground state could be $|\Psi\rangle = \prod_{\mathbf{k}} c^{\dagger}_{A,K,\mathbf{k}}c^{\dagger}_{B,K',\mathbf{k}}|0\rangle$. This state fills completely a Chern sector with $C = 2$, corresponding to an anomalous quantum Hall state.

Another effect of interactions is that bands are strongly renormalized by interaction effects and have much larger bandwidth than that from single-particle calculations.

1.4 Magneto-exciton condensation in double layer structures

Electrons form discrete Landau levels (LLs) under a magnetic field B. For a parabolic band dispersion with $H = \frac{\mathbf{p}^2}{2m}$, the LLs are evenly spaced in energy. The energy separation, known as cyclotron energy, is $\hbar\omega = \hbar\frac{eB}{m}$. For example, bilayer graphene has an effective electron mass of $m \sim 0.04m_e$[18],

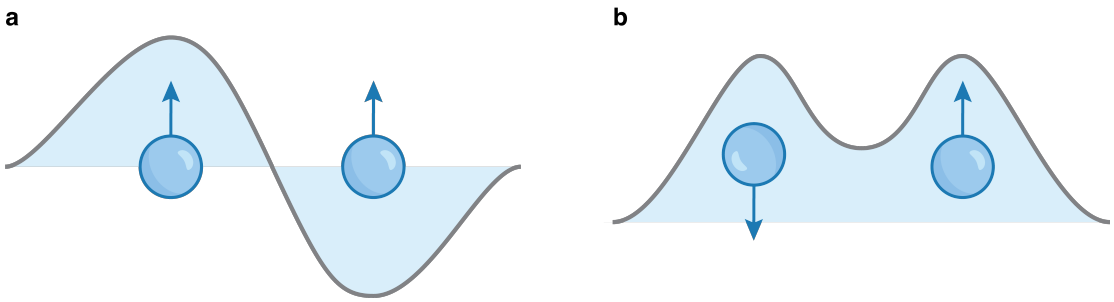

Figure 1.5: A illustration of a two-electron spatial wavefunction when their spins are **a**, aligned and **b**, anti-aligned.

giving $\hbar\omega = \hbar\frac{eB}{m} \approx 33.5K/T \times B$, where K is temperature unit Kelvin and T is magnetic field unit Tesla. For graphene, which has a Dirac dispersion, cyclotron energy has a different form: $\hbar\omega_c = v_F\sqrt{2e\hbar B} \approx 420K/\sqrt{T} \times \sqrt{B}$. If we define the filling factor ν as the number of occupied LLs, integer quantum Hall (IQH) effect emerges at integer ν and interactions can lead to fractional quantum Hall (FQH) at fractional ν. The average electron separation within LLs is on the order of magnetic length: $l_B = \sqrt{\hbar/eB} = 25.6\text{nm}/\sqrt{T} \times \sqrt{B}$. Therefore, the Coulomb interaction is on the scale of $e^2/\varepsilon l_B \approx (650/\varepsilon)K/\sqrt{T}$, where ε is the dielectric constant of the material.

Interactions can also play an important role at integer fillings and affect the spin degrees of freedom. The electron's Zeeman energy $\Delta E_{\text{Zeeman}} = g\mu_B B = 2 \times \frac{\hbar e}{2m_e}B = 1.34K/T \times B$, which is often much smaller than the cyclotron and Coulomb interaction energy, rendering spin up and down effectively degenerate. Recall Hunt's rule, as illustrated in Fig1.5: when two electrons' spins are aligned (or anti-aligned), their spatial wavefunction is antisymmetric (or symmetric) and has less (or more) overlap, thus lowering (or raising) the interaction energy. Consequently, interactions force all the spins of the electrons in the LL to align with each other, spontaneously breaking $SU(2)$ spin rotation symmetry and forming a ferromagnet. This phenomenon is known as quantum Hall ferromagnetism.

We can apply the principle of quantum Hall ferromagnetism to a double layer system, which consists of one layer of electrons stacked on top of another, separated by a thin insulator. In this

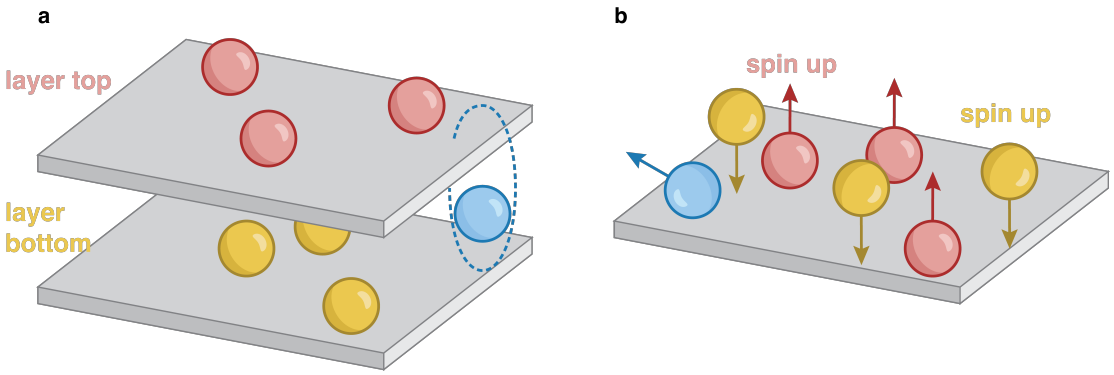

Figure 1.6: **a,** An illustration of double layer system with red balls representing electrons in the top layer and yellow balls representing electrons with a different layer index or layer peusospin quantum number that is "bottom". The blue ball represents a superposition state between top and bottom layers. **b,** An illustration of single layer system with two species of electron with up or down spin, similar to the layer top and bottom species in the double layer structure. The blue ball represents a superposition state between spin up and down states.

combined system, electrons can interact across layers and layer index becomes a new quantum number. Electrons in the top and bottom layers act like two species with different pseudospins, akin to a single layer electron system with two spin species of spin up or down. Spins can also be in arbitrary orientations, which corresponds to a superposition state of electrons coherently coexisting in both layers in a double-layer structure.

At a combined total integer filling factor $\nu_{tot} = \nu_{top} + \nu_{bot}$, the double layer structure exhibits quantum Hall ferromagnetism physics similar to that in a single layer at integer ν, but with anisotropic interactions. The interlayer interaction is typically weaker than the intralayer interaction due to the non-zero separation between layers. This situation corresponds to an equivalent single layer spin system, in which interactions between opposite spins are weaker than those among identical spins. This discrepancy causes all spins to prefer alignment within the x-y plane (assuming spin up and down are along z direction), spontaneously breaking an in-plane spin rotation $U(1)$ symme-

try. The spin ground state is described by

$$|\Psi\rangle = \prod_m \frac{1}{\sqrt{2}} \left(|\uparrow\rangle_m + e^{i\varphi} |\downarrow\rangle_m \right)$$

, where m labels the different degenerate wavefunctions within a LL and φ is the phase resulting from $U(1)$ symmetry breaking.

Recall that $U(1)$ symmetry is the essential physics of spin XY model and superfluidity. In fact, if we reinterpret the spin wavefunction in terms of layer index:

$$|\Psi\rangle = \prod_m \frac{1}{\sqrt{2}} \left(c^\dagger_{m,\text{top}} + e^{i\varphi} c^\dagger_{m,\text{bot}} \right) |0\rangle$$

, where $c^\dagger_{m,\text{top}}$ and $c^\dagger_{m,\text{bot}}$ are the create operators for the mth LL wavefunction in top and bottom layer, respectively, and $|0\rangle$ is the vacuum state in which both layers are empty. This wavefunction is indeed that of a exciton condensation. To see this, instead of starting with the vacuum state $|0\rangle$ and then filling elelctrons to the state, we use a different vacuum state where top layer is already fully filled: $|0'\rangle = \prod_m c^\dagger_{m,\text{top}} |0\rangle$, and we subsequently only add holes to the top layer. Consequently, the ground state becomes

$$|\Psi\rangle = \prod_m \frac{1}{\sqrt{2}} \left(1 + e^{i\varphi} c^\dagger_{m,\text{bot}} c_{m,\text{top}} \right) |0'\rangle$$

. This state mirrors the BCS superconducting wavefunction, except here is not pairing between electrons but between electrons in the bottom layer and holes in the top layer, indicative of exciton condensation.

1.5 Quantized transport signatures of interlayer quantum Hall states in Coloumb drag measurements

2

Tunable Spin-polarized Correlated States in Twisted Double Bilayer Graphene

Reducing the energy bandwidth of electrons in a lattice below the long-range Coulomb interaction energy promotes correlation effects. Created by stacking van der Waals (vdW) heterostructures with a controlled twist angle [19,20,21], moiré superlattices enable the engineering of electron band structure. In an engineered moiré flat band, exotic quantum phases can emerge. The correlated insulator, superconductivity, and quantum anomalous Hall effect found in the flat band of the magic angle twisted bilayer graphene (MA-TBG) [22,23,24,25,26] have sparkled exploration of correlated electron states in other moiré systems [27,28,29]. The electronic properties of vdW moiré superlattices can further be tuned by adjusting the interlayer coupling [24] or the band structure of constituent layers [27].

Here, employing vdW heterostructures of twisted double bilayer graphene (TDBG), we demonstrate a flat electron band that is tunable by perpendicular electric fields in a range of twist angles. Similar to the MA-TBG, TDBG exhibits energy gaps at the half- and quarter-filled flat bands, indicating the emergence of correlated insulating states. We find that the gaps of these insulating states increase with in-plane magnetic field, suggesting a ferromagnetic order. Upon doping the half-filled insulator, a sudden drop of resistivity is observed with lowering temperature. This critical behavior is confined in a small area in the density-electric field plane, and is attributed to a phase transition from a normal metal to a spin-polarized correlated state. Spin-polarized correlated states discovered in the electric field tunable TDBG provide a new route to engineering interaction-driven quantum phases.

2.1 Twisted double bilayer graphene configuration and band calculation

Moiré superlattices of two dimensional (2D) van der Waals materials provide a new scheme for creating correlated electronic states. By controlling the twist angle θ between atomically thin vdW layers, the size of the moiré unit cell can be tuned [19,20,21]. In particular, in twisted bilayer graphene (TBG), the weak interlayer coupling can open up energy gaps at the boundary of the mini-Brillouin zone, which modifies the energy bands of the coupled system. Theoretically, it has been predicted that around $\theta \approx 1.1^\circ$ (the so-called magic-angle (MA)), the interlayer hybridization induces isolated flat bands with drastically reduced bandwidth and enhanced density of states [30]. The combination of flat band and moiré periodic potential fosters an environment where strongly correlated states can emerge. Recent experiments performed in MA-TBG indeed confirmed the appearance of correlated insulating states associated with the flat bands [22]. Intriguingly, upon doping the half-filled insulator, superconductivity was discovered. The phase diagram of MA-TBG thus phenomenologically resembles that of high temperature superconductors, whose undoped parent compounds are

Mott insulators[31]. As a result, there is hope that MA-TBG could be a gateway to understanding the long-lasting puzzle of high temperature superconductivity. Yet, in recent works, the connection between superconductivity and the correlated insulator is under debate[32,33,34,35,36,37].

One of the ways to study the MA-TBG system is to tune the band structure through the flat band condition and observe how the correlated physics changes. To date, such an experimental control is largely achieved by fabricating samples with different twist angles. However, different samples, due to differences in uncontrollable factors such as the alignment with hBN, strain, and dielectric thickness, often yield contradicting results regarding where the correlated insulator and superconductivity appear. Only limited tunability has been demonstrated in TBG by the application of hydrostatic pressure[24]. In ABC trilayer graphene/hBN superlattices, the electric field was shown to modulate the correlated insulator gap[27], opening up the possibility of continuous tuning of the moiré flat band with electric field. However, the difficulty in identifying and preserving the unstable ABC trilayer graphene, together with the precise alignment required between the graphene and hBN layers, makes it a less accessible platform. In this work, we demonstrate a wide range of electric field tunability in the moiré flat band of twisted double bilayer graphene (TDBG), consisting of two Bernal-stacked bilayer graphene sheets misaligned with a twist angle θ (Figure 2.1a).

In twisted systems, the twist angle for achieving a flat band is determined by the individual layer band structure and the interlayer coupling strength. Unlike monolayer graphene, the band structure of Bernal-stacked bilayer graphene can be tuned by a perpendicular displacement field D[4]. As $|D|$ increases, the parabolic band touching at charge neutrality of bilayer graphene opens up a gap and the bottom (top) of the conduction (valence) band lifts up (down) into a shallow Mexican-hat energy dispersion distorted by trigonal warping[38]. The gap in bilayer graphene can be as big as 200 meV for large $|D|$ before the gate dielectric breaks down[39]. In TDBG, where two bilayers are stacked, the displacement field affects the energy dispersion of each constituent bilayer graphene, allowing a new experimental knob to tune the flat band condition (Fig. 2.1d). Fig. 2.2a shows

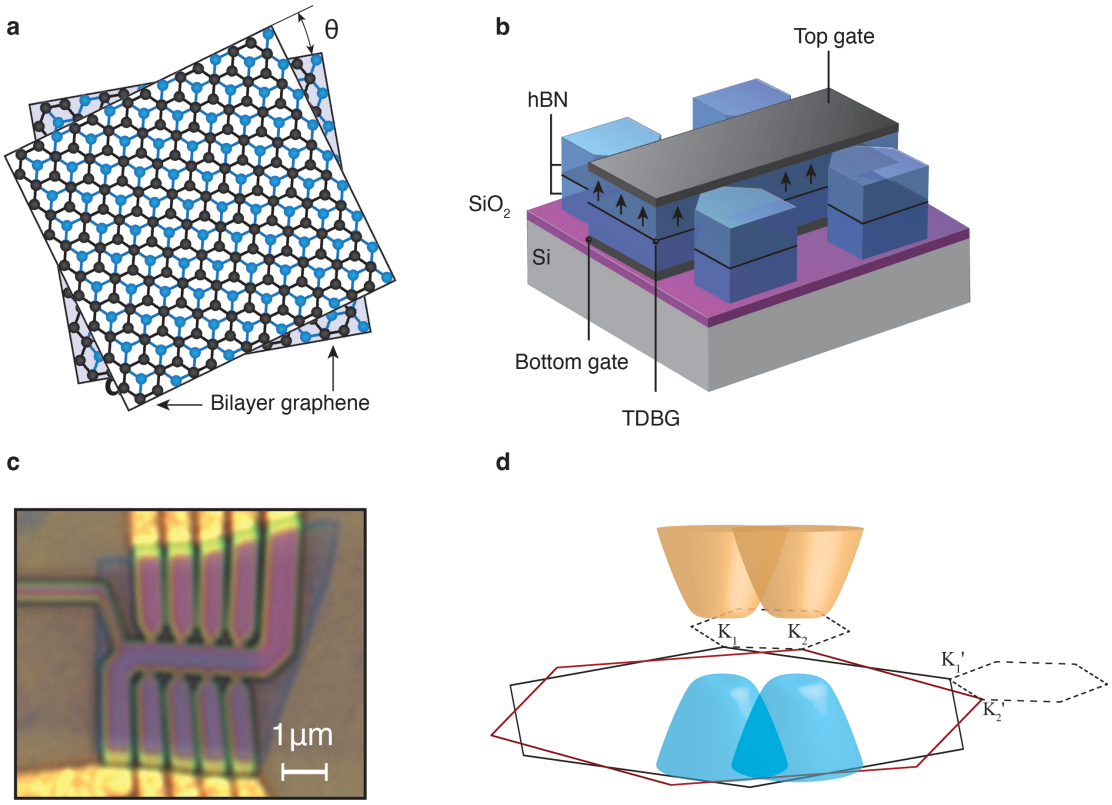

Figure 2.1: a, Schematic diagram of twisted double bilayer graphene with a twist angle θ. **b,** Device schematic with graphite top and bottom gates.**c,** Optical microscope image of the 1.33° device. **d,** Brillouin zone and band structure of the two individual bilayer graphene under perpendicular displacement field. The dashed hexagons represent the mini-Brillouin zone of the moiré superlattice.

moiré band structures computed at finite D using the single-particle continuum model approximation [40,30,41,42,43,44]. We find that a well-isolated narrow conduction band can appear in a range of twist angle θ, where the inter-band energy gaps and bandwidth can be controlled by the displacement field (see Methods for details).

We fabricated TDBG devices by tearing and stacking Bernal-stacked bilayer graphene [45,46]. We measured in total seven devices with twist angle θ =1.26, 1.32, 1.33, 1.41, 1.48, 1.53 and 2.00°, with the first six devices showing signatures of correlation effects. All of the devices measured are encapsulated by hBN. Top gates are made from graphite or metal, while bottom gates are made from graphite or silicon (details for each device structure are shown in Extended Data Fig. 9). We focus our study on the two representative devices θ =1.33° and θ =1.26°, while summarizing the behaviors of the other devices in Methods and Extended Data Table. 1. The top and bottom gates with voltages V_{TG} and V_{BG} are used to control the density of electrons, n, and displacement field, D, independently: $n = (C_{TG}V_{TG} + C_{BG}V_{BG})/e, D = (C_{TG}V_{TG} - C_{BG}V_{BG})/2$, where C_{TG} (C_{BG}) is the capacitance between the TDBG and the top (bottom) gate.

2.2 Spin-polarized correlated insualtors

Fig. 2.2b shows the four-probe resistivity ρ measured in the TDBG with $\theta = 1.33°$ as a function of V_{TG} and V_{BG} at temperature $T = 1.6$ K. CNP represents the charge neutral point of the TDBG, while n_S denotes the full filling of the flat band, corresponding to four electrons per moiré unit cell, originating from the spin and valley degeneracy. For a linecut along a constant displacement field $D \sim (D_1 + D_2^-)/2$ (positions of D_1, $D_2^{\pm}$ are labeled in Fig. 2.2b), ρ exhibits several insulating states where the corresponding conductance $\sigma = \rho^{-1}$ vanishes as temperature T decreases (Fig. 2.3b), suggesting a gap opening at the Fermi level of the system. Some insulating regions identified in Fig. 2.2b can be well explained by the single particle band structure presented in Fig. 2.2a. For example, we

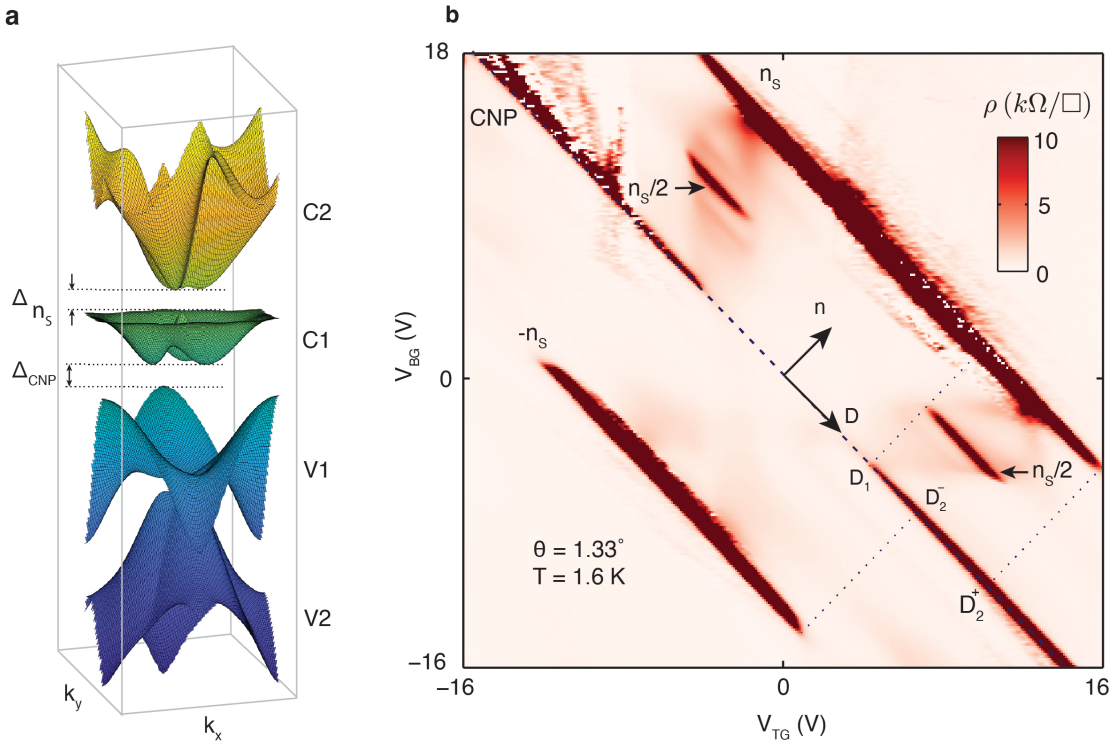

Figure 2.2: a, Calculated band structure for $\theta = 1.33^\circ$ TDBG at optimal displacement field. **b,** Resistivity as a function of top and bottom gate voltages. Charge neutral point (CNP), full-filled gaps ($\pm n_S$) and half-filled gaps ($n_S/2$) are marked. The displacement field where the CNP starts to open up a gap is labeled with D_1 and $D_2^{\pm}$ labels where the gap at full electron (hole) band filling closes.

find that the CNP is gapless at $D = 0$ but develops a gap for $|D| > D_1 \neq 0$. Similarly, at full moiré band filling $n = \pm n_S$, energy gaps $\Delta_{\pm n_S}$ are present within displacement field ranges $|D| < D_2^{\pm}$. Consequently, for $D_1 < |D| < D_2^{+}$ ($D_1 < |D| < D_2^{-}$), there is an isolated conduction (valence) band. Note that $D_2^{\pm}$ are different in the conduction band (+) and valence (−) band, due to the lack of electron-hole symmetry in TDBG. All these single particle band gaps are nicely captured by our calculation based on a continuum model (Extended Data Fig. 1). The calculation also captures the cross-like feature in Fig. 2.2b, which matches with the van Hove singularities of the bands (details in Methods). Lastly, the calculated band structure (Fig. 2.2a) indeed demonstrates the existence of an isolated flat band at $\theta = 1.33°$ under finite displacement field with a bandwidth around 10 – 15 meV.

In this single particle band structure, we expect a narrow but uninterrupted spectrum within the lowest moiré conduction band (c_1), separated by band gaps from both the valence band (v_1) and higher conduction band (c_2) for $D_1 < |D| < D_2^{+}$. However, we observe the development of a well-defined insulating behavior at half-filling $n = n_S/2$ (Fig. 2.2b, 2.3b). The onset displacement field of this insulating state coincides with D_1. But it ends well before D reaches D_2^{+}, suggesting both the isolation and the flatness of the band are required for creating the observed correlated gap (Fig. 2.2b, 2.3b). Along the same linecut shown in Fig. 2.3b ($D \sim (D_1 + D_2^{-})/2$), we measure the effective cyclotron mass m^* from the temperature dependent magnetoresistance oscillations (Extended Data Fig. 8). Fig. 2.3a shows that $m^* \approx 0.2m_e$ for the first valence band (v_1) and $m^* \approx 0.3m_e$ for the first conduction band (c_1), where m_e is the bare electron mass. Considering the effective mass of Bernal-stacked bilayer graphene is $\approx 0.04m_e$[47], the experimentally observed large m^* indicates an order of magnitude narrower bandwidth than that of bilayer graphene bands folded in the moiré superlattice Brillouin zone, especially for the c_1 band. We then use the conduction band effective mass $m^* = 0.3m_e$ to estimate the bandwidth of c_1 band to be $\sim$ 10 meV. This bandwidth matches with the continuum model calculation of TDBG[40], confirming the existence of the flat

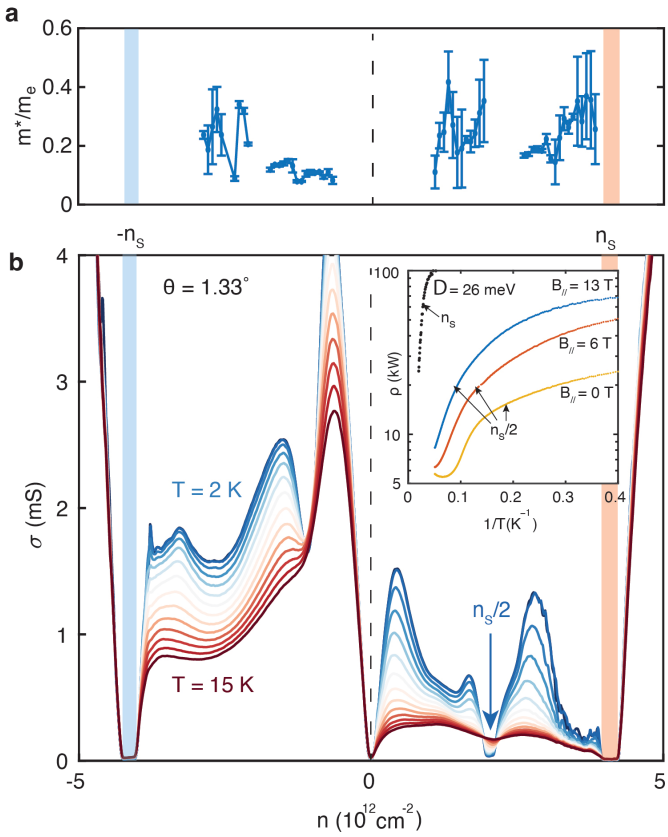

Figure 2.3: a, Effective mass measured by temperature dependent quantum oscillations corresponding to **b**. **b,** Temperature dependence of conductivity as a function of carrier density at a constant displacement field that passes through the half-filled insulator (D $\sim$ (D_1+D_2)/2). Inset, Arrhenius plot for the full-filled insulating state (n_S) and the half-filled insulating state ($n_S/2$) under different in-plane magnetic fields.

band experimentally. The absence of correlated insulating behavior in the hole-doped regime under similar experimental conditions can be explained by the larger bandwidth of the moiré valence band v_1 than that of c_1 (Methods).

We measure the size of the insulating gaps from the activating behavior of ρ (Fig. 2.3b inset). For $\theta = 1.33°$ TDBG, the half-filled insulator is robust with an energy gap of $\Delta_{n_S/2} = 3$ meV and persists up to a perpendicular magnetic field $B_\perp \approx 7$ T (Extended Data Fig. 7). Since the c_1 band is spin and valley degenerate in a single particle picture, the half-filled insulator is likely polarized in

the four-fold spin-valley space. In-plane magnetic field $B_{\|}$ can be used to probe the spin structure of the state without significantly coupling to the valley degrees of freedom in the regime where in-plane orbital effect is negligible. In MA-TBG, it has been shown that $B_{\|}$ reduces $\Delta_{n_S/2}$. Fig. 2.3b inset and Fig. 2.4a show the change of ρ as a function of $B_{\|}$ in our TDBG sample. We find that the half-filled insulator becomes more insulating as $B_{\|}$ increases (Fig. 2.3b inset) and the displacement field range spanned by the half-filled insulator expands (Fig. 2.4a). More quantitatively, we find that the growth of $\Delta_{n_S/2}$ roughly follows the Zeeman energy scale $g\mu_B B_{\|}$, where μ_B is the Bohr magneton and the effective g-factor $g = 2$ (dotted black line in Fig. 2.4b). This observation is consistent with a picture where the occupied states (half of the states in c_1) are spin-polarized along the direction of the external magnetic field. The unoccupied excited states then carry the opposite spin, separated by a ferromagnetic gap due to spontaneous symmetry breaking at half-filling. For spin-1/2, the Zeeman term lowers the energy of the filled states $\Delta E_{\downarrow} = -g\mu_B B/2$, while boosting the energy of the empty states with opposite spins by $\Delta E_{\uparrow} = g\mu_B B/2$, pushing the two bands further apart and enhancing the gap (as illustrated by Fig. 2.4b insets). Calculations from the Hartree-Fock approximation also supports the existence of a spin-polarized correlated insulating state at half-filling in TDBG[40,41].

In the $\theta = 1.33°$ device, applying $B_{\|}$ also induces additional correlated insulating states at quarter-filling ($n = \frac{1}{4}n_S$) and three-quarter-filling ($n = \frac{3}{4}n_S$) (Fig. 2.4a). The quarter-filled insulating gap opens at $B_{\|} \approx 4$ T and increases as $B_{\|}$ increases (Fig. 2.4b). According to the hierarchy of the symmetry broken states within mean field theory[40], the quarter-filled gaps separate the ground state and the excited state of the same spin and opposite valleys, and thus should be relatively insensitive to in-plane magnetic fields. However, the enhancement of quarter-filled gaps with $B_{\|}$ and the positions where quarter-filled insulating states appear in the n–D plane (Extended Data Fig. 2) suggest they are likely to separate states of the opposite spins, hinting that the origin of these strongly correlated states goes beyond a simple mean field approach.

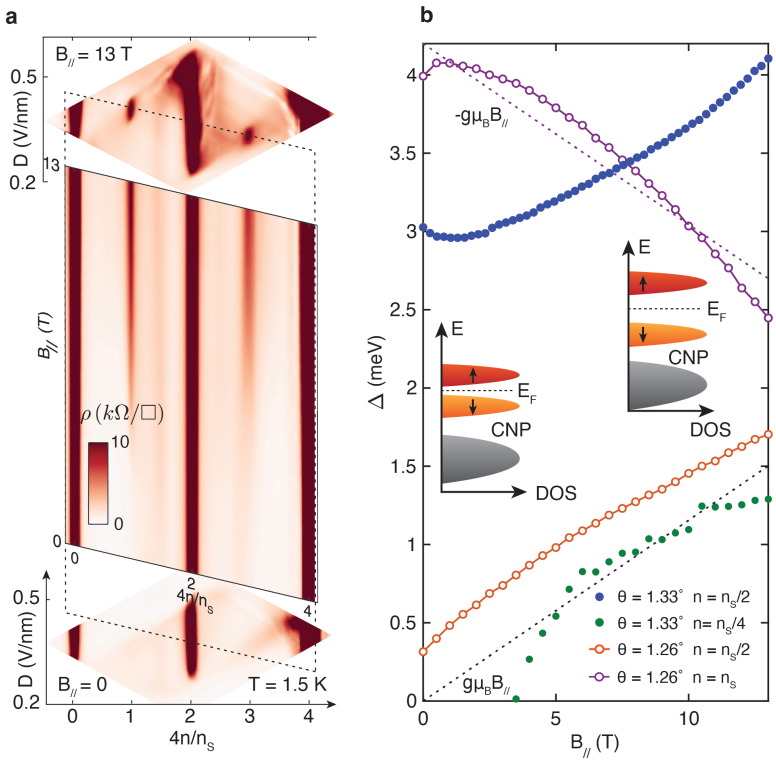

Figure 2.4: a, Development of the correlated insulating states with in-plane magnetic fields. Top and bottom panels compare resistivity as a function of n and D under different in-plane magentic fields. The middle panel shows the continuous evolution of the correlated states by taking a line-cut along the dashed lines in the top and bottom panels. All three panels are measured at a temperature of T = 1.5 K. **b,** Half-filled insulating gap $\Delta_{n_S/2}$, quarter-filled insulating gap $\Delta_{n_S/4}$ and full-filled gap Δ_{n_S} as a function of in-plane magnetic field. The dashed lines indicate Zeeman energy with $g = 2$. $\Delta_{n_S/2}$ of both devices increase with in-plane magnetic field, indicating spin-polarization of the half-filled insulator. We also note that the single particle gap, Δ_{n_S} between c1 and c2 (purple curve), decreases linearly with Zeeman energy with g-factor of 2. Insets, schematic of the half-filled insulating state at zero and large in-plane fields.

2.3 "Halo" region – correlated metallic state

In the $\theta = 1.26°$ sample, a similar spin-polarized half-filled insulating state is observed (Fig. 2.5a), with much smaller correlated gap $\Delta_{n_S/2} = 0.3$ meV (red line in Fig. 2.4b). Upon doping the half-filled insulator, we identify the appearence of a 'halo' (marked with a dashed circle in Fig. 2.5a) surrounding the half-filled insulating state in the V_{TG}–V_{BG} plane. On the halo, the resistivity is slightly higher than the nearby region. Such a halo-like feature commonly appears around the correlated insulating states in different samples with varying twist angles (Fig. 2.6a-d, Extended Data Fig. 9). The half-filled insulting state divides the halo-like region into two. For the samples with a strong half-filled insulating gap, Hall measurements performed at low magnetic fields (Extended Data Fig. 2) exhibit a sign change of the Hall signal across the boundary of the halo and also across the correlated insulator. A similar observation has been noted in a recent related work[48]. The sign of Hall signal inside the halo complies with the carrier concentration counted from half-filling. This suggests the metallic state in the halo is obtained by adding carriers to the spin-polarized band at half-filling while retaining the spin-splitting of the band (Fig. 2.4b inset), and therefore is likely a ferromagnetic metal. Since the Hall signal outside the halo matches the expectation for a moiré band without correlation, the halo marks the border between the spin-polarized and the spin-unpolarized metallic states (Extended Data Fig. 2.4a).

Studying the temperature dependence of the resistivity, $\rho(T)$, inside the halo, we identify a critical transition with a sudden drop of resistivity as the temperature decreases. Fig. 2.5b shows resistivity measured at different gate configurations marked by matching symbols in Fig. 2.5a. We note that the critical transition behavior, namely the sudden drop of resistivity, only occurs inside the halo. In contrast, resistivity outside the halo increases linearly with temperature. The resistivity behavior outside the halo is most likely due to ballistic transport at low temperatures and enhanced phonon scattering at elevated temperatures. The critical transition behavior of $\rho(T)$ inside the halo, how-

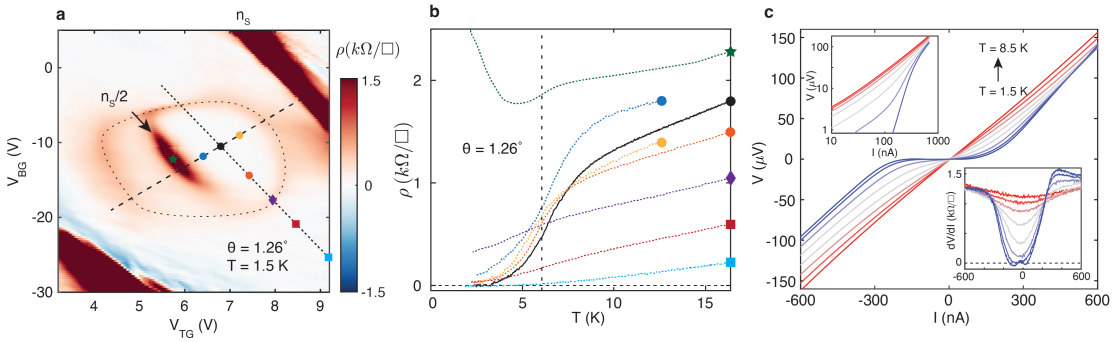

Figure 2.5: a, Resistivity map around the half-filled insulator. Dashed circle marks the halo. **b,** Resistivity as a function of temperature at different spots marked by the colored symbols in **a** using the corresponding colors and shapes. **c,** Current-Voltage (I–V) curves at the black circle in Fig. 2.5**a**, Top left inset, I–V in log scale, demonstrating the BKT like power-law behaviour (see Extended Data Fig. 2.6 for more details). Bottom right inset, dV/dI as a function of bias current, which shows a critical current of about 300 nA.

ever, appears non-trivial. The $\rho(T)$ curve of the 1.26° device (black curve in Fig. 2.5b) in particular strongly resembles that of a superconductor, with near-zero resistivity below 3.5 K. The current-voltage (I-V) curve also exhibits superconducting-like non-linear behaviors: dV/dI vanishes for bias current smaller than a critical current, $I < I_c$, and rises to a near-constant value that is close to the normal resistivity above the critical transition for $I > I_c$ (Fig. 2.5c bottom right inset). This non-linear I-V characteristic is distinct from that of a heating effect (see Methods for a more detailed analysis) and seemingly follows that of the Berezinskii-Kosterlitz-Thouless (BKT) transition (Extended Data Fig. 2.6e).

While $\rho(T)$ and the I-V characteristic discussed above for the 1.26° device are suggestive of superconductivity, we note that several factors require careful consideration. First, we have not observed direct evidence of superconducting phase coherence, such as the Fraunhofer pattern under magnetic fields. Second, $\rho(T \ll T_c) \approx 0$ has been observed only for the 1.26° device. Fig. 2.6a-d show four other devices we measured with the twist angle ranging between 1.32-1.48°. In these devices, similar to the 1.26° device, critical transition behaviors in $\rho(T)$ curves are commonly observed inside the halo region that surrounds the half-filled insulator. These critical behaviors are best illustrated by

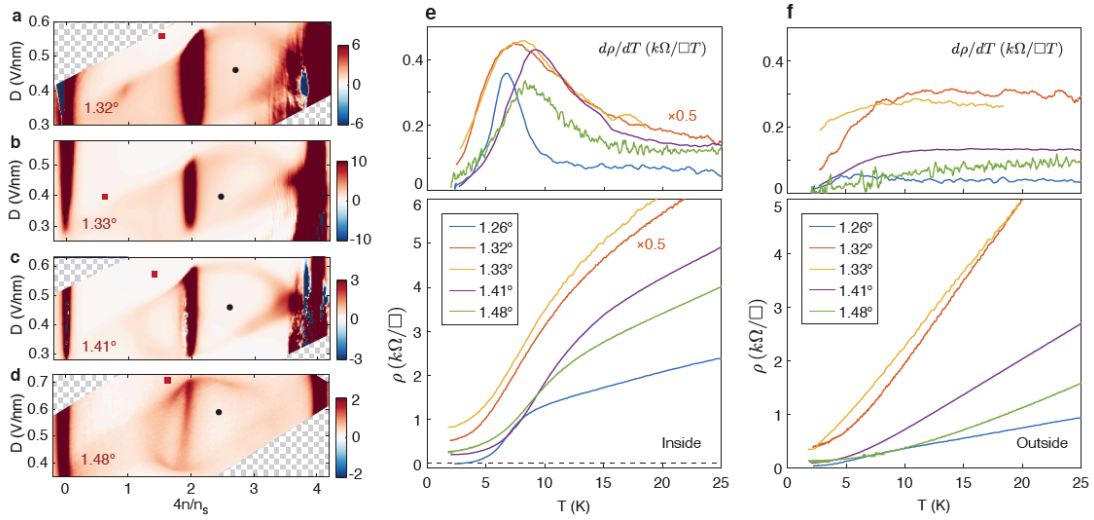

Figure 2.6: a-d, Resistivity as a function of filling fraction and displacement field around the half-filled insulators measured in four different samples with the twist angles 1.32, 1.33, 1.41 and 1.48°. **e, f,** resistivity as a function of temperature inside and outside the halo regions surrounding the correlated insulator. The gate configuration for each curve is marked by the red (outside the halo) and the black (inside the halo) symbols in **a-d**. Upper panels show the derivative of the resistivity to highlight the critical transition behavior.

the clear peaks in $d\rho/dT$, which are absent outside the halo (Fig. 2.6e-f). The critical temperatures, defined as the temperature where $d\rho/dT$ is maximum, are similar across all devices ($T_c = 6 - 9$ K), despite their very different half-filled insulating gap sizes (Extended Data Table. 1). However, the low-temperature resistivity $\rho(T \ll T_c)$ does not reach zero, unlike in the 1.26° device (Fig. 2.6e, Extended Data Table. 1). Strong non-linear I-V at low temperatures is also absent in these devices.

Based on these experimental findings, we propose a few scenarios to explain the observed critical transition behavior. One possibility is that the critical transition is a result of Cooper pair formation, but superconductivity is only developed in the 1.26° device. In other devices, the establishment of phase coherence may be inhibited by an inhomogeneous distribution of strains or disorder. Alternatively, the critical transition may correspond to a ferromagnetic transition of the doped half-filled insulating states. Here, we note that the critical transition behaviors only occur inside the halo region which we associate with ferromagnetic metallic states. As temperature increases, the

ferromagnetic metal turns into a normal metal when correlation effect vanishes. Below the critical temperature, carrier scattering processes related to spin-flip can potentially be suppressed by the ferromagnetic order, resulting in a reduced resistivity. These two scenarios do not necessarily compete with each other, leaving open the possibility of a ferromagnetic superconductor (Methods, Extended Data Fig. 5). The highly tunable electronic structures of TDBG demonstrated here and in related works[49,50,51,48] may provide a new route to engineer correlated phenomena in a moiré superlattice.

3

Unconventional superconductivity in magic-angle twisted trilayer graphene

We construct a van der Waals heterostructure consisting of three graphene layers stacked with alternating twist angles $\pm\theta$. At the average twist angle $\theta \sim 1.56°$, a theoretically predicted magic angle for the formation of flat electron bands, narrow conduction and valence moiré bands together with a linearly dispersing Dirac band appear. Upon doping the half-filled moiré valence band with holes, or the half-filled moiré conduction band with electrons, displacement field tunable superconductivity emerges, reaching a maximum critical temperature of 2.1 K. By tuning the doping level and displacement field, we find that superconducting regimes occur in conjunction with flavor polarization of moiré bands bounded by a van Hove singularity at high displacement fields. These

experimental results are inconsistent with a weak coupling description, suggesting that the observed moiré superconductivity has an unconventional nature.

3.1 Twisted trilayer graphene configuration and band structure

The experimental realization of twisted bilayer graphene (TBG) opened up new possibilities for studying interaction effects in moiré engineered electronic bands. It was first predicted theoretically that the hybridization of two twisted graphene sheets could produce nearly flat bands at the so called "magic angles" (MA)[52,53,54,55]. Initial experiments showed that a significant reduction of kinetic energy gives rise to correlated insulating phases and superconductivity upon doping these insulating states[22,56]. In the follow-up experiments, additional interaction-driven phases were discovered in MA-TBG, including isospin symmetry breaking metals[57], orbital ferromagnetism[58,59,60], and magnetic field induced Chern insulators[61,62,63]. Despite the rapid progress of the field, the question of whether the superconductivity is unconventional, driven by strong electron-electron interactions, or conventional, arising from electron-phonon interaction at weak coupling, remains under debate. Some experiments suggested that the superconducting and insulating phases are independent or maybe even competing, with the superconductivity persisting or strengthening when Coulomb interaction is screened[64,65,37,66]. However, others have provided evidence that the superconductivity has unconventional features, such as coexisting nematic order[67] and a lack of correlation between large density of states and higher critical temperature[68], pointing to unconventional superconductivity of non-phononic origin.

The creation of moiré engineered van der Waals (vdW) interfaces has been extended to other two-dimensional (2D) material systems as well, leading to the observation of many interesting interaction-driven phases, such as quantum anomalous Hall states in twisted monolayer- bilayer graphene[69,70] and generalized Wigner crystal in WSe_2/WS_2 moiré superlattices[71,72]. On the other

hand, MA-TBG remains the only system where superconductivity is unambiguously well-established[56,73,59,37]. In contrast, initial reports of superconductivity in other 2D flat band systems such as ABC trilayer graphene aligned with BN[74], twisted double bilayer graphene[75,48], and twisted WSe_2[76] have proven less conclusive[77].

In this work, we study a new type of moiré engineered graphene multi-layer system, MA twisted trilayer graphene (TTG) with vertical mirror symmetry[78]. We present a clear signature of superconductivity controlled by applied electric field. The continuously tunable band structure of MA-TTG provides a new experimental knob for probing the superconducting mechanism.

Our TTG consists of three layers of graphene, with the twist angle between the top layer (T) and middle layer (M) being θ, and the twist angle between the middle layer and the bottom layer (B) being $-\theta$ as shown in the schematic in Fig. 3.1a. The stacking with this alternating sequence of angles with opposite signs preserves the vertical mirror plane symmetry (see Supplementary Material (SM), S1), differing from the previously studied trilayer systems[79]. A recent theoretical work predicted that the Hamiltonian for this system can be effectively decoupled into that of a monolayer graphene and a TBG with the inter-layer coupling strength enhanced by a factor of $\sqrt{2}$[78]. As a result, the band structure of TTG consists of a Dirac cone from the monolayer graphene coexisting with TBG flat bands. Interestingly, the magic angle is predicted to be the TBG magic angles multiplied by $\sqrt{2}$: $\theta_{\mathrm{TTG}} = 1.56°$[78]. Fig. 3.1c shows a band structure of TTG at this angle. To experimentally realize such a system, we utilize the "cut and twist" technique[65] (see SM S1 for details). An image of the completed device is shown in Fig. 3.1b. The colored lines trace the original positions of the three pieces of graphene. In addition to the TTG device fabricated in the three-layer overlapped region (TMB), we made two other TBG devices, one in the region with only the top and middle layers (TM), and the other in the region where there are only the middle and bottom layers (MB). These two devices allow us to measure the TM twist angle, θ_{TM}, and MB twist angle, θ_{MB}, individually to characterize our devices.

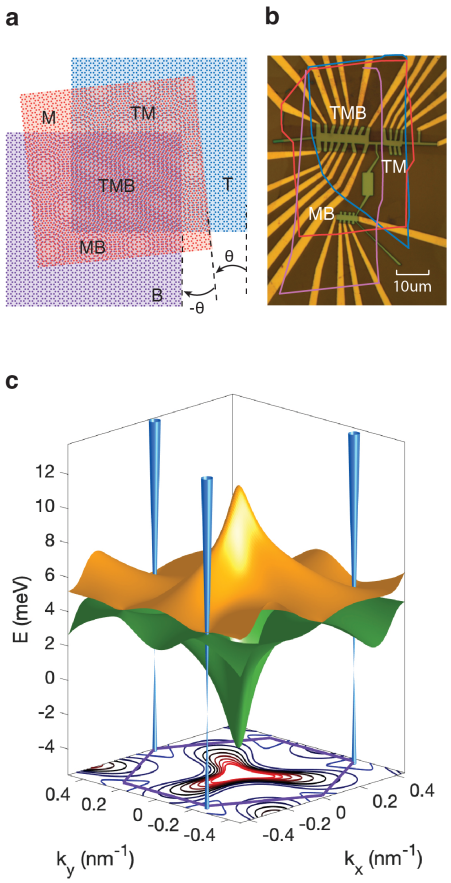

Figure 3.1: (**a**) Schematic diagram of the three layers of TTG with alternating twist angles θ and $-\theta$. The top and bottom layers are aligned while the middle layer is twisted by θ relative to both layers, preserving the in-plane mirror symmetry. (**b**) Optical microscope image of the TTG device fabricated in the TMB region and two TBG devices fabricated in the TM and MB regions. (**c**) Theoretical band structure for MA-TTG at $D/\varepsilon_0 = 0$ plotted on the mini Brillouin zone (BZ) marked in purple in the bottom face. The blue Dirac cones sit at the mini BZ K points, while the flat bands, orange (conduction) and green (valence) are the most dispersive at the mini BZ Γ point. A contour plot of the valence band is projected on the x–y plane.

Fig. 3.2a and b show the longitudinal resistivity, ρ, as a function of perpendicular magnetic field B and carrier density n, controlled by both top and bottom gates of the two TBG devices, TM and MB. They exhibit typical magnetotransport features of large-angle TBG [80], with no insulating resistivity peaks other than at $\nu = 0$ and 4. Here, ν is the moiré band filling factor $\nu = 4n/n_s$, where n_s is the carrier density at full filling of the four-fold degenerate moiré bands. From these fan diagrams, we estimate $\theta_{\mathrm{TM}} = 1.35°$ and $\theta_{\mathrm{MB}} = -1.69°$. The difference in angles is expected due to imperfect angle control in experiments as well as the ubiquitous angle disorder in twisted devices. Interestingly, however, we find such small angle difference between TM and MB regions yields no appreciable effects in the TTG device formed in the TMB region. Fig. 1c shows the Landau fan diagram of the TTG device at a fixed back gate voltage, $V_{\mathrm{BG}} = 0$. $\rho(B, n)$ exhibits emergent Landau fans at integer fillings $\nu = 0, \pm 2, 1, 3$ which correspond to a twist angle of 1.55°. In addition, the device is highly uniform across most pairs of contacts, with angle disorder on the order of 0.02° estimated from similar magneto-transport data (SM, S3). Such high uniformity of twist angle in the TMB region might indicate that the strain relaxation on atomic length scales forces $\theta_{\mathrm{TM}} = -\theta_{\mathrm{MB}}$ to be the average twist angle, favoring alignment between the top and bottom layer to reduce the structural energy [81]. An alternative scenario is that the three layers are coupled so strongly that they behave as a single system with the measured angle the average of θ_{TM} and θ_{MB}. In either case, the resulting uniform device indicates that TTG is relatively robust against small angle misalignment and disorder.

We find that, unlike in MA-TBG samples, $\rho(n)$ measured in the TMB device at $B = 0$ (Fig. 3.2d) does not exhibit strong insulating behavior at any filling, consistent with the additional Dirac cone in the proposed TTG band structure in Fig. 3.1c. The Landau fan emanating from the charge neutrality has sequence -2, -6, -10, ... on the hole doped side and 2, 6 on the electron doped side. This sequence indicates that Landau levels are four-fold degenerate but is different from the typical 4, 8, 12, ... sequence obtained in MA-TBG [56]. This change is similar to the sequence in ABA trilayer

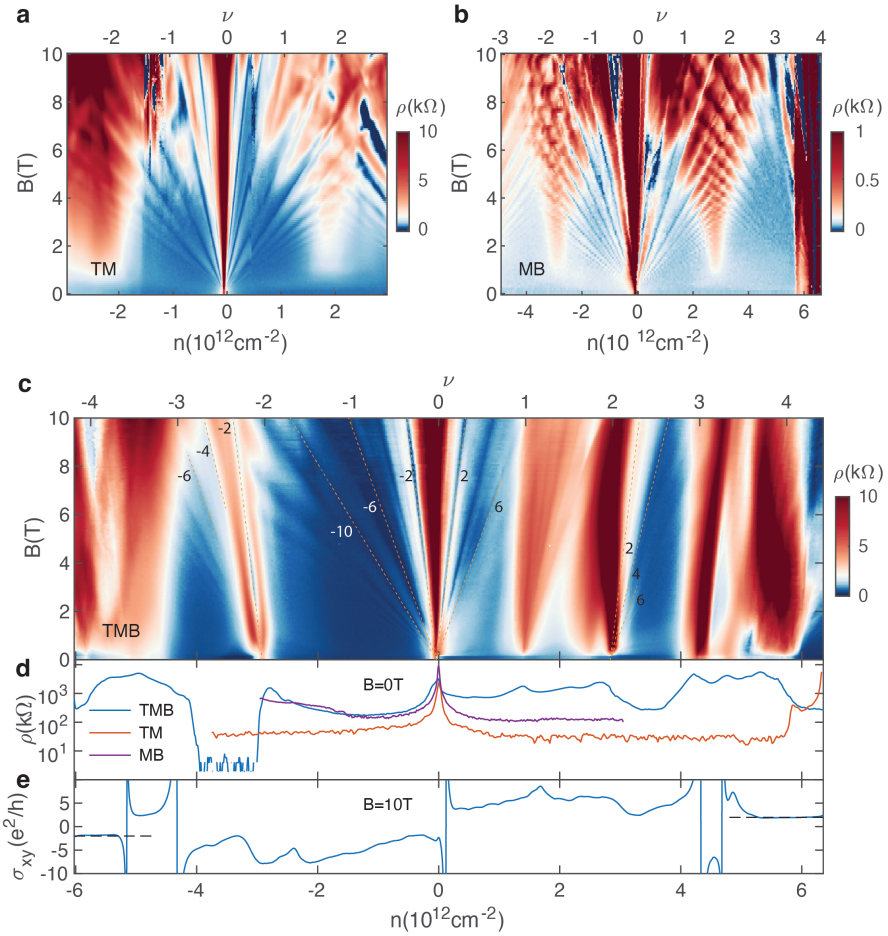

Figure 3.2: **a** and **b** Landau fan diagrams of the two TBG hall bars TM and MB. In each device, fans are visible emanating from $\nu = 0$ and $\nu = \pm 4$ as well as an increase in resistance at the vHSs near $\nu = \pm 2$. **c** Landau fan diagram of the TTG Hall bar TMB. Resistive states and fans emerge at $\nu = 0, +1, \pm 2$ and $+3$. The most prominent sequences are traced out by orange dashed lines (more details in Fig. S4). **d** Zero magnetic field resistivity as a function of filling in TM, MB and TMB. **e** Hall conductivity in TMB at $B = 10$ T.

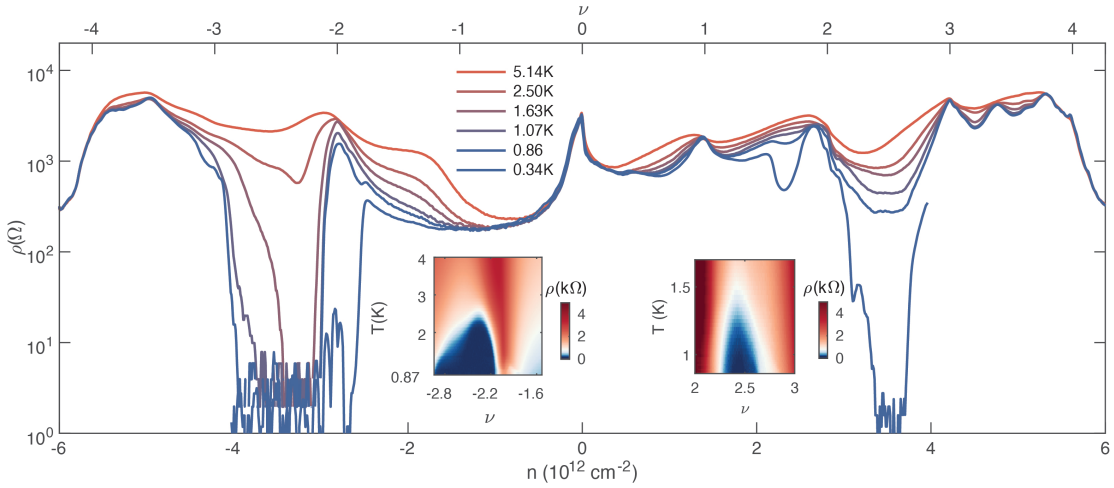

Figure 3.3: ρ as a function of ν taken at a fixed $V_{BG} = 0$ V at several different temperature values. The formation of superconducting regions is visible at $\nu < -2$ and $\nu > 2$. The left inset shows the superconducting dome in the $T - \nu$ plane taken along a cut at $V_{BG} = 0$ V for $\nu < -2$, the right inset at $D/\varepsilon_0 = -0.56$ V/nm for $\nu > 2$.

graphene[82], and likely results from the presence of the Dirac cone. Fig. 3.2e shows $\sigma_{xy}(n)$ taken at $B = 10$ T. Interestingly, we see large regions of $\sigma_{xy} = -2e^2/h$ near $\nu = -4$ and $\sigma_{xy} = -2e^2/h$ (e is the electron charge and h is the Planck constant) near $\nu = 4$ (also see $1/\rho_{xy}(B, n)$ in Fig. S3). More direct experimental evidence of the additional Dirac cone is present in the Landau fan diagram taken at zero displacement field, where we observe quantum Hall sequences originating from the Dirac cone at low magnetic fields (see SM, S4). Flavor symmetry breaking is evident in the Landau fan coming from $\nu = -2$ with sequence -2, -4, -6, ... and from $\nu = 2$ with sequence 2, 4, 6, ..., showing only two-fold degeneracy. Above a perpendicular magnetic field of 1 T, the resistive state at $\nu = -2$ shows a resistivity minimum and quantized Hall resistance along the slope of -2, with hysteresis observed near 1 T (Fig. S6). This is an indication of a magnetic field induced Chern insulator with Chern number $C = -2$ and orbital ferromagnetism associated with it.

3.2 Superconductivity in twisted trilayer graphene

At low temperature and magnetic field, we find large regions of robust superconductivity in the TTG sample. Fig. 3.3 shows $\rho(n)$ at different temperatures at $V_{\mathrm{BG}} = 0$ V. At our lowest experimental temperature of $T = 0.34$ K, zero resistance regions appear on the hole-doped side of $\nu = -2$ and electron-doped side of $\nu = 2$. The two insets show $\rho(\nu, T)$ near $\nu = -2$ and $\nu = 2$ respectively, both displaying clear superconducting domes. The transition in $\rho(T)$ across the dome boundary is sharp as shown in Fig. 3.4a at $\nu = -2.3$, the optimal filling for $\nu < -2$. It is noteworthy that $\rho = 0$ at $T \sim 2.1$ K, which is higher than most MA-TBG devices in published literature [56,73,59,37]. At $\nu = -2.3$, we extract a Berezinskii–Kosterlitz–Thouless (BKT) transition temperature of 2 K from the power law dependence of the current and voltage I-V characteristics in the low current and voltage range as shown in the inset of Fig. 3.4a (see SM, S7 for the analysis details). Phenomenologically, we characterize, T_c, as the temperature at which ρ falls to 10% of the normal state resistance, ρ_N, which we find to be consistent with the BKT transition temperature and a better measure for 2D superconductivity (SM, S6). Additional clear signatures of superconductivity are also visible in the differential resistance, dV/dI, as a function of DC bias current as shown in Fig. 3.4b, which shows a sharply defined critical current I_c. At $B = 0$ T, the sudden increase of dV/dI occurs at $I_c = 880$ nA. At low temperature, there are oscillations of I_c in a Fraunhofer-like pattern demonstrating phase coherence (Fig. S15). As the magnetic field increases, I_c becomes smaller and the shape of dV/dI becomes more smooth, a characteristic behavior of 2D superconducivity suppressed by perpendicular magnetic field. The resulting critical field, B_c, is evident in $\rho(T, B)$ in Fig. 3.4c. We extract the Ginzburg-Landau (GL) coherence length ξ_{GL} from the theory for a 2D superconductor: $B_{\mathrm{c}} = [\Phi_0/(2\pi\xi_{\mathrm{GL}}^2)](1 - T/T_{\mathrm{c}})$ [83], where Φ_0 is the superconducting flux quantum. Using the BKT transition temperature as T_c in the above relation, we estimate $\xi_{\mathrm{GL}} = 34$ nm, several times the interparticle distance of 9 nm set by the moiré periodicity. Using T_c extracted at $\rho = 0.5\rho_N$, considering

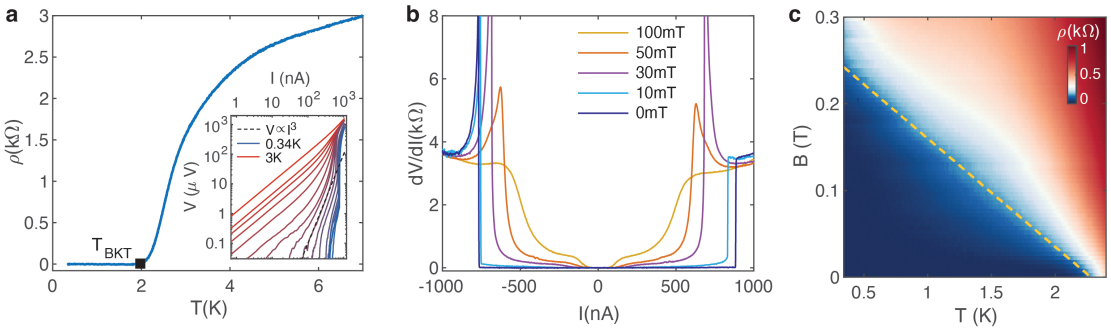

Figure 3.4: a Superconducting transition in resitivity at $\nu = -2.3$ and $D/\varepsilon_0 = 0.29$ V/nm. The BKT transition temperature T_{BKT} is marked by the black square. Inset shows $I - V$ characteristic of the superconductor from 0.34K (blue) to 3K (red) on a log-log scale, displaying a crossover from high power polynomial to linear behavior in low V range. The black dashed line marks where $V \propto I^3$, defining T_{BKT}. **b** Differential resistance as a function of DC bias current at different magnetic fields. **d** ρ as a function of temperature and perpendicular magnetic field at $\nu = -2.3$ and $D/\varepsilon_0 = 0.4$ V/nm. The dashed line corresponds to a GL theory fit with a coherence length of $\xi_{\text{GL}} = 34$ nm (see SM for more details).

prevailing fluctuation effects, we find $\xi_{\text{GL}} = 13.4$ nm, only slightly larger than the interparticle distance. We have also seen superconductivity in an additional TTG device with $\theta = 1.39°$, shown in Fig. S17.

Employing both the top and bottom gates, we can control both n and the displacement field D independently, tuning the superconductivity in TTG by the electric field. Fig. 3.5 shows ρ as a function of ν and displacement field D at temperature $T = 0.86$ K. We observe at charge neutrality a resistive peak that is not disturbed by D. This is expected for the Dirac cone crossings in the flat bands. At $\nu = \pm 2$, 1 and 3, there are resistivity peaks that are modulated by D. At $\nu = \pm 4$, the system has low ρ, which is expected due to the existence of the additional Dirac cone and lack of band insulators at full filling. The superconductivity appears as the dark blue regions both on the hole side between $\nu = -3$ and $\nu = -2$, and on the electron side between $\nu = 2$ and $\nu = 3$. The hole side superconductivity persists for all D, with a width that first increases with D, and starts to decrease at $D/\varepsilon_0 \sim 0.4$ V/m. The electron side superconductivity is weaker and affected more strongly by D. At $T = 0.86$ K, it only starts to emerge at $D/\varepsilon_0 \sim -0.4$ V/nm. At a lower temper-

ature $T = 0.34$ K, superconductivity on both sides extends to larger ranges (Fig. S16A). To better illustrate the evolution of the superconductors with D, we have measured $\rho(\nu, T)$ at several discrete Ds, as shown in Fig. 3.6a to c for holes and Fig. 3.6d to f for electrons, showing dome-like superconducting regimes (several representative $\rho(T)$ curves are shown in Fig. 3.5 insets). While the optimal doping ν_{op} where the maximum T_c occurs is insensitive to D, we find the maximum T_c of the dome and the filling range, $\Delta\nu$, i.e., the height and width of the dome, are sensitive to D. We measure $\rho(T)$ at different D at optimal filling to extract the transition temperature T_c at each D, providing a quantitative description of the D dependence of superconductivity. Fig. 3.6g and h show T_c as a function of D for the hole-side and electron-side superconductors respectively. For the hole-side superconductor, starting from $D/\varepsilon_0 = 0$, T_c first increases, reaches maximum at around $D/\varepsilon_0 = 0.4$ V/nm and then decreases quickly. The electron-side superconductor displays a similar trend, with T_c increasing after appearing at $D/\varepsilon_0 \sim -0.5$ V/nm then decreasing below $D/\varepsilon_0 = -0.62$ V/nm.

3.3 Signature of unconventional superconductivity

The electric field tunable superconductivity in TTG can be ascribed to the tuning of single particle bands controlled by D[84]. Fig. 3.7a shows renormalized Hall density (measured Hall density divided by n_s) $n_H = \sigma_{xy}B/en_s$ at a low magnetic field $B = 0.5$ T, near the region where the hole-side superconductor resides. At $D/\varepsilon_0 = 0.2$ V/nm, away from zero filling, $n_H(\nu)$ increases linearly with a unity slope and then resets to 0 near $\nu = -2$. This reseting behavior has been considered as a signature of the spin and valley isospin symmetry breaking, where the four-fold degeneracy turns into two-fold. After this flavor symmetry breaking, the electrons completely fill the two lower energy bands and n_H corresponds to the density in the two higher energy bands. Similar flavor symmetry breaking in moiré flat bands has been observed and discussed in MA-TBG[65,61,85,86]. This symmetry breaking can be better illustrated by the quantity $|n_H - \nu|$, which directly gives the degeneracy of the

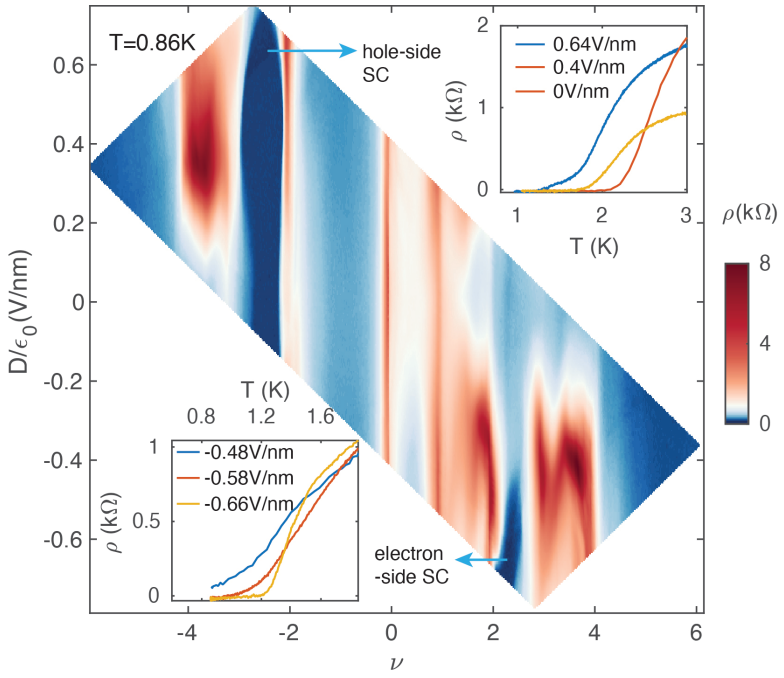

Figure 3.5: ρ map as a function of ν and D at 0.86K. Superconducting regions appear for $\nu < -2$ and $\nu > 2$. The upper (lower) inset shows the ρ at the superconducting transition in the hole (electron) region.

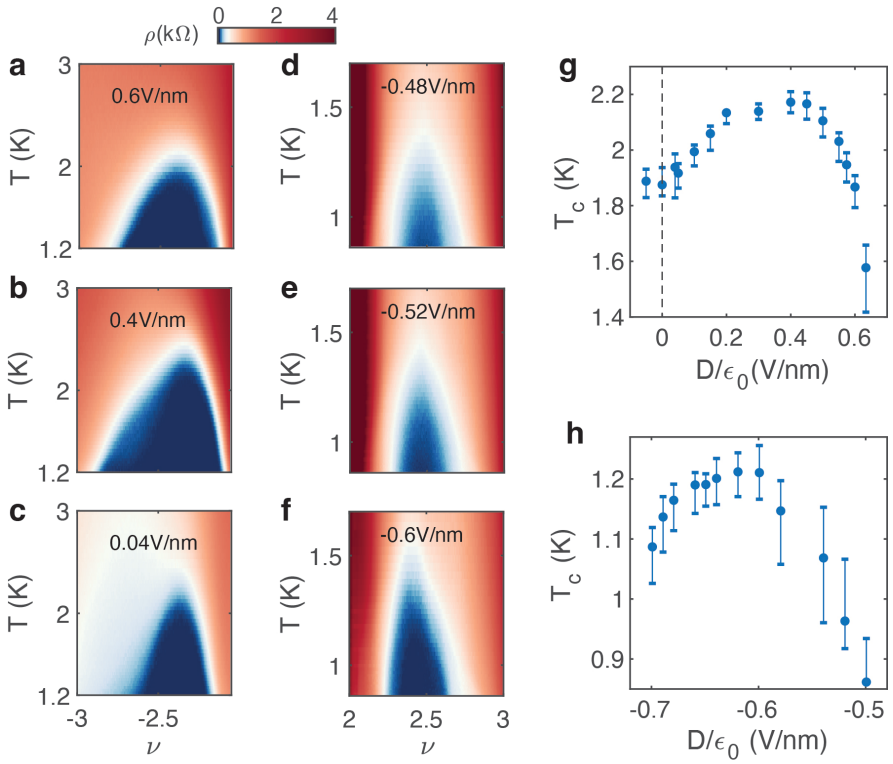

Figure 3.6: **a** to **f** Dome shaped superconducting regions in the $T-\nu$ plane at different D for $\nu<-2$ [a to c] and $\nu>2$ [d to f]. The size and shape of the domes are tuned by D. **g** and **h** T_c as a function of D taken at $\nu=-2.3$ (g) and $\nu=2.45$ (h). T_c is chosen to be the point where $\rho=10\%\rho_N$ and error bars correspond to $5\%\rho_N$ and $15\%\rho_N$.

symmetry breaking phase[57]. Fig. 3.7b shows $|n_H-\nu|$ as a function of ν and D, showing several symmetry breaking regions. At $0>\nu>-2$, the large area of $|n_H-\nu|=0$ shown as dark blue indicates that the holes are filling the four bands equally. At $-2>\nu>-3$, the system enters the symmetry breaking phase with two degenerate bands where $|n_H-\nu|=2$, shown in white. At $\nu=-3$ at small D another reset occurs, and at $\nu<-3$, $|n_H-\nu|$ is not integer valued, changing gradually from 3 to 4. This symmetry breaking behavior is affected as D tunes the single particle band structure of the MA-TTG. In particular, for the hole side band ($\nu<0$), above $D/\varepsilon_0=0.35$ V/nm a large region $|n_H-\nu|=4$ emerges at $\nu<-3$ (marked as I in Fig. 3.8b), indicating that the four bands are being filled equally with no symmetry breaking. Interestingly, we find this region is bounded on

the right by a van Hove singularity (vHS), whose existence can be detected from diverging n_H followed by a sign change[61]. The characteristic sharp divergences of two vHSs can be seen in Fig. 3.7a at $D/\varepsilon_0 = 0.4$ V/nm near $\nu = -3$ (marked by vertical arrows), combining into one large divergence at larger D. The left boundary of region I also shows a discontinuity. However, n_H value across this boundary is continuous, indicating that this is not a vHS. As D increases, the flavor-polarizing vHS moves to the right, expanding the $|n_H - \nu| = 4$ region. Importantly we note that this evolution correlates with the reduction of superconductivity. In Fig. 3.7b, we superimpose the boundaries of the zero magnetic field superconducting region at 0.34K (Fig. S16A) and 0.86K (Fig. 3.5) onto the $|n_H - \nu|$ plot as blue and orange dashed lines respectively. The 0.34K superconducting region boundary aligns well with the $|n_H - \nu| = 2$ symmetry breaking phase boundary. More interestingly, at 0.86K where superconductivity becomes weaker, we can see that the superconducting region is reduced as the vHS and $|n_H - \nu| = 4$ region crowd out the $|n_H - \nu| = 2$ region. For the electron side superconductor, similar analysis (Fig. 3.8d) shows that the superconducting region also shrinks when the vHS starts to cross the symmetry breaking phase boundary.

The region near a vHS has an increased density of states (DOS), which promotes superconductivity in conventional Bardeen-Cooper-Schrieffer (BCS) theory in the weak coupling limit[87,88]. Here, instead it is observed that superconductivity weakens as a vHS approaches and subsequently flavor polarization occurs.The prominent role of vHS in the system can also be captured in single particle band calculations. Fig. 3.8c shows calculated DOS as a function of ν and interlayer electric potential U, which is directly proportional to the experimental D. The calculated DOS is symmetric between positive and negative U so only the positive part is shown. We observe that at low D, there is high density of states concentrated near charge neutrality, which is a reflection of the flatness of the bands. An example band structure at low D with $U = 11$ meV is shown in Fig. 3.8a. As D increases, the bands become more dispersive and vHSs become prominent, shown as the white lines in the DOS calculation at larger U. An example band structure in this range is shown in Fig. 3.8b. The

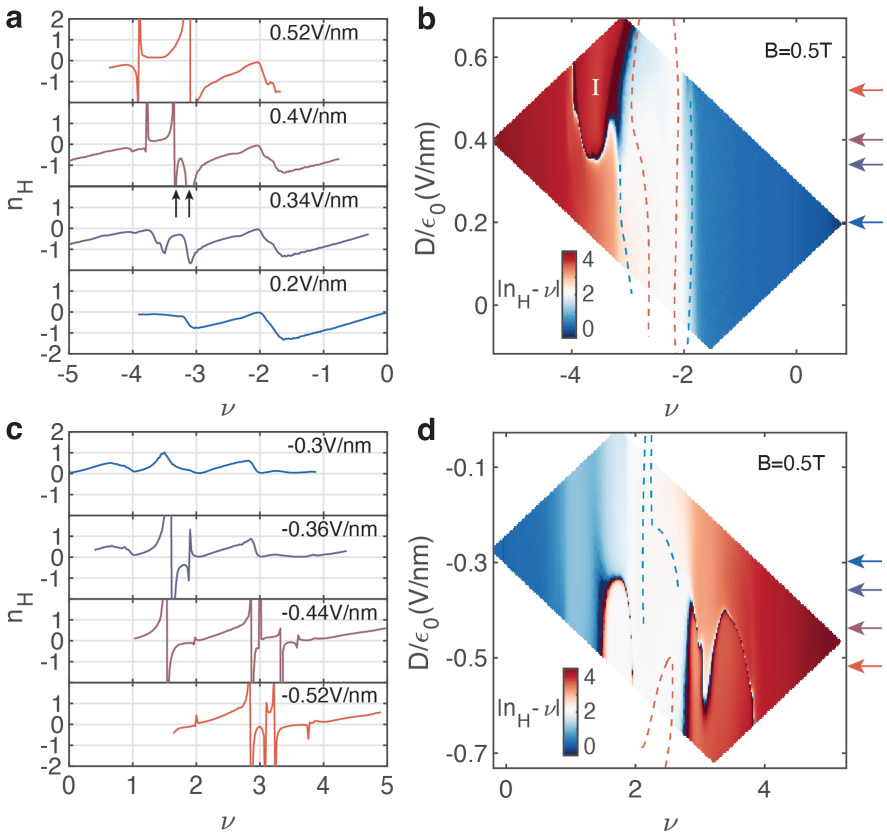

Figure 3.7: a Renormalized Hall density n_H at 0.5 T at several D. Several resets in n_H are visible at flavour symmetry breaking boundaries. Sign reversal vHS with flavor symmetry breaking is marked by vertical arrows. **b** Subtracted Hall density $|n_H - \nu|$ as a function of ν and D in the same region. The four arrows with different colors mark the locations of the line cuts in a. The blue and orange dashed lines trace out the boundaries of the superconducting region at 0.34K (Fig. S16A) and 0.86K (Fig. 3.5) respectively. The $|n_H - \nu| = 4$ region marked by I crowds out the superconducting region at large D. **d** and **d** The same as a and b but near the $\nu = 2$ superconducting state.

prominent vHS in the theoretical density of states at large U agrees with the vHS that appear at large D in experiments.

The intrusion of this vHS, and the subsequent flavor ordering which limits the width of the $|n_H - \nu| = 2$ region and consequently the region of superconductivity, accounts for the reduction of the superconducting dome at large D. However, the initial enhancement of the superconductivity seems to lie in the region where band flatness dominates the physics. In this regime, the average DOS and bandwidth of the individual conduction and valence band remain roughly constant as shown in Fig. 3.8c and d. The major change in the single particle band structure in this small D range happens at the K point, where the conduction and valence bands gradually split away from each other, increasing the combined bandwidth at this point. Recent theoretical work has suggested the importance of a second order process coupling flat bands, reminiscent of super-exchange, as the driving force for pairing[89,90]. This process leads to an energy scale $J \sim t^2/E_c$, where t is related to the overall effective bandwidth and E_c is a measure of the repulsion. This pairing mechanism also invokes the presence of $C_{2z}T$ symmetry. Indeed, this symmetry requirement is consistent with the fact that, at present, MA-TBG and alternating MA-TTG are the only two platforms exhibiting robust superconductivity, and they are also unique among existing moiré systems in retaining this symmetry. Within this picture, changing the overall effective bandwidth t can enhance superconductivity, which may be related to the observed enhancement of both bandwidth and T_c on increasing the displacement field at small D. Further evidence for the strong coupling nature of superconductivity is provided by the rapid increase of $T_c(\nu)$ with doping observed in the superconducting domes for $|\nu| < |\nu_{op}|$. This suggests a picture where tightly bound Cooper pairs condense leading to T_c which is limited by density and therefore grows with doping. One possible strong coupling mechanism that is broadly consistent with these observations is skyrmion superconductivity[90], wherein the J interaction binds charged skyrmions into pairs. We estimate J to be a few meV from the experimentally obtained slope of $T_c(\nu)$ in the regime of $|\nu| < |\nu_{op}|$, consistent with theoretical expectations[90]

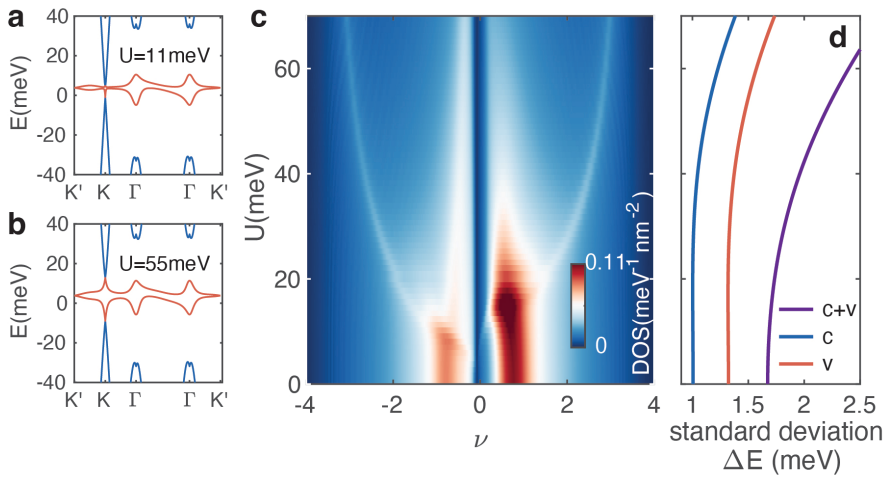

Figure 3.8: a and **b** Theoretical single-particle band structures at small (a) and large (b) interlayer potential U. The major change in the band structure is a splitting at the K point. **c** Calculated density of states as a function of ν and U. The large flat band density of states at small U diverge into prominent vHSs diverge at large U. **d** Bandwidth displayed as the standard deviation of the conduction (c), valence (v), and combined (c+v) flat bands as a function of U.

(SM, S8). We anticipate these results to stimulate further theoretical and experimental investigations into these novel correlation driven phenomena.

4

Artificial Josephson junction between magic-angle twisted trilayer graphene and a conventional s-wave NbN superconductor

The understanding of twisted graphene superconductors remains challenging due limited experimental probes for two dimensional superconductors. Motivated by the proven effectiveness of phase sensitive Josephson junctions in revealing the unconventional d-wave paring symmetry in cuprate superconductors, here we realize a Josephson junction formed between magic-angle twisted trilayer graphene (TTG) and a conventional s-wave superconductor niobium nitride (NbN). We fabricate superconducting niobium nitride contacts to a TTG device and the contact resistance fully

drops to zero when TTG turns superconducting near half-filling on both the hole- and electron-doped side. We simultaneously measure the resistance of the TTG bulk and across the junction and observe that the junction exhibits an independent superconducting critical current that is no bigger than those of the intrinsic TTG superconducting states, accompanied by a quantum interference pattern under a magnetic field that also has distinct behaviors than those from the TTG superconductors. The realization of such a Josephson junction paves the way for elucidating the pairing symmetry in the emerging graphene-based superconductors and developing hybrid quantum devices leveraging these novel materials.

4.1 Introduction

Following the discovery of superconductivity in magic angle twisted bilayer graphene (TBG)[23], tremendous efforts have been made both to expand the material systems that host similar superconducting states, and to understand the nature of the superconducting pairing. It was first discovered that twisted trilayer graphene (TTG) with alternating twist angles, which has a Hamiltonian that can be decomposed into that of twisted bilayer graphene and single layer graphene[91], hosts more robust superconductivity with higher superconducting transition temperature (T_c)[92,93]. This alternating twist approach was subsequently applied to more graphene layers and continue to produce similar superconducting phenomenology[94,95,96]. Concurrently, superconductivity was also found in non-moiré graphene systems such as Bernal bilayer graphene and rhombohedral trilayer graphene at high electric fields, where interaction effects become strong[97,98]. Meanwhile, there have been accumulating evidence suggesting possible unconventional nature of the superconductivity in these multilayer graphene systems. For example, superconducting states are consistently found only within or in vicinity of the interaction driven iso-spin symmetry breaking phases[92,93,97,98]; large Pauli limit violation in TTG and and Bernal bilayer graphene superconductors are suggestive of

spin triplet paring[99,98]; superconductivity in TBG was shown to possess nematicity[100]; scanning tunneling microscopy studies on TBG and TTG show possible nodal superconducting gap structures[101,102]. However, most of the evidence is indirect or complicated to interpret, given the limited information these experimental methods can provide about the superconducting order parameter. More direct approaches are needed to study properties such as pairing symmetry.

One of the most effective methods for identifying d-wave pairing symmetry in cuprates is constructing a phase-sensitive Josephson junction (JJ) between a cuprate and a conventional s-wave superconductor[103,104]. By configuring the junction into a 90-degree "corner" shape – aligning the two perpendicular faces with the cuprate crystal's two main in-plane axes respectively – the d-wave order parameter's internal phase modulation induces a π phase shift between the currents across the two faces, leading to a critical current minimum at zero magnetic field and a significantly altered quantum interference pattern compared to a s-wave to s-wave JJ. This phenomenon was experimentally confirmed in $YBa_2Cu_3O_{7-\delta}$[105,106], providing robust evidence for d-wave paring. This approach is valid only in the short junction regime with $L \ll \lambda_J$[107,108], where L is the junction length (the length perpendicular to the current flow) and $\lambda_J \sim \sqrt{\Phi_0/\mu_0 J_c d}$ is the Josephson penetration depth for superconducting thin films. Here, Φ_0 is the flux quantum, μ_0 is the vacuum permeability, J_c is the Josephson junction critical current, and d is the superconducting film thickness. The ultra-thin graphene superconductors naturally fit into the short junction regime, making the corner JJ approach directly applicable for probing their pairing symmetry. Compared to cuprate bulk crystals, graphene superconductors further offer fabrication flexibility, where various device shapes and integration of multiple superconducting contacts in different orientations can be achieved with relative ease. Apart from exploring the fundamental nature of superconductivity, the ability to fabricate transparent superconducting contacts that coherently couple to these novel superconductors is a potentially important technological advancement for superconducting quantum circuits, where large inductance with small footprints is highly desirable and the gate-tunability of gatemons opens

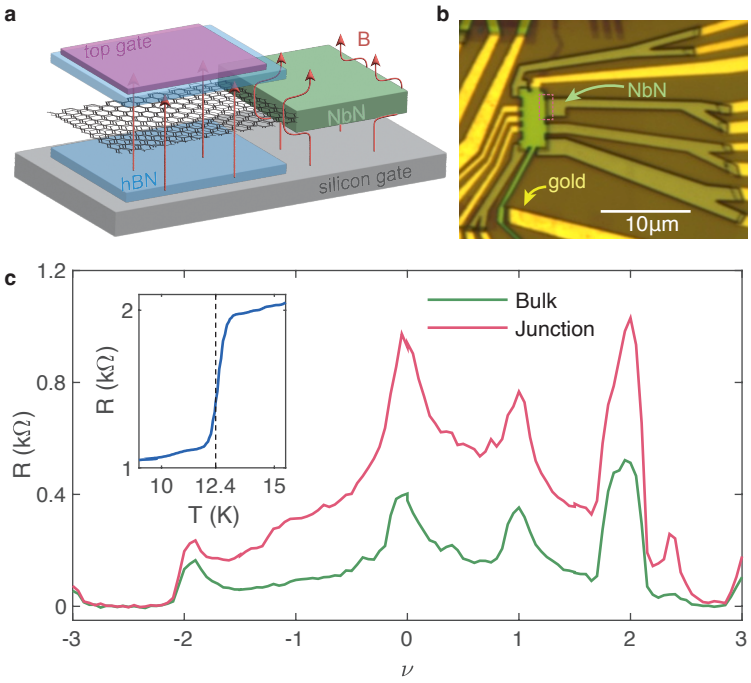

Figure 4.1: a, Schematic of the device configuration. Twisted trilayer graphene is encapsulated by hexagonal boron nitride, gated by a top graphite gate and a global silicon back gate, and connected to a NbN contact. The orange arrows illustrate that magnetic field is screened by NbN superconductor but can completely penetrate the two dimensional twisted graphene superconductor. **b**, The device image. Arrows denote gold and NbN contacts and the red dashed rectangle denotes the junction which most of the junction data presented in the paper is from. **c**, Resistance v.s. filling factor ν for both the TTG bulk and junction. Inset shows the temperature dependence of the resistance across a NbN junction and NbN turns normal at 12.4 K.

up avenues for new architectures of quantum computers. Graphene superconductors are gate-tunable low density superconductors with large kinetic inductance and can be potentially applied to the next generation superconducting qubit construction.

4.2 Fabrication of s-wave superconducting contacts using NbN

In this chapter we demonstrate that by fabricating niobium nitride (NbN) superconducting contacts to magic-angle TTG, we can achieve a JJ between TTG superconductors and NbN superconductors. NbN is a conventional s-wave superconductor with a short coherence length $\xi \sim 5$ nm [109],

which can minimize the proximity effect to TTG compared to other choices of superconducting materials and ensure that we are probing the intrinsic superconductivity in TTG. Depending on the extent of disorder, NbN films exibit a T_c of $9 \sim 16$ K. Fig. 4.1a is a schematic of the device configuration. TTG is encapsulated by hexagonal boron nitride and gated by a local graphite top gate and a global silicon back gate. We fabricate NbN contacts to TTG by ebeam evaporating 4nm of titanium followed by sputtering 70 nm of NbN. We intentionally leave a 200 nm gap between the contacts and the top gate defined channel region so that the graphene within the gap and graphene-NbN interface may together act as a weak link and result in a superconductor-normal metal-superconductor (S-N-S) junction.

Fig. 4.1b shows a picture of the device, where NbN contacts are in dark green color and gold contacts in gold. Having gold contacts allows us to measure the intrinsic TTG bulk resistance without being affected by NbN contacts. Each NbN contact branches into two before connecting to the gold electrodes on the chip. This allows us to perform a quasi-4-probe measurement of the TTG-NbN junction, where we source and drain a current through one gold contact and one branch of a NbN contact, and measure the voltage between the other branch of the NbN contact and a different but nearby gold contact. The measured resistance will primarily reflect the junction resistance, with small contribution from a short section of the TTG bulk and a section of NbN metal. Simultaneously we measure the 4-probe resistance of the bulk resistance in the same sample area using two nearby gold contacts (see supplementary information for the detailed measurement configuration). By comparing the bulk and junction measurements, we can distill the features unique to the junction. We focus on the junction denoted by a red dashed rectangle as shown in Fig. 1b and we mainly use the global silicon back gate to tune the carrier density in the TTG device. Unless specified otherwise, all measurements are done at a temperature of 250 mK.

Fig. 4.1c shows the resistance for both the TTG bulk and TTG-NbN junction as a function of filling factor $\nu = n/n_0$, where n is the carrier density and n_0 is the carrier density required for filling

one electron per moiré cell area. The twist angle and corresponding moiré cell area are determined based on fan diagram measurements, giving a twist angle of 1.5°(see supplementary information). The bulk resistance curve shown in green exhibits pronounced peaks at integer fillings ν = -2, 0, 1, 2 and goes down to zero between ν = -3∼-2 on the hole side and in a narrower range within ν = 2∼3 on the electron side. This is fully consistent with our previous study of TTG [92] with no indication of any extra effects from the NbN contacts. The junction resistance shown in red follows a similar trend with understandably larger resistance due to the inclusion of the contact resistance. Remarkably, the resistance vanishes when the bulk TTG becomes superconducting. The disappearance of the contact resistance suggests that coherent transport is established between the TTG superconductor and NbN. Since this effect happens strictly when TTG is superconducting, it cannot come from NbN-induced proximity effect. The inset shows the measured junction resistance at high temperature and the sharp resistance drop at 12.4K indicates the superconducting transition of the NbN contact.

4.3 Signatures of a twisted trilayer graphene to NbN Josephson junction

To further investigate the junction, we measure the current bias I_{DC} dependence. Fig. 4.2a shows the two dimensional (2D) map of differential resistance dV/dI as a function of I_{DC} and ν for the TTG bulk. The superconductivity states manifest as the deep blue zones of zero resistance between ν = 2∼3 and -3∼-2, each bounded by a pair of positive and negative critical currents shown as resistance peaks. They form dome shapes in ν and the hole-side dome is larger with stronger superconductivity than the electron-side. These features are typical of TTG superconductors. Noticeably, in similar ranges of ν, there are another set of resistive peaks at higher I_{DC} values on both the hole- and electron-dope side. They form larger domes enclosing the zero-resistance domes. This is most likely caused by the probed region being relatively inhomogeneous and containing two supercon-

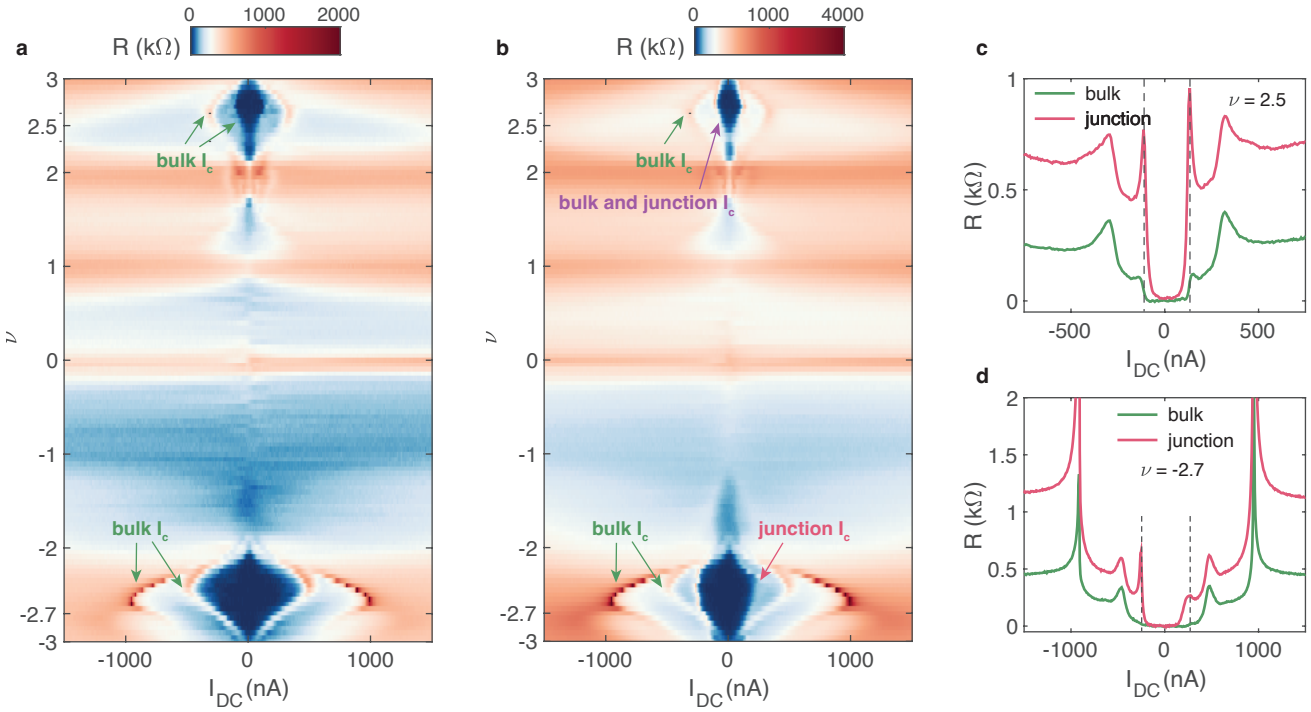

Figure 4.2: a, 4-terminal resistance of the sample as a function of DC bias current and filling factor ν. **b,** Junction resistance as a function of DC bias current and filling factor ν. **c** and **d**, Resistance as a function of DC bias current at fixed filling $\nu = 2.5$ and -2.7 respectively.

ducting areas with different strengths, presumably resulting from different twist angles. Fig. 4.2b is the simultaneous measurement of the TTG-NbN junction resistance, which shows almost identical features with elevated resistance in most regions, in particular the two sets of critical currents on both the hole- and electron-doped sides. However, the zone of zero resistance on the hole side now becomes smaller and bounded by a new pair of critical currents. This critical current is smaller than the bulk critical currents at the optimal doping and converge together with the lower bulk critical current near the dome edge. Fig.4.2d shows a linecut at $\nu = -2.7$ clearly showing two sets of large critical currents in both the bulk and junction curves and a third set of critical currents with smaller values only in the junction, denoted by two dashed lines. This is the sign of the emergence of a JJ, which tends to be a "weaker" superconductor than the two superconducting reservoirs and therefore has a smaller critical current. Note that the critical current of the NbN contact far exceeds the range of the current bias applied in our experiments.

The critical current of a S-N-S JJ can depend on several factors such as the S-N interface transparency, the scattering within the normal metal weak link, and the coherence length and strength of the superconducting banks [110]. In our measurements near optimal doping, the formal two factors dominate and lead to a smaller junction critical current whereas close to the dome edge where junction and bulk critical currents start to converge, the strength of the TTG bulk superconductivity becomes the limiting factor. On the electron-doped side, given the weak bulk superconductivity across all fillings, we always observe only two sets of critical currents, with the JJ critical current aligning with the smaller bulk critical current, clearly shown in Fig. 4.2c marked by two black dashed lines.

4.4 Quantum interference pattern of the Josephson junction

The most striking difference between the bulk and junction physics shows up in the magnetic field dependent critical current measurements, which result in Fraunhofer patterns due to quantum in-

terference effects in JJs. Fig. 4.3a and 4.3b are 2D maps of differential resistance at $\nu = -2.55$ as a function of I_{DC} and magnetic field B for the TTG bulk and TTG-NbN JJ respectively. Both of them show Fraunhofer patterns but they look distinct. The Fraunhofer pattern in TTG bulk has been previously prevalently observed in various twisted graphene superconducting devices and is attributed to an inhomogenerou distribution of superconducting and metallic phases within the device. The Fraunhofer patterns of this kind are highly dependent on doping and usually more easily observed near the dome where islands of non-superconducting phases start to proliferate. By taking the first minimum of the critical current as the end of the first period, we obtain a periodicity of ~ 13 mT which gives an effective junction area of $0.16\,\mu m^2$. The magnetic field distribution in a 2D superconductor is governed by the so-called Pearl length $\Lambda = 2\lambda^2/d$ where λ is the superconducting penetration depth and d is again the 2D superconductor's thickness. On the other hand, the TTG-NbN JJ shows a very different Fraunhofer pattern with a much smaller periodicity of ~ 3.4 mT, corresponding to a bigger effective junction area of $0.66\,\mu m^2$. The Fraunhofer pattern is also different from a typical $\sin(\pi\Phi/\Phi_0)/(\pi\Phi/\Phi_0)$ form. More interestingly, the junction pattern is significantly affected by field sweeping directions and suffer irregular jumps (see supplementary information), whereas the bulk Fraunhofer pattern is unaffected. This is possibly due to the trapping of vortices in NbN, which should only affect the electrical transport across the junction. To obtain the more normal-looking Fraunhofer pattern shown in Fig. 4.3b and minimize the effects of flux trapping, we needed to warm up above NbN's T_c, conduct two separate zero-field cools, and sweep field up and down, respectively to obtain the data at positive and negative fields. These phenomena further prove the existence of an artificial JJ that is distinct from the intrinsic TTG superconducting states. Finally, the periodicity of the junction is unaffected by filling factor as shown in supplementary information, consistent with having a junction formed by junction since the junction area is mainly determined by the device geometry and not too much affected by doping as long as the sample is mostly superconducting.

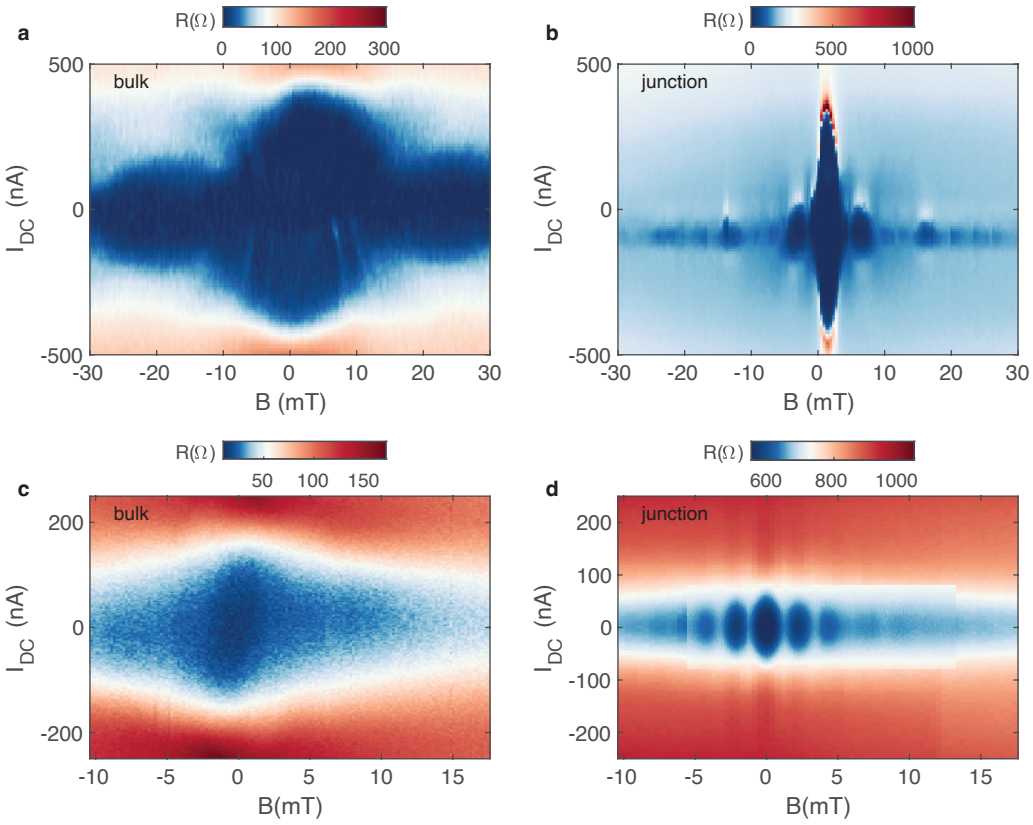

Figure 4.3: **a**, Sample bulk resistance as a function of perpendicular magnetic field and DC bias current, showing an intrinsic quantum interference pattern with large periodicity. **b**, Junction resistance shows a distinct interference pattern with much stonger modulation and smaller periodicity. **c** and **d**, Sample bulk resistance and junction resistance for a second device.

Fig. 4.3c and 4.3d show measurements of the bulk and junction in a second TTG device. Here the TTG bulk doesn't show any interference pattern, presumably because the probed sample area is uniformly superconducting. The junction in this device is a 90°corner junction. The junction here at zero current bias and magnetic field doesn't fully go to zero possibly due to certain portions of the sample along the measurement path being not superconducting. Nevertheless it clearly shows an interference pattern which is also affected by hysteresis. This pattern here is more close to that of a superconducting quantum interference device (SQUID), with relatively equal distanced critical current minimum. Future experiments are needed to produce twist angle free samples.

5

Relectometry measurement of superfluid stiffness in magic-angle twisted trilayer graphene

5.1 Introduction

The two-fluid model of superconductors assumes that there are two components that can contribute to the EM field response of a superconductor: the superfluid part, which is essentially condensed Cooper pairs, and the normal fluid part, which comes from quasi-particle excitations. Let's denote the superfluid density as n_s, and normal fluid density as n_n. In the simplest transport model

of charged particles, the Drude mode, we have

$$m\frac{dv}{dt} = i\omega vm = eE - m\frac{v}{\tau}, \quad J = nev = \frac{ne^2\tau}{m}\frac{1}{i\omega\tau + 1}$$

Here v is velocity, m is particle mass, ω is the EM field frequency, e is the particle charge, τ is the scattering time and J is the current density. Given this, we can obtain the complex conductivity:

$$\sigma(\omega) = \sigma_1(\omega) - i\sigma_2(\omega) = \frac{ne^2\tau}{m}\left(\frac{1}{1+\omega^2\tau^2} - \frac{i\omega\tau}{1+\omega^2\tau^2}\right)$$

We apply this model to the superfluid component, for which $\tau_s = \infty$ by definition. Recall that $\lim_{\eta\to 0}\frac{\eta}{x^2+\eta^2} = \pi\delta(x)$. Consequently, the resulting expressions for the conductivities are:

$$\sigma_{1s}(\omega) = \frac{n_s e^2}{m}\pi\delta(\omega), \quad \sigma_{2s}(\omega) = \frac{n_s e^2}{m\omega}$$

Similarly, the conductivities for the normal component, which has a finite scattering time τ_n, are:

$$\sigma_{1n}(\omega) = \frac{n_n e^2\tau_n}{m}\frac{1}{1+\omega^2\tau_n^2}, \quad \sigma_{2n}(\omega) = \frac{n_n e^2}{m}\frac{\omega\tau_n^2}{1+\omega^2\tau_n^2}$$

In the low frequency regime of $\omega\tau_n \ll 1$

$$\sigma_{1n}(\omega) = \frac{n_n e^2\tau_n}{m}, \quad \sigma_{2n}(\omega) = \frac{n_n e^2}{m}\omega\tau_n^2 \ll \sigma_{2s}(\omega)$$

As a result, the real part of the conductivity of a superconductor is given by:

$$\sigma_1(\omega) = \frac{n_s e^2}{m}\pi\delta(\omega) + \frac{n_n e^2\tau_n}{m}$$

This formulation shows that at $\omega = 0$, the superfluid component enables dissipationless transport by shunting the normal fluid, and at finite frequencies, dissipation arises from the normal fluid component. Meanwhile, the imaginary part of the conductivity is solely contributed by the superfluid component:

$$\sigma_2(\omega) = \frac{n_s e^2}{m\omega}$$

. Therefore, we can model the superconductor as a parallel circuit comprising a resistor with resistance R, defined by $1/R = \sigma_1 = \frac{n_n e^2 \tau_n}{m}$, and an inductor L_k, given by $1/\omega L_k = \frac{n_s e^2}{m\omega}$. We call L_k the kinetic inductance:

$$L_k = \frac{m}{n_s e^2}$$

Another characteristic frequency, $\omega = R/L$, demarcates the system's behavior: below this frequency, the response is predominantly inductive; above it, it is resistive.

Regarding the sample size effect, because R satisfies $V = RI$ and kinetic inductance L_k satisfies $V = L_k \frac{dI}{dt}$, L_k has the same sample size dependence as R, namely:

$$\text{in 3D,} \quad L_k = \frac{m}{ne^2}\frac{L}{Wd}, \quad \text{where } n \text{ is the volume density}$$

$$\text{in 2D,} \quad L_k = \frac{m}{ne^2}\frac{L}{W}, \quad \text{where } n \text{ is the surface density, ensuring consistent units for } L_k$$

Superfluid stiffness ρ_s characterizes the rigidity of the phase of the superconducting order parameter, and is normally defined through $\mathcal{H} = \frac{1}{2}\rho_s \int dx^d \left(\nabla\theta\right)^2$. If we write ρ_s as a temperature scale, when temperature $T < \rho_s$, there is high cost in energy to have phase gradients so the superfluid can have long-range phase coherence; when $T > \rho_s$, thermal energy gives rise to large phase fluctuations and destroy phase phase coherence. To understand the relationship between kinetic inductance L_K and superfluid stiffness ρ_s, we use the Ginzburg-Landau Hamiltonian for superconductors as out-

lined in Tinkham's textbook[111]:

$$\mathcal{H} = \frac{1}{2m^*}\int dx^d \left(\hbar\nabla\theta - \frac{e^*}{c}\mathbf{A}\right)^2 |\psi|^2, \quad n_s^* = |\psi|^2$$

where ψ represents the Ginzburg-Landau wavefunction for superconducting particles, m^* the particle mass, e^* the particle charge, $\mathbf{A}$ the vector potential and n^* the particle density. Given that superconducting particles consist of Cooper pairs, with each pair containing two electrons, we have $m^* = 2m$, $e^* = 2e$ and $n_s^* = n_s/2$, where m, e and n represent the mass, charge and density of electrons, respectively.

Therefore, we have

$$\rho_s = \frac{\hbar^2 n_s^*}{m^*} = \frac{\hbar^2}{e^{*2}}\frac{n_s^* e^{*2}}{m^*} = \frac{\hbar^2}{4e^2}\frac{n_s e^2}{m} = \frac{\hbar^2}{4e^2}\frac{1}{L_k}$$

Fundamentally, both the kinetic inductance and diamagnetism of a superconductor come from the kinetic term in the Hamiltonian, thus both kinetic inductance L_K and Meissner effects are features of a superconductor's electric-magnetic (EM) field response, and L_K is related to penetration depth λ. Meissner effect, the expulsion of electromagnetic fields from the bulk of a superconducting material is one of the defining characteristics of the superconducting state of matter. While a host of techniques such as magnetic penetration depth[112] and muon spin relaxation[113] are available in bulk materials to probe and characterize the Meissner effect, alternative methods are required for two-dimensional materials with a small sample volume. A direct manifestation of the Meissner effect is the inductive response of phase-coherent Cooper pairs to an oscillating electromagnetic field.

5.2 Reflectometry measurement setup and kinetic inductance extraction

In this chapter, we develop a technique to measure the superconducting kinetic inductance, or equivalently its inverse, the superfluid stiffness in micron-sized samples of 2D superconductors, and apply it to twisted trilayer graphene (TTG)[114,115]. TTG is a recently discovered superconductor from the twisted graphene family where the combination of moiré lattice potential, electronic correlations, and band structure topology is expected to have unusual and possibly exotic influences on the nature of the superconducting state. Our measurements of the superfluid stiffness as a function of carrier density and temperature (T) show linear-in-T behavior within the entire superconducting dome, consistent with nodal superconductivity: an unconventional superconducting state where the superconducting gap disappears along certain directions on the Fermi surface. We also measure the superfluid response as a function of supercurrent bias and show evidence for the non-linear Meissner effect, another hallmark of nodal pairing. Finally, we observe a roughly linear dependence of the superconducting transition temperature (T_c) on the measured superfluid stiffness, indicating that phase fluctuations, rather than the suppression of Cooper pairing, destroy superconductivity in TTG. Altogether, our observations provide strong evidence for unconventional superconductivity in this system, and show close parallels with the phenomenology of superfluid stiffness in high T_c materials such as the cuprate superconductors.

Inspired by recent developments in quantum measurement technologies, we adapt radio-frequency reflectometry to measure the superfluid response of micron-sized flakes of twisted trilayer graphene. Flakes of 2D materials have an additional impedance arising from the typically large contact resistances (R_c) that appears in series with the kinetic inductor L_K [5.1a], making the device impedance much larger than the characteristic impedance $Z_0 = 50\ \Omega$ of a standard microwave measurement circuit. Notably, previous kinetic inductance measurement implementations have either been conducted in quasi-2D and 3D materials samples where contact resistances are small [116,117], or in 2D

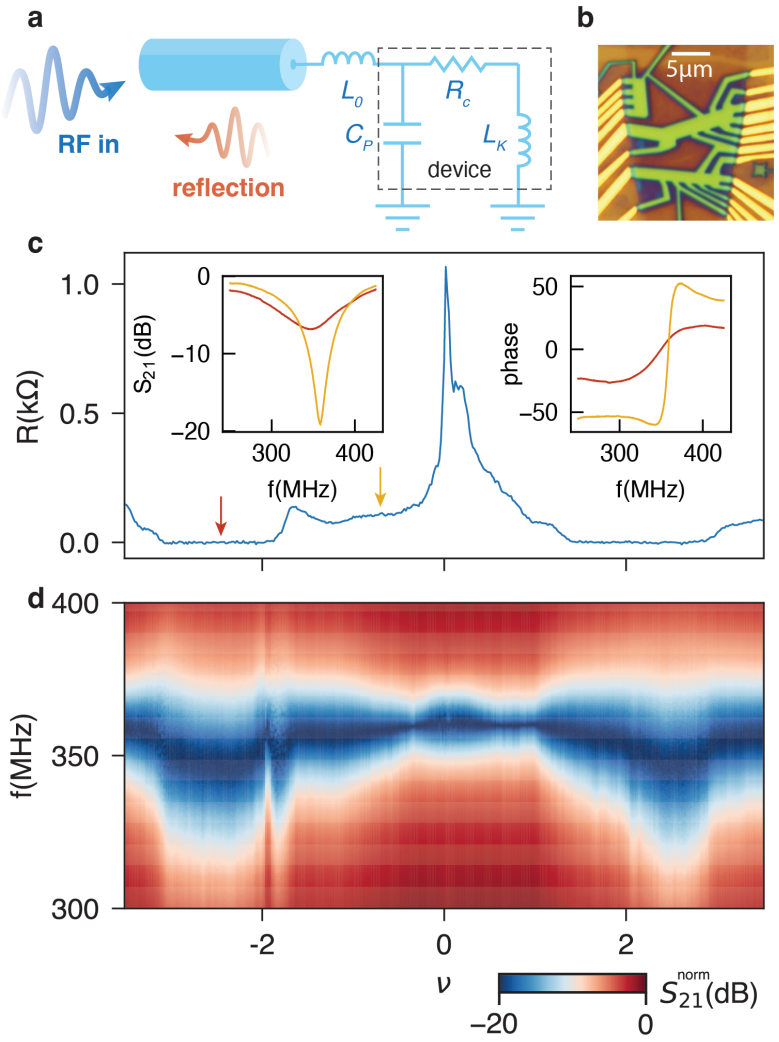

Figure 5.1: **a** Schematic of the RF reflectometry setup. An L-matching network consisting of L_0 and C_P transforms the device impedance $1 - 5\text{k}\Omega$ to the 50 Ω characteristic impedance of the RF measurement circuit. **b** Optical micrograph of the twisted-trilayer graphene device reported in the main paper. **c** DC resistance R of the device as a function of Moire filling factor ν. The sample is superconducting ($R = 0$) in both the electron and hole-doped sectors. Insets show the amplitude and phase response of the complex reflection co-efficient S_{21} showing shifts in resonance frequency between the normal and superconducting states. **d** 2D map of the normalized amplitude of S_{21} shown as a function of frequency f and filling factor ν. The resonator undergoes large frequency shifts $\Delta f_r \simeq 10 - 15$ MHz when the sample changes from normal to superconducting states.

materials where the normal contact is substituted with a superconducting contact, with carefully chosen superconducting materials to avoid Josephson junctions and superconducting proximity effect from the contact material. Our approach toward this problem is the use of impedance matching networks. We use an L-matching circuit consisting of an external inductor $L_0 \simeq 100 - 200$ nH and the naturally build-in parasitic capacitance in a typical experiment, $C_P \simeq 1 - 10$ pF. The effective $L - C - R$ circuit resonates with a frequency $f_r = f_{r0}\left(1 + L_K/(2R_c^2 C_P)\right)$, where the change of kinetic inductance is linearly proportional to the relative shift of the resonance frequency: $\Delta L_K = 2R_c^2 C_P\,(\Delta f_r/f_{r0})$, for $L_K \ll R_c^2 C_P \simeq 10\,\mu H$.

Our experimental setup allows simultaneous DC electrical transport and microwave measurements. We observe zero resistance for a range of moiré filling factors $-3 < \nu < -2$ for hole doping and $-1.5 < \nu < -3$ for electron doping, as shown in Fig. 5.1c. Simultaneously, the complex reflection coefficient of the resonator S_{21} shows distinct frequency shifts $\Delta f_r \simeq 10 - 15$ MHz in both the amplitude and phase response as the sample transits from normal to superconducting (inset of Fig. 5.1c). This is captured in Fig. 5.1d as a function of ν where the resonator shifts to lower frequencies in the range of filling factors where the device is superconducting as measured with simultaneous DC transport. We perform a fitting of the resonances in the complex plane to accurately estimate the resonance frequency f_r, together with the internal (Q_I) and coupling (Q_C) quality factors, which are related to the high-frequency resistance $R_s = \left(\frac{L_0}{Z_0 C_P}\right)\frac{Q_C}{Q_I}$, while f_r is used to obtain the kinetic inductance L_K and the superfluid stiffness $\rho_s = (w/l)L_K$, $w/l \simeq 5$ is the geometrically estimated aspect ratio of the device, where w and l are the sample width and length, respectively.

5.3 Linear in T behavior and doping dependence of superfluid stiffness

Focusing on the hole-side superconducting dome, we measure the DC and microwave response of the device as a function of ν and sample temperature T, with a range of $-1.5 \leq \nu \leq -3.5$, and

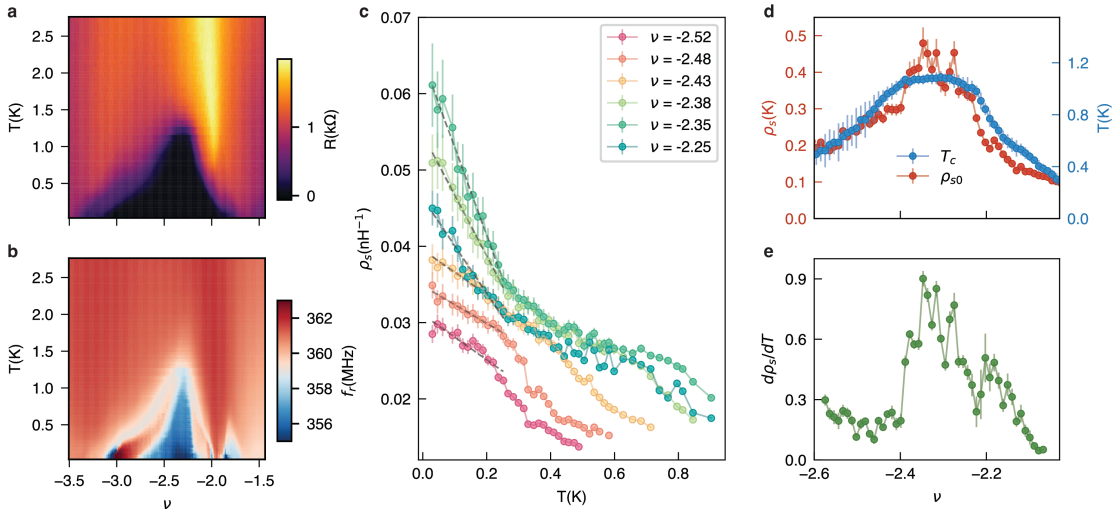

Figure 5.2: Two-dimensional map of the **a** DC resistance R and **b** resonator frequency f_r measured as a function of Moire filling factor ν and sample temperature T. **c** Superfluid stiffness ρ_s as a function of T for a range of filling factors around $\nu = -2.4$. **d** (Left-axis) Zero-temperature superfluid stiffness obtained by linear extrapolation of curves in **c** as a function of ν. (Right axis) T_c obtained from DC resistance measurements as a function of ν. **e** Low-temperature slope $d\rho/dT$ obtained as a function of ν.

$0.03 \leq T \leq 2.55$ K, as shown in Fig. 5.2a and 5.2b. In Fig. 5.2c we show measurements of ρ_s as a function of T for a range of filling factors around optimal doping $\nu = -2.4$ with the largest $T_c \simeq 1.2$ K. T_c is defined as the onset temperature for non-zero values of the DC resistance. $\rho_s(T)$ shows pronounced linear-in-T behavior for 0.03 K$< T < 0.2 - 0.5$ K, covering roughly an order of magnitude in T. The onset of linearity occurs at $T \simeq 0.4T_c$ in this range of filling factors.

The low-temperature behavior of the stiffness response can be characterized by a zero temperature superfluid stiffness ρ_{s0} and the low-temperature slope $d\rho_s/dT$. In Fig. 5.2d, we express ρ_{s0} in Kelvin and compare it with the superconducting transition temperature T_c extracted from DC measurements. The two quantities appear to roughly track each other as a function of filling, and produce a bell-shaped curve that is centered around $\nu = -2.3$. On the other hand, the low-temperature slope $d\rho_s/dT$ is roughly constant $\sim 0.2 - 0.3$ for fillings $-2.6 \leq \nu \leq -2.4$ and then shows a change rising to almost $\simeq 0.9$ around $\nu = -2.3$ before tapering off to a lower value as we approach

the right edge of the dome at $\nu = -2$.

We first explore the relationship between ρ_{s0} and T_c. We observe a roughly linear dependence between the two quantities as shown in Fig. 5.3b, with a saturation at $T_c \simeq 1.2$ K for larger values of ρ_{s0}. A linear dependence of T_c on ρ_{s0} suggests that phase-fluctuations, characterized by ρ_{s0}, play a strong role in determining the superconducting transition temperature T_c. Such behavior has been observed in unconventional superconductors, most notably the cuprates where the superfluid stiffness (expressed in units of energy) is much lower than the the BCS gap, Δ, associated with the energy scale that determines Cooper pairing [118,119]. This is consistent with STM measurements of the superconducting gap in TTG where $\Delta \simeq 10$ K [120], whereas $T_c \simeq 1$ K and $\rho_s \simeq 0.5$ K as obtained from our measurements, indicating that phase coherence (rather than Cooper pairing) determines the gross value of T_c in TTG.

We investigate the role of phase-fluctuations further by estimating a Berezinskii–Kosterlitz–Thouless (BKT) transition temperature (T_{BKT}) through the Nelson–Kosterlitz criterion [121]: $T_{BKT} = \frac{\pi}{2}\rho_s$ [Fig. 5.3(a)]. Two notable observations emerge: i) T_{BKT} is smaller than T_c roughly by a factor of 3; ii) the scaling of T_{BKT} with ρ_{s0} shows a linear dependence with a slope of ~ 1 [Fig. 5.3(b)]. While we expect $T_{BKT} \simeq T_c$ in a perfect two-dimensional superconductor, the factor of $\sim$3 difference between the two may arise from two possible effects. First, inhomogeneity within the superconducting state may lead to an underestimation of the superfluid stiffness purely from geometric reasons, where the effective aspect ratio of the superconducting region $(l/w)^*$ is larger than $(l/w) \simeq 5$ estimated from the device geometry [Fig. 5.1a, Fig. 5.3c]. Second, we speculate that a BKT-like transition in our samples may be pushed to higher temperatures due to finite-size effects or large vortex core energies. The BKT transition proceeds through the unbinding and motion of vortex-antivortex pairs and applies in the thermodynamic limit where the sample dimension $l, w \gg \lambda$, where λ is the superconducting penetration depth and determines the spatial extent of the supercurrent circulation around the vortex core (size ξ, the coherence length). We estimate penetration depth $\lambda \simeq 2\,\mu$m

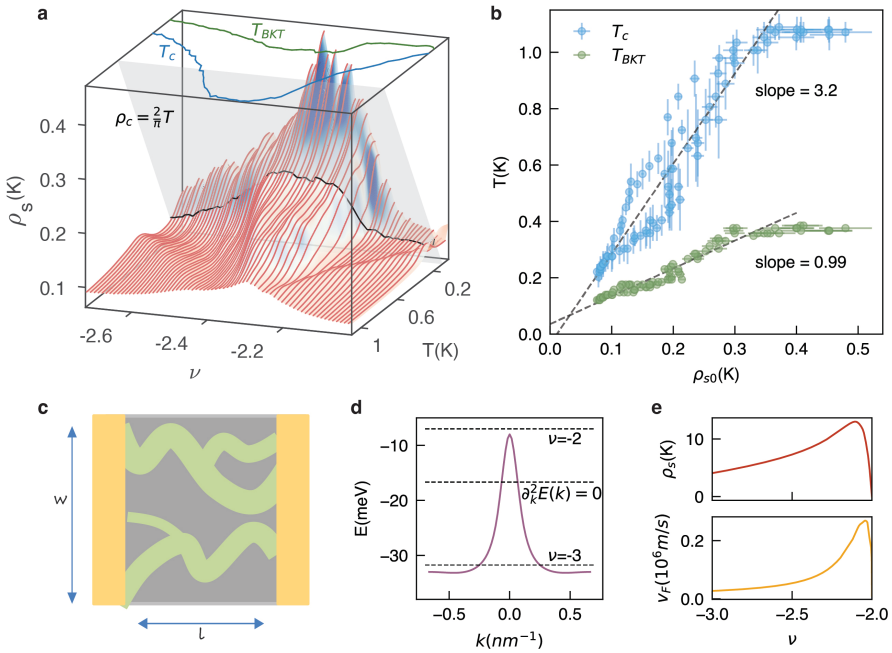

Figure 5.3: a Waterfall plot showing ρ_s as a function of T and ν. The curves have been smoothed with a 5-pt moving mean average to aid visualization. The BKT transition temperature (T_{BKT}) is obtained from the intersection between the universal BKT plane represented as $\rho_c = 2T/pi$ and the experimental stiffness curves. **b** T_c and T_{BKT} as a function of rho_{s0} **c** Schematic showing inhomogeneous superconducting paths that may lead to an underestimation of the superfluid stiffness. **d** Hartree-Fock renormalized bands in TTG as a function of momentum k within the mini-Brillouin zone. **e** (Top) Theoretical calculation of the superfluid stiffness and (Bottom) Fermi velocity based on the renormalized band model.

from our stiffness measurements ($\lambda = \sqrt{\hbar^2 d/(4e^2\mu_0\rho_s)}$, $d = 1$ nm is the sample thickness) which is comparable to the sample dimensions $2-5$ μm. Furthermore, the BKT mechanism assumes that the energy of a vortex is predominantly of order ρ_s, the contribution arising from the circulation of supercurrent around the core, but neglects the vortex-core energy itself. If vortex-core energies are high, then thermal fluctuations may not produce a proliferation of vortices at the universal value of $2T/\pi$ but instead at a higher temperature.

We now focus on the behavior of ρ_{s0} as a function of ν. Recalling that $\rho_s = n_s/(e^2 m_s)$, we expect a linear relationship between ρ_{s0} and $\nu \propto n_s$ for parabolic bands that are well described by a single effective mass m_e. The bell-shaped dependence observed in the experiment [Fig. 5.3d], particularly the drop of the ρ_{s0} with increasing hole doping for $\nu < -2.4$ suggests a departure from the parabolic-band approximation. Theoretical modeling of the twisted graphene band structure for moiré fillings between $-3 < \nu < -2$ suggests the presence of strongly renormalized bands that are highly non-parabolic, as shown in Fig. 5.3d. An interplay between strong Coulomb repulsion and quantum geometric effects, particularly the concentration of Berry curvature near $k = 0$, leads to a bandstructure that is highly dispersive close to $\nu = -2$ but gets progressively flatter on approaching $\nu = -3$. The superfluid stiffness now admits a more general formulation $\rho_s(\nu) = \sum_{k=0}^{k_F(\nu)} n_k d^2E/dk^2$ and leads to a doping dependence as shown in Fig. 5.3e. Starting at $\nu = -2$, the initial steep rise of ρ_s is enabled by the strong dispersion of the bands at $k = 0$. However, on further doping, the negative curvature ($d^2E/dk^2 < 0$) of the bands [Fig. 5.3d] causes a drop of the superfluid stiffness with increasing doping, followed by an eventual saturation when the filling reaches the flat sectors of the bandstructure. It is worth noting that a similar drop of superfluid stiffness with increasing doping is observed in the overdoped cuprates and remains a subject of active investigation [118,122].

We now turn to the temperature dependence of ρ_s. The linear-in-T suppression of ρ_s implies a T-linear increase in quasiparticle excitations. This is not expected in a fully gapped superconductor where the quasiparticle population is exponentially suppressed for $T \leq 0.3\ T_c$. Instead, the T-

linear behavior is consistent with a nodal superconducting order where the superconducting gap vanishes along certain directions on the Fermi surface. Within a picture of nodal superconductivity, the low-temperature slope $d\rho_s/dT = -\log 2/4\pi(v_F/v_\Delta)$ [123,124], v_F is the Fermi velocity of the normal carriers and $v_\Delta = d\Delta/dk$ describes the slope of the superconducting gap at the nodal point as a function of momentum k. From the experimentally measured $d\rho_s/dT$ [Fig. 5.2(e)], we obtain $v_F/v_\Delta \simeq 10-50$. We compare this to Cuprates that generally show d-wave nodal superconductivity with $v_F/v_\Delta \simeq 10$. Furthermore, if we assume that v_Δ does not vary with ν, we expect $d\rho_s/dT(\nu) \propto v_F(\nu)$ which is qualitatively consistent with $v_F(\nu)$ obtained from our theoretical model of the TTG bands (compare Fig. 5.2(e) with Fig. 5.3d).

5.4 Nonlinear Meissner effect in TTG superconductors

To solidify our interpretation of nodal superconductivity, we measure ρ_s in the presence of a finite supercurrent bias I at $T = 30$ mK [Fig. 5.4a and b]. In fully gapped superconductors, finite supercurrents do not affect the superfluid stiffness for $I \ll I_c$, where I_c is the critical current. On the other hand, for nodal superconductors, even small supercurrents are expected to produce a suppression of the superfluid stiffness [125,126,127]. This phenomenon is known as the non-linear Meissner effect and was initially proposed as a "zero"-temperature test for nodal superconductivity in Cuprates [125]. Our experiments indicate a rapid suppression of ρ_s with increasing I [Fig. 5.4c], with the strongest signatures close to optimal doping ($\nu = -2.4$, $I_c \simeq 0.12\mu$A). The suppression follows a characteristic shape with a quadratic behavior, $\delta\rho_s = -bI^2$ close to $I \to 0$, that turns linear with $\delta\rho_s = -cI$ after the supercurrent exceeds a temperature-dependent cross-over scale I^*. This is exemplified in [Fig. 5.5c] where we investigate $\rho_s(I)$ measured at optimal doping ($\nu = -2.4$) at different temperatures. We observe a drastic suppression of the quadratic coefficient b with increasing T [Fig. 5.5b].

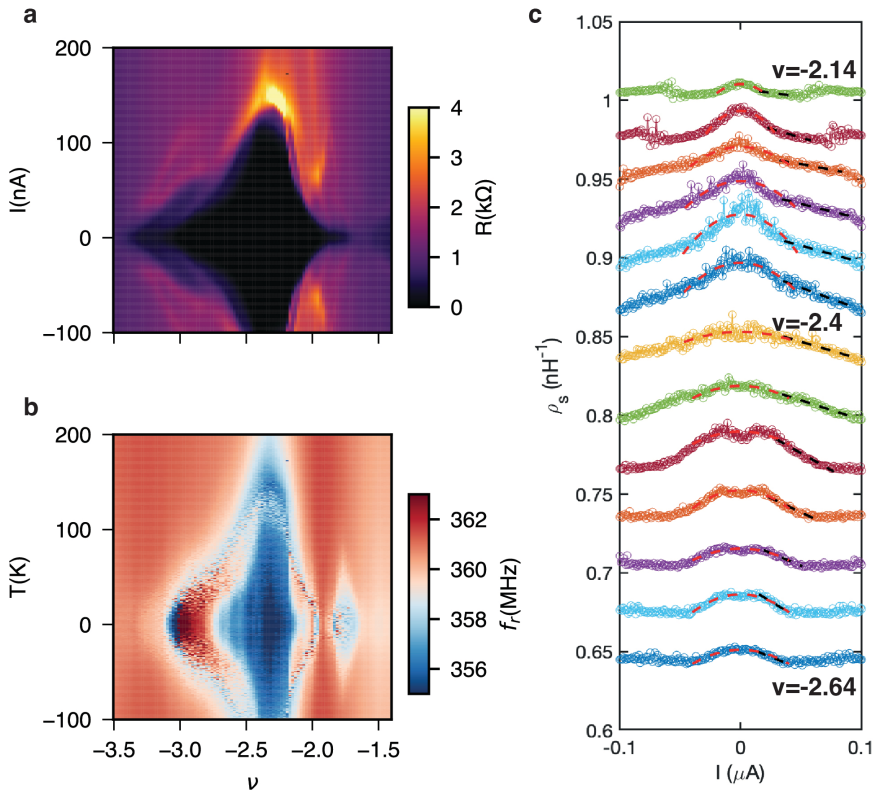

Figure 5.4: Two-dimensional map of the **a** DC resistance R and **b** Resonator frequency f_r measured as a function of Moire filling factor ν and supercurrent bias I. **c** Superfluid stiffness ρ_s as a function of I for a range of filling factors $\nu = -2.14$ to $\nu = -2.64$ ($T = 30$ mK). $\rho_s(I) \propto -I^2$ for $I \to 0$ with a crossover to linear dependence $\rho_s(I) \propto -I$. The linear behavior persists for a large range of $I < I_c \simeq 0.12\,\mu$A at $\nu = -2.4$. Curves are shifted for clarity.

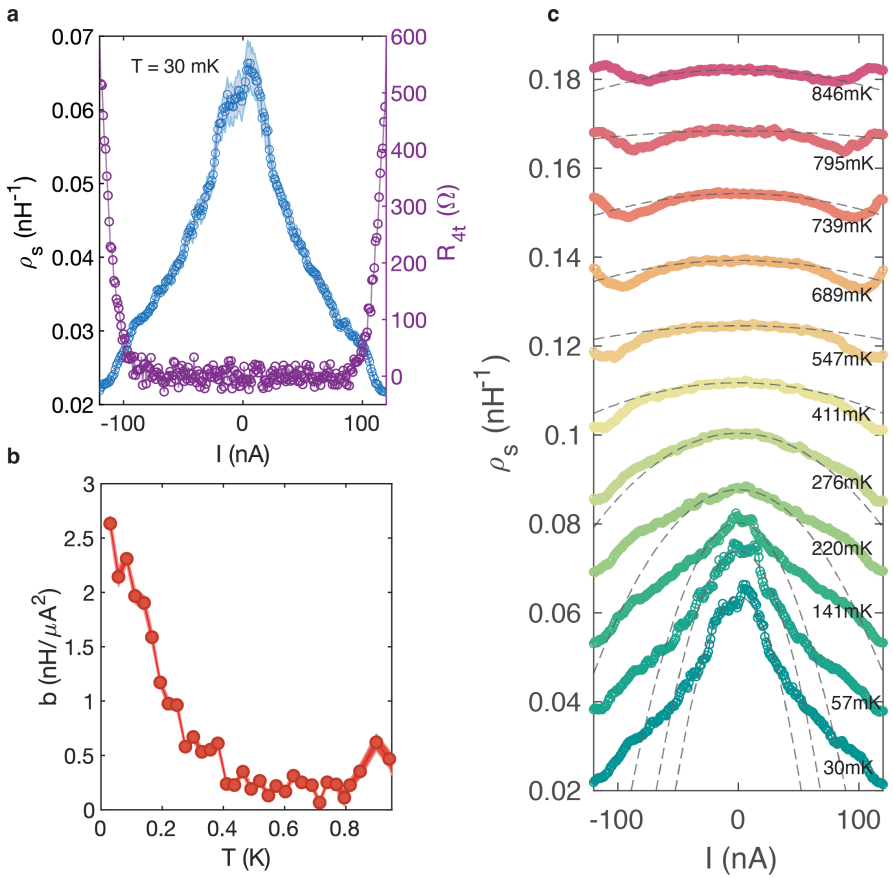

Figure 5.5: **a,** sample resistance and superfluid stiffness as a function of bias current. **b,** The curvature of $\rho_s(I)$ at $I = 0$, b as a function of T shows diverging behavior as $T \to 0$, a signature of nodal superconductivity. **c,** $\rho_s(I)$ measured at $\nu = -2.4$ at different values of sample temperature T. The curvature of $\rho_s(I)$ at zero current decays with increasing temperature.

To understand this effect, we model the electrodynamic response of a 2D nodal superconductor in the presence of a supercurrent bias. We obtain $\Delta\rho_s(I) \propto (v_F/v_\Delta)(1/T)(\hbar I^2/(ne^2W^2))$ for $I \to 0$ and $\Delta\rho_s(I) \propto I/(v_\Delta neW)$ for $I > I^*$, where the crossover current $I^*(T) = (neW/mV_F)T$ that separates the quadratic and linear regimes of $\rho_s(I)$. Our model explains all three experimental features: the quadratic suppression of stiffness at $I \to 0$, the crossover to a linear dependence at a current threshold I^* , and the divergence of the quadratic coefficient b for $T \to 0$.

To summarize, we have three key findings. First, phase fluctuations play a dominant role in determining the superconducting transition temperature, a feature that TTG shares with other unconventional superconductors with low superfluid stiffness. Second, the linear-T suppression of superfluid stiffness combined with the observation of non-linear Meissner effect in the presence of a supercurrent provides strong evidence for nodal superconductivity in TTG. Finally, a parabolic band approximation fails to explain our superfluid stiffness data even at a qualitative level. On the other hand, a relatively simple model that accounts for Coulomb interactions and quantum geometric effects of the flat bands provides a reasonable understanding of our experimental results, highlighting the strongly correlated nature of superconductivity in TTG.

6

Interplay between Superconductivity, Symmetry breaking and Single Particle Dispersion in Twisted Quadrilayer Graphene

Superconductivity in twisted multilayer graphene systems has been studied extensively due to its potentially unconventional nature. Several studies have used monolayer graphene in close proximity to twisted graphene in order to measure the chemical potential in the twisted system, providing evidence of symmetry breaking due to strongly correlated interactions. In our study, we demonstrate

how the unique combination of flat and dispersive bands in TQG allows us to simultaneously tune the band structure through carrier density and displacement field, measure the chemical potential (inverse compressibility), and probe superconductivity in a single system. The low-density dispersive bands provide a sensitive measure of the inverse compressibility in the flat bands, which ties to symmetry-breaking phase transitions at integer fillings. Using displacement field to tune the bandwidth of, and hybridization between, the flat band and dispersive band sectors, we are able to turn on and off symmetry-breaking in the system. We discover that the emergence of the superconductivity is strongly tied to the $\nu = \pm 2$ symmetry-broken state. In addition, the hybridization between the dispersive and flat bands results in a Lifshitz transition, and superconductivity is enhanced in the high density of states regime where the flat and dispersive band Fermi surface merge. Overall, we show the high degree of tunability in TQG paves a route for understanding the relationship between symmetry-breaking, band structure, and superconductivity in twisted multilayer graphene systems.

6.1 Twisted quadrilayer graphene configuration and transport properties

Since the 2018 discovery of superconductivity in twisted bilayer graphene (TBG), the field of twisted graphene, and, generally, moire systems, has grown immensely. TBG offers gate- and twist angle-tunable narrow electronic bands, which easily lend themselves to the study of strongly correlated physics. Many interesting phases have been observed in these flat band systems, including superconductivity, correlated insulators, and ferromagnetism, all of which are likely tied to correlated electron interactions. The superconducting phase has drawn particular interest because of the potential for unconventional superconductivity. Recently, the family of moire graphene has been extended to include alternating angle twisted multilayer graphene (TMG), where electric field and density tunable superconductivity have been observed, adding an additional degree of freedom be-

yond TBG. Moreover, unlike in TBG, the superconductivity in TMG systems generally exhibits an in-plane critical field approximately 3 times larger than that of the Pauli limit for conventional BCS superconductors. This series of discoveries has provided additional motivation for the tantalizing possibility of unconventional superconductivity in moire graphene systems. However, much still remains to be understood about the nature of this family of superconductors. We will seek to address some of these questions in our work on alternating angle twisted quadrilayer graphene (TQG).

In our work, we use displacement field to sensitively tune the band structure of TQG to explore the effects of bandwidth and Fermi surface size on symmetry-breaking and superconductivity. We demonstrate that the dispersive sector of the band structure can be used as a sensitive probe of the physics in the flat band sector, and use it to show superconductivity is enhanced by high density of states near a Lifshitz transition.

We study three devices, TQG1 (1.6°), TQG2 (1.6° with disorder near 1.9°), and TQG3 (1.6°), all below the predicted largest magic angle of 1.77° . We focus primarily on TQG1 in the main figures, with additional data presented in the Supplementary Information.

Near the magic angle, the strongly correlated behavior of TMG systems is characterized by the flat bands ("flat" or "magic sector") which can be mapped to that of a magic angle ($\approx$ 1.1○) twisted bilayer. Each additional pair of layers beyond the first two contributes a dispersive band that can be mapped directly to that of an off-magic-angle twisted bilayer ("dispersive sector"), while odd-layered TMG contains and additional monolayer-like Dirac cone ("dispersive cone"). For our samples twisted at 1.6° the flat and dispersive sectors are equivalent to TBG at $\approx$ 0.99° and $\approx$ 2.6°, respectively.

This is illustrated in Figure 6.1a, with the magic sector in red and the dispersive sector in blue. Despite their seemingly different low energy band structures, all TMG systems ($n_{\text{layers}} = 2 - 5$) studied experimentally thus far exhibit very similar behavior, namely pockets of superconductivity near half filling of the conduction and valence band of the magic sector and symmetry breaking near

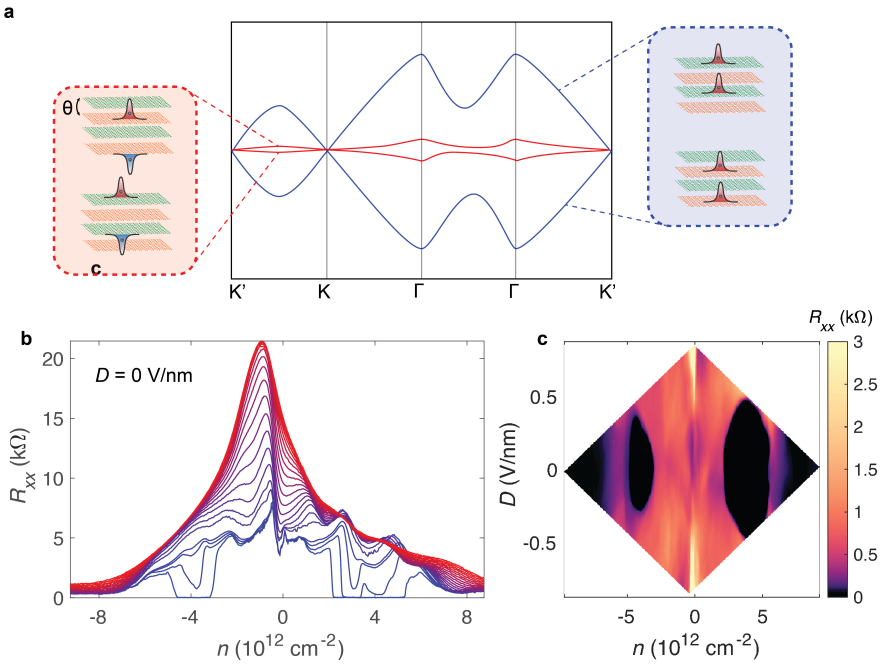

Figure 6.1: a) Four layers of monolayer graphene are stacked with alternating twist angle (layers 1 and 3, purple: $+\theta/2$, layers 2 and 4, orange: $-\theta/2$). Each set of aligned layers (1 and 3, 2 and 4) energetically prefers AA stacking, such that the four layers align A-B'-A-B' where the ' indicates a relative twist. The k_m (k'_m) points of within a single moiré brillouin zone come from the same K valley of the even (odd) monolayers as indicated in the sketch. The 8×8 Hamiltonian describing the tunneling between the four layers can be decomposed into 4×4 block-diagonal matrices, where the tunneling in each block is scaled up (down) by a factor of φ. Each block directly describes a twisted bilayer scaled by φ, such that near the magic angle of TQG θ_{TQG}, $\varphi\theta_{TQG} = 1.1$, the magic angle of TBG. **b)** Temperature dependence from 250 mK (blue) to 50 K (red) of TQG1, showing superconductivity emerging around 1 K near $|n| = 4 \times 10^{12}$ cm^{-2} of the electron and hole sides. **c)** Four-terminal resistivity versus carrier density n and displacement field D. Two oblong pockets of superconductivity (black) emerge on both the electron and hole side, and are displacement field tunable. The green dashed line indicates the zero displacement field line along which **b** and **d** are measured.

quarter, half, and three-quarter fillings. Several previous works have intimated that the interaction-induced symmetry-broken state near half filling appears to bound the observed superconducting state, implying that the origin of superconductivity may be unconventional and that the pairing mechanism may require the specific flavor polarization. However, a number of competing theories suggest alternative origins, including a more conventional electron-phonon mediated pairing. Thus, exploring the nature of the superconductor from a variety of perspectives is imperative to a complete understanding of this fascinating system.

Twisted quadrilayer graphene is a particularly interesting system to explore because the dispersive band sector can act as an extremely sensitive probe of the strongly interacting physics in the flat band sector. At $D = 0$ the two sectors are fully orthogonal, as shown in Figure 6.1a, where the flat (dispersive) band in red (blue) is comprised of antisymmetric (symmetric) wavefunctions with a total degeneracy of 8 in each sector (spin ($\uparrow\downarrow$), valley ($\pm$), odd/even layer). Away from charge neutrality, the Fermi surface of the magic sector is generally much larger than that of the dispersive sector.

Magneto-oscillations provide a measure of the number and size of Fermi surfaces active in each sector at any given filling, and are one of the primary probes we utilize to study the effect of hybridization and Fermi surface changes on symmetry-breaking and superconductivity in TBG. For example, from the $D = 0$ Landau fan (LF) in Figure 6.2a, we can clearly observe Landau levels (LLs) at high field that extrapolate back to non-zero filling, resulting from the symmetry broken states of the flat bands. At the same time, oscillations at low field originate from the simultaneous filling of the dispersive sector, indicating the general form of the predicted band structure matches experimental data well. The periodicity of the Shubnikov de Haas oscillations (SdHO) gives the carrier density, n, in each subsystem:

$$n_{\text{sector}} = \frac{ge}{\Delta(B^{-1})\hbar} \tag{6.1}$$

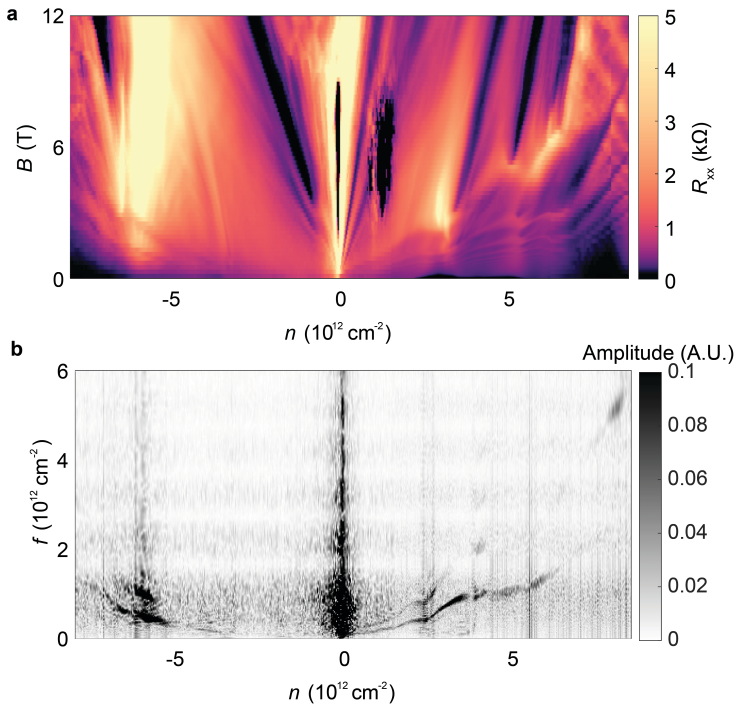

Figure 6.2: a) Landau fan at $D = 0$ from 0 to 12 T. **b)** Fourier transform of the Landau fan in **d**, in units of carrier density, $|n| = 4e/B_F^{-1}h$. The carriers in the dispersive band show up as the black, scalloped feature.

where $\Delta(B^{-1})$ is the period in units of Tesla^{-1}, e is the charge of an electron, h is Planck's constant, and the degeneracy $g = 8$. Using this to calculate the number of charges in the dispersive sector and that $n = n_{\text{flat}} + n_{\text{dispersive}}$, we find $\approx 15\%$ of the carriers reside in the dispersive bands for $n_{\text{total}} > 0$, as shown in Figure. 6.2b. For $n_{\text{total}} < 0$, however, only $\approx 10\%$ of the carriers reside in the dispersive bands. This electron-hole asymmetry must be accounted for in a theoretical description of the TQG band structure.

It is convenient to use full-filling of the moire unit cell as a metric, rather than the carrier density, so we will discuss our observations in terms of $\nu = 4n/n_s$, where $n_s = \frac{\sqrt{3}\theta^2}{8a^2}$ is the total number of carriers required to fill one moire unit cell. Because of the two or more co-existing sectors in twisted multilayer systems, it is also useful to define the filling of the flat sector alone: i.e., $\nu_{\text{flat}} = 4n_{\text{flat}}/n_s =$

$4(n - n_{\text{dispersive}})/n_s$, where $n_{\text{flat}} \approx 0.85n$ for $n > 0$ and $n_{\text{flat}} \approx 0.9n$ for $n < 0$. This is an important distinction to make as it is expected that the superconductivity primarily arises due to the flat band subsystem, rather than the dispersive subsystem. Indeed, many of the strongly correlated features in the data, including superconductivity, align with integer values of ν_{flat} rather than ν.

6.2 Symmetry breaking and superconducvitiy

In this flat band sector, similar to previous observations in other moire flat-band systems, we see evidence of physics beyond the single particle picture, most obviously through spontaneous symmetry-breaking of the 8-fold degenerate flat band sector at integer fillings, ν_{flat}. Figure 6.2a shows Chern insulators appearing as dark black lines particularly visible on the electron side, with Chern numbers matching that of a symmetry-broken 8-fold degenerate flat band (see Supplementary Information). Since the two sectors are in equilibrium, the dispersive sector can be used as a probe of the chemical potential μ of the flat sector and thereby extract the inverse compressibility $d\mu/dn$. We calculate μ using the linear dispersion of the low energy cones of the dispersive bands,

$$\mu_{\text{dispersive}} = v_F^* k_F = v_F^* \sqrt{\pi n_{\text{dispersive}}/2} \tag{6.2}$$

$$\mu_{\text{flat}} = \mu_{\text{dispersive}} \tag{6.3}$$

Drawing a direct comparison to Refs. [128,129,130], we can interpret the vanishing of $d\mu/dn$ near integer fillings as symmetry-breaking phase transitions. Broadly, when μ plateaus as a function of carrier density, this indicates an ongoing phase transition, or a region of extremely flat bands. A more detailed discussion is included in the Supplementary Information.

These symmetry-breaking features strongly resemble those seen in TBG, indicating the flat band physics in bilayer versus multilayer systems is very similar. However, one of the main differences between TBG and TMG systems is the degree to which their band structure can be tuned by dis-

placement field. Away from the magic angle, out-of-plane electric field can push charges to be more strongly localized on the top or bottom layer in twisted bilayer graphene, which in turns shifts the Dirac-like points at the minibrillouin zone corners K_{m} and K'_{m} in opposite directions. However, near the magic angle, the layers are strongly hybridized, so this layer polarization effect is very small, therefore displacement field has a weak effect. TMG systems, on the other hand, have one or more additional dispersive sectors on top of the flat band sector, and thus displacement field can have a larger effect: it will be able to appreciably shift the weakly hybridized dispersive sector in opposite directions at K_{m} and K'_{m} as well as allow tunneling between the flat and dispersive sectors. The latter can greatly change the overall band structure, for example, allowing the flat and dispersive sectors to hybridize near the K_{m} and K'_{m} points and open a gap. We will take advantage of displacement field as an additional tuning knob in our exploration of TQG to explore the effect of dispersion and Fermi surface on superconductivity.

Figure 6.3a shows the subtracted Hall density over the maximum range of D and n accessible in TQG1. The subtracted Hall density, $\nu - \nu_H$, is a convenient quantity to use to identify regions of symmetry-breaking: the symmetry broken state at half filling, for example, appears as a broad white plateau of value $\nu - \nu_H = 2$ on both the electron and hole sides. Even more telling is how closely the region of superconductivity matches these boundaries (Figure 6.1c), showing that superconductivity in TQG is strongly tied to the symmetry-broken state at $\nu_{flat} = 2$. Notably, the system appears to favor the flavor polarized ground state of $\nu = 2$ and symmetry-breaks to this state even before reaching $\nu = 2$, presumably meaning the carriers in the flat bands will be hole-like in this small region. The superconductivity correspondingly extends over this entire region.

From the subtracted hall density, we can see there are regions of clear symmetry-breaking but also regions that follow a simpler single particle picture. For example, starting above $|D| \approx 0.6$ V/nm, moving from charge neutrality outwards, we see the system does not symmetry break but rather maintains the single particle band structure, switching directly from $\nu - \nu_H = 0$ to $\nu - \nu_H = 4$

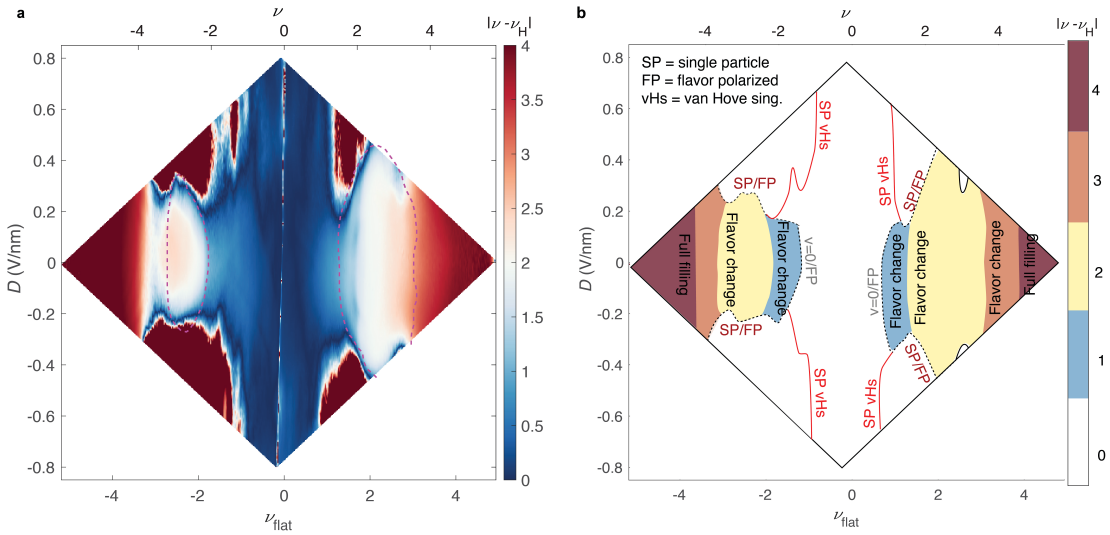

Figure 6.3: The band structure of TQG can be tuned by displacement field. **a)** Subtracted Hall density, $\nu - \nu_H$, anti-symmetrized at ± 0.5 T. The large white plateaus indicate the $\nu = 2$ symmetry broken regime where superconductivity appears at zero field. **b)** Cartoon of the n vs. D phase diagram. At low displacement field, the system symmetry-breaks at integer filling. However, at high displacement field, the bands are sufficiently dispersive that they do not symmetry break. Red line: van Hove singularity (vHs) of the single particle (SP) bands. Dashed black: boundary between SP and flavor polarized (FP) regions. Blue: $\nu = 1$ FP. Yellow: $\nu = 2$ FP. Orange: $\nu = 3$ FP. Dark red: $\nu = 4$. Flat bands fully filled. White: SP or $\nu = 0$ flavor polarization, which are indistinguishable in transport.

across the single particle van Hove singularity (SP vHs). In contrast, for $|D| \lesssim 0.4$, the system symmetry-breaks at each integer filling $\nu = 1, \ldots, 4$, as indicated by the four different colors for each flavor in both Figure 6.3a and b. The dashed dark grey line in Figure 6.1b generically indicates a boundary between the single-particle (SP) and flavor polarized (FP) regimes. However, because the $\nu = 0$ symmetry-broken state and the single particle state cannot be distinguished in transport (as they both have $\nu - \nu_H = 0$), we extend the dark grey line to surround the $\nu = 0$ state and color the entire $\nu - \nu_H = 0$ white. The superconductivity, indicated by the dashed magnenta line in Figure 6.3a, is clearly bounded by the single-particle regime, further supporting the claim that the physics of the symmetry-broken $\nu = 2$ state is vitally tied to the origin of the superconducting state.

The electron-side superconductivity has a maximum $T_c = 1.7$ K, as shown in Figure 6.4b, a similar order of magnitude compared to other twisted graphene systems. Additionally, both the electron and hole superconducting domes violate the Pauli limit by nearly a factor of 2 (Supplementary Information), similar to previously published works. This may indicate that the superconductivity observed is likely triplet or at least mixed singlet and triplet. We provide conventional metrics for the superconductivity on both the electron and hole side, demonstrating both support Fraunhofer oscillations and calculating the critical temperature T_c and the Kosterlitz-Thouless transition temperature T_{BKT} in the Supplementary Information.

6.3 Band dispersion and superconductivity

One unusual feature of the superconducting dome in TQG1 is that there are obvious regions of stronger and weaker superconductivity. Somewhat similar observations have been made by other groups, but without the degree of displacement field tunability this device posseses. Figure 6.4a shows the electron-side superconducting dome at $B_\perp = 50$ mT, while Figure 6.4b shows the temperature dependence along $D = 0$. Both figures show stronger superconductivity at $\nu = 2 - \delta$, and

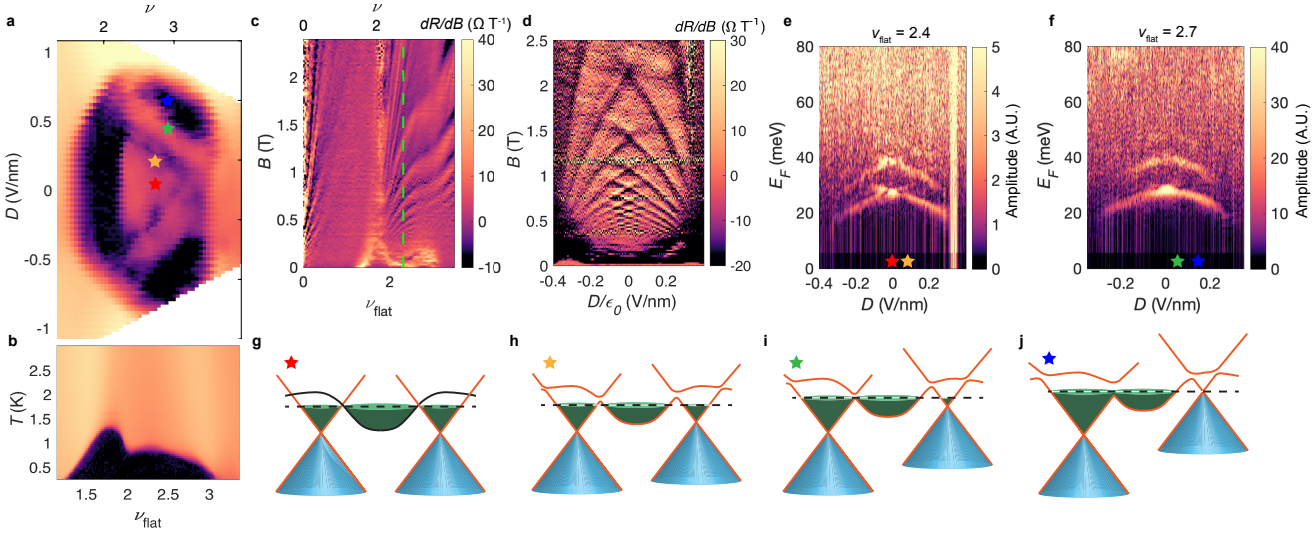

Figure 6.4: Magnetotransport showing a Lifshitz transition occuring at high displacement field. **a)** Electron-side superconducting dome at $B_\perp = 50$ mT. Two regions of stronger superconductivity symmetric in displacement field are visible as black, zero-resistance states. **b)** Superconducting dome at $D = 0$ versus temperature, showing stronger superconductivity for $\nu_{\text{flat}} = 2 - \delta$. **c)** Quantum oscillations at finite displacement field $D = 0.4$ V/nm. The dashed green line indicates the carrier density $\nu_{\text{flat}} = 2.4$ where **c** is measured.**-e)** Fourier transform of low field quantum oscillations arising from the dispersive subsector versus D, assuming a linear dispersion at low energy. From left to right: increasing carrier density. **f-i)** Cartoon showing the flat band and dispersive bands as a function of displacement field and filling. *f* $D = 0, \nu_{\text{flat}} = 2 + \delta$. *g* $D > 0, \nu_{\text{flat}} = 2 + \delta$. *h* $D >> 0, \nu_{\text{flat}} = 2 + \delta$. *i* $D > 0, \nu_{\text{flat}} = 2 + \Delta$, where $\Delta > \delta$.

interestingly, at high displacement field for $\nu = 2 + \delta$. We provide additional characterization of the superconducting dome in n and D in the Supplementary Information versus T, $H_\perp$, and $H_\parallel$. In order to have a better understanding of the band structure in this regime and how it might relate to the varying strength of superconductivity, we can use the dispersive bands to probe the band structure as a function of displacement field using magnetotransport on their small Fermi surfaces. We attempt to correlate features observed in the superconductivity with our "spectroscopic" observations.

We measure the quantum oscillations of the dispersive cones versus B up to $\approx$ 3 T as shown in Figure 6.4c. Then, at fixed n, we can measure the same quantum oscillations as a function of D (Figure 6.4d). Taking an FFT to get the carrier density $n_{\text{dispersive}}$ and assuming a linear dispersion, we

calculate the distance between the Fermi level and the Dirac point of the two cones in meV, plotted in Figure 6.4e and f versus D at two different carrier densities ν_{flat}. At $D = 0$, the two cones are equally spaced in energy and their Fermi surfaces are the same size. However, as we apply D, two sets of Fermi surfaces appear, one of which moves down with $D > 0$ and the other moves in the opposite direction. These two Fermi surfaces appear to "cross" at $D = 0$ in Figures 6.4e and f. To first order, we know D couples linearly to the dispersive subsector, acting with opposite sign at K_m and K'_m, the minibrillouin zone valleys. This will push the cone at K_m up while pushing the cone at K'_m down in energy, and vice versa for opposite D. The observed difference in energy ($\approx$ 5 meV at $D = 0.3$) matches that predicted by theory [131,132].

We also note the cone that is pushed down in energy (therefore appearing as larger Fermi surface or higher energy branch in Figure 6.4d-f) seems to disappear at smaller D as n increases. With finite displacement field applied, we expect the flat bands and dispersive bands to hybridize near where they cross in energy, as shown in the cartoon in Figure 6.4f-i. When the lower cone's Fermi surface "vanishes", it is simply hybridizing with the flat band (Figure 6.4i), and the system undergoes a Lifshitz transition as the two Fermi surfaces merge into a single larger one. The second strongest region of superconductivity seems to occur exactly after this point: when one of the cones hybridizes with the flat band and the Fermi level is high enough to encircle this new larger Fermi surface. From this we can conclude a higher density of states benefits superconductivity in this case.

6.4 Conclusion

We demonstrate how the unique combination of flat and dispersive bands in TQG allows us to simultaneously tune the band structure through carrier density and displacement field, measure the chemical potential (inverse compressibility), and probe superconductivity in a single system. The low-density dispersive bands provide a sensitive measure of the inverse compressibility in the flat

bands, which ties to symmetry-breaking phase transitions at integer fillings. Using displacement field to tune the bandwidth of and hybridization between the flat band and dispersive band sectors, we are able to modify the flavor symmetry-breaking in the system. We discover that the emergence of the superconductivity is strongly tied to the $\nu = \pm 2$ symmetry-broken state. In addition, the hybridization between the dispersive and flat bands results in a Lifshitz transition, and superconductivity is enhanced in the high density of states regime where the flat and dispersive band Fermi surface have merged. Overall, we show the high degree of tunability in TQG paves a route for understanding the relationship between symmetry-breaking, band structure, and superconductivity in multilayer moire graphene systems.

7

Exciton condensation between N=1 Landau level orbitals in double bilayer graphene

In the quantum Hall regime, electrons in different Landau levels experience distinct Coulomb interactions, which plays a crucial role in determining the ground states. For instance N = 1 orbitals in GaAs and bilayer graphene give rise to exotic even denominator states. On the other hand, when two two-dimensional electron systems are brought close to each other, the introduction of interlayer Coulomb interaction leads to a range of new interlayer correlated states, including exciton condensation. Combining these two levels of interaction engineering, double bilayer graphene pro-

vides a new platform for exploring novel correlated states. Here we report observation of interlayer quantum Hall states with fractional total fillings when both layers are in the N = 0 Landau level, as confirmed by Coulomb drag measurement. More interestingly, we also observe integer interlayer states when both layers are in the N = 1 Landau level, and their drag and drive responses are consistent with exciton condensation between the N = 1 Landau levels. This paves way for exploring more exotic interlayer fractional states in N = 1 orbitals and novel phase transitions to even denominator states.

7.1 Introduction to quantum Hall double layer physics

Electrons moving in two dimensional space and under a strong magnetic field are quantized into discrete Landau levels (LLs), indexed by an orbital quantum number N = 0, 1, 2..., with N = 0 corresponding to the lowest LL and the wavefunction becoming increasingly nodal as N increases. These ultra flat electronic bands create an ideal environment for Coulomb interactions to dominate and induce various many-body ground states, such as Wigner crystal, charge density wave, and most notably, fractional Quantum Hall (FQH) effect, where quasi-particles with fractional charge and statistics can emerge. The nature of the electronic wavefunction plays a crucial role in interaction physics due to the different forms of Haldane pseudopotential in LLs with different N[133]. Particularly, the even-denominator FQH states at half-filled LLs, believed to be described by a class of states including Moore-Read Pfaffian state[134], which can host non-Abelian Majorana excitations, have been predominantly observed in N = 1 LL[135,136,137,138,139,140]. There is also numerical evidence that composite fermions can pair in N = 1 LL due to softened Coulomb repulsion, unlike in N = 0[141]. Although it remains unclear what specific features of N = 1 LL stabilize these non-Abelian even-denominator states given the challenging energetics numerically[142], recent theories has revealed a fundamental difference between lowest LL (N = 0) and higher LLs, termed vortexability[143]. Ex-

perimentally, the ability to access different LLs effectively provides an important knob for tuning electron-electron interactions and fostering exotic phases of matter.

Quantum Hall (QH) physics can be further enriched by placing two parallel layers of two-dimensional electron systems close to each other but electrically isolated so that electrons in one layer interact with those in the other layer solely through Coulomb interaction. This double layer structure not only enables more complex multi-component states by introducing a new pseudospin component—the layer index, but also provides unique experimental access to these states by allowing for spatially separate probing in the two layers, which is impossible in a regular multi-component state composed of internal spin or valley degrees of freedom. In particular, the multi-component Halperin (1 1 1) state [144] composed of layer pseudospins becomes an interlayer exciton condensate (EC) formed between electrons in the partially filled LL in one layer and holes in the other [145,146]. This EC was first observed in GaAs double well [147,148], and later realized in double layer structures of monolayer or Bernal bilayer graphene [149,150,151,152]. The flexibility and tunability of these graphene double layer structures further enabled the observation of BEC-BCS crossover [153], novel interlayer fQH states [151,152], and exciton solids [154]. However, all of these interlayer states are realized when both layers are in the N = 0 LL, and no interlayer states between N = 1 LLs have been observed. As N = 1 can give rise to distinct FQH states in a single layer, it could potentially support a different interlayer state structure in double layer systems. Furthermore, once an EC between N = 1 LLs is realized, the transition between this interlayer coherent EC and individual-layer even-denominator states could be a highly nontrivial topological phase transition [155]. Previously it has been shown through quantum capacitance measurements that 2H-stacked bilayer WSe_2 hosts gapped states that are consistent with interlayer EC in higher LLs up to N = 6 [156]. However, while the lack of layer separation helps achieve ultra-strong interlayer coupling, it excludes the possibility of directly probing the interlayer nature the EC state and also limits the tunability of the phase diagram. Here we report the first realization of interlayer correlated states between N = 1 LLs in a

highly tunable double bilayer graphene structure, and their transport signatures are consistent with those of an EC.

7.2 Double layer structure of Bernal bilayer graphene

Fig. 7.1a and 7.1b depict the device and a schematic of its configuration, respectively. Two layers of Bernal bilayer graphene are stacked on top of each other separated by a thin hexagonal boron nitride (hBN) insulator layer of 2.5 nm thickness. They are further encapsulated by layers of hBN and graphite on both the top and bottom, with the graphite layers acting as local gates. Separate gold contacts are made to the top and bottom bilayer graphene where they do not overlap. This configuration inevitably results in long graphene leads and poor equilibrium between the gold contacts the channel region, which seriously affects measurements of QH states at high magnetic fields. To remedy this, we utilize the global silicon back gate and fabricate additional aluminum oxide dielectrics and gold contact gates on top of the heterostructure to heavily dope the top and bottom graphene leads respectively.

The phase diagram of bilayer graphene at high magnetic fields is controlled by both the displacement field and the carrier density. When ignoring higher-order energy anisotropies, the zeroth LL of bilayer graphene consists of 8 degenerate flavours, spin up and down, valley K and K', and an orbital degree of freedom, N = 0 and 1. Fig. 1c illustrates these latter two flavors. The N = 0 orbital has a LL wavefunction similar to the lowest LL in GaAs while the N = 1 orbital is a mixture of the traditional lowest and second LL wavefunctions. Depending on the valley flavour, these wavefunctions are polarized in one of the layers within the bilayer graphene. Previous studies on QH states in bilayer graphene have shown that these 8 flavours form a hierarchy in energy due to next-order energy anisotropies and are sequentially filled when carrier density increases [139,138]. This hierarchy is altered by a displacement field, which shifts the relative potential energy of the two graphene layers.

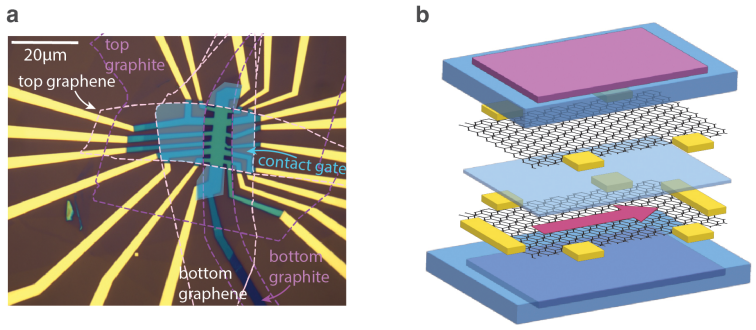

Figure 7.1: a, Device picture with dashed lines denoting the original flake placement. The semi-transparent region is covered by contact gate. **b,** Schematic of the double layer structure and device configuration.

In our experiment, by applying direct current (dc) voltages to the top and bottom graphite gates, V_{TG} and V_{BG}, as well as between the two graphene layers V_{int} (with the top bilayer graphene grounded), we can control the carrier density and displacement field in both the top and bottom bilayer graphene. This control allows us to selectively tune each layer into different flavours, facilitating the study of their combined phases of different flavour combinations. More specifically the carrier densities are given by $n_{top} = \frac{1}{e}(C_t(V_{TG} - V_{int}) - C_{int}V_{int})$ and $n_{bot} = \frac{1}{e}(C_bV_{BG} + C_{int}V_{int})$, and the displacement fields $D_{top}/\varepsilon_0 = \frac{1}{2}(C_t(V_{TG} - V_{int}) + C_{int}V_{int})$ and $D_{bot}/\varepsilon_0 = \frac{1}{2}(-C_bV_{BG} + C_{int}V_{int})$. Here, e is the electron charge, and C_t, C_{int} and C_b are geometric capacitances between the top graphite and top bilayer, between the top and bottom bilayer, and between the bottom bilayer and bottom graphite, respectively. We perform Coulomb drag measurements, similar to our previous experiment [151], where longitudinal and Hall resistance for both the drive and drag layers $R^{xx/xy}_{drive/drag}$ are measured. A non-trivial drag signal often provides an unambiguous indication of an interlayer state. Unless specified otherwise, most of the data presented in the main text involve using the bottom bilayer graphene as the drive layer and the top as the drag layer, taken at a temperature of 250 mK and a magnetic field of 16 T.

7.3 Quantum Hall phase diagram of a single Bernal bilayer graphene

We first examine the QH phase diagram of the single bottom bilayer graphene by fixing $V_{TG} = 0$ and changing only V_{int} and V_{BG}, effectively using the top bilayer graphene as a top gate for the bottom layer. Fig. 7.2a displays R_{xx}^{drive} as a function of the displacement field D_{bot} and filling factor ν_{bot}. the filling factor of LLs is defined as $nu = n/n_0$, where $n_0 = eB/h$ is the LL degeneracy per unit area, B is the magnetic field, and h is the Planck constant. The range of ν_{bot} spans from -2 to 4, covering part of the zeroth LL manifold of bilayer graphene. We observe generally vertical features consistent with the previous studies; large regions of zero R_{xx}^{drive}, shown in deep blue at integer ν_{bot}, correspond to integer QH states, while the resistive regions in between indicate partially filled LLs. There are visually two distinct types of partially filled LLs in the data: one characterized by sharp resistance minima, most prominent between $0 < \nu_{bot} < 1$ and $2 < \nu_{bot} < 3$, indicative of FQH states with a denominator of 3. Zoom-in data with better resolution around these regions also reveal FQH states with a denominator of 5 (see supplementary information). This is characteristic of N = 0 LL orbitals. The other type is generally featureless and predominantly in the range of $1 < \nu_{bot} < 2$ and $3 < \nu_{bot} < 4$, with very weak development of denominator 3 FQH states, indicative of N = 1 LL orbitals. Additionally, sharp horizontal resistive features at around $D_{bot}/\varepsilon_0 = 0$ in all ranges and $D_{bot}\varepsilon_0 = \pm 100$ mV/nm around $\nu_{bot} = 1$ intersect the vertical features, marking the hierarchy change transitions. These features are pictorially depicted in Fig. 7.2b, where solid black lines mark FQH states and the boundaries of integer QH states, and dashed lines represent the hierarchy change transitions. We obtain a phase diagram in good agreement with previous studies conducted at similar magnetic fields. By comparing them, we can assign different sections of our data to LLs with different valley and orbital flavours. Notably, the spin is polarized on each side of $\nu_{bot} = 0$.
A key difference between our data and previous measured phase diagrams is that feature are not perfectly vertical and exhibit zig-zag shapes. This is because the top bilayer graphene intermittently

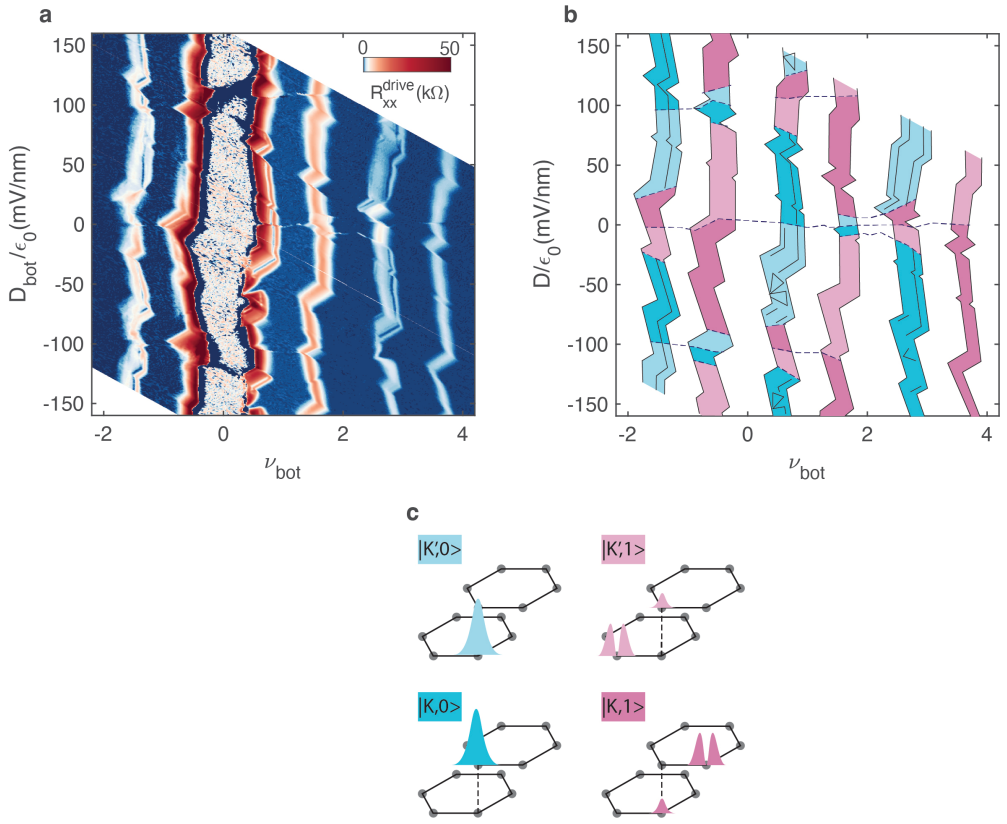

Figure 7.2: a, Drive resistance (bottom layer) as a function of displacement field D_{bot} and filling factor ν_{bot}. **b,** Schematic of the features in a. **c,** Illustration of valley and orbital flavor of zeroth Landau level in bilayer graphene. Spin flavor is not included.

enters gapped QH states as V_{int} changes, making it unable to act as a gate.

We notice that we do not observe any even denominator FQH states in the N = 1 orbitals. Given that the device is made with both top and graphite gates, fabricated under the cleanest conditions possible, and considering that we observe interlayer FQH states, which will be mentioned later, we attribute this lack of even-denominator states to the enhanced screening effects due to the relative small thickness of the hBN layers (top hBN at 12 nm and bottom hBN at 17 nm). Previous studies that demonstrated even denominator FQH states generally used thicker hBN layers. The visually distinct FQH structures within the partially N = 0 and N = 1 LLs in R_{xx}^{drive} already makes the orbital

flavor of the bottom bilayer graphene obvious. However, the QH phase diagram of single bilayer graphene serves as a more accurate reference, from which the flavours of both layers for any combination of V_{int}, V_{TG} and V_{BG} can be deduced.

7.4 Exciton condensation and interlayer quantum Hall states between N = 0 Landau level orbitals

We now fix $V_{int} = 0$ and use V_{TG} and V_{BG} to independently control ν_{top} and ν_{bot}, and study the two layers' collective phase diagram. Fig. 7.3a and b show R_{xx}^{drive} and the corresponding R_{xx}^{drag} as a function of ν_{top} and ν_{bot}, covering the range of $-4 \leq \nu_{top} \leq 4$ and $0 \leq \nu_{bot} \leq 4$. We again observe vertical features that are mostly QH states of the drive layer — the bottom bilayer graphene. Based on the FQH features, we can already directly see that the bottom bilayer graphene is within N = 0 LL for $0 \leq \nu_{bot} \leq 1$ and $2 \leq \nu_{bot} \leq 3$, and within N = 1 LL for $1 \leq \nu_{bot} \leq 2$ and $3 \leq \nu_{bot} \leq 4$. These assignments of LL orbitals are further confirmed by calculating the corresponding D_{bot} and comparing with the single-layer phase diagram. The top bilayer graphene has a similar correspondence between the LL orbital and ν_{top} range. The zig-zag shape of the vertical features reflects quantitative chemical potential change in the top bilayer graphene. ν_{bot} and ν_{top} shown in the x and y axis here are directly proportional to V_{BG} and V_{TG} when $V_{int} = 0$. However, the more accurate formula of $n_{bot} = \nu_{bot} n_0$, which includes chemical potential, is $n_{bot} = \frac{1}{e}\left(C_b V_{BG} - (C_b + C_{int})\mu_{bot} + C_{int}\mu_{top}\right)$, where μ_{top} and μ_{bot} are the chemical potentials of each bilayer graphene. Therefore, if we follow a resistance feature of bottom bilayer graphene that signals a fixed n_{bot} and μ_{bot}, the V_{BG} value of that feature is directly proportional to μ_{top}. Indeed a negative slope in the $\nu_{bot} - \nu_{top}$ plane (or more accurately $V_{BG} - V_{TG}$ plane) is a sign of gapped state across which the chemical potential of top layer jumps up.

In addition to these individual layer features, we also observe features of interlayer nature, which

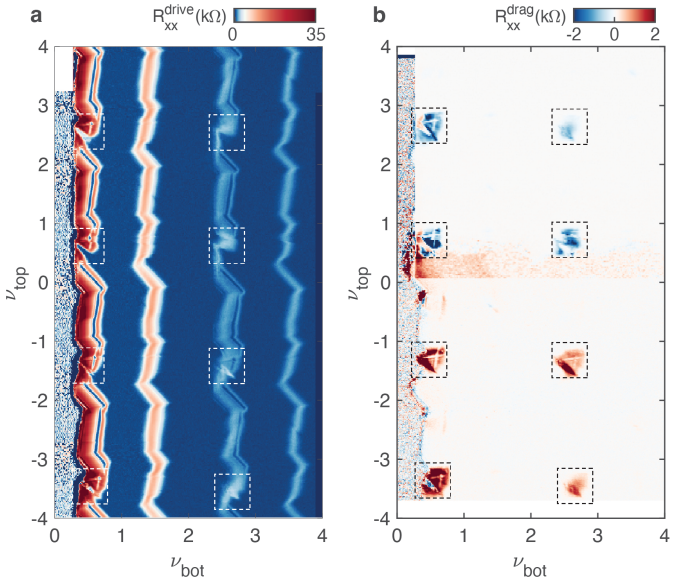

Figure 7.3: a, Drive resistance (bottom layer) as a function of ν_{top} and ν_{bot}. **b,** The corresponding drag signal R_{xx}^{drag}

are highlighted by 8 dashed squares in both Fig. 7.3a and 7.3b. They occur when both bilayer graphene are in partially filled N = 0 LL orbitals and manifest as diamond-shape features with a diagonal feature in the middle. The diagonal features are along a line of $\nu_{tot} = \nu_{top} + \nu_{bot} =$ integer, where the number of quasi-holes in one layer equals to the number of quasi-electrons in the other layer. Furthermore, when $\nu_{top} > 0$ and $\nu_{bot} > 0$, the diagonal features manifest as a resistance minimum close to 0 in both R_{xx}^{drag} and R_{xx}^{drive}, and close to $\frac{1}{\nu_{tot}}\frac{h}{e^2}$ in both R_{xy}^{drag} and R_{xy}^{drive} (see supplementary information), consistent with the transport signatures of EC previously studied in double layer structures of both monolayer and bilayer graphene. Indeed, Fig. 7.4a and 7.4b are zoomed-in on R_{xx}^{drag} near $(\nu_{bot}, \nu_{top}) = (0.5, 2.5)$ at $B = 16$ T and 25 T, respectively, and Fig. 7.4c near $(\nu_{bot}, \nu_{top}) = (0.5, 0.5)$ at $B = 16$ T, all of which clearly show a wide feature of zero R_{xx}^{drag} along the diagonal line (see zoomed-in on other channels of resistance in supplementary information). In particular, Fig. 7.4d shows a linecut of the data in Fig. 7.4a along the off-diagonal line $\nu_{bot} = \nu_{top} - 2$. At $(\nu_{bot}, \nu_{top}) = (0.5, 2.5)$, where the EC is, $R_{xx}^{drag} = R_{xx}^{drive} = 0$ and $R_{xy}^{drag} = R_{xy}^{drive} = \frac{1}{3}\frac{h}{e^2}$.

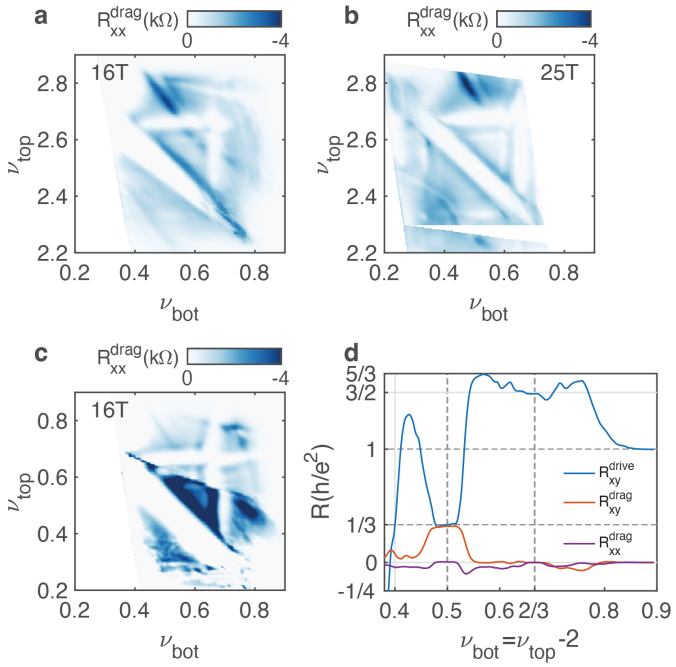

Figure 7.4: Drag resistance R_{xx}^{drag} near $(\nu_{top}, \nu_{bot}) = (0.5, 2.5)$ at B = 16 T **a,**, B = 25 T **b,** and near $(\nu_{top}, \nu_{bot}) = (0.5, 0.5)$ at B = 16 T **c. d,** Linecut across the EC state in **a** showing R_{xx}^{drag} as well R_{xy}^{drag} and R_{xx}^{drive}.

The areas surrounding the EC within these diamond-shaped features also present other interlayer correlations driven phenomena. Whereas the vertical $R_{xx}^{drag} = 0$ features at $\nu_{bot} = \frac{2}{3}$ in Fig. 7.4a and 7.4c, and the horizontal $R_{xx}^{drag} = 0$ features at $\nu_{top} = 2\frac{2}{3}$ in Fig. 7.4a and $\nu_{top} = \frac{2}{3}$ in Fig. 7.4c are trivial individual FQH states, we observe features with slopes that are not -1. Specifically, we see R_{xx}^{drag} peaks along $\nu_{bot} + \frac{2(\nu_{top}-2)}{3} = 1$ and $\nu_{bot} + \frac{3(\nu_{top}-2)}{5} = 1$ in Fig. 7.4A, and along $\nu_{bot} + \frac{2\nu_{top}}{3} = 1$, $\nu_{bot} + \frac{\nu_{top}}{3} = 1$ and $\frac{\nu_{bot}}{3} + \nu_{top} = 1$ in Fig. 7.4c (see supplementary information for more detail analysis). Fig. 7.4b is measured at 25 T in similar ranges to Fig. 7.4a. At this field, the state structure is slightly altered, with individual QH states at ν_{bot} and ν_{top} equal to 1/3 and 3/5 appearing and additional line features along $\frac{3\nu_{bot}}{2} + (\nu_{top} - 2) = 1$ and $\nu_{bot} + \frac{3(\nu_{top}-2)}{2} = 1$. These line features are termed as semi-quantized states, previously observed in double monolayer graphene but not in double bilayer graphene. These states are interlayer fractional states that can be understood as resulting from electrons in one layer attaching interlayer vortices due to interlayer Coulomb interactions. The observation of these fractional states indicates the high quality of the sample. Fig. 7.4c has an additional sharp transition in the middle of the structure. This occurs as the top bilayer graphene switches valley flavour near zero D but remains in the N = 0 orbital. There is an overall drop of R_{xx}^{drag}, but the general state structure remains unchanged.

7.5 Exciton condensation between N = 1 Landau level orbitals

Having seen that the data at $V_{int} = 0$ accesses the combinations of partially filled N = 0 LLs in each layer and produces similar phenomenology to that from N = 0 LLs in double monolayer graphene, suggesting that interlayer QH state structures are dependent more on the LL wavefunction and less on the specific material, we switch on V_{int} and try to access the combinations of N = 1 LLs in each layer. Fig. 7.5a and 7.5b are R_{xx}^{drive} and the corresponding R_{xx}^{drag} at $V_{int} = 0.07\ V$. At this voltage, we first again observe the N = 0 interlayer states that manifest as diamond-shaped features at the 4

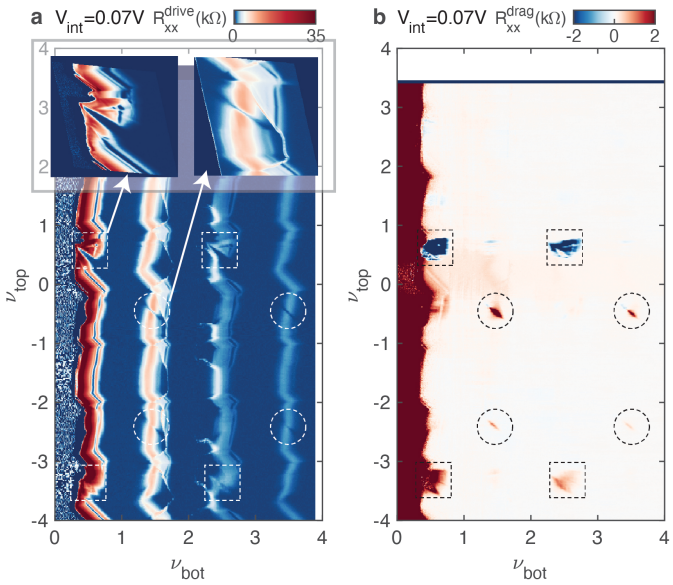

Figure 7.5: textbfa, Drive resistance as a function of ν_{top} and ν_{bot} at $V_{int} = 0.07V$. Dashed squares labels the EC states formed by N = 0 orbitals. Dashed circles marks the newly observe states formed by N = 1 orbitals. **b,** The corresponding drag signal R_{xx}^{drag}

locations with the combination of bottom filling $0 < \nu_{bot} < 1$ or $2 < \nu_{bot} < 3$, and top filling $-4 < \nu_{top} < -3$ or $0 < \nu_{top} < 1$, again marked by dashed squares. Intriguingly, new interlayer states emerge at locations with the combinations of bottom filling $1 < \nu_{bot} < 2$ or $3 < \nu_{bot} < 4$, and top filling $-3 < \nu_{top} < -2$ or $-1 < \nu_{top} < 0$, marked by the dashed circles. These are locations where both layers are in N = 1 orbitals. These new states also manifest as resistance minimum in R_{xx}^{drive} and non-zero drag signals along diagonal lines with $\nu_{tot} =$ integer, unambiguously indicating their interlayer nature. However they display distinct appearances than the N = 0 interlayer states. On top of Fig.7.5a overlays two zoomed-in views of R_{xx}^{drive} for the two classes of states. Whereas the N = 0 state has a characteristic wide diagonal zero R_{xx}^{drive} feature cutting into the resistive region from one side which is surrounded by other fractional states, the new N = 1 states show as a narrow zero R_{xx}^{drive} line cutting into the resistive region from both sides and completely through, with no additional interlayer features in their surroundings. These new N = 1 states appear at more locations

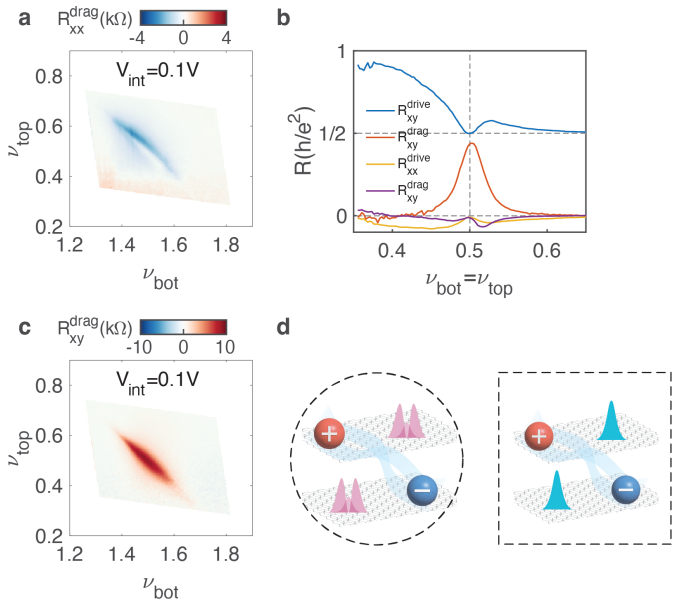

Figure 7.6: Zoom-in on the state near $(\nu_{top}, \nu_{bot}) = (1.5, 0.5)$ at $V_{int} = 0.1V$ for R_{xx}^{drag} **a** and R_{xy}^{drag} **b. c,** Linecuts across the state showing all other transport channels. Dashed lines denote the state location and quantization value. **d,** Illustration of two different states formed by coupling N=0 and N=1 orbitals.

when we go to higher $V_{int} = 0.1\ V$ (see supplementary information).

Despite these visually distinct appearances, the N = 1 states seem to be consistent with EC that has $R_{xx}^{drag/drive} = 0$ and $R_{xy}^{drag/drive} = \frac{1}{\nu_{tot}} \frac{h}{e^2}$. Fig. 7.6a and 7.6c show R_{xx}^{drag} and R_{xy}^{drag} for the N = 1 state near $(\nu_{bot}, \nu_{top}) = (1.5, 0.5)$ at $V_{int} = 0.1\ V$, which has a resistance dip in R_{xx}^{drag} encircled by more resistive region, and a resistance peak in R_{xx}^{drive}. By doing a linecut along $\nu_{bot} = \nu_{top} - 1$ across this state, as shown in Fig. 7.6b, we clearly see that at $(\nu_{bot}, \nu_{top}) = (1.5, 0.5)$, both R_{xy}^{drag} and R_{xy}^{drive} approach to the quantization value $1/\nu_{tot} = 1/2\frac{h}{e^2}$, and both R_{xx}^{drag} and R_{xx}^{drive} dip to 0, characteristic signatures of EC. Fig. 7.6d illustrates the two types of EC states formed by coupling N = 0 and N = 1 LL orbital wavefunctions, respectively. This is the first time a N = 1 EC has been observed in double layer graphene heterostructures. More careful study is needed to investigate the aspects where the N = 1 EC has different properties than the N = 0 EC.

Another interesting question is how to understand the strong V_{int} dependence of these N = 1 EC

states, i.e., what is their existence condition in the parameter space of $\nu_{top/bot}$ and $D_{top/bot}$. To study this, we first note that the $V_{int} = 0.07\ V$ data shown in Fig. 7.5a and 7.5b, and the $V_{int} = 0.1\ V$ data shown in supplementary information Fig. D.4 ensure that these N = 1 EC states can appear at $\nu_{bot} = 3.5$ or 1.5. Then we change all three gates V_{TG}, V_{BG} and V_{int} simultaneously while keeping the bottom filling factor fixed to $\nu_{bot} = 3.5$ or 1.5, or more accurately keeping $V_{BG} + \frac{C_{int}}{C_b} V_{int}$ a constant. The resulted 2D $V_{TG} - V_{int}$ (or equivalently $V_{TG} - V_{BG}$) map varies ν_{top}, D_{top} and D_{bot}, from which we can directly see how the N = 1 EC states evolve. It is more intuitive to convert the $V_{TG} - V_{int}$ map into $n_{top} - D_{top}$ map, which is effectively a phase diagram of top layer bilayer graphene with additional effects from changing D_{bot}.

Fig. 7.7a and 7.7b are these 2D maps of R_{xx}^{drive} and R_{xx}^{drag} for fixed $\nu_{bot} = 3.5$ and Fig. 7.7c is R_{xx}^{drive} for fixed $\nu_{bot} = 1.5$. Despite the different appearances of Fig. 7.7a and 7.7c, they both show resistive patterns that are generally periodic in ν_{top}, indicative of the top bilayer graphene QH states that manifest in bottom bilayer resistance R_{xx}^{drive} due to screening effects. Fig. 7.7a and 7.7b also show identical horizontal features around $(\nu_{top}, D_{top}/\varepsilon_0) = (-1 \sim 0, 0\ \text{mV/nm})$, $(0 \sim 1, 108\ \text{mV/nm})$, and $(1 \sim 2, 108\ \text{mV/nm})$, as well as curved line features roughly along a line connecting $(0.1, 95\ \text{mV/nm})$ and $(0.8, 73\ \text{mV/nm})$, and a line connecting $(-1.6, 20\ \text{mV/nm})$ and $(-1, 35\ \text{mV/nm})$. These features are consistent with the hierarchy transitions in the top bilayer graphene. We illustrate these features pictorially as shown in Fig. 7.7d and assign each region with different colors representing different valley flavors and orbital numbers.

The N = 1 EC states show as non-zero drag resistance peaks in the mostly zero R_{xx}^{drag} in Fig. 7.7b, with corresponding resistance dips in R_{xx}^{drive} in Fig. 7.7a and 7.7c. Note that an EC should have zero resistance in both R_{xx}^{drag} and R_{xx}^{drive} but an imperfect location of ν_{bot} can move away from the narrow resistance dip and lead to the resistance peaks of R_{xx}^{drag} in Fig. 7.7b. We represent the N = 1 EC states in Fig. 7.7d as thick solid lines and it is immediately clear that they only appear when the top bilayer graphene is in N = 1 orbitals and K' valley, which means that the N = 1 LL wavefunction is mostly

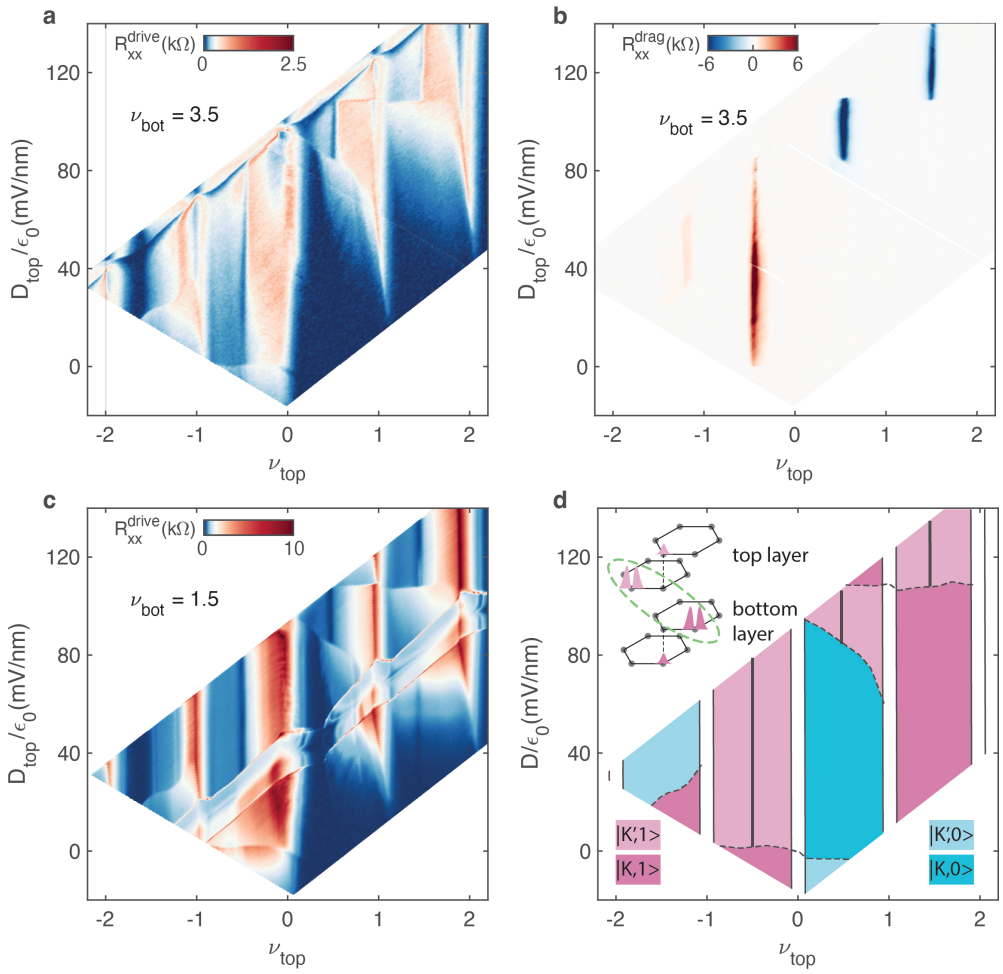

Figure 7.7: **a,** R_{xx}^{drive} at fixed $\nu_{bot} = 3.5$ as a function D_{top} and ν_{top}. **b,** R_{xx}^{drag} in the same range. Showing clearly interlayer states. **c,** R_{xx}^{drive} at fixed $\nu_{bot} = 1.5$. **d,** Schematic of the features in the resistance data. This shows the $N = 1$ interlayer states only forms when N=1 orbitals are on the nearest layers.

populated in the bottom part of the top bilayer graphene. Meanwhile, we can also work out that in the ranges where the N = 1 EC states exist, the bottom bilayer graphene is in N = 1 orbital and K valley, with most of the N = 1 LL wavefunction in its top part. Taking these together, we conclude that the N = 1 EC states can only exist when the N = 1 LL wavefunctions in the two layers are the closest to each other, as depicted on the top left of Fig. 7.7d.

A

Twisted double bilayer supplementary information

S1 Band structure of twisted double bilayer graphene

The band structure of TDBG with Bernal-stacked bilayers is obtained as the following. In TDBG, each bilayer graphene has a tight-binding Bloch Hamiltonian at a momentum k given by

$$H(k) = \begin{pmatrix} U_1 + \Delta & -\gamma_0 f(k) & \gamma_4 f^*(k) & \gamma_1 \\ -\gamma_0 f^*(k) & U_1 & \gamma_3 f(k) & \gamma_4 f^*(k) \\ \gamma_4 f(k) & \gamma_3 f^*(k) & U_2 & -\gamma_0 f(k) \\ \gamma_1 & \gamma_4 f(k) & -\gamma_0 f^*(k) & U_2 + \Delta \end{pmatrix}, \tag{A.1}$$

which is labelled in the order of A_1, B_1, A_2, B_2 sites of the top (1) and the bottom (2) Bernal stacked bilayer graphene. $f(k) \equiv \sum_l e^{ik\cdot\delta_l}$, where $\delta_1 = a(0,1)$, $\delta_2 = a(\sqrt{3}/2, -1/2)$, $\delta_3 = a(-\sqrt{3}/2, -1/2)$ with $a = 1.42$ Å. In particular, the electrostatic energy difference U between top and bottom-most layers is an important tuning parameter controlled by D. With this Hamiltonian, one can follow the continuum model approach in Ref.[157] to calculate the moiré band structure.

In the numerical simulation, we use phenomenological parameters

$$(\gamma_0, \gamma_1, \gamma_3, \gamma_4, \Delta) = (2610, 361, 283, 138, -15)\ \text{meV} \tag{A.2}$$

obtained from Ref.[158]. Compared to TBG, TDBG has additional parameters γ_1, γ_3 (trigonal warping), γ_4 (particle-hole asymmetry) and Δ, in addition to γ_0 (nearest-neighbor hopping). Here, γ_1 and Δ are the inter-layer hopping and the on-site energy at A-B stacked sites where the A-site of the first layer (A_1) sits on top of the B-site of the second layer (B_2), respectively. Although these parameters are much smaller than γ_0, they are important to understand the experimental data. Particularly, for vanishing U, a finite value of γ_3 yields a larger bandwidth and overlap between c_1 and v_1. This is why the system is metallic at CNP and there is no magic-angle condition at $D = 0$. Furthermore, γ_4 and Δ give rise to the electron-hole asymmetry. Due to these terms, the bandwidth of v_1 is much larger than that of c_1, resulting in smaller band isolation for v_1 (Fig. SA.1). For the moiré hopping parameters, $(w_0, w_1) = (0.08, 0.1)$ eV is used to account for the relaxation effect described by Ref.[159]. The relaxation increases the gap between c_1 and c_2 (v_1 and v_2), stabilizing the insulating states for the range of D at $\nu = \pm 4$ fillings. For more details, See Ref.[160].

Fig. SA.1c-d shows a direct comparison between experimental resistivity and the calculated density of states at the Fermi energy for the $\theta = 1.33°$ TDBG. The experimental results are plotted against displacement field D while the calculation is plotted against onset potential difference between the top-most and bottom-most graphene layer U. The conversion between experimental

parameter D and calculation parameter U is not straightforward due to the screening of the electric field by the graphene layers themselves. Thus converting D to U requires a self-consistent calculation of the screening effect produced by the TDBG band-structure, which in turn depends on U. However, in Fig. SA.1, we see a very good match between experimental single particle insulating states and theoretical gaps at the Fermi energy when we convert D into U with an empirical factor: $U = 0.1nm \times eD$, where e is the electron charge. Besides the single particle gaps, the calculation also displays regions of high density of states. Particularly, in experimental data, there are two lines with higher resistivity than the surroundings: from (n,D) = (-1, -0.2) to (1, 0.6) and from (n,D) = (-1, 0.2) to (1, -0.6). These two lines form a cross and pass through the half filled insulator as well as the halo features. By comparing with the calculation, we recognize these experimental features correspond to the regions of high density of states shown in Fig. SA.1.

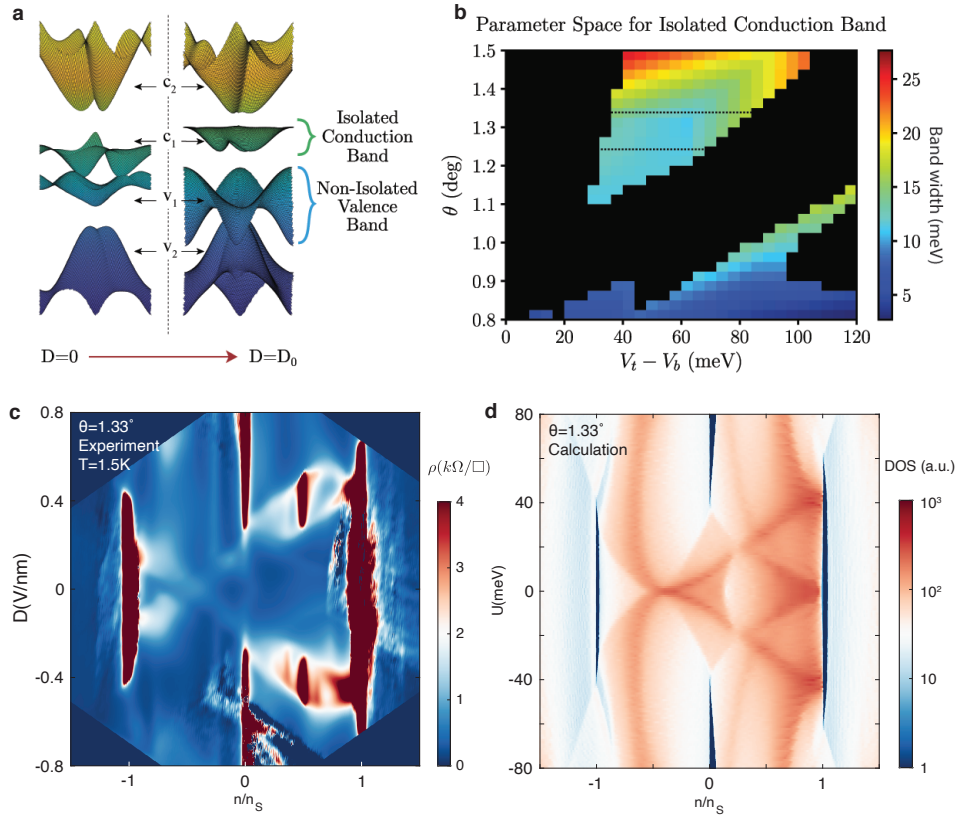

Figure A.1: a, calculated band structure of TDBG at zero displacement field and optimal displacement field D_0 for the isolated flat band. b, calculated parameter space for isolated conduction band (x-axis is onsite potential difference $U = V_t - V_b$ between the top and bottom bilayer graphene, y-axis is twist angle). Color represent bandwidth of the first conduction band c_1 (meV). In the colored parameter space, c_1 is isolated from the remote band and valence bands. Dotted line represents cuts at $\theta = 1.26, 1.33°$. c, resistivity as a function of filling fraction and displacement field in the $\theta = 1.33°$ sample. A cross-like feature of high resistivity is formed along two lines from (n,D) = (-1, -0.2) to (1, 0.6) and (-1, 0.2) to (1, -0.6), passing through the half-filled insulating state. d, density of states at the Fermi energy calculated by the continuum model. The single particle insulators ($n = 0, \pm 1$) in experiment match well with the gaps shown in the calculation and the van Hove singularity captures the cross-like pattern in experiment.

S2 Hall measurements

S2.1 Hall effect and ferromagnetism phase boundary

In Fig. SA.2, we show the Hall effect measured in the sample with the most robust half-filled insulating states ($\theta = 1.41^\circ$, $\Delta_{n_S/2}$=4.2meV). There is a clear change of Hall resistance behavior across the halo boundary, which is identifiable in the longitudinal resistance measurement (Fig. SA.2a). Inside the halo, the Hall resistance changes sign across the half-filled insulating state, with a positive value above half filling and negative value below half filling. This Hall measurement demonstrates that the metallic states inside the halo are closely related to the half-filled insulator, likely by a change of Fermi level from half filling to the inside of the sub-band (Fig. SA.2c). Given that the half-filled insulator is spin-polarized, the metallic states are likely a ferromagnetic metal, which contains two spin bands that are shifted in energy by the ferromagnetic exchange coupling (Fig. SA.2c (2)). Outside the halo, the Hall effect follows the expectation of a continuous moiré band without correlation effects such as in large angle twisted bilayer graphene, indicating the system recovers to a normal metallic state.

In Fig. S A.2a, we also notice a three quarter filled insulating state appears on the border of the halo. The simplest possible candidate of this state is a spin and valley polarized state. However, within a simple mean field picture, we expect the lowest lying excitations in this state to be associated with valley-flip rather than spin-flip since the spin exchange coupling is expected to be larger than the valley exchange splitting [160]. This naive picture appears to be inconsistent with the enhancement of the gap by in-plane magnetic field shown in Fig. 2d in the main text. In addition, the appearance of the quarter filling state right at the edge of the halo suggests a mean field picture may fail to capture the relevant physics. We leave this question regarding the nature of the quarter filling state to future theoretical works.

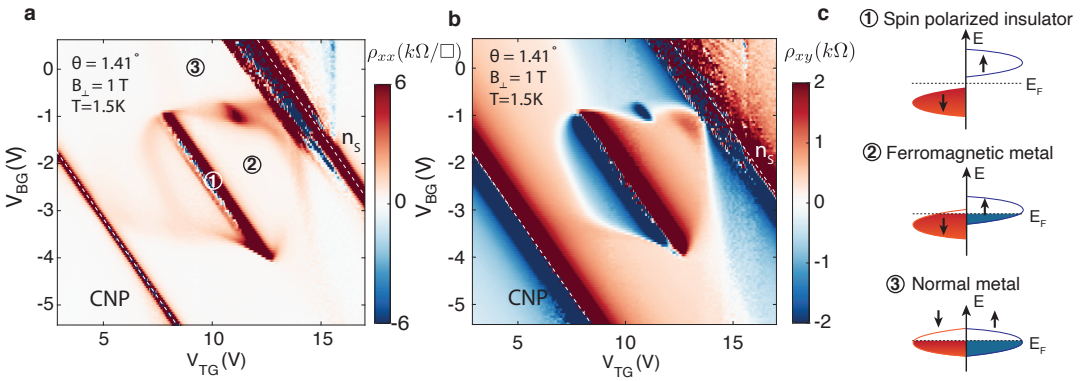

Figure A.2: a,b, longitudinal resistivity and Hall resistance of $\theta = 1.41^\circ$ device around half filling at $T = 1.5$ K and perpendicular magnetic field $B_\perp = 1$ T. Data is symmetrized between positive and negative fields to eliminate mixing. The halo structure is apparent around the half filling insulator and a three quarter filled insulating state resides on the border of the halo. The Hall resistance changes sign across the half-filled insulator inside the halo. c, illustration of electron orders for different regimes. The left half (right half) of the cartoon represents the filling status of spin down (up) electrons. For half filling, only one species of spin is filled. Inside the halo, one spin species is populated more than the other. Outside the halo, both spins are equally populated.

S2.2 Magnetic field induced Chern insulator state in the 1.26° sample

In the $\theta = 1.26$ sample, we observed distinctly different behavior of Hall resistance. Under a small perpendicular magnetic field, Hall resistance is always positive inside the halo (Fig. SA.3b), rather than changing signs across half-filling. The absent sign change of Hall signal across half filling may relate to thermal excited carriers of both types due to the small insulating gap, or relate to the Chern insulator behavior discussed below. Measuring Hall resistance with changing magnetic field and density at a fixed displacement field, Fig. SA.3d reveals a single line of large Hall signal tracing to half filling with a slope corresponding to $\nu = 4$. At the same time, longitudinal resistance develops a minimum along the same line (Fig. SA.3c). Following the $\nu = 4$ line (black guiding lines in Fig. SA.3c-d), Fig. SA.3e shows the Hall resistance reaches close to a quantized value of $h/4e^2$ when perpendicular magnetic field $B_\perp > 3T$.

The fact that a single Hall plateau emerges from half filling strongly suggests this is not a normal

quantum Hall state. Instead, the data highly resembles the Chern insulator shown in MA-TBG ([35]). Indeed, our theory predicts that in TDBG, the first conduction band has a Chern number $C = 2$ in one valley and an opposite Chern number $C = -2$ in the other valley [160]. As shown in the main text, without a perpendicular magnetic field, the half-filled state is spin polarized and valley un-polarized, giving a total Chern number of 0. However, perpendicular magnetic fields couples to the valley degree of freedom through orbital valley Zeeman effect. When the spin-polarized gap is small such as in the 1.26° device, the valley Zeeman energy can overcome the spontaneous spin-polarized gap and converts the spin-polarized half-filled insulating state into valley polarized Chern insulator. Using valley Zeeman factor from STM study (cite:Xiaomeng etc unpublished) and calculation [160], we estimate valley Zeeman energy exceed 0.3meV at a perpendicular field of 0.2T. This valley polarized half-filled state fills two moire bands (of two spins) in one valley, adding up to a total Chern number of four.

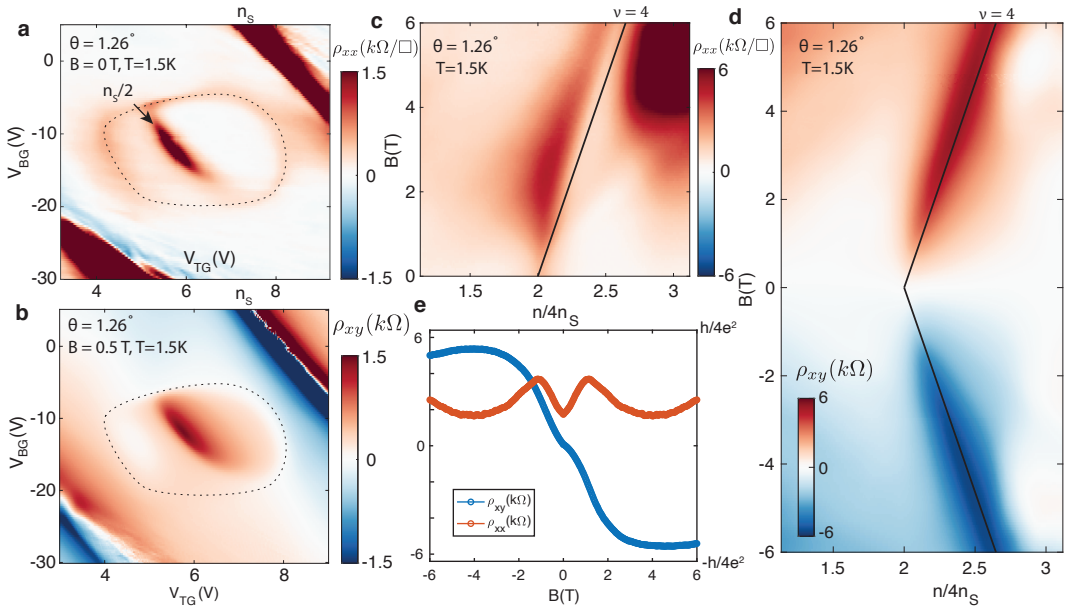

Figure A.3: a-b, longitudinal resistivity at $B = 0$ and Hall resistance at $B = 0.5$ T in the $\theta = 1.26^\circ$ sample at $T = 1.5$ K. The Hall resistance here is symmetrized with both directions of the magnetic field. c-d, fan diagram of longitudinal resistivity and Hall resistance at $T = 1.5$ K at a constant displacement field. The black line marks the expected position for $\nu = 4$ Chern insulator state originating from half filling. e, longitudinal resistivity and Hall resistance along the black line shown in c-d.

S3 Critical transition behaviors in $\theta = 1.26^\circ$ sample

S3.1 Density, displacement field and magnetic field dependence

In Fig. SA.4c, a dome of the superconducting-like state, similar to MA-TBG, can be seen next to the half filled insulator. In addition, cutting through a constant density line, a similar dome structure is visible over the displacement field axis (Fig. SA.4b). The dome in the displacement field terminates on the boundary of the halo. It may first appear that the low resistance state outside the halo boundary resembles a superconductor as well. However, as we discussed in the main text, there is no critical transition outside the halo. In addition, the IV characteristic outside the halo is very different from inside. Within the halo, differential resistance shows a critical current that reduces to zero

when approaching the halo boundary (Fig. SA.4f). Outside the halo, in contrast, the I–V characteristic does not fit that of a superconductor (Fig. SA.4g). We believe the low resistance outside the halo is purely caused by ballistic transport. Fig. SA.4d shows the superconducting-like state has a critical perpendicular magnetic field of ~ 0.1 T.

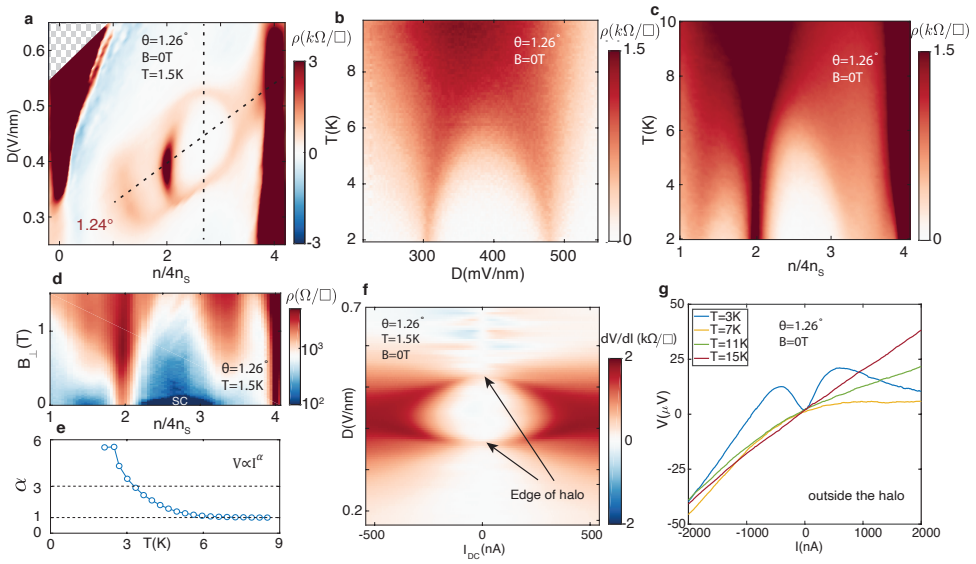

Figure A.4: a, resistivity in $1.26°$ device plotted against filling factor and displacement field. b, resistivity as a function of displacement field and temperature along the constant density line shown in a. c, resistivity as a function of filling and temperature along the tilted line in a. A dome of low resistance state can be seen next to the half filled insulator. d, resistivity in log scale as a function of filling and perpendicular magnetic field. e, the power α in $V \propto I^{\alpha}$ as a function of temperature from fitting the top left inset of Fig. 3c. α=3 is defined as the BKT transition temperature. f, differential resistance as a function of current and displacement field along the constant density line shown in a. g, I–V curves outside the halo.

S3.2 Nonlinear transport and heating effect estimation

In a recent work[48], He *et al.* observe a sudden drop of resistance with a residue resistance about 1 kΩ, similar to our $1.32°$ device. They also reported a nonlinear I–V curve, where $dV/dI(I)$ gradually increases with current in a parabolic manner to up to a factor of two without signs of critical current. This observation is in stark contrast to the data from our superconducting-like sample,

where dV/dI reaches zero at zero bias and saturates to a finite value above critical current. In their paper, they explain this nonlinear I–V as an effect from temperature rise due to bias current heating. While this argument can explain the nonlinear I–V observed in their sample with large residue resistance, we demonstrate that our superconductor-like nonlinear I–V is unlikely caused by heating.

At 2 K, the zero-bias resistivity of the sample is close to zero. If we assume the sample is metallic, we can translate resistivity to thermal conductivity. Taking the upper bound of resistivity to be 50 Ω, it converts to 1 nW/K in heat conductivity according to Wiedemann-Franz law at 2 K. From the I–V curve shown in Fig. 3c, we can extract the heating power to be $\sim$ 13 pW at the critical current of $\sim$300 nA. As a result, the temperature rise is about 13 mK. In contrast, it requires 5 K temperature rise to bring the sample resistance to the normal value (Fig. 3b). This provides additional confirmation that our observed nonlinear I–V is likely the intrinsic property of the device rather than a heating effect.

S3.3 Enhancement of the transition temperature with $B_{\|}$

If the superconducting-like behavior in 1.26° is indeed from superconductivity, the parallel field dependence shown below suggests it might be an exotic spin polarized superconductor. We investigate the behavior of $\rho(T)$ as a function of $B_{\|}$. Fig. SA.5a shows that the superconducting dome in $(n, B_{\|})$ plane with the maximum critical parallel magnetic field $B_{\|}^{c} \approx 1$ T. The salient experimental feature is the $B_{\|}$ dependence of the superconducting state below the critical field $B_{\|}^{c}$. Fig. SA.5b shows ρ at optimal density and displacement field (n_m, D_m) as a function of T and $B_{\|}$. In this optimal superconducting state, ρ vanishes critically as T and $B_{\|}$ decreases. We use a phenomenological definition of the critical temperature $T_{50\%}$ defined as the 50% transition point. Interestingly, $T_{50\%}(B_{\|})$ follows a non-monotonic behavior. In particular, $T_{50\%}$ increases as $B_{\|}$ increases from 0 to $\sim$0.3 T before it decreases for $B_{\|} > 0.3$ T. We also performed I–V characterization at the optimal gate configuration (n_m, D_m) as a function of $B_{\|}$ and T to obtain T_{BKT} (Fig. SA.4e). Similar to $T_{50\%}$

above, $T_{BKT}(B_{\|})$ also exhibits a non-monotonic behavior as shown in Fig. SA.5b (black circles). This set of evidence suggest that a small $B_{\|}$ can strengthen the superconductivity.

The increase of T_{BKT} with $B_{\|}$ suggests the Cooper pairs responsible for the superconductivity here, if confirmed, are likely to be spin-polarized. One possible scenario for such a state is illustrated in Fig. SA.5d, where the Cooper pairs form between Fermi surfaces with the same spin (spin-triplet) and opposite valley. This model is consistent with our previous discussion of a ferromagnetic metal parent state inside the halo next to the half filled insulator (S2.1), where Fermi surfaces of two different spins have different filling status. In this spin-polarized pairing scheme, a parallel magnetic field enlarges the majority spin Fermi surface, and strengthens the superconductivity, inducing the change of the critical temperature $\Delta T_c \propto B$[160]. The eventual destruction of superconductivity at high magnetic fields can result from the following mechanism. Magnetic flux in between layers leads to a momentum shift which has an opposite sign in the two valleys, thereby bringing the two pairing Fermi surfaces out of alignment. The latter effect is expected to reduce the critical temperature, $\Delta T_c \propto -B^2$ [160]. Alternatively, if the ferromagnetic pairing is caused by spin fluctuations, as suggested in the heavy fermion metals[161,162,163], strong parallel magnetic field can suppress the superconductivity by suppressing spin fluctuations[164].

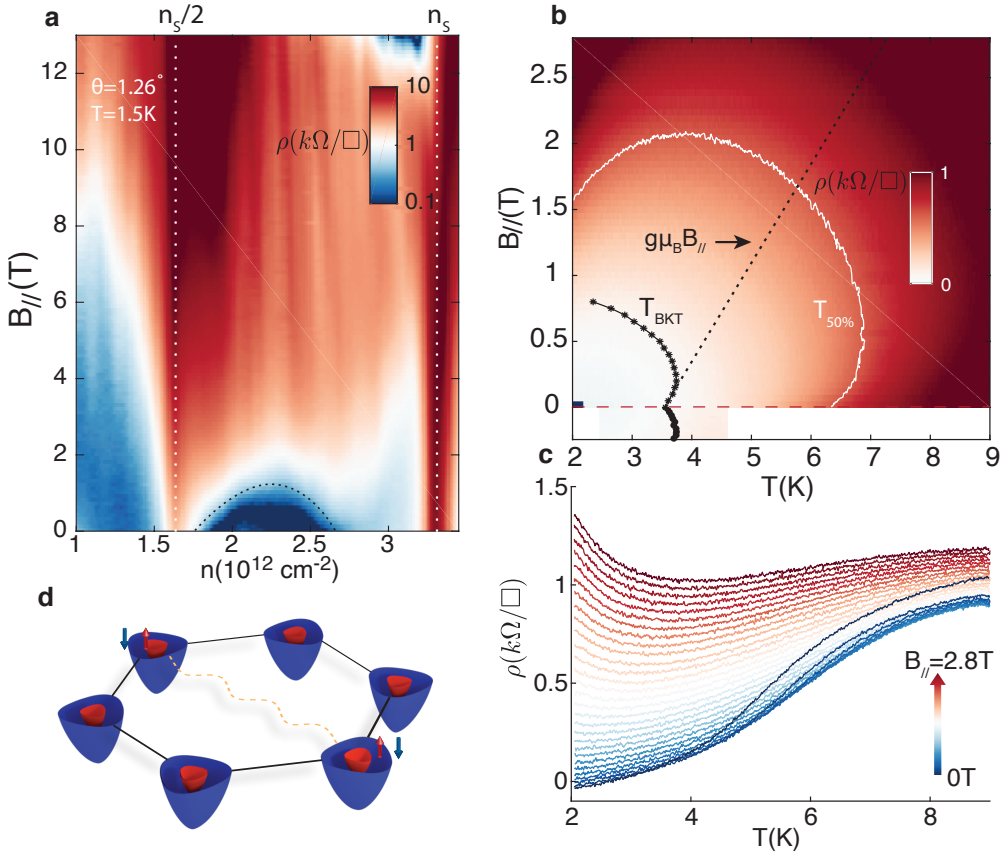

Figure A.5: a, resistivity as a function of in-plane magnetic field across the half-filled insulator and superconducting-like state in the 1.26° device. b, Resistivity as a function of temperature and in-plane magnetic field at optimal doping and displacement field. T_{BKT} denote Berezinskii--Kosterlitz--Thouless (BKT) temperature extracted from nonlinear IV measurements. $T_{50\%}$ marks the temperature where resistance is half of the normal resistance. c, line traces at different in-plane magnetic fields. d, Illustration of pairing in spin-polarized superconductor. The blue (red) surface represents spin down (up) electron band. The two bands are filled differently due to the parent ferromagnetic metallic state. The hexagon represents the Brillouin zone of graphene lattice. Pairing thus happens between Fermi surfaces of the same spin and opposite valleys.

S3.4 Origin of a small residual resistivity at $T \ll T_c$

Meanwhile, in the measurement shown in Fig. SA.5d, we notice that the 0 T resistivity goes slightly negative (∼-30 Ω) at the lowest temperature for this specific thermal cycle. Generally, we find the 4-

terminal resistivity we measure in the 1.26° device sometimes shows a small residue (-50–50 Ω) that varies between different thermal cycles. The residual resistance is not present in the measurement shown in Fig. 3b. This residual resistance (when it is present in a specific thermal cycle) is sensitive to the measurement configuration. Fig. SA.6 shows two different 4-terminal resistance measurement configurations. Between the two configurations (blue curve and red curve), we essentially flip the direction of the current. Since we use low-frequency AC ($\sim$ 17 Hz) for the current source and lock-in amplifier for voltage probe, in an ideal condition, we expect to obtain the same signal with opposite polarity. However, we find that the measured signals deviate from this expectation when there is residual resistance at low temperature. Specifically, when flowing current from top to bottom (blue curve in Fig. SA.6), 4-terminal resistance is positive, and a positive residual resistance about 50 Ω remains at the lowest temperature, 2 K. However, when the current is flowing from the bottom to the top (red curve), the 4-terminal resistance at higher temperature is negative as expected, but the residual resistance at lower temperature is still positive and is nearly identical to that in the blue curve (see inset).

We believe that the observed anomaly in the residual resistance originates from bias induced gating in combination with thermoelectric voltages present in our cryostat wiring. Due to the temperature gradient in the cryostat, a DC thermoelectric voltage is always present between different pairs of wires. This DC voltage is simply added to the voltage probes on top of the AC voltage induced by bias current. In such cases, the AC bias voltage on the sample (about half of the bias voltage on the source lead, since the drain is grounded) can modulate the DC thermalelectric voltage through bias induced gating effect (see [165] for the similar effect observed in a drag experiment), producing in a voltage signal synchronizing with the applied AC bias current. We can eliminate this bias induced AC gating effect of thermalelectric voltage by subtracting the blue curve from the red curve, where we obtain a near-zero residual resistance within noise level. During the thermal cycle in obtaining the data in Fig. SA.5d, we did not collect the data in two different configurations, and thus such cor-

rection was not possible. Note that this AC gating effect becomes only appreciable when the device resistivity is really small($< 50\ \Omega$).

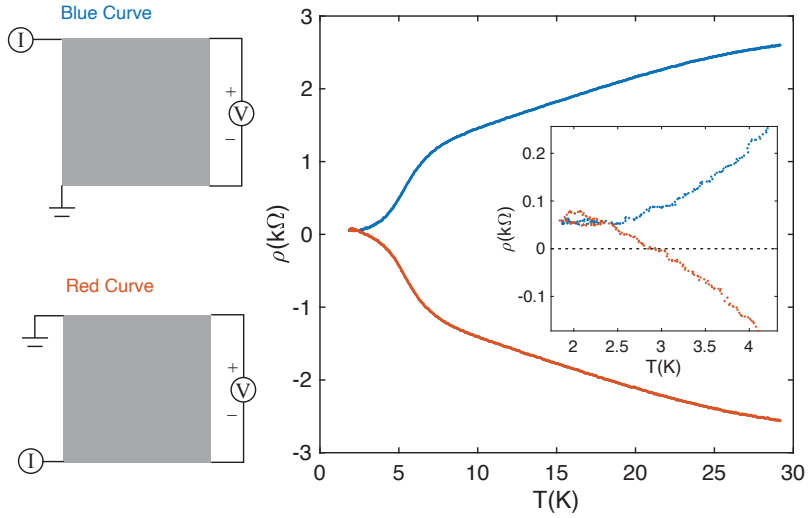

Figure A.6: $R(T)$ curve measured in the superconducting regime of the 1.26° device in two measurement configurations. The voltage probes are kept the same between the two configurations while the source and the drain contacts are switched.

S4 Landau Fan diagram

S4.1 Landau level sequence of the 1.33° device

Under a perpendicular magnetic field, clear fans can be identified coming from the charge neutral point, full-fillings $\pm n_s$ ($\approx \pm 4.1 \times 10^{12}$ cm^{-2}) as well as half-filling $n_s/2$ on the electron-doped side (Fig. SA.7). The Landau fan from the charge neutral point exhibits well-developed quantum Hall (QH) sequence with four-fold degeneracy on the valence band side under low magnetic fields, and subsequently develops the full degeneracy-lifted QH states under higher magnetic fields. The Landau fans on the conduction band side ($n > 0$) are highly unusual. The fan from the charge neutral point exhibits only a sequence of odd filling fractions $\nu = 3$ and 5. While the fan coming from the

correlated insulating state at half-filling shows a degeneracy of two, consistent with the picture of a spin-polarized half-filled band, the sequence is also of odd numbers $\nu = 3$, 5 and 7. The odd integer sequenced quantum Hall effect from the half-filling gap may relate to a Berry phase effect on the Landau level, similar to the QHE in monolayer graphene. Theory [160] predicts that the isolated flat conduction band (c_1) in TDBG carries non-trivial Berry curvature and non-zero Chern number. It is then possible that the Berry curvature accumulates to a π or 3π phase on certain Landau orbits, resulting in a quantum Hall filling fraction sequence of $2(N\text{-}1/2)$ or $2(N\text{-}3/2)$, with integer N.

There is also a single QH state $\nu = 3$ projected down to the quarter-filled conduction band. This state could be a magnetic field induced Chern insulator, similar to S2.2. Since this fan projects down to quarter filling, it is likely that both spin and valley are polarized for this state. We note that the valley Chern number corresponding to this specific state is $C = 3$, although a $C = 2$ is generally expected [160]. Further study is required to clarify these experimental observations. Above a perpendicular magnetic field of 7 T, the half-filled insulator disappears, presumably due to the orbital effect of the perpendicular magnetic field.

S4.2 Hofstadter's butterfly in the 1.26° device

The fan diagram of 1.26° is also intriguing. Beside the Landau fans, we point out there is an obvious oscillation of longitudinal resistance around $n = -n_S/2$ that does not sensitively depend on doping (horizontal features marked in Fig. SA.7 bottom panel). These oscillations are not from quantum Hall states, but from Hofstadter's butterfly. They are a result of the interplay between two different periodicities in the system: moire superlattice and magnetic length. When one moire superlattice contains $1/N$ magnetic flux (N is an integer), the two length scale becomes commensurate and produces a minimum in resistivity. These features are indicative of highly uniform twisting angle distribution in the sample. We use these features to determine the twist angle in this device.

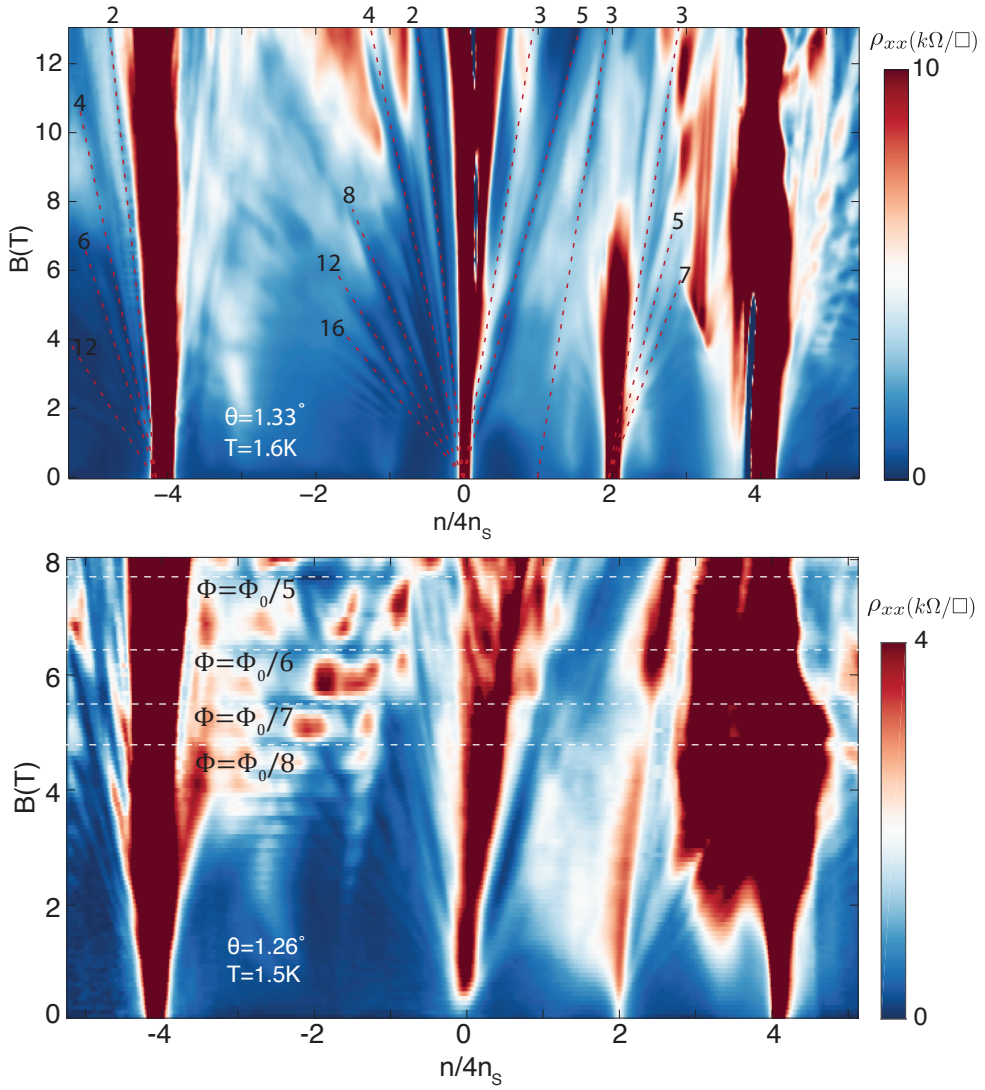

Figure A.7: The Landau fan diagram of two devices as a function of filling fraction and perpendicular magnetic field. In the top panel, the numbers next to the guiding lines indicate Landau level filling factors. In the bottom panel, horizontal lines highlight the Hofstadter's butterfly features that occur when a simple fraction of flux quantum Φ_0/N(N is an integer) penetrates through a moire unit cell.

S5 Effective mass of $\theta = 1.33°$ and $\theta = 1.26°$ samples

We calculate the effective cyclotron mass from temperature dependent magnetoresistance (SdH) oscillations. The cyclotron mass is a measure of the density of states and thus directly related to the Landau level separation (cyclotron gap) under a given magnetic field. As temperature rises, the SdH oscillation amplitude is reduced following $\Delta R \propto \chi / \sinh(\chi)$, where $\chi = \frac{2\pi^2 k m^*}{\hbar e} \frac{T}{B}$.

For $\theta = 1.33°$ sample, we measured SdH oscillations at all densities between filling factor n/n_S = -1 and 1, at $T = 0.3, 2, 3, 4, 6, 9, 14$ K (example: Fig. SA.8a-c). We then extracted the oscillation amplitudes and plot them as a function of T/B. Fitting $\Delta R(T/B)$ with the above formula with m^* being the only fitting parameter, we obtain the effective cyclotron mass shown in main text. Similarly, we measured SdH oscillations for the $\theta = 1.26°$ sample and extracted an effective mass $m^* = 0.23 m_e$, as shown in Fig. SA.8e-f.

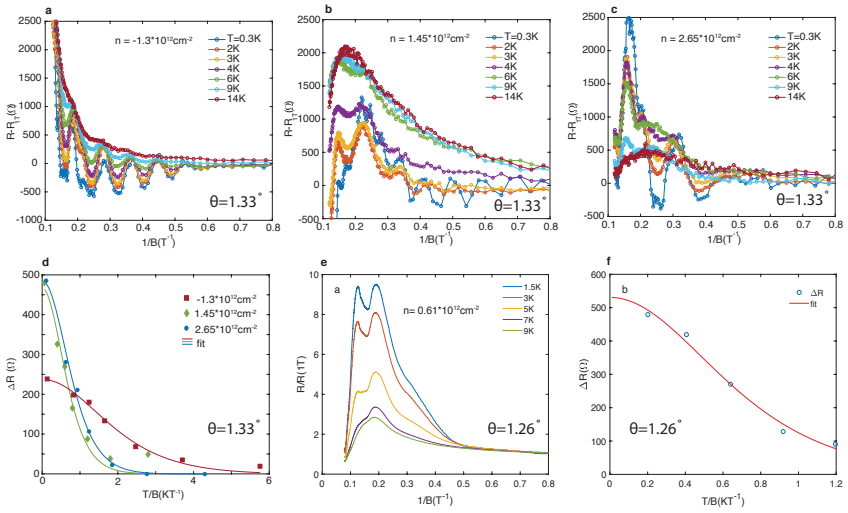

Figure A.8: **a-c**, temperature dependent SdH oscillations in the $\theta = 1.26°$ device at a few representative density points: **d**, extracted oscillation amplitudes as a function of T/B for the density configuration shown in **a-c** and corresponding fitting curves. **e**, temperature dependent SdH oscillations in th $\theta = 1.26°$ device at $n = 0.61 \times 10^{12}$ cm^{-2}, which is above half filling and inside the halo. **f**, extracted oscillation amplitudes as a function of T/B in the $\theta = 1.26°$ device.

S6 Characterization of devices used in this work

We measured in total of six devices with different twist angles in this study. All samples are encapsulated by the hBN layers. In 1.32°, 1.33°, 1.41° and 2.00° devices, both the top and bottom gates are made from graphite. 1.26° device utilizes a graphite top gate and a heavily doped silicon bottom gate below the hBN substrate and 300 nm SiO_2 dielectric. The 1.48° device employs a silicon bottom gate and a metal top gate. Most of the devices are fabricated into Hall bars with the exception of the 1.26° and 1.41° samples, which are fabricated into a Van der Pauw geometry. The gate configurations and device images are shown in Fig. SA.9

Fig. 1f and Fig. SA.10a,c-f show large scale gate scans of the longitudinal resistivity in all samples. These samples exhibit insulating states at fulling filling under zero displacement field and at CNP under large displacement field. Moreover, particularly, the 1.32°, 1.48°, 2.00° devices exhibit a CNP gap under the zero displacement field, which closes and reopens with increasing displacement field. We note that neither the 1.26° nor the 1.41° device has a gap at the CNP under zero displacement field. For the 1.32° device, we also notice that the gate scan diagram exhibit a wide insulating region at full filling and double peaks at half filling, suggesting that there is additional moire periodicity in the channel other than 1.32°. The CNP gap in 1.32° under zero displacement field is likely originated from the larger twist angle region of the sample. We remark that theory [160] predicts a gap at CNP opens up even at zero displacement field when $\theta > 1.5$, qualitatively agreeing with our experimental observation.

In Fig. SA.10a, we observe negative resistivity in a part of the 2D gate scan. These anomalous signals can be attributed to nontransparent contacts in these gate regions. Comparing with the 2D map of the 2-terminal resistance measured in this device (Fig. SA.10b), we find that the gate regions where negative resistivity were observed in Fig. SA.10a in general correspond to the gate regions where a large contact resistance is demonstrated by the 2-terminal measurement. This strong cor-

relation between the apparent 'negative' 4-terminal resistivity and high contact resistance suggests that the negative 4-terminal resistivity originates from inefficient contact equilibration in these gate regimes. Indeed, the contact transparency can be hindered by the unintended PN junction formation near the metal contacts when the applied gate voltages conspire with the work function mismatch between graphene and metal to cause an accumulation of the opposite polarity of charges near the contact and in the channel. However, near the half-filled insulator region, where most of our research is focused, the 2-terminal resistance stays less than 10 kΩ, demonstrating excellent contact transparency. Thus, we conclude that the contact anomaly can be excluded as a possible cause of our experimental observation near the correlated insulator regime. We also notice that the correlated insulating state in the positive displacement field side ($V_{TG} < 0$ and $V_{BG} > 0$) shows a much weaker signature than the negative displacement field side. The absence of a clear signature of correlated insulator on the opposite side of the displacement field is also likely due to the inefficient contact equilibration in these particular gate configurations, as shown in Fig. SA.10b.

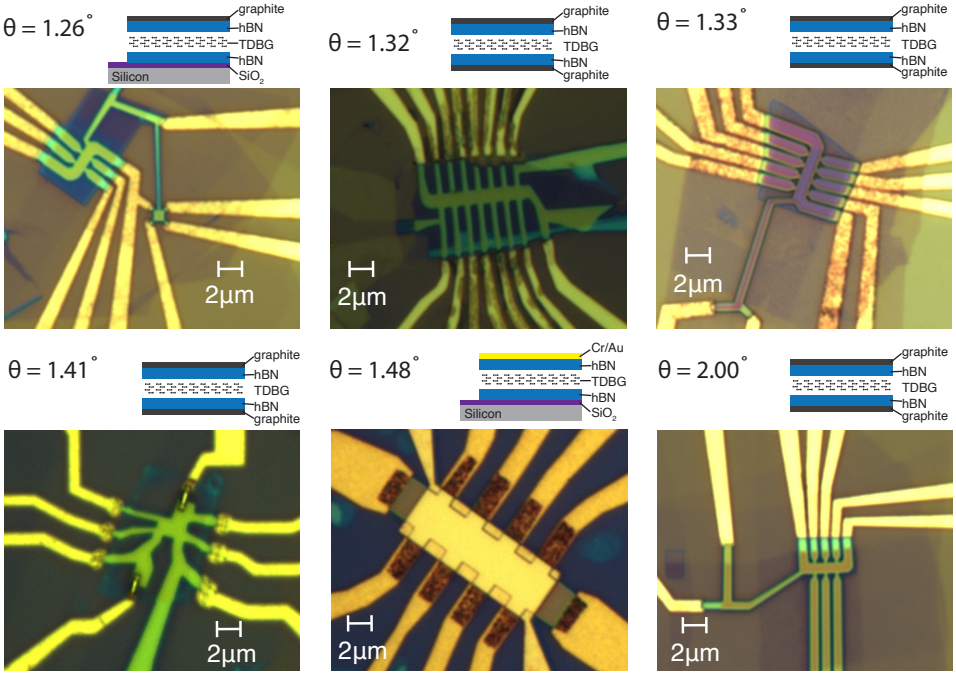

Figure A.9: Optical images of all devices measured in this paper. For 1.26° the active device is the four-terminal Van der Pauw sample. The structure of each device is depicted by the cross-section illustration above the optical image.

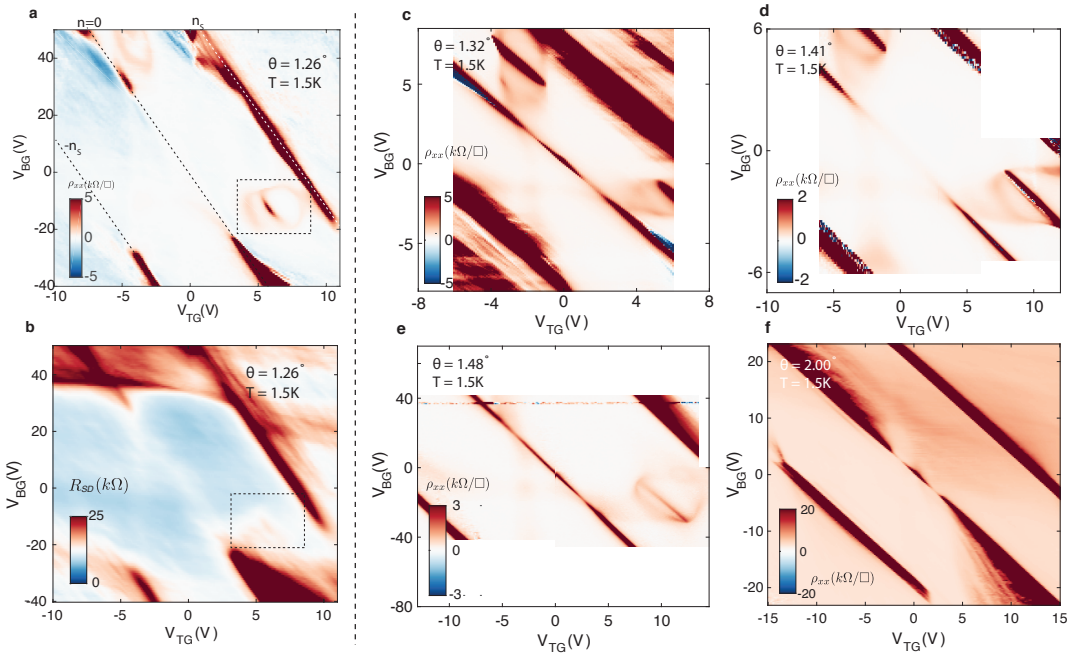

Figure A.10: a, four-terminal resistivity in the 1.26° device measured in a large top and bottom gate voltage range. Dashed square marks the active area studied. **b**, two-terminal resistance measured in the 1.26° device in the same gate voltage range presented in a. **c**-**f**, four-terminal resistivity in other samples studied in this work in a large top and bottom gate voltage range.

B

Twisted trilayer graphene supplementary information

S1: Device fabrication and characterization

Our twisted trilayer graphene (TTG) device TMB (device names used in Fig. 1) and the twisted bilayer graphene (TBG) device TM have both top and bottom graphite gates. The TBG device MB is controlled by top graphite gate and silicon back gate. The van der Waals heterostructure stack for making the devices consists of 8 layers of two-dimensional materials in the order of hBN, few-layer graphite, hBN, mono-graphene, mono-graphene twisted with angle θ, mono-graphene twisted with angle $-\theta$, hBN and few-layer graphite. The stack was prepared using the dry transfer method, similar to the procedures introduced in most published literature on twisted graphene devices. We

make stamps consisting polycarbonate (PC) polymer and polydimethylsiloxane and pick up each layer sequentially. The temperature is kept under 180 °C through out the transfer process. We find that generally graphene flakes with large area (e.g., 70 μm by 70 μm) give higher yield in making twisted graphene samples. In order to minimize the movement of graphene flakes during transfer processes, we use an atomic force microscope (Asylum Cypher S) to precut the graphene flakes. For this, we follow the general procedure described in reference[65], using a platinum doped AFM cantilever and contact mode. An 100kHz AC bias of 30V is applied to the cantilever during cutting. We find that this AC bias is critical but its exact role in cutting is currently unknown. The stack is deposited on top of a 300-nm SiO_2/Si substrate that has evaporated gold alignment marks on it. Alignment marks are made beforehand so the twisted sample is not subject to the high temperature of the evaporation process before being etched. Three Hall bar devices were fabricated in the regions of TMB, TM and MB following the standard e-beam lithography and dry etch procedures.

The transport data was measured at 17.7 Hz using the standard lock-in technique, with a 0.5–1 mV voltage bias and a current-limiting-resistor of 180 kΩ connected in series with the sample, which limits the current in the sample to an upper bound of 2–5 nA. The sample is connected to the cryostat probe through an RC filter to reduce noise.

We calculate twist angles using two independent methods. The first is to use the geometric capacitance between the twisted samples and gates. The carrier density is determined by the top gate voltage V_t and the bottom gate voltage V_b through $n = c_t V_t + c_b V_b$, where c_t (c_b) is the capacitance between the top (bottom) gate and the sample , and it can be directly calculated $c_{t(b)} = \kappa\varepsilon_0/d_{t(b)}$. κ is the dielectric constant for hBN and is usually taken as 3.9. ε_0 is the vacuum permittivity. $d_{t(b)}$ is the top (bottom) hBN thickness. Using the resistivity, ρ, versus gate voltage $V_{t(b)}$ at zero magnetic field, we can associate the resistive peaks with integer fillings of the moiré bands, and therefore obtain the gate voltage, or equivalently using the above formulae the carrier density n_s for full filling at $\nu = 4$. This carrier density corresponds to 4 electrons per moiré unit cell $n_s = 4/A_m$, where

A_m is the moiré unit cell area and is connected to the small twist angle by $A_m = \frac{\sqrt{3}a^2}{2\theta^2}$, where a is the lattice constant for graphene. The main uncertainty in this method comes from the uncertainty in the value of the dielectric constant κ and the finite width of the integer-filling resistive features. The second method uses the Landau fan diagrams shown in magnetotransport data. By comparing the longitudinal resistivity data with the Hall conductance, we can assign each line in the Landau fans with a Chern number C so that $\sigma_{xy} = Ce^2/h$, where e is the electron charge and h is the Planck's constant. The slopes of the lines in Landau fans are connected to the Chern numbers through $BA_m/\varphi_0 = Cn/n_s + s$, where B is magnetic field, $\varphi_0 = e/h$ is the magnetic flux quantum, s is the filling fraction from which the Landau fan emanates. The main uncertainty in this method comes from how well the slopes are fit. This gives an uncertainty of $\pm 0.02^\circ$ in calculating the angle.

S2: Band structure calculation and DOS

In this section we discuss the single particle band structure of magic angle twisted trilayer graphene, shown in Fig. 1C and 4E, F. The density of states was also plotted in Fig. 4G. The band structure was computed from the trilayer analogue[78] of the Bistritzer-Macdonald model[52] of twisted bilayer graphene. In this case, however, the in-plane displacement between layers matters. As shown in Ref.[78], the Hamiltonian can be brought to a form where only the relative displacement between the top and bottom layers appears. We denote this distance d. For a single spin and graphene valley, the Hamiltonian is

$$H(d) = \begin{pmatrix} -iv\sigma_{\theta/2}\cdot\boldsymbol{\nabla} & T(r-d/2) & 0 \\ T^\dagger(r-d/2) & -iv\sigma_{-\theta/2}\cdot\boldsymbol{\nabla} & T^\dagger(r+d/2) \\ 0 & T(r+d/2) & -iv\sigma_{\theta/2}\cdot\boldsymbol{\nabla} \end{pmatrix}. \tag{B.1}$$

Here, $\sigma_{\theta/2} = e^{-\frac{i}{4}\theta\sigma_z}(\sigma_x, \sigma_y)e^{\frac{i}{4}\theta\sigma_z}$, v is the graphene Fermi velocity, and

$$\begin{aligned} T(r) &= \begin{pmatrix} w_0 U_0(r) & w_1 U_1(r) \\ w_1 U_1^*(-r) & w_0 U_0(r) \end{pmatrix}, \\ U_0(r) &= e^{-iq_1\cdot r} + e^{-iq_2\cdot r} + e^{-iq_3\cdot r}, \\ U_1(r) &= e^{-iq_1\cdot r} + e^{i\varphi}e^{-iq_2\cdot r} + e^{-i\varphi}e^{-iq_3\cdot r}, \end{aligned} \tag{B.2}$$

with $\varphi = 2\pi/3$. The vectors q_i are $q_1 = k_\theta(0, -1)$ and $q_{2,3} = k_\theta(\pm\sqrt{3}/2, 1/2)$. The wavevector $k_\theta = 2k_D \sin\frac{\theta}{2}$ is the moiré version of the Dirac wavevector $k_D = 4\pi/3a_0$, where a_0 is the graphene lattice constant. For the other graphene valley, the Hamiltonian is the complex conjugate of (B.1). The spectrum of $H(d)$ depends strongly on d. However, Ref.[81] finds that $d = 0$ has the lowest energy due to relaxation effects, and that the system is likely to slide into this configuration naturally. We therefore focus on $d = 0$ which corresponds to AA stacking between the top and bottom layers.

For $d = 0$, the Hamiltonian has a symmetry under exchanging the top and bottom layer.

$$M_z = \begin{pmatrix} 0 & 0 & 1 \\ 0 & 1 & 0 \\ 1 & 0 & 0 \end{pmatrix}. \tag{B.3}$$

We may then consider separately the Hamiltonian in the $M_z = \pm 1$ sectors. For $M_z = +1$ we find a TBG Hamiltonian

$$H_+ = \begin{pmatrix} -iv\sigma_{\theta/2}\cdot\boldsymbol{\nabla} & \sqrt{2}T(r) \\ \sqrt{2}T^\dagger(r) & -iv\sigma_{-\theta/2}\cdot\boldsymbol{\nabla} \end{pmatrix}, \tag{B.4}$$

where the tunneling is $\sqrt{2}$ times stronger. On the other hand for $M_z = -1$ we obtain ordinary graphene

$$H_- = -iv\sigma_{+\theta/2}\cdot\boldsymbol{\nabla}. \tag{B.5}$$

Here, the ordinary graphene electrons come from the top and bottom layers only and the Dirac cone is centered around the moiré K point. Similarly in the other graphene valley the Dirac cone is centered at the moiré K' point. Thus, for this system we expect that when the angle is $\sqrt{2}$ times the TBG magic angle, we will obtain flat bands from (B.4) together with a Dirac cone from (B.5). This band structure is depicted in Fig. 1C. with parameters $\theta = 1.55^\circ$, $w_1 = 110$meV, and $\kappa = w_0/w_1$.

A nonzero displacement field mixes the TBG and graphene sectors by breaking M_z; its effect is largest at the K point where the bands intersect. There, the two Dirac points near charge neutrality, one from each of the graphene and TBG subsystems, split and hybridize so that there is one above zero energy and one below zero energy. These Dirac points are still protected by inversion combined with time reversal which acts as $H(r) \rightarrow \sigma_x H^*(-r)\sigma_x$ and is a symmetry when $d = 0$. Band structures with nonzero displacement fields are shown in Fig. 4E and F. with the same parameters as Fig. 1C.

The density of states is shown in Fig. 4G in the main text. It is obtained from the band structure of the Hamiltonian (B.1) by a gaussian-smoothing over energy levels with standard deviation 0.03 meV. Here we also include the density of states plotted versus energy instead of filling, see Fig. SB.1.

S3: Sample homogeneity

Fig. S2 shows a comparison of ρ versus n measured with $V_{\mathrm{BG}} = 0$ for different pairs of contacts. From Fig. S2A to E, the blue circles in the device image illustrate the pair of contacts, labeled P1 - P5, used for measuring the data on the right. Red dashed lines label the resistive states at integer fillings ν =-2, 0, 1, 2, 3. It can be seen that for different contacts, the red dashed lines are slightly misaligned with respect to each other, indicating that the regions between the contacts have different angles. We calculated the angle for P2 using quantum oscillations. Then using their relative ratio of full filling densities, we obtained angle for each pair of contacts. The measured angles are $\theta_1 = 1.552^\circ$,$\theta_2 = 1.567^\circ$, $\theta_3 = 1.567^\circ$, $\theta_4 = 1.572^\circ$, and $\theta_5 = 1.572^\circ$ all with uncertainty

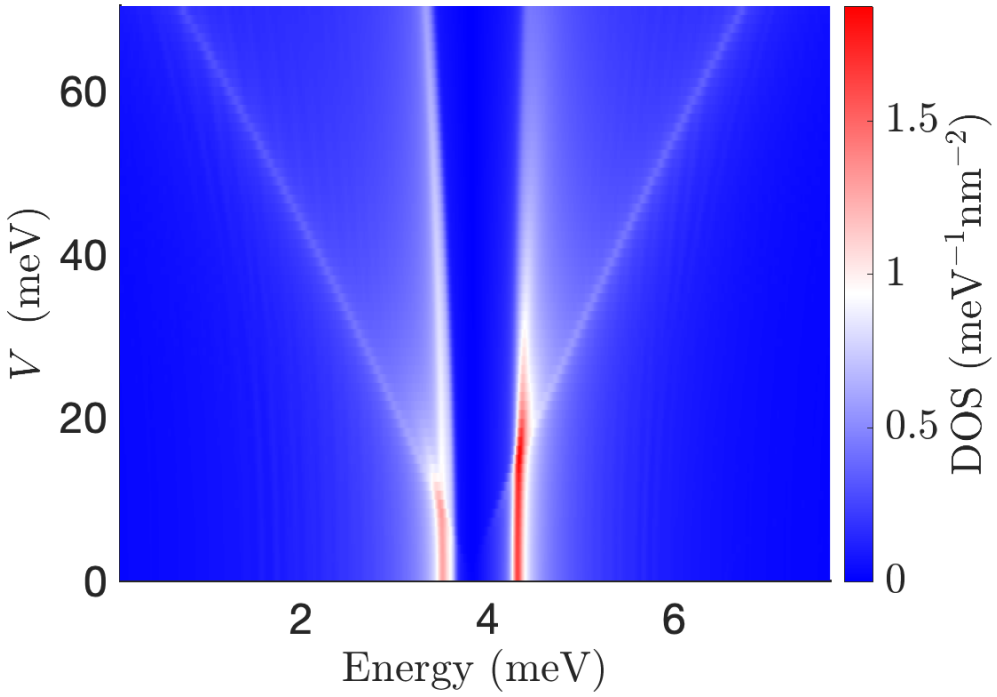

Figure B.1: Density of states versus energy and displacement field. Similar to Fig. 4G in the main text, one sees two flat bands that spread out after a sufficiently large displacement field is applied. Prominent van Hove singularities are visible in white and spread out with increasing displacement field.

$\pm 0.02°$. Although the third digit in the angles maybe seem meaningless given the magnitude of the uncertainty, they indicate the relative angle difference between different pairs of contacts, which has smaller uncertainty. There are double peak features in P5 indicating a region of $\theta = 1.61°$. None of the presented data was taken in this more diordered region. We note that over the majority of the sample, the angle is extremely uniform changing less that $0.02°$. The angle gradually becomes larger from the left to the right. And there is more angle disorder on the right side of the sample. The superconductivity is strongest at the left end of the sample with $\theta_1 = 1.552°$, and the majority of the presented data was taken in this region.

S4: Fan diagram comparison

Fig. S3A shows longitudinal resistivity ρ and inverse Hall resistivity $1/\rho_{xy}$ as a function of ν and B at $V_{\mathrm{BG}} = 0$ and $T = 0.86$ K. This is complementary to the $\rho(B, n)$ data shown in Fig. 1F. We can see large area of $1/\rho_{xy} = -2e^2/h$ near $\nu = -4$ and $2e^2/h$ near $\nu = 4$. From the single particle band calculation we know that when a displacement field is applied, the originally independent Dirac cone and flat bands at zero displacement field mix resulting in two Dirac cones splitting to higher and lower energy respectively. The large regions of quantized reverse Hall resistivity are likely from the quantum Hall states of these Dirac cones. Fig. S2C is a schematic of the quantum Hall structure observed in Fig. 1F. Emanating from the charge neutrality, the main sequences are $C = -2, -6, -10, \ldots$ on the hole doped side and $C = 2, 6, 10$ on the electron doped side. At higher magnetic field, between $C = -2$ and $C = -6$, symmetry breaking states with $C = -3, -4$ and -5 emerge and the sequence $C = -14, -18, -20$ transitions into $C = -12, -16, -20$.

Fig. S4 shows the fan diagram at zero displacement field. The Landau fan sequences emerging from neutrality, $\nu = \pm 2$ are similar to that observed in the $V_{BG} = 0$ fan. Interestingly, in low field range, we observe "arc-like" features or a coexisting quantum oscillation structure distinct from those of the flat bands. We argue these are in fact the quantum Hall states of the additional

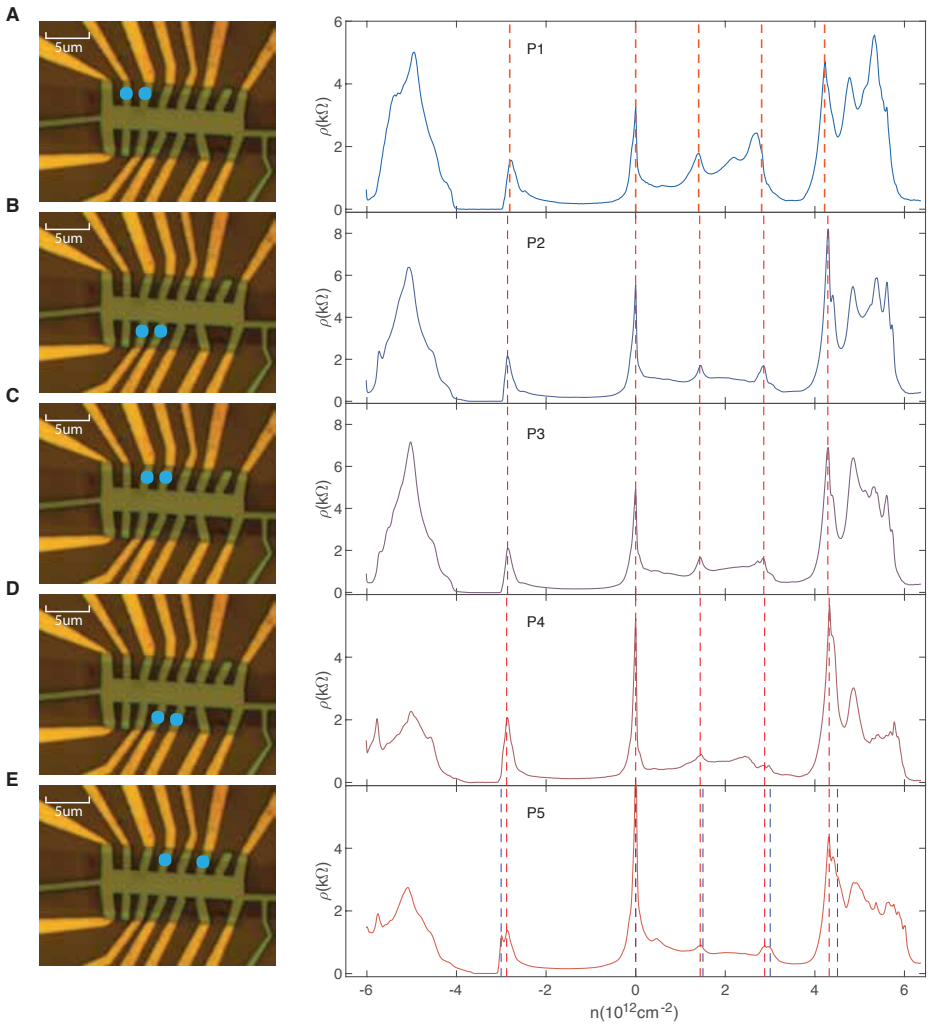

Figure B.2: Angle inhomogeneity. The blue circles mark which pair of contacts are measured for the $\rho(n)$ data in each figure from (A) to (E). Red dashed lines label integer fillings from left to right ν =-2, 0, 1, 2 and 3 in each figure.

Dirac cone. Fig. S5A shows ρ and Hall conductance σ_{xy} as a function of inverse magnetic field at $\nu = -3.82$, where the arcs are prominent. We see clear quantum oscillations, displayed as the equally distanced minima in ρ. The σ_{xy} values corresponding to the first two minima are quantized to $-2e^2/h$ and $-6e^2/h$, the same as the Dirac Landau level sequence. σ_{xy} for the other minima are not well quantized. Most likely because they appear at lower magnetic fields and are not well developed. Fig. S5B shows $\frac{d\rho}{dB}$ to make these quantum oscillations more prominent.

The quantum Hall states of the Dirac cone appear as arcs instead of the normal straight lines emanating from $\nu = 0$ because the flat bands and the Dirac cones are filled simultaneously. Kinks in the Dirac cone states correspond to changes in the flat band chemical potential due to strong-interaction induced symmetry breaking as has been observed in TBG[86,85,68]. To confirm that these structures are the Landau fan of the additional Dirac cone, in Fig. S5C and D, we trace out ρ minima for the visible states which we assume are the $C = 6$, 10 and 14 states for the Dirac cone, labeled by the triangle symbols with different colors. With these traces, we obtain the positions in magnetic field B_6, B_{10}, and B_{14} as a function of ν for the $C = 6$, 10 and 14 states respectively. According to Diophantine equation $\nu - s = C\varphi/\varphi_0$ (where s is the filling where the Landau fan emerges from and $\varphi = BA$ is the magnetic flux through the sample and A is the sample area), if these structures are quantum Hall states of $C = 6$, 10, 14, we expect that $6B_6 = 10B_{10} = 14B_{14}$ even with charge carriers filling both the Dirac cone and the flat bands. Fig S5B and C shows the normalized ratio between $6B_6$, $10B_{10}$ and $14B_{14}$ and indeed they are roughly one, confirming that the states originate from the Dirac cone. We also note that these arcs are not present in the fan diagram with $V_{\mathrm{BG}} = 0$, in which D is mostly nonzero. This is consistent with the theoretical prediction that a gap opens at the Dirac cone when a displacement field is applied, causing the Dirac cones to not fill until after the flat bands.

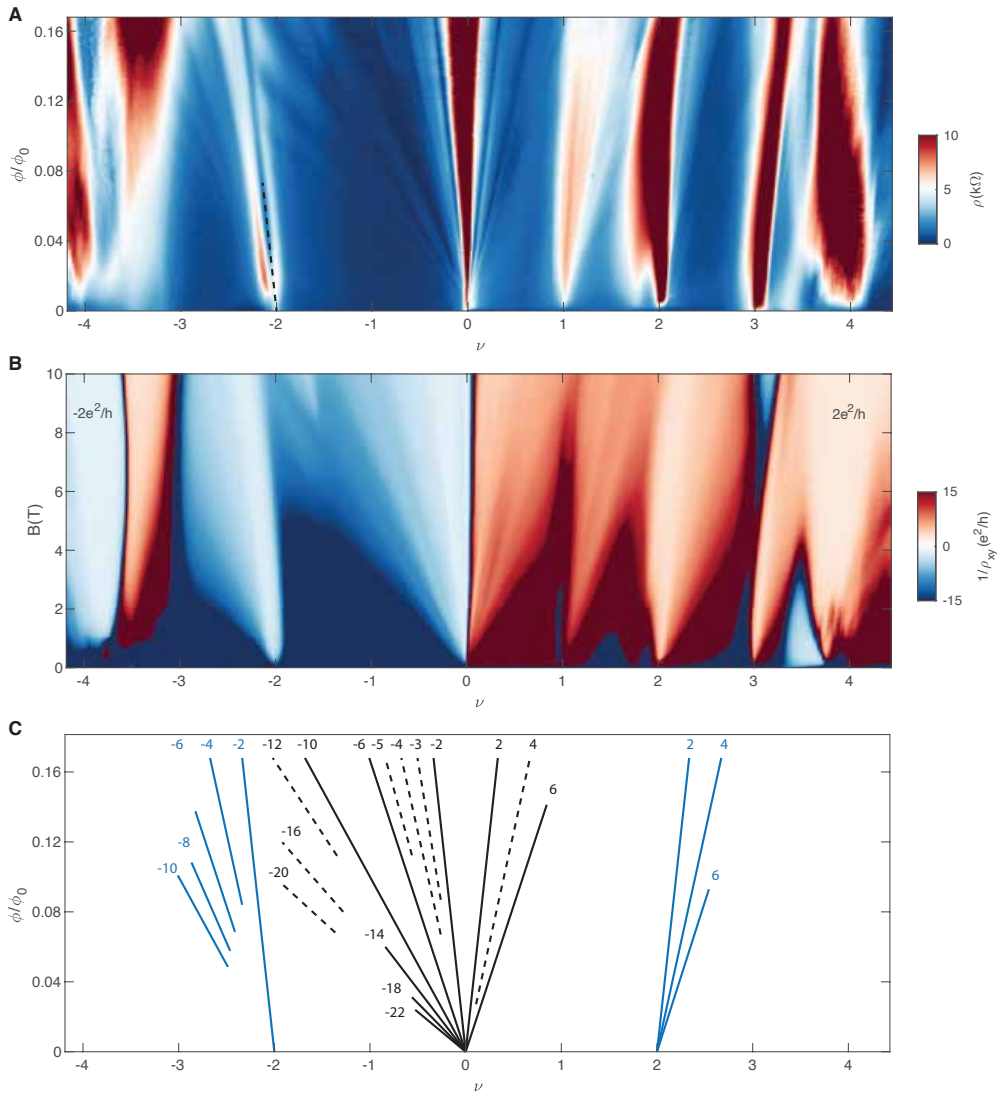

Figure B.3: TTG Landau fan diagrams at $V_{BG} = 0$ and $T = 0.86$ K. (A) and **(B)** ρ and $1/\rho_{xy}$ as a function of ν and B. Large regions of $1/\rho_{xy} = \pm 2e^2/h$ are marked. **(C)** Schematic of the quantum Hall structure in the Landau Fan diagram.

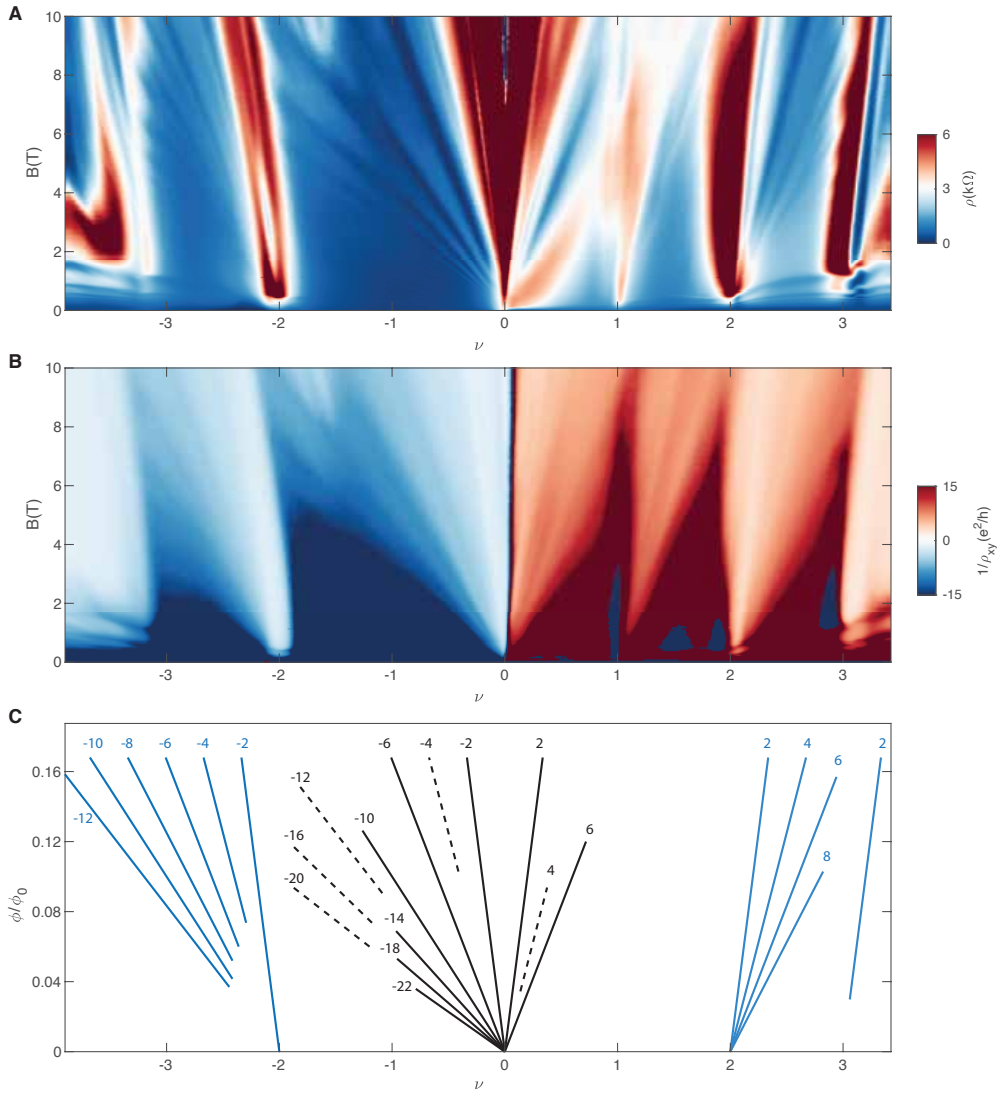

Figure B.4: TTG Landau fan diagrams at $D = 0$ and $T = 0.86$ K. (A) and **(B)** ρ and $1/\rho_{xy}$ as a function ν and B. **(C)** Schematic of the quantum Hall structure.

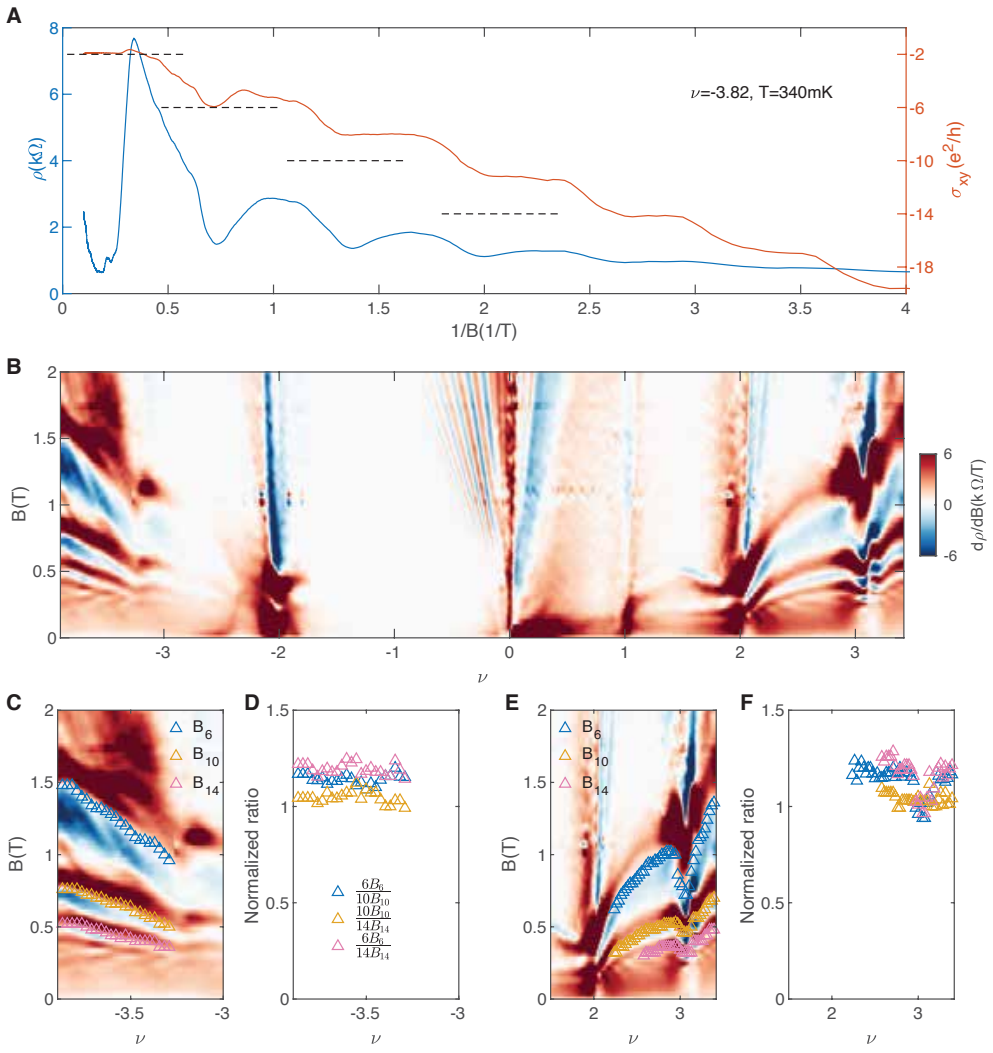

Figure B.5: Evidence of the additional Dirac cone. (A) Quantum oscillations at $\nu = -3.82$. Blue curve is longitudinal resistivity ρ and orange curve is Hall conductance σ_{xy}. Black dashed lines mark quantized conductance values corresponding to sequence -2, -6, -10,... **(B)** $\frac{d\rho}{dB}$ of the ρ data in Fig. S4A below 2T. (**C** and **E**) zoom-ins of the oscillations on the hole side and the electron side. Triangles trace ρ minima. B_6, B_{10} and B_{14} correspond to the Dirac cone Landau fan sequence 6, 10 and 14. (**D** and **F**) Normalized ratio between the magnetic field values multiplied by the sequence number of different traces. The ratios are all approximately 1.

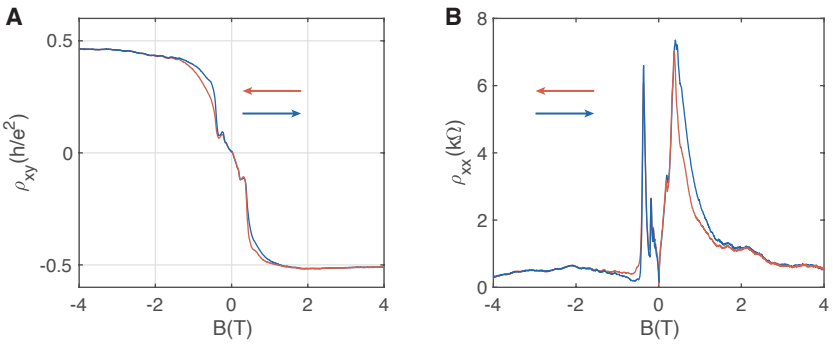

Figure B.6: Hysteresis of the field induced Chern insulator at $\nu = -2$. (A) Hall resistivity ρ_{xy} and **(B)** longitudinal resistivity ρ_{xx} along the slope with chern number $C = -2$. Blue and orange curves are data for different sweep directions, indicated by the corresponding blue and orange arrows.

S5: Hysteresis of the field induced Chern insulator at $\nu = -2$

Fig. S6 shows the Hall resistivity ρ_{xy} and longitudinal resistivity ρ_{xx} along the black dashed line emanating from $\nu = -2$ as shown in Fig. S3. It corresponds to a slope with Chern number -2. ρ_{xy} is 0 at B=0 but increases rapidly with a small B and saturates to a quantized resistance $h/2e^2$ above 1 T. ρ_{xx} first increases but then drops to a low value above 1 T. This behavior in transport is a signature of magnetic field induced Chern insulator with a Chern number $C = -2$ that is only fully developed above 1 T. Furthermore, we observe a difference between magnetic field sweep directions in both ρ_{xy} and ρ_{xx} near the onset of the Chern insulator. This indicates the presence of orbital ferromagnetism associated with it.

S6: Critical temperature and GL coherence length

We extract T_c from $\rho(T)$ by first fitting a line to the high temperature linear part of $\rho(T)$, then extrapolating this normal state resisitivty ρ_N to low temperature, and finally finding the temperature where $\rho(T) = x\rho_N(T)$, where x is a percentage. An example of this linear fit for data at 2 T is shown in Fig SB.7 as well as $\rho(T)$ taken at several different magnetic fields. We note that a dip in ρ at low

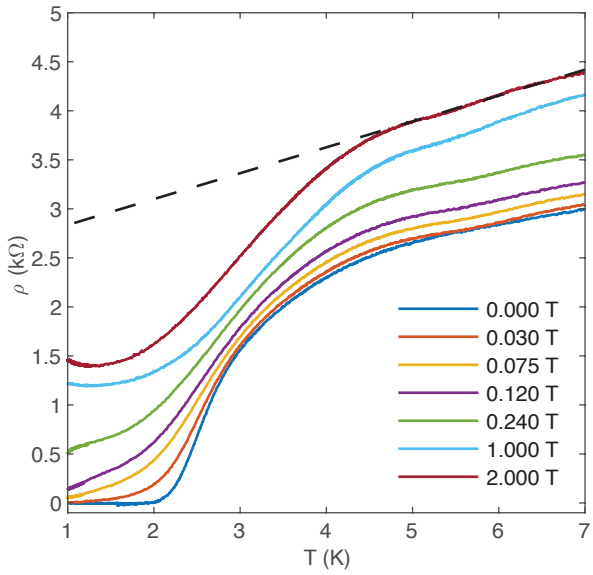

Figure B.7: T_c extraction $\rho(T)$ measured at several different fields at $\nu = -2.3$ and $D/\varepsilon_0 = 0.29$ V/nm. The dashed line is a fit to the normal state resistivity at 2 T.

temperature is evident in the data even at high B although ρ does not go to zero. A similar tail of low ρ extending to high field is evident in the dV/dI data and $\rho(\nu, B)$, shown in Fig. SB.8. It is possible that this dip is due to a vortex phase with non-zero ρ.

This dip in resistivity results in very different results for T_c depending on the choice of x. Fig. SB.9 shows this difference for $x = 0.1$ and $x = 0.5$. For $x = 0.1$ we find a linear relationship as described by the Ginzburg-Landau (GL) theory for a two-dimensional superconductor: $B_c = [\Phi_0/(2\pi\xi_{GL}^2)](1 - T/T_c)$ where ξ_{GL} is the GL coherence length[83]. For $x = 0.1$, $\xi_{GL} = 34$ nm. For $x = 0.5$ the resulting T_c is much higher and remains above 1.5 K to fields larger than 2 T. It is also very non-linear, although fitting the low field portion gives $\xi_{GL} = 13.4$ nm. We have chosen $x = 0.1$ as the standard for this paper as it more clearly defines the region where we observe $\rho = 0$ at low temperature, and agrees well with the measured BKT transtion temperature.

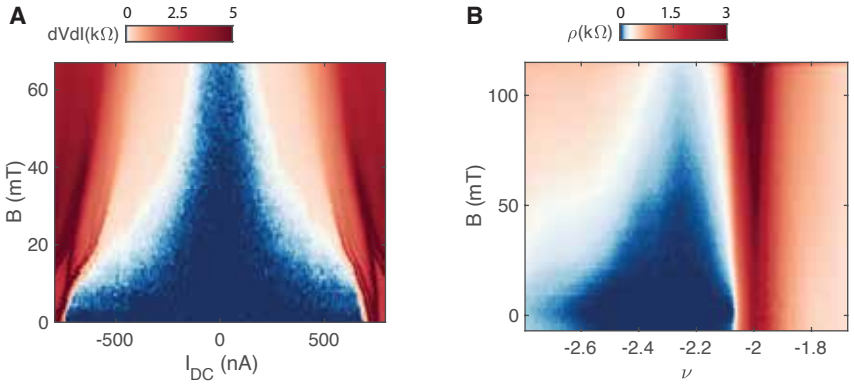

Figure B.8: B dependence of the superconductor at $\nu = -2.3$ and $D/\varepsilon_0 = 0.29$ V/nm (A) Differential resistance as a function of DC bias current showing a long low resistance tail extending to large B. **(B)** Resistivity as a function of nu and B also with low resistivity at larger B.

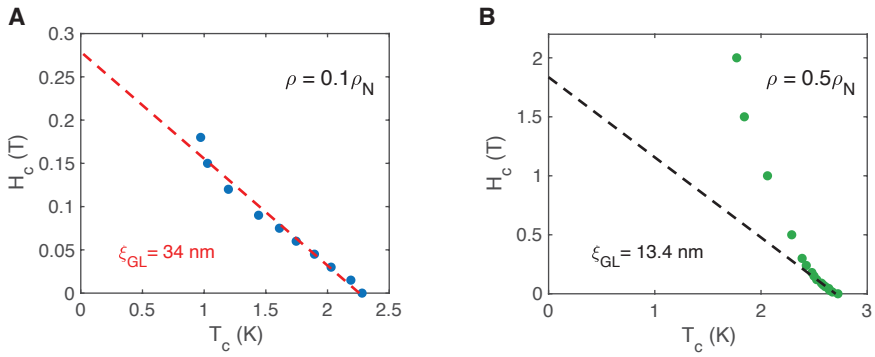

Figure B.9: Coherence Length T_c determined using $x = 0.1$ **(A)** and $x = 0.5$ **(B)**. Dashed lines are fits to GL theory with different ξ_{GL}.

S7: Berezinskii–Kosterlitz–Thouless (BKT) transition analysis

Like other ordered phases in 2D, a 2D superconductor does not have a true finite-temperature phase transition but can go through a topological phase transition called BKT transition. Below the BKT transition temperature T_{BKT}, vortices and anti-vortices of the order parameter bind closely with each other and above T_{BKT}, these vortices and anti-vortices proliferate and become independent, dominating the physics in the system. One manifestation of this transition in a 2D superconductor is that its $V - I$ dependence follows a power law below T_{BKT} and the power exponent, α goes through a rapid crossover near the transition, with $\alpha = 3$ at T_{BKT}. To analyze the BKT transition, at each temperature, we use a lock-in to measure dV/dI as a function of DC bias current, as shown in Fig. SB.10a. We integrate this and assign $V = 0$ at zero I to obtain the $V(I)$ curves shown in Fig. 2 and Fig. SB.10B. When fitting to a power law to obtain α, we fit only the low voltage behaviour below 1 μV. This low voltage behaviour captures the initial unbinding of vortex-anti-vortex pairs under the effect of temperature [166,167]. We note that if α is extracted at high current it captures unbinding of the vortices and anti-vortices due to current instead of temperature. This is common error in experimental analysis and one that we made in out initial analysis of the BKT temperature. Fig. SB.10B shows clearly shows the $V - I$ curves follow a power-law in low current range and the power exponent rapidly decreases with increasing temperature. The black dashed line has $\alpha = 3$. The α values extracted from this procedure are shown in the inset of Fig. SB.10a.

S8: Strong-coupling superconductivity

The rapid increase in T_c with doping in addition to the suppression of superconductivity due to the van Hove singularity point towards a strong coupling (BEC) scenario for superconductivity where preformed bosonic charge $2e$ objects are condensed. One such model is the skyrmion model of superconductivity proposed in Ref. [90] where such bosonic charge $2e$ objects were proposed to be

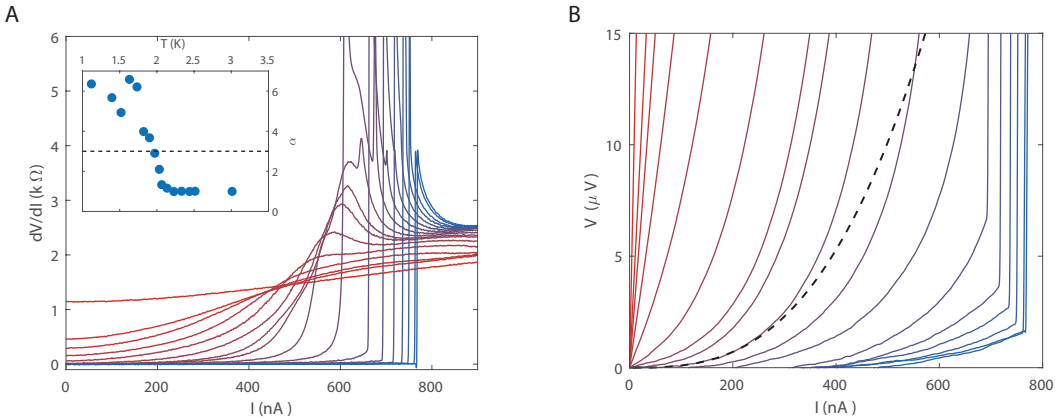

Figure B.10: BKT Transition. (A) Differential resistance as a function of DC bias current from 3 K (red) down to 0.8 K (blue). Inset: Extracted power, α, from power law fits to IV curves **(B)** IV curves obtained by integrating the data in (A) plotted in linear scale. The dashed line shows the fit with $\alpha = 3$.

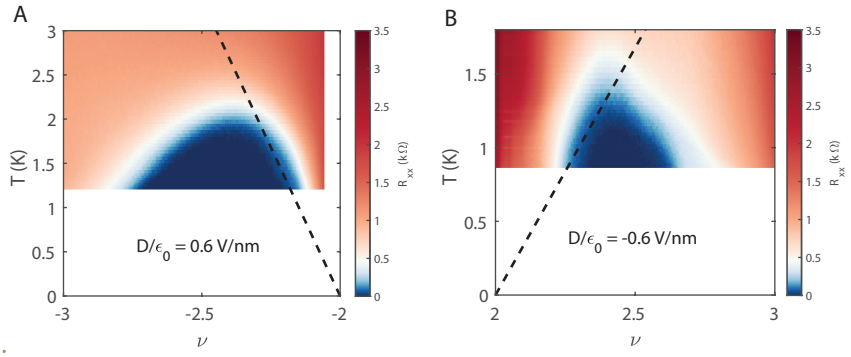

Figure B.11: Strong coupling fit Examples of typical fits to extract the slope of T_c for comparison with a strong-coupling model of superconductivity. The black dashed lines show fits to T_c near the optimal point on the superconducting domes constrained to pass through $\nu = \pm 2$.

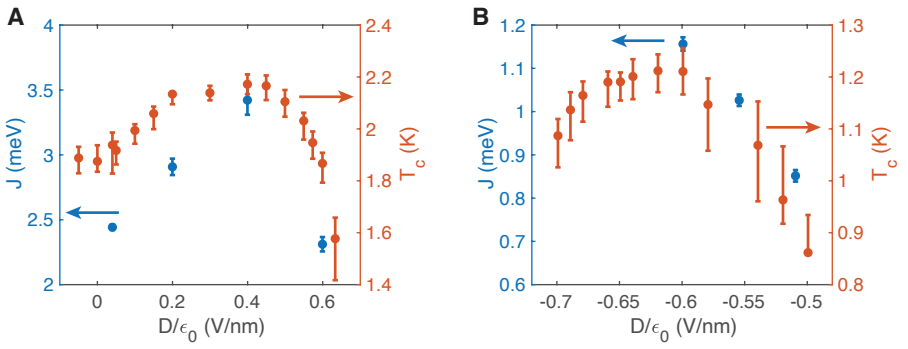

Figure B.12: Extracted pairing scale Extracted values of J from the fits to the strong-coupling model in the hole (**A**) and electron (**B**) regions of superconductivity compared with maximum T_c at each D from Fig. 3 of the main text. We see J and the T_c are correlated.

topological skyrmion textures in some pseudospin variable. Regardless of the actual mechanism, a strong-coupling BEC superconductor obtained by condensing charge $2e$ objects whose density is ν_{2e} and mass is M_{2e} is characterized by the critical temperature [121]

$$k_B T_c = \frac{\nu_{2e}\pi\hbar^2}{2A_M M_{2e}} = \frac{\nu_{2e} J}{2}, \tag{B.6}$$

Here, we take the filling fraction of the charge $2e$ objects ν_{2e} to be equal to half the filling fraction measured relative to half-filling $\nu = \pm 2$. A_M denotes the area of the moiré unit cell and J is an effective pairing scale. We can use this formula to extract J from our data by fitting $T_c(\nu)$ near its maximum, where we expect this formula to apply. Fig. SB.11 Shows examples of these fits in the electron and hole superconducting domes superimposed onto the dome resistivty. Since the superconductivity appears only in the flavour symmetry broken regions where $n_H - \nu = 2$, where the relevant carrier filling fraction is related to $\nu = \pm 2$, we constrain the fits so that $T_c(\nu = \pm 2) = 0$. The resulting fits agree reasonably well with our data and correspond to values of J between 2.5 and 3.5 meV on the hole side and 0.6 and 1.2 meV on the electron side. This is roughly of the same order as the coupling scale predicted theoretically [90]. Moreover, as shown in Fig. SB.12, we find that

J is correlated with the maximum T_c at a given D as we would expect if J is a measure of the pairing strength. We note that based on our extracted values of J we calculate $M_{2e} \sim m_e$ for the hole superconductivity and $M_{2e} \sim 3m_e - 5m_e$ for the electron superconductivity.

The presence of dispersive Dirac band may affect the interaction between electrons in the flat band. Considering, small density of state of the Dirac electrons, this screening effect can be small. If we take a bandwidth of flat band 20 meV, as shown in Fig. 1c, and count all the states in this window, the ratio of Dirac electrons to flat band electrons is only $\sim$ 3%. We estimate the effective dielectric constant increases by around 3.5 using the method presented in Ref. [168]. It is also noted that Dirac electrons could aid Cooper pairing in the flat band [169,170,171]. Further detailed calculations and experiments are needed to check this possibility.

S9: Sample Temperature Calibration

The data shown in Fig. 2A insets and Fig. 3 was taken without heavy filtering of signal lines. By comparing the data taken before and after refined filtering, we found that the only effect is that the electronic temperature of the samples T_{real} without heavy filtering is higher than the RuO_2 thermometer reading T_{meas}. This noise induced heating is significant only below $\sim$ 1.4 K and does not have an effect above. This effect is experimentally visible in the resistance curves measured before and after filtering in Fig. SB.13. In order to get the real electron temperature, we compare the resistance as a function of measured temperature at the same ν and D before filtering, R_i, and after filtering, R_f. We can find the mapping from T_{meas} to T_{real} by finding where $R_f(T_{real}) = R_i(T_{meas})$. We have performed this calibration at several points, and find good agreement, as shown in Fig. SB.14A. After correcting for the higher electron temperature, we find good agreement between data taken before and after improving the filtering, as shown in Fig. SB.14B. We implement this temperature recalibration to the data taken in Fig. 2A insets and Fig. 3. The rest of the data involving temperature measurements is taken with improved filtering.

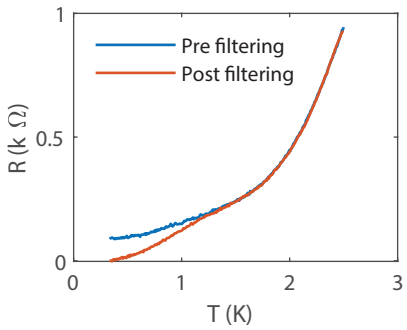

Figure B.13: Changes with reduced noise. Resistance curves taken before and after improving the electronics set up.

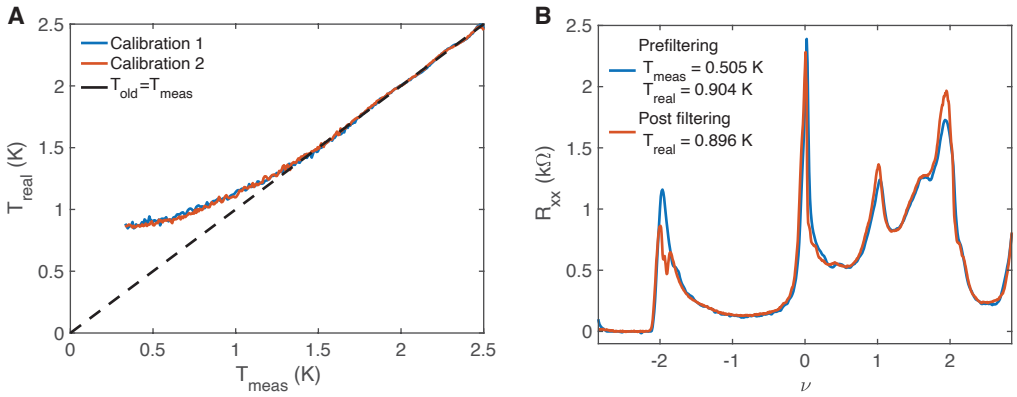

Figure B.14: Temperature Correction (**A**) Two different calculations of the real electron temperature compared to the measured temperature in old measurements with poor filtering. (**B**) After temperature correction we see good agreement between pre-filtering (blue) and post-filtering (red) data taken at the same electron temperature, T_{real}.

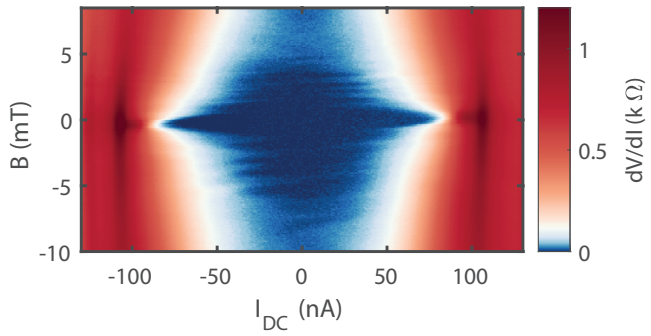

Figure B.15: Fraunhofer Interference. Fraunhofer-like interference pattern taken where the superconducting region borders the resistive state at $\nu = -2$, and $D/\varepsilon_0 = 0.2$ V/nm at 340 mK.

S10: Fraunhofer Pattern

With improved filtering, we see a clear Fraunhofer-like pattern at low temperature, as shown in Fig. SB.15. The Fraunhofer oscillations providing a clear indication of superconducting phase coherence and confirms the nature of the zero resistance state.

S11: Low Temperature Data

With improved filtering we are able to reach our actual base temperature of 340 mK, ans see an expanded region of superconductivity both near $\nu = -2$ and $\nu = 2$ as shown in Fig. SB.16A. Due to a limited gate range in the later measurements we are unable to cover the range of ν and D shown at higher temperature in the main text. However, we note that when comparing the region of superconductivity with the subtracted hall data in Fig. SB.16B, the boundaries of the superconductivity region aligns exactly with the region with $n_H - \nu = \pm 2$.

S12: Superconductivity in an additional sample

In addition to the device shown in the main text, we have observed signatures of superconductivity in a second TTG device, which has a twist angle of 1.39°. The device is encapsulated by both top

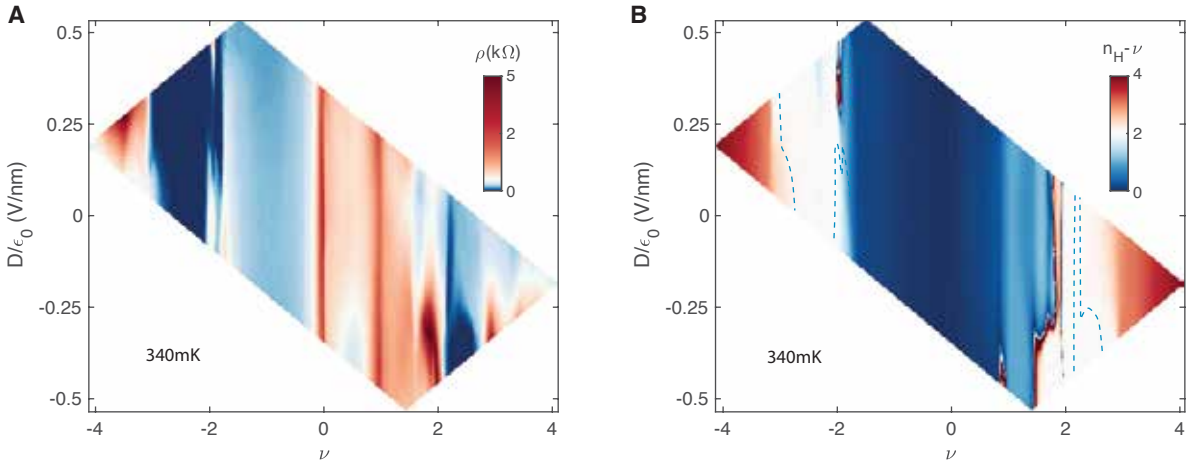

Figure B.16: Low temperature transport data. (A) Resistivity and **(B)** subtracted Hall data at the base temperature of 340 mK after improved filtering. The blue dashed line traces out the 0 resistance region.

and bottom graphite gates but the data shown here were taken with the top gate floating. Fig S17A shows resistance as a function of temperature at $\nu = 2.05$. The resistance drops quickly below 2 K and reaches 0 at 0.4 K. The inset shows an image of the device. Fig S17B shows the differential resistance and the $I - V$ characteristic at the same filling. They show the typical nonlinear $I - V$ behavior of a 2D superconductor. Furthermore, Fig S17C shows Fraunhofer pattern at $\nu = 2.05$, confirming the observed 0 resistance and nonlinear $I - V$ characteristic are a result of superconductivity.

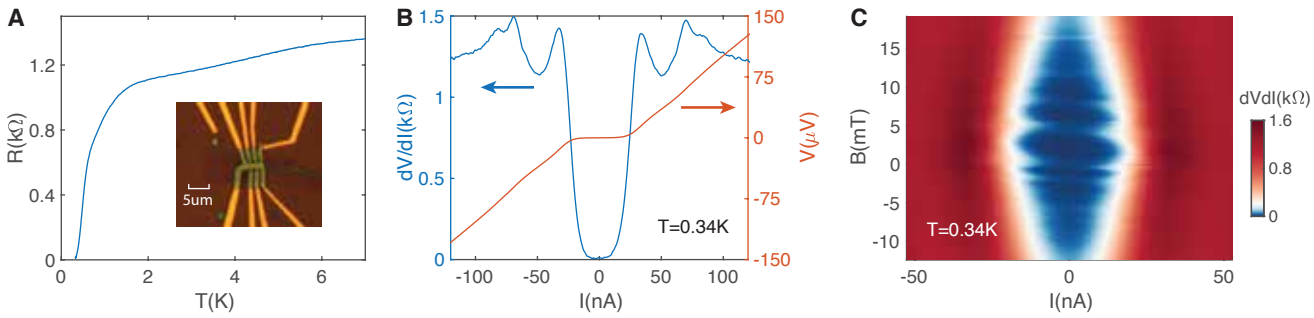

Figure B.17: Superconductivity in a second TTG device with twist angle $1.39°$**. (A)** Resistance versus temperature at $\nu = 2.05$. Inset, the device image. **(B)** dV/dI at $\nu = 2.05$ and the corresponding I-V characteristic. **(C)** Fraunhofer pattern at $\nu = 2.05$.

C

TTG JJ supplementary information

Like described before, we can use the fan diagrams in the magnetotransport measurements to extract twist angles. Fig. C.1a to C.1d show 4 fan diagrams measured using 4 pairs of voltage probes that are located near the top, mid-top, mid-bottom and bottom of the sample, as marked by the green, orange, pink and purple solid circles in Fig. C.1e, giving a twist angle of 1.5°, 1.45°, 1.39°and 1.31°, respectively. This shows that the sample is relatively inhomogeneous, which explains why we see TTG-NbN JJ in only one of the NbN contacts, and more than one critical currents in the superconducting states.

Fig. C.2 shows two measurement configurations used for the data shown in the main text, both of which focus on the same top-right TTG-NbN junction, but use different current source probes and voltage probes. The measurement configuration 1 shown in Fig. C.2a is used for data shown Fig. 1 and Fig. 2 and the measurement configuration 2 shown in Fig. C.2b for the Fraunhofer pat-

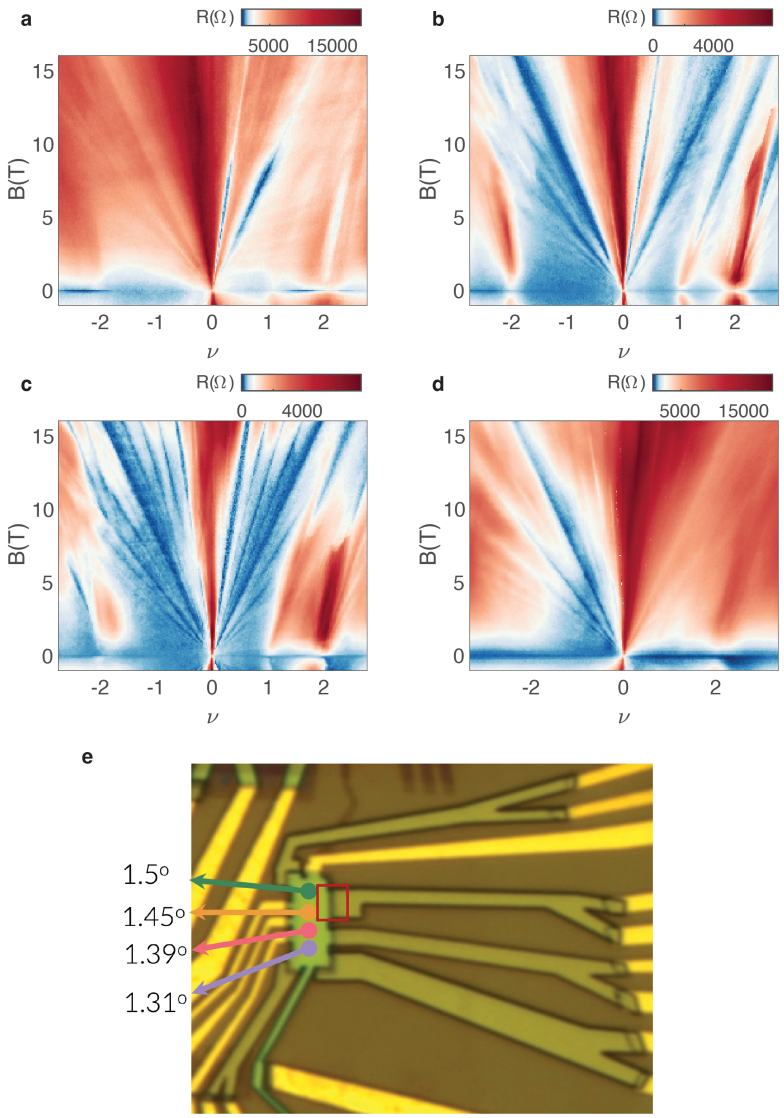

Figure C.1: a-d, fan diagrams measured using the voltage probes located close to the green, orange, pink and purple circles in **e**, respectively. **e,** the 4 circles mark where the fan diagrams are measured and the corresponding twist angle extracted from the fan diagrams.

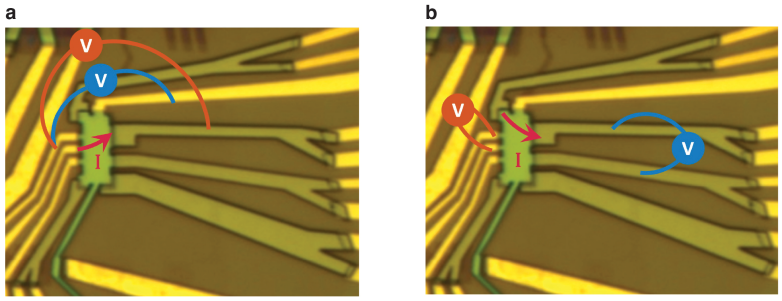

Figure C.2: a, measurement configuration 1, with the red arrow denoting the current bias path, blue voltage probes measuring the TTG sample bulk resistance and red voltage probes measuring the resistance across the TTG-NbN junction **b,** measurement configuration 2 with similar annotations.

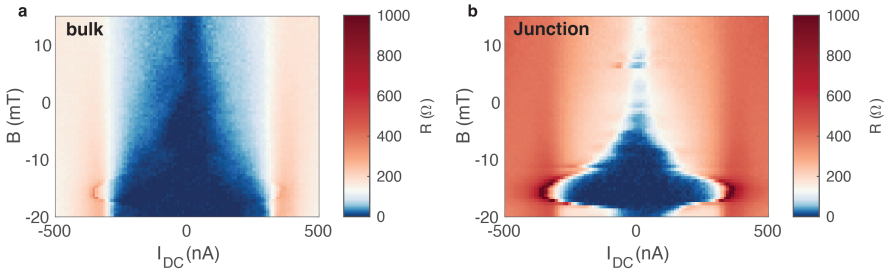

Figure C.3: Fraunhofer patterns measured at $\nu = -2.63$ using measurement configuration 1 for **a,** TTG bulk and **b,** the TTG-NbN junction, respectively.

terns in Fig. 3.

Fig. C.3 shows resistance measured using the measurement configuration 1 as a function of B and I_{DC} for the TTG bulk and TTG-NbN junction, displaying clearly different B dependence. While the sample bulk has a critical current monotonically decreasing as B increases, the junction resistance has a Fraunhofer pattern.

Fig. C.4 shows resistance measured at $\nu = -2.55$ using the measurement configuration 2, same as the main text Fig. 3a and 3b. Fig. C.4a and C.4b are obtained by sweeping magnetic field up from -30 mT and Fig. C.4c and C.4d are sweeping down from 30 mT. While the bulk resistance and its Fraunhofer pattern are unaffected by the sweeping direction, the interference pattern in the junction is drastically altered by the change of the sweeping direction. The junction pattern also

experience frequent discrete jumps after the field sweeps up (or down), after which it is as if the field was reduced (or enhanced) by certain amount, consistent with the effects of trapping or detrapping of vortices, which should contribute quantized magnetic flux.

Fig. C.5 shows similar comparisons of bulk and junction resistance using the measurement configuration 2 at $\nu = -2.2$ and $\nu = -3$, away from the optimal doping.

In order to see how the Fraunhofer pattern, or more specifically the periodicity of the pattern depends on doping, we measure the bulk and junction resistance as a function of B and ν at a finite current bias $I_{DC} = 90nA$, as shown Fig. C.6. The junction resistance shows a sharp horizontal resistive line at around 4 mT, corresponding to where the first period of the junction Fraunhofer pattern ends. The doping-independent period supports again that there is a JJ as long as the sample is superconducting and the Fraunhofer pattern in the junction is primarily dependent on the junction and sample geometry.

Finally, Fig. C.7 shows the image of a second TTG device where we focus on the top left corner junction. The junction also shows a Fraunhofer pattern that is unseen in the bulk measurement, as shown in the main text.

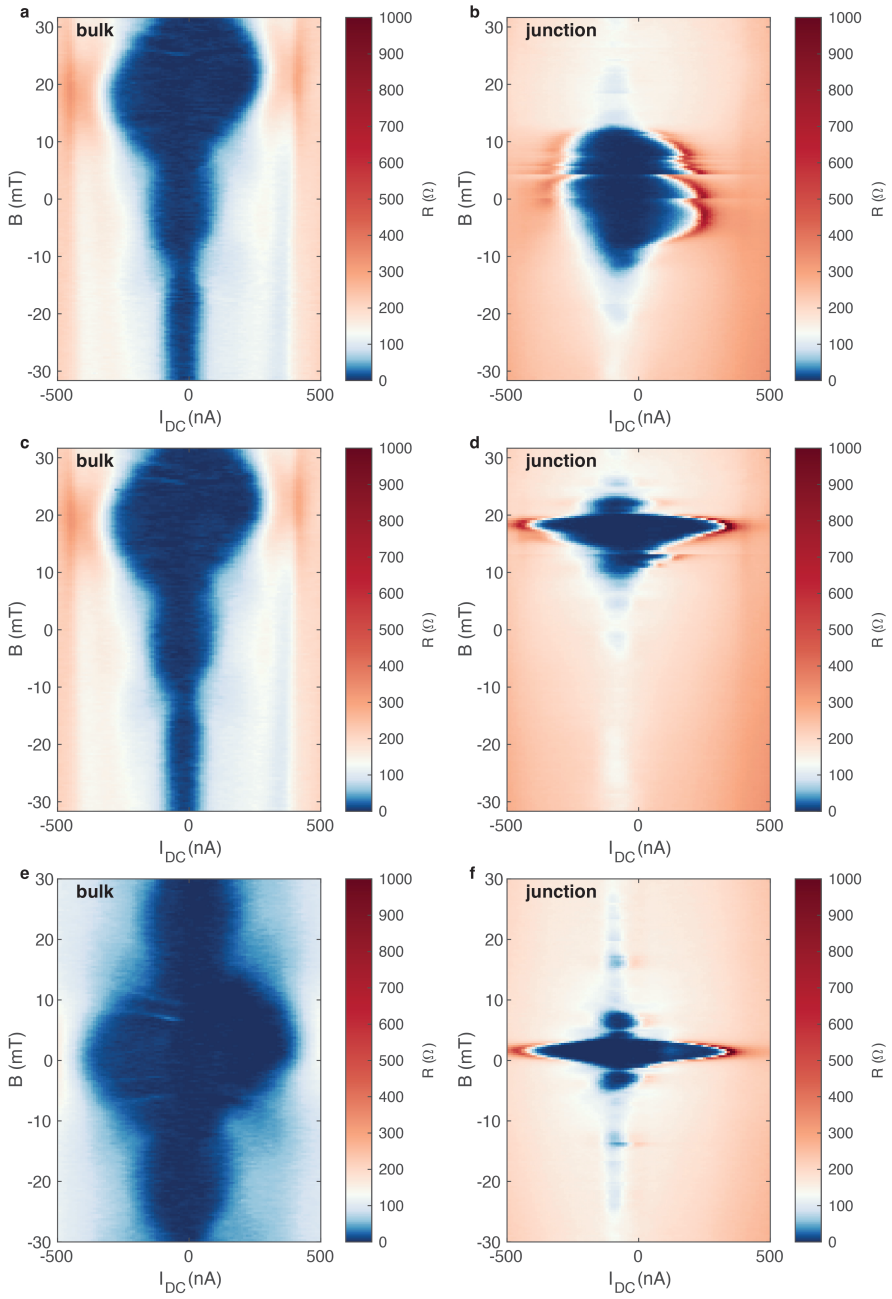

Figure C.4: Fraunhofer patterns measured at $\nu = -2.55$ using measurement configuration 2 by **a** and **b,** sweeping the magnetic field up from -30 mT to 30 mT, **c** and **d,** sweeping the magnetic field down from 30 mT to -30 mT, **e** and **f,** doing two separate zero-field cool-downs and sweeping the magnetic field from 0 to 30 mT and -30 mT, respectively, as described in the main text. The junction patterns in **b** and **d** suffer severely from jumps due to vortex trapping.

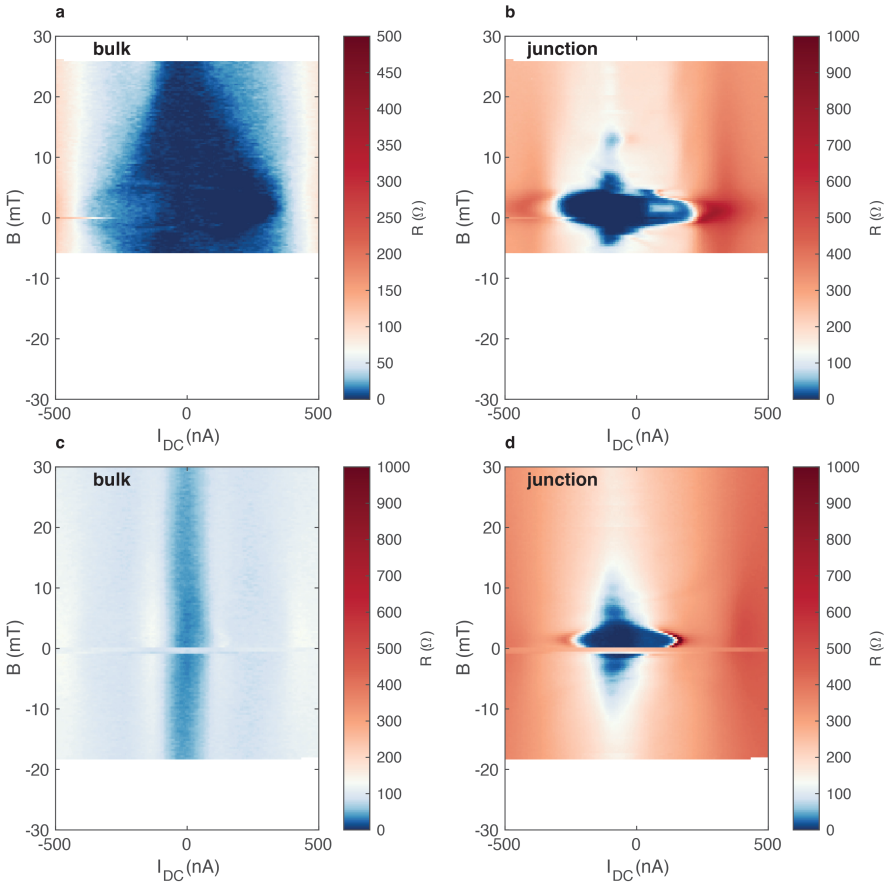

Figure C.5: Fraunhofer patterns measured using measurement configuration 2 at **a** and **b**, $\nu = -2.2$, **c** and **d**, $\nu = -3$.

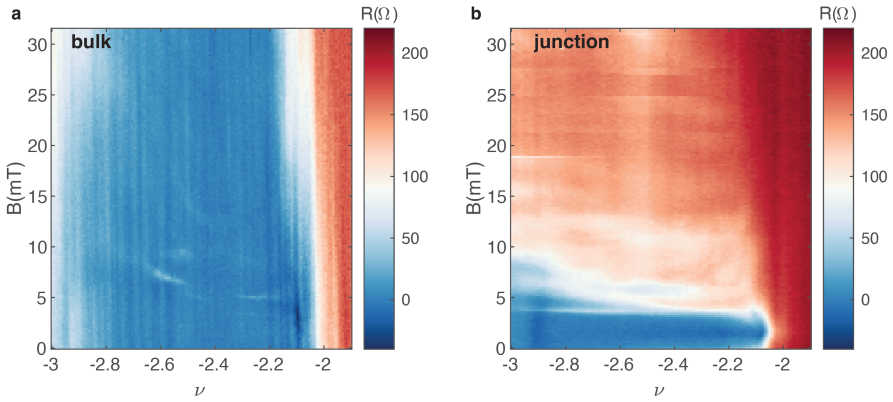

Figure C.6: Resistance for **a**, the TTG bulk and **b**, TTG-NbN junction measured at a finite current bias of 90 nA using measurement configuration 2.

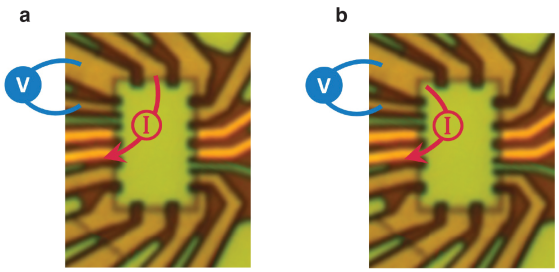

Figure C.7: Device image and measurement configurations for the second device. **a,** measurement configuration the TTG sample bulk resistance. **b,** measurement configuration the top left TTG-NbN junction resistance.

D

Double bilayer graphene supplementary information

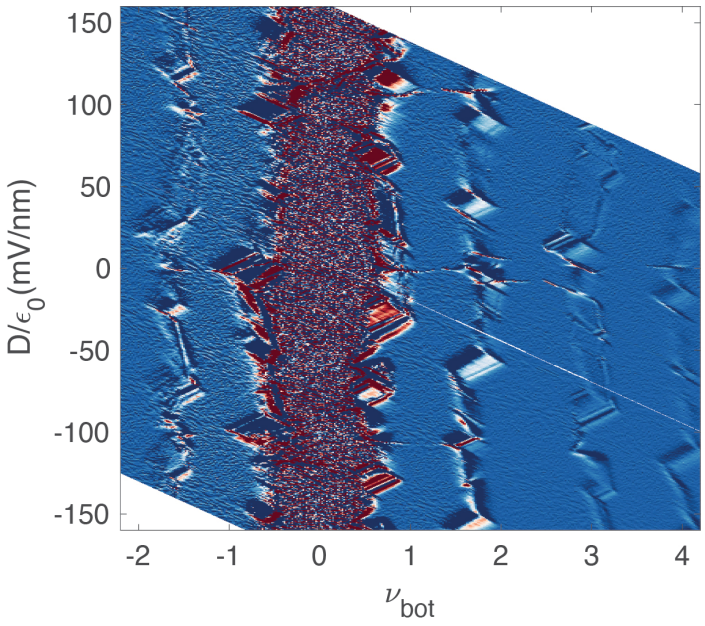

Figure D.1: Resistance derivative $dR_{xx}^{drive}/d\nu_{bot}$ corresponding to the data in Fig. 1d, which more prominently shows quantum Hall state and hierarchy transition features.

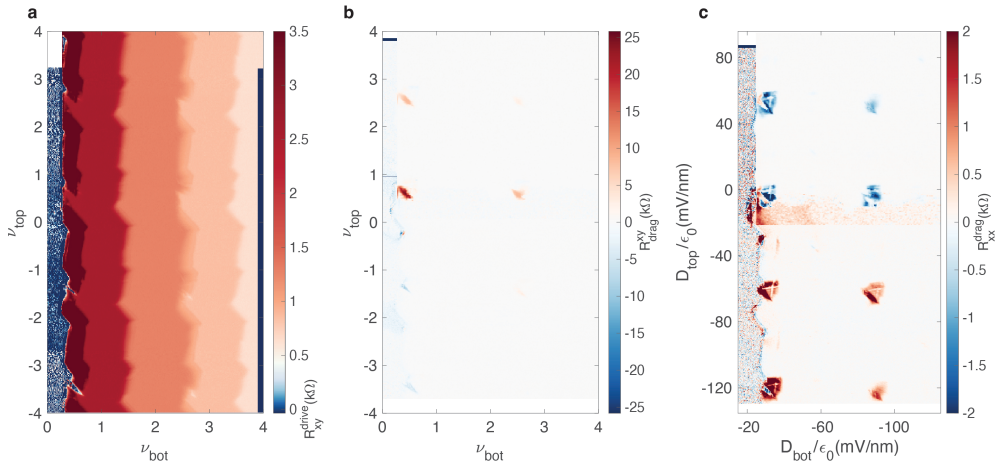

Figure D.2: Other resistance channels at $V_{int} = 0$. **a**, R_{xy}^{drive}, **b**, R_{xy}^{drag}, **c**,R_{xx}^{drag} plotted as a function of D_{top} and D_{bot}.

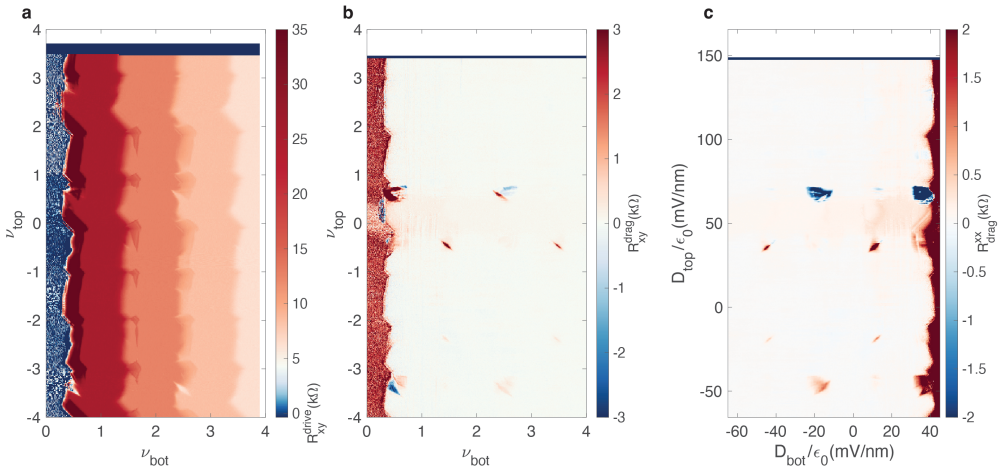

Figure D.3: Other resistance channels at $V_{int} = 0.07\ V$. **a,** R_{xy}^{drive}, **b,** R_{xy}^{drag}, **c,**R_{xx}^{drag} plotted as a function of D_{top} and D_{bot}.

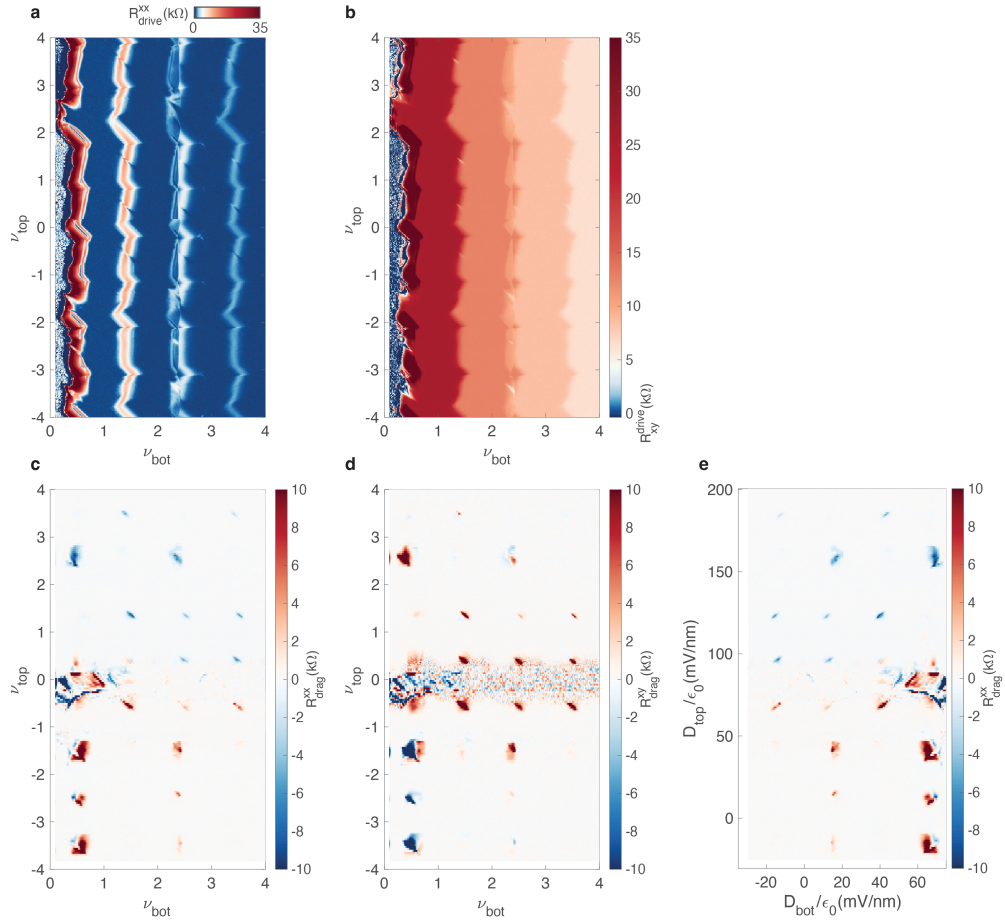

Figure D.4: All resistance channels at $V_{int} = 0.1\ V$. **a,** R_{xx}^{drive}, **b,** R_{xy}^{drive}, **c,** R_{xx}^{drag}, **d,** R_{xy}^{drag}, **e,** R_{xx}^{drag} plotted as a function of D_{top} and D_{bot}.

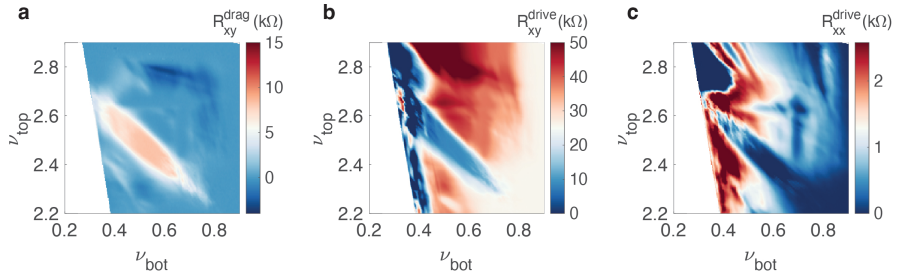

Figure D.5: Zoomed-in on the N = 0 interlayer states near $(\nu_{bot}, \nu_{top}) = (0.5, 2.5)$ at $V_{int} = 0$ and at 16 T. **a,** R_{xy}^{drag}, **b,** R_{xy}^{drive}, **c,** R_{xx}^{drive}.

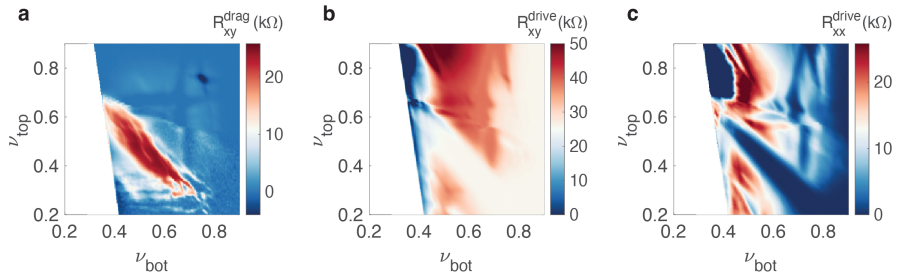

Figure D.6: Zoomed-in on the N = 0 interlayer states near $(\nu_{bot}, \nu_{top}) = (0.5, 0.5)$ at $V_{int} = 0$ and at 16 T. **a,** R_{xy}^{drag}, **b,** R_{xy}^{drive}, **c,** R_{xx}^{drive}.

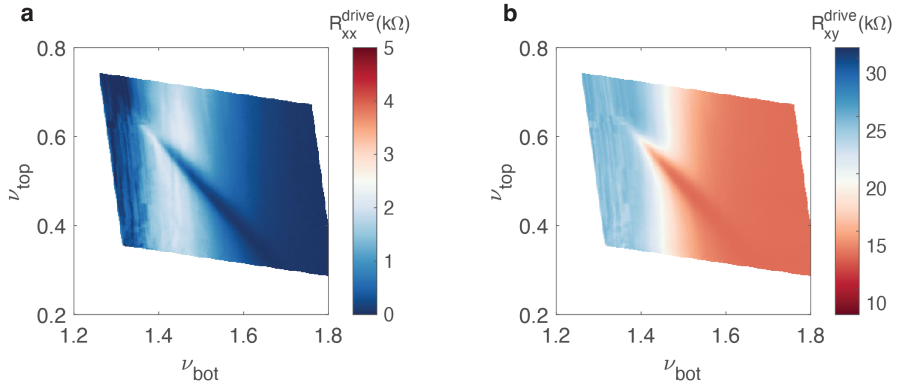

Figure D.7: Zoomed-in on the N = 1 interlayer states near $(\nu_{bot}, \nu_{top}) = (1.5, 0.5)$ at $V_{int} = 0$ and at 16 T. **a,** R_{xx}^{drive}, **b,** R_{xy}^{drive}.

References

[1] P. W. Anderson. More Is Different. *Science*, 177(4047):393–396, August 1972. Publisher: American Association for the Advancement of Science.

[2] Markus Greiner and Simon Fölling. Optical lattices. *Nature*, 453(7196):736–738, June 2008. Publisher: Nature Publishing Group.

[3] Sepehr Ebadi, Tout T. Wang, Harry Levine, Alexander Keesling, Giulia Semeghini, Ahmed Omran, Dolev Bluvstein, Rhine Samajdar, Hannes Pichler, Wen Wei Ho, Soonwon Choi, Subir Sachdev, Markus Greiner, Vladan Vuletić, and Mikhail D. Lukin. Quantum phases of matter on a 256-atom programmable quantum simulator. *Nature*, 595(7866):227–232, July 2021. Publisher: Nature Publishing Group.

[4] A. H. Castro Neto, F. Guinea, N. M. R. Peres, K. S. Novoselov, and A. K. Geim. The electronic properties of graphene. *Reviews of Modern Physics*, 81(1):109–162, January 2009.

[5] G. Catarina, B. Amorim, Eduardo V. Castro, J. M. Viana Parente Lopes, and N. M. R. Peres. Twisted bilayer graphene: low-energy physics, electronic and optical properties. *arXiv:1908.01556 [cond-mat]*, pages 177–231, June 2019. arXiv: 1908.01556.

[6] Jeil Jung and Allan H. MacDonald. Accurate tight-binding models for the π bands of bilayer graphene. *Phys. Rev. B*, 89:035405, Jan 2014.

[7] Rafi Bistritzer and Allan H. MacDonald. Moiré bands in twisted double-layer graphene. *Proceedings of the National Academy of Sciences*, 108(30):12233–12237, 2011.

[8] J. M. B. Lopes dos Santos, N. M. R. Peres, and A. H. Castro Neto. Graphene bilayer with a twist: Electronic structure. *Phys. Rev. Lett.*, 99:256802, Dec 2007.

[9] Stephen Carr, Shiang Fang, Ziyan Zhu, and Efthimios Kaxiras. Exact continuum model for low-energy electronic states of twisted bilayer graphene. *Phys. Rev. Res.*, 1:013001, Aug 2019.

[10] Eslam Khalaf, Alex J. Kruchkov, Grigory Tarnopolsky, and Ashvin Vishwanath. Magic angle hierarchy in twisted graphene multilayers. *Phys. Rev. B*, 100:085109, Aug 2019.

[11] Leon Balents. Lecture notes for physics 217b. 2018. https://spinsandelectrons.files.wordpress.com/2019/08/notes.pdf.

[12] Youngkuk Kim, Benjamin J. Wieder, C. L. Kane, and Andrew M. Rappe. Dirac line nodes in inversion-symmetric crystals. *Phys. Rev. Lett.*, 115:036806, Jul 2015.

[13] Hoi Chun Po, Liujun Zou, Ashvin Vishwanath, and T. Senthil. Origin of mott insulating behavior and superconductivity in twisted bilayer graphene. *Phys. Rev. X*, 8:031089, Sep 2018.

[14] Liujun Zou, Hoi Chun Po, Ashvin Vishwanath, and T. Senthil. Band structure of twisted bilayer graphene: Emergent symmetries, commensurate approximants, and wannier obstructions. *Phys. Rev. B*, 98:085435, Aug 2018.

[15] Grigory Tarnopolsky, Alex Jura Kruchkov, and Ashvin Vishwanath. Origin of magic angles in twisted bilayer graphene. *Phys. Rev. Lett.*, 122:106405, Mar 2019.

[16] Nick Bultinck, Eslam Khalaf, Shang Liu, Shubhayu Chatterjee, Ashvin Vishwanath, and Michael P. Zaletel. Ground state and hidden symmetry of magic-angle graphene at even integer filling. *Phys. Rev. X*, 10:031034, Aug 2020.

[17] Patrick J. Ledwith, Eslam Khalaf, and Ashvin Vishwanath. Strong coupling theory of magic-angle graphene: A pedagogical introduction. *Annals of Physics*, 435:168646, December 2021.

[18] K. Zou, X. Hong, and J. Zhu. Effective mass of electrons and holes in bilayer graphene: Electron-hole asymmetry and electron-electron interaction. *Phys. Rev. B*, 84:085408, Aug 2011.

[19] C. R. Dean, L. Wang, P. Maher, C. Forsythe, F. Ghahari, Y. Gao, J. Katoch, M. Ishigami, P. Moon, M. Koshino, T. Taniguchi, K. Watanabe, K. L. Shepard, J. Hone, and P. Kim. Hofstadter's butterfly and the fractal quantum Hall effect in moiré superlattices. *Nature*, 497(7451):598–602, May 2013.

[20] L. A. Ponomarenko, R. V. Gorbachev, G. L. Yu, D. C. Elias, R. Jalil, A. A. Patel, A. Mishchenko, A. S. Mayorov, C. R. Woods, J. R. Wallbank, M. Mucha-Kruczynski, B. A. Piot, M. Potemski, I. V. Grigorieva, K. S. Novoselov, F. Guinea, V. I. Fal'ko, and A. K. Geim. Cloning of Dirac fermions in graphene superlattices. *Nature*, 497(7451):594–597, May 2013.

[21] B. Hunt, J. D. Sanchez-Yamagishi, A. F. Young, M. Yankowitz, B. J. LeRoy, K. Watanabe, T. Taniguchi, P. Moon, M. Koshino, P. Jarillo-Herrero, and R. C. Ashoori. Massive Dirac Fermions and Hofstadter Butterfly in a van der Waals Heterostructure. *Science*, 340(6139):1427–1430, June 2013.

[22] Yuan Cao, Valla Fatemi, Ahmet Demir, Shiang Fang, Spencer L. Tomarken, Jason Y. Luo, Javier D. Sanchez-Yamagishi, Kenji Watanabe, Takashi Taniguchi, Efthimios Kaxiras, Ray C. Ashoori, and Pablo Jarillo-Herrero. Correlated insulator behaviour at half-filling in magic-angle graphene superlattices. *Nature*, 556(7699):80–84, March 2018.

[23] Yuan Cao, Valla Fatemi, Shiang Fang, Kenji Watanabe, Takashi Taniguchi, Efthimios Kaxiras, and Pablo Jarillo-Herrero. Unconventional superconductivity in magic-angle graphene superlattices. *Nature*, 556(7699):43–50, March 2018.

[24] Matthew Yankowitz, Shaowen Chen, Hryhoriy Polshyn, Yuxuan Zhang, K. Watanabe, T. Taniguchi, David Graf, Andrea F. Young, and Cory R. Dean. Tuning superconductivity in twisted bilayer graphene. *Science*, 363(6431):1059–1064, March 2019.

[25] Aaron L Sharpe, Eli J Fox, Arthur W Barnard, Joe Finney, Kenji Watanabe, Takashi Taniguchi, M A Kastner, and David Goldhaber-Gordon. Emergent ferromagnetism near three-quarters filling in twisted bilayer graphene. *Science*, 365(6453):605–608, 2019.

[26] M. Serlin, C. L. Tschirhart, H. Polshyn, Y. Zhang, J. Zhu, K. Watanabe, T. Taniguchi, L. Balents, and A. F. Young. Intrinsic quantized anomalous Hall effect in a moiré heterostructure. *Science*, 367(6480):900–903, dec 2020.

[27] Guorui Chen, Lili Jiang, Shuang Wu, Bosai Lyu, Hongyuan Li, Bheema Lingam Chittari, Kenji Watanabe, Takashi Taniguchi, Zhiwen Shi, Jeil Jung, Yuanbo Zhang, and Feng Wang. Evidence of a gate-tunable Mott insulator in a trilayer graphene moiré superlattice. *Nat. Phys.*, 15(3):237–241, March 2019.

[28] Lei Wang, En-Min Shih, Augusto Ghiotto, Lede Xian, Daniel A. Rhodes, Cheng Tan, Martin Claassen, Dante M. Kennes, Yusong Bai, Bumho Kim, Kenji Watanabe, Takashi Taniguchi, Xiaoyang Zhu, James Hone, Angel Rubio, Abhay N. Pasupathy, and Cory R. Dean. Correlated electronic phases in twisted bilayer transition metal dichalcogenides. *Nature Materials*, 19(8):861–866, August 2020. Publisher: Nature Publishing Group.

[29] Emma C. Regan, Danqing Wang, Chenhao Jin, M. Iqbal Bakti Utama, Beini Gao, Xin Wei, Sihan Zhao, Wenyu Zhao, Zuocheng Zhang, Kentaro Yumigeta, Mark Blei, Johan D. Carlström, Kenji Watanabe, Takashi Taniguchi, Sefaattin Tongay, Michael Crommie, Alex Zettl, and Feng Wang. Mott and generalized Wigner crystal states in WSe_2 /WS_2 moiré superlattices. *Nature*, 579(7799):359–363, March 2020.

[30] R. Bistritzer and A. H. MacDonald. Moire bands in twisted double-layer graphene. *Proc. Natl. Acad. Sci.*, 108(30):12233–12237, July 2011.

[31] B. Keimer, S. A. Kivelson, M. R. Norman, S. Uchida, and J. Zaanen. From quantum matter to high-temperature superconductivity in copper oxides. *Nature*, 518(7538):179–186, February 2015.

[32] Mikito Koshino, Noah F. Q. Yuan, Takashi Koretsune, Masayuki Ochi, Kazuhiko Kuroki, and Liang Fu. Maximally Localized Wannier Orbitals and the Extended Hubbard Model for Twisted Bilayer Graphene. *Phys. Rev. X*, 8(3):031087, September 2018.

[33] Jian Kang and Oskar Vafek. Symmetry, Maximally Localized Wannier States, and a Low-Energy Model for Twisted Bilayer Graphene Narrow Bands. *Phys. Rev. X*, 8(3):031088, September 2018.

[34] Hoi Chun Po, Liujun Zou, Ashvin Vishwanath, and T. Senthil. Origin of Mott Insulating Behavior and Superconductivity in Twisted Bilayer Graphene. *Phys. Rev. X*, 8(3):031089, September 2018.

[35] Petr Stepanov, Ipsita Das, Xiaobo Lu, Ali Fahimniya, Kenji Watanabe, Takashi Taniguchi, Frank H. L. Koppens, Johannes Lischner, Leonid Levitov, and Dmitri K. Efetov. Untying the insulating and superconducting orders in magic-angle graphene. *Nature*, 583(7816):375–378, July 2020. Publisher: Nature Publishing Group.

[36] Yu Saito, Jingyuan Ge, Kenji Watanabe, Takashi Taniguchi, and Andrea F. Young. Independent superconductors and correlated insulators in twisted bilayer graphene. *Nature Physics*, 16(9):926–930, September 2020. Publisher: Nature Publishing Group.

[37] Harpreet Singh Arora, Robert Polski, Yiran Zhang, Alex Thomson, Youngjoon Choi, Hyunjin Kim, Zhong Lin, Ilham Zaky Wilson, Xiaodong Xu, Jiun-Haw Chu, Kenji Watanabe, Takashi Taniguchi, Jason Alicea, and Stevan Nadj-Perge. Superconductivity in metallic twisted bilayer graphene stabilized by wse2. *Nature*, 583(7816):379–384, Jul 2020.

[38] Edward McCann and Mikito Koshino. The electronic properties of bilayer graphene. *Rep. Prog. Phys.*, 76(5):056503, May 2013.

[39] Yuanbo Zhang, Tsung-Ta Tang, Caglar Girit, Zhao Hao, Michael C. Martin, Alex Zettl, Michael F. Crommie, Y. Ron Shen, and Feng Wang. Direct observation of a widely tunable bandgap in bilayer graphene. *Nature*, 459(7248):820–823, June 2009.

[40] Jong Yeon Lee, Eslam Khalaf, Shang Liu, Xiaomeng Liu, Zeyu Hao, Philip Kim, and Ashvin Vishwanath. Theory of correlated insulating behaviour and spin-triplet superconductivity in twisted double bilayer graphene. *Nature Communications*, 10(1):1–10, dec 2019.

[41] Ya-Hui Zhang, Dan Mao, Yuan Cao, Pablo Jarillo-Herrero, and T. Senthil. Nearly flat Chern bands in moiré superlattices. *Phys. Rev. B*, 99(7):075127, February 2019.

[42] Mikito Koshino. Band structure and topological properties of twisted double bilayer graphene. *Physical Review B*, 99(23):235406, jun 2019.

[43] Narasimha Raju Chebrolu, Bheema Lingam Chittari, and Jeil Jung. Flat bands in twisted double bilayer graphene. *Phys. Rev. B*, 99:235417, Jun 2019.

[44] Young Woo Choi and Hyoung Joon Choi. Intrinsic band gap and electrically tunable flat bands in twisted double bilayer graphene. *Phys. Rev. B*, 100:201402, Nov 2019.

[45] Y. Cao, J. Y. Luo, V. Fatemi, S. Fang, J. D. Sanchez-Yamagishi, K. Watanabe, T. Taniguchi, E. Kaxiras, and P. Jarillo-Herrero. Superlattice-Induced Insulating States and Valley-Protected Orbits in Twisted Bilayer Graphene. *Phys. Rev. Lett.*, 117(11):116804, September 2016.

[46] Kyounghwan Kim, Matthew Yankowitz, Babak Fallahazad, Sangwoo Kang, Hema C. P. Movva, Shengqiang Huang, Stefano Larentis, Chris M. Corbet, Takashi Taniguchi, Kenji Watanabe, Sanjay K. Banerjee, Brian J. LeRoy, and Emanuel Tutuc. van der Waals Heterostructures with High Accuracy Rotational Alignment. *Nano Lett.*, 16(3):1989–1995, March 2016.

[47] J. Li, L. Z. Tan, K. Zou, A. A. Stabile, D. J. Seiwell, K. Watanabe, T. Taniguchi, Steven G. Louie, and J. Zhu. Effective mass in bilayer graphene at low carrier densities: The role of potential disorder and electron-electron interaction. *Phys. Rev. B*, 94(16):161406, October 2016.

[48] Minhao He, Yuhao Li, Jiaqi Cai, Yang Liu, K. Watanabe, T. Taniguchi, Xiaodong Xu, and Matthew Yankowitz. Symmetry breaking in twisted double bilayer graphene. *Nature Physics*, pages 1–5, September 2020. Publisher: Nature Publishing Group.

[49] Cheng Shen, Yanbang Chu, QuanSheng Wu, Na Li, Shuopei Wang, Yanchong Zhao, Jian Tang, Jieying Liu, Jinpeng Tian, Kenji Watanabe, Takashi Taniguchi, Rong Yang, Zi Yang Meng, Dongxia Shi, Oleg V. Yazyev, and Guangyu Zhang. Correlated states in twisted double bilayer graphene. *Nature Physics*, 16(5):520–525, May 2020. Publisher: Nature Publishing Group.

[50] Yuan Cao, Daniel Rodan-Legrain, Oriol Rubies-Bigorda, Jeong Min Park, Kenji Watanabe, Takashi Taniguchi, and Pablo Jarillo-Herrero. Tunable correlated states and spin-polarized phases in twisted bilayer–bilayer graphene. *Nature*, 583(7815):215–220, July 2020. Publisher: Nature Publishing Group.

[51] G. William Burg, Jihang Zhu, Takashi Taniguchi, Kenji Watanabe, Allan H. MacDonald, and Emanuel Tutuc. Correlated Insulating States in Twisted Double Bilayer Graphene. *Physical Review Letters*, 123(19):197702, November 2019. Publisher: American Physical Society.

[52] Rafi Bistritzer and Allan H. MacDonald. Moiré bands in twisted double-layer graphene. *Proc. Natl. Acad. Sci.*, 108(30):12233–12237, 2011.

[53] J. M. B. Lopes dos Santos, N. M. R. Peres, and A. H. Castro Neto. Graphene bilayer with a twist: Electronic structure. *Phys. Rev. Lett.*, 99:256802, Dec 2007.

[54] S. Shallcross, S. Sharma, E. Kandelaki, and O. A. Pankratov. Electronic structure of turbostratic graphene. *Phys. Rev. B*, 81:165105, Apr 2010.

[55] E. Suárez Morell, J. D. Correa, P. Vargas, M. Pacheco, and Z. Barticevic. Flat bands in slightly twisted bilayer graphene: Tight-binding calculations. *Phys. Rev. B*, 82:121407, Sep 2010.

[56] Yuan Cao, Valla Fatemi, Shiang Fang, Kenji Watanabe, Takashi Taniguchi, Efthimios Kaxiras, and Pablo Jarillo-Herrero. Unconventional superconductivity in magic-angle graphene superlattices. *Nature*, 556(7699):43–50, Apr 2018.

[57] Yu Saito, Fangyuan Yang, Jingyuan Ge, Xiaoxue Liu, Kenji Watanabe, Takashi Taniguchi, J. I. A. Li, Erez Berg, and Andrea F. Young. Isospin pomeranchuk effect and the entropy of collective excitations in twisted bilayer graphene, 2020.

[58] Aaron L. Sharpe, Eli J. Fox, Arthur W. Barnard, Joe Finney, Kenji Watanabe, Takashi Taniguchi, M. A. Kastner, and David Goldhaber-Gordon. Emergent ferromagnetism near three-quarters filling in twisted bilayer graphene. *Science*, 365(6453):605–608, 2019.

[59] Xiaobo Lu, Petr Stepanov, Wei Yang, Ming Xie, Mohammed Ali Aamir, Ipsita Das, Carles Urgell, Kenji Watanabe, Takashi Taniguchi, Guangyu Zhang, Adrian Bachtold, Allan H. MacDonald, and Dmitri K. Efetov. Superconductors, orbital magnets and correlated states in magic-angle bilayer graphene. *Nature*, 574(7780):653–657, Oct 2019.

[60] M. Serlin, C. L. Tschirhart, H. Polshyn, Y. Zhang, J. Zhu, K. Watanabe, T. Taniguchi, L. Balents, and A. F. Young. Intrinsic quantized anomalous hall effect in a moiré heterostructure. *Science*, 367(6480):900–903, 2020.

[61] Shuang Wu, Zhenyuan Zhang, K. Watanabe, T. Taniguchi, and Eva Y. Andrei. Chern insulators and topological flat-bands in magic-angle twisted bilayer graphene, 2020.

[62] Kevin P. Nuckolls, Myungchul Oh, Dillon Wong, Biao Lian, Kenji Watanabe, Takashi Taniguchi, B. Andrei Bernevig, and Ali Yazdani. Strongly Correlated Chern Insulators in Magic-Angle Twisted Bilayer Graphene. *arXiv:2007.03810 [cond-mat]*, July 2020. arXiv: 2007.03810.

[63] Yu Saito, Jingyuan Ge, Louk Rademaker, Kenji Watanabe, Takashi Taniguchi, Dmitry A. Abanin, and Andrea F. Young. Hofstadter subband ferromagnetism and symmetry broken chern insulators in twisted bilayer graphene, 2020.

[64] Petr Stepanov, Ipsita Das, Xiaobo Lu, Ali Fahimniya, Kenji Watanabe, Takashi Taniguchi, Frank H. L. Koppens, Johannes Lischner, Leonid Levitov, and Dmitri K. Efetov. Untying the insulating and superconducting orders in magic-angle graphene. *Nature*, 583(7816):375–378, Jul 2020.

[65] Yu Saito, Jingyuan Ge, Kenji Watanabe, Takashi Taniguchi, and Andrea F. Young. Independent superconductors and correlated insulators in twisted bilayer graphene. *Nat. Phys.*, 16(9):926–930, Sep 2020.

[66] Xiaoxue Liu, Zhi Wang, K. Watanabe, T. Taniguchi, Oskar Vafek, and J. I. A. Li. Tuning electron correlation in magic-angle twisted bilayer graphene using coulomb screening, 2020.

[67] Yuan Cao, Daniel Rodan-Legrain, Jeong Min Park, Fanqi Noah Yuan, Kenji Watanabe, Takashi Taniguchi, Rafael M. Fernandes, Liang Fu, and Pablo Jarillo-Herrero. Nematicity and competing orders in superconducting magic-angle graphene, 2020.

[68] Jeong Min Park, Yuan Cao, Kenji Watanabe, Takashi Taniguchi, and Pablo Jarillo-Herrero. Flavour hund's coupling, correlated chern gaps, and diffusivity in moiré flat bands, 2020.

[69] H. Polshyn, J. Zhu, M. A. Kumar, Y. Zhang, F. Yang, C. L. Tschirhart, M. Serlin, K. Watanabe, T. Taniguchi, A. H. MacDonald, and A. F. Young. Electrical switching of magnetic order in an orbital chern insulator. *Nature*, Nov 2020.

[70] Shaowen Chen, Minhao He, Ya-Hui Zhang, Valerie Hsieh, Zaiyao Fei, K. Watanabe, T. Taniguchi, David H. Cobden, Xiaodong Xu, Cory R. Dean, and Matthew Yankowitz. Electrically tunable correlated and topological states in twisted monolayer–bilayer graphene. *Nat. Phys.*, Oct 2020.

[71] Emma C. Regan, Danqing Wang, Chenhao Jin, M. Iqbal Bakti Utama, Beini Gao, Xin Wei, Sihan Zhao, Wenyu Zhao, Zuocheng Zhang, Kentaro Yumigeta, Mark Blei, Johan D. Carlström, Kenji Watanabe, Takashi Taniguchi, Sefaattin Tongay, Michael Crommie, Alex Zettl, and Feng Wang. Mott and generalized wigner crystal states in wse2/ws2 moiré superlattices. *Nature*, 579(7799):359–363, Mar 2020.

[72] Yang Xu, Song Liu, Daniel A. Rhodes, Kenji Watanabe, Takashi Taniguchi, James Hone, Veit Elser, Kin Fai Mak, and Jie Shan. Correlated insulating states at fractional fillings of moiré superlattices. *Nature*, 587(7833):214–218, November 2020.

[73] Matthew Yankowitz, Shaowen Chen, Hryhoriy Polshyn, Yuxuan Zhang, K. Watanabe, T. Taniguchi, David Graf, Andrea F. Young, and Cory R. Dean. Tuning superconductivity in twisted bilayer graphene. *Science*, 363(6431):1059–1064, 2019.

[74] Guorui Chen, Aaron L. Sharpe, Patrick Gallagher, Ilan T. Rosen, Eli J. Fox, Lili Jiang, Bosai Lyu, Hongyuan Li, Kenji Watanabe, Takashi Taniguchi, Jeil Jung, Zhiwen Shi, David Goldhaber-Gordon, Yuanbo Zhang, and Feng Wang. Signatures of tunable superconductivity in a trilayer graphene moiré superlattice. *Nature*, 572(7768):215–219, Aug 2019.

[75] Xiaomeng Liu, Zeyu Hao, Eslam Khalaf, Jong Yeon Lee, Yuval Ronen, Hyobin Yoo, Danial Haei Najafabadi, Kenji Watanabe, Takashi Taniguchi, Ashvin Vishwanath, and Philip Kim. Tunable spin-polarized correlated states in twisted double bilayer graphene. *Nature*, 583(7815):221–225, Jul 2020.

[76] Liheng An, Xiangbin Cai, Ding Pei, Meizhen Huang, Zefei Wu, Zishu Zhou, Jiangxiazi Lin, Zhehan Ying, Ziqing Ye, Xuemeng Feng, Ruiyan Gao, Cephise Cacho, Matthew Watson, Yulin Chen, and Ning Wang. Interaction effects and superconductivity signatures in twisted double-bilayer wse2. *Nanoscale Horiz.*, 5:1309–1316, 2020.

[77] Leon Balents, Cory R. Dean, Dmitri K. Efetov, and Andrea F. Young. Superconductivity and strong correlations in moiré flat bands. *Nat. Phys.*, 16(7):725–733, Jul 2020.

[78] Eslam Khalaf, Alex J. Kruchkov, Grigory Tarnopolsky, and Ashvin Vishwanath. Magic angle hierarchy in twisted graphene multilayers. *Phys. Rev. B*, 100:085109, Aug 2019.

[79] Kan-Ting Tsai, Xi Zhang, Ziyan Zhu, Yujie Luo, Stephen Carr, Mitchell Luskin, Efthimios Kaxiras, and Ke Wang. Correlated insulating states and transport signature of superconductivity in twisted trilayer graphene moiré of moiré superlattices, 2020.

[80] Y. Cao, J. Y. Luo, V. Fatemi, S. Fang, J. D. Sanchez-Yamagishi, K. Watanabe, T. Taniguchi, E. Kaxiras, and P. Jarillo-Herrero. Superlattice-induced insulating states and valley-protected orbits in twisted bilayer graphene. *Phys. Rev. Lett.*, 117:116804, Sep 2016.

[81] Stephen Carr, Chenyuan Li, Ziyan Zhu, Efthimios Kaxiras, Subir Sachdev, and Alexander Kruchkov. Ultraheavy and ultrarelativistic dirac quasiparticles in sandwiched graphenes. *Nano Letters*, 20(5):3030–3038, May 2020.

[82] E. A. Henriksen, D. Nandi, and J. P. Eisenstein. Quantum hall effect and semimetallic behavior of dual-gated aba-stacked trilayer graphene. *Phys. Rev. X*, 2:011004, Jan 2012.

[83] Michael Tinkham. *Introduction to Superconductivity*. Courier Corporation, 1996.

[84] Alejandro Lopez-Bezanilla and J. L. Lado. Electrical band flattening, valley flux, and superconductivity in twisted trilayer graphene. *Phys. Rev. Research*, 2:033357, Sep 2020.

[85] Dillon Wong, Kevin P. Nuckolls, Myungchul Oh, Biao Lian, Yonglong Xie, Sangjun Jeon, Kenji Watanabe, Takashi Taniguchi, B. Andrei Bernevig, and Ali Yazdani. Cascade of electronic transitions in magic-angle twisted bilayer graphene. *Nature*, 582(7811):198–202, Jun 2020.

[86] U. Zondiner, A. Rozen, D. Rodan-Legrain, Y. Cao, R. Queiroz, T. Taniguchi, K. Watanabe, Y. Oreg, F. von Oppen, Ady Stern, E. Berg, P. Jarillo-Herrero, and S. Ilani. Cascade of phase transitions and dirac revivals in magic-angle graphene. *Nature*, 582(7811):203–208, Jun 2020.

[87] J. Bardeen, L. N. Cooper, and J. R. Schrieffer. Theory of superconductivity. *Phys. Rev.*, 108:1175–1204, Dec 1957.

[88] Masayuki Ochi, Mikito Koshino, and Kazuhiko Kuroki. Possible correlated insulating states in magic-angle twisted bilayer graphene under strongly competing interactions. *Phys. Rev. B*, 98:081102, Aug 2018.

[89] Nick Bultinck, Eslam Khalaf, Shang Liu, Shubhayu Chatterjee, Ashvin Vishwanath, and Michael P. Zaletel. Ground state and hidden symmetry of magic-angle graphene at even integer filling. *Phys. Rev. X*, 10:031034, Aug 2020.

[90] Eslam Khalaf, Shubhayu Chatterjee, Nick Bultinck, Michael P. Zaletel, and Ashvin Vishwanath. Charged skyrmions and topological origin of superconductivity in magic angle graphene, 2020.

[91] Eslam Khalaf, Alex J. Kruchkov, Grigory Tarnopolsky, and Ashvin Vishwanath. Magic angle hierarchy in twisted graphene multilayers. *Phys. Rev. B*, 100:085109, Aug 2019.

[92] Zeyu Hao, A. M. Zimmerman, Patrick Ledwith, Eslam Khalaf, Danial Haie Najafabadi, Kenji Watanabe, Takashi Taniguchi, Ashvin Vishwanath, and Philip Kim. Electric field–tunable superconductivity in alternating-twist magic-angle trilayer graphene. *Science*, 371(6534):1133–1138, 2021.

[93] Jeong Min Park, Yuan Cao, Kenji Watanabe, Takashi Taniguchi, and Pablo Jarillo-Herrero. Tunable strongly coupled superconductivity in magic-angle twisted trilayer graphene. *Nature*, 590(7845):249–255, February 2021.

[94] Jeong Min Park, Yuan Cao, Li-Qiao Xia, Shuwen Sun, Kenji Watanabe, Takashi Taniguchi, and Pablo Jarillo-Herrero. Robust superconductivity in magic-angle multilayer graphene family. *Nature Materials*, 21(8):877–883, August 2022.

[95] Yiran Zhang, Robert Polski, Cyprian Lewandowski, Alex Thomson, Yang Peng, Youngjoon Choi, Hyunjin Kim, Kenji Watanabe, Takashi Taniguchi, Jason Alicea, Felix von Oppen, Gil Refael, and Stevan Nadj-Perge. Promotion of superconductivity in magic-angle graphene multilayers. *Science*, 377(6614):1538–1543, September 2022.

[96] G. William Burg, Eslam Khalaf, Yimeng Wang, Kenji Watanabe, Takashi Taniguchi, and Emanuel Tutuc. Emergence of correlations in alternating twist quadrilayer graphene. *Nature Materials*, 21(8):884–889, August 2022.

[97] Haoxin Zhou, Tian Xie, Takashi Taniguchi, Kenji Watanabe, and Andrea F. Young. Superconductivity in rhombohedral trilayer graphene. *arXiv:2106.07640 [cond-mat]*, June 2021.

[98] Haoxin Zhou, Ludwig Holleis, Yu Saito, Liam Cohen, William Huynh, Caitlin L. Patterson, Fangyuan Yang, Takashi Taniguchi, Kenji Watanabe, and Andrea F. Young. Isospin magnetism and spin-polarized superconductivity in Bernal bilayer graphene. *Science*, 375(6582):774–778, February 2022.

[99] Yuan Cao, Jeong Min Park, Kenji Watanabe, Takashi Taniguchi, and Pablo Jarillo-Herrero. Pauli-limit violation and re-entrant superconductivity in moiré graphene. *Nature*, 595(7868):526–531, July 2021.

[100] Yuan Cao, Daniel Rodan-Legrain, Jeong Min Park, Fanqi Noah Yuan, Kenji Watanabe, Takashi Taniguchi, Rafael M. Fernandes, Liang Fu, and Pablo Jarillo-Herrero. Nematicity and Competing Orders in Superconducting Magic-Angle Graphene. *arXiv:2004.04148 [cond-mat]*, April 2020.

[101] Myungchul Oh, Kevin P. Nuckolls, Dillon Wong, Ryan L. Lee, Xiaomeng Liu, Kenji Watanabe, Takashi Taniguchi, and Ali Yazdani. Evidence for unconventional superconductivity in twisted bilayer graphene. *Nature*, 600(7888):240–245, December 2021.

[102] Hyunjin Kim, Youngjoon Choi, Cyprian Lewandowski, Alex Thomson, Yiran Zhang, Robert Polski, Kenji Watanabe, Takashi Taniguchi, Jason Alicea, and Stevan Nadj-Perge. Evidence for unconventional superconductivity in twisted trilayer graphene. *Nature*, 606(7914):494–500, June 2022.

[103] D. J. Van Harlingen. Phase-sensitive tests of the symmetry of the pairing state in the high-temperature superconductors-evidence for d_{x2-y2} symmetry. *Reviews of Modern Physics*, 67(2):515–535, April 1995.

[104] C. C. Tsuei and J. R. Kirtley. Pairing symmetry in cuprate superconductors. *Reviews of Modern Physics*, 72(4):969–1016, October 2000.

[105] D. A. Wollman, D. J. Van Harlingen, W. C. Lee, D. M. Ginsberg, and A. J. Leggett. Experimental determination of the superconducting pairing state in ybco from the phase coherence of ybco-pb dc squids. *Phys. Rev. Lett.*, 71:2134–2137, Sep 1993.

[106] D. A. Wollman, D. J. Van Harlingen, J. Giapintzakis, and D. M. Ginsberg. Evidence for $d_{x^2-y^2}$ pairing from the magnetic field modulation of $yba_2cu_3o_7$-pb josephson junctions. *Phys. Rev. Lett.*, 74:797–800, Jan 1995.

[107] J. H. Miller, Jr., Q. Y. Ying, Z. G. Zou, N. Q. Fan, J. H. Xu, M. F. Davis, and J. C. Wolfe. Use of tricrystal junctions to probe the pairing state symmetry of $yba_2cu_3o_{7-\delta}$. *Phys. Rev. Lett.*, 74:2347–2350, Mar 1995.

[108] J. H. Xu, J. H. Miller, and C. S. Ting. π-vortex state in a long 0-π josephson junction. *Phys. Rev. B*, 51:11958–11961, May 1995.

[109] S. P. Chockalingam, Madhavi Chand, John Jesudasan, Vikram Tripathi, and Pratap Raychaudhuri. Superconducting properties and hall effect of epitaxial nbn thin films. *Phys. Rev. B*, 77:214503, Jun 2008.

[110] Gil-Ho Lee and Hu-Jong Lee. Proximity coupling in superconductor-graphene heterostructures. *Reports on Progress in Physics*, 81(5):056502, March 2018.

[111] Michael Tinkham. *Introduction to Superconductivity*. Courier Corporation, 2004.

[112] WN Hardy, DA Bonn, DC Morgan, Ruixing Liang, and Kuan Zhang. Precision measurements of the temperature dependence of λ in yba 2 cu 3 o 6.95: Strong evidence for nodes in the gap function. *Physical Review Letters*, 70(25):3999, 1993.

[113] YJ Uemura, A Keren, LP Le, GM Luke, BJ Sternlieb, WD Wu, JH Brewer, RL Whetten, SM Huang, Sophia Lin, et al. Magnetic-field penetration depth in k3c60 measured by muon spin relaxation. *Nature*, 352(6336):605–607, 1991.

[114] Zeyu Hao, AM Zimmerman, Patrick Ledwith, Eslam Khalaf, Danial Haie Najafabadi, Kenji Watanabe, Takashi Taniguchi, Ashvin Vishwanath, and Philip Kim. Electric field–tunable superconductivity in alternating-twist magic-angle trilayer graphene. *Science*, 371(6534):1133–1138, 2021.

[115] Jeong Min Park, Yuan Cao, Kenji Watanabe, Takashi Taniguchi, and Pablo Jarillo-Herrero. Tunable strongly coupled superconductivity in magic-angle twisted trilayer graphene. *Nature*, 590(7845):249–255, 2021.

[116] Anthony J Annunziata, Daniel F Santavicca, Luigi Frunzio, Gianluigi Catelani, Michael J Rooks, Aviad Frydman, and Daniel E Prober. Tunable superconducting nanoinductors. *Nanotechnology*, 21(44):445202, 2010.

[117] Gyanendra Singh, A Jouan, L Benfatto, F Couëdo, P Kumar, A Dogra, RC Budhani, S Caprara, M Grilli, E Lesne, et al. Competition between electron pairing and phase coherence in superconducting interfaces. *Nature communications*, 9(1):407, 2018.

[118] I Božović, X He, J Wu, and AT Bollinger. Dependence of the critical temperature in overdoped copper oxides on superfluid density. *Nature*, 536(7616):309–311, 2016.

[119] VJ Emery and SA Kivelson. Importance of phase fluctuations in superconductors with small superfluid density. *Nature*, 374(6521):434–437, 1995.

[120] Hyunjin Kim, Youngjoon Choi, Cyprian Lewandowski, Alex Thomson, Yiran Zhang, Robert Polski, Kenji Watanabe, Takashi Taniguchi, Jason Alicea, and Stevan Nadj-Perge. Evidence for unconventional superconductivity in twisted trilayer graphene. *Nature*, 606(7914):494–500, 2022.

[121] David R Nelson and JM Kosterlitz. Universal jump in the superfluid density of two-dimensional superfluids. *Physical Review Letters*, 39(19):1201, 1977.

[122] Fahad Mahmood, Xi He, Ivan Božović, and N. P. Armitage. Locating the missing superconducting electrons in the overdoped cuprates $la_{2-x}sr_xcuo_4$. *Phys. Rev. Lett.*, 122:027003, Jan 2019.

[123] Patrick A Lee and Xiao-Gang Wen. Unusual superconducting state of underdoped cuprates. *Physical review letters*, 78(21):4111, 1997.

[124] AJ Millis, SM Girvin, LB Ioffe, and AI Larkin. Anomalous charge dynamics in the superconducting state of underdoped cuprates. *Journal of Physics and Chemistry of Solids*, 59(10-12):1742–1744, 1998.

[125] SK Yip and JA Sauls. Nonlinear meissner effect in cuo superconductors. *Physical review letters*, 69(15):2264, 1992.

[126] D Agassi and DE Oates. Nonlinear surface reactance of a superconductor strip. *Journal of superconductivity*, 16:905–911, 2003.

[127] Seokjin Bae, Yuewen Tan, Alexander P Zhuravel, Lingchao Zhang, Shengwei Zeng, Yong Liu, Thomas A Lograsso, Ariando Ariando, T Venkatesan, and Steven M Anlage. Dielectric resonator method for determining gap symmetry of superconductors through anisotropic nonlinear meissner effect. *Review of Scientific Instruments*, 90(4), 2019.

[128] Yu Saito, Fangyuan Yang, Jingyuan Ge, Xiaoxue Liu, Takashi Taniguchi, Kenji Watanabe, J. I. A. Li, Erez Berg, and Andrea F. Young. Isospin Pomeranchuk effect in twisted bilayer graphene. *Nature*, 592(7853):220–224, January 2021.

[129] Jeong Min Park, Yuan Cao, Kenji Watanabe, Takashi Taniguchi, and Pablo Jarillo-Herrero. Flavour Hund's Coupling, Correlated Chern Gaps, and Diffusivity in Moiré Flat Bands. *arXiv e-prints*, page arXiv:2008.12296, August 2020.

[130] Asaf Rozen, Jeong Min Park, Uri Zondiner, Yuan Cao, Daniel Rodan-Legrain, Takashi Taniguchi, Kenji Watanabe, Yuval Oreg, Ady Stern, Erez Berg, Pablo Jarillo-Herrero, and Shahal Ilani. Entropic evidence for a Pomeranchuk effect in magic-angle graphene. *Nature*, 592(7853):214–219, January 2021.

[131] Stephen Carr, Chenyuan Li, Ziyan Zhu, Efthimios Kaxiras, Subir Sachdev, and Alexander Kruchkov. Ultraheavy and Ultrarelativistic Dirac Quasiparticles in Sandwiched Graphenes. *Nano Letters*, 20(5):3030–3038, May 2020.

[132] Patrick J. Ledwith, Eslam Khalaf, Ziyan Zhu, Stephen Carr, Efthimios Kaxiras, and Ashvin Vishwanath. TB or not TB? Contrasting properties of twisted bilayer graphene and the alternating twist n-layer structures ($n = 3, 4, 5, \dots$). *arXiv e-prints*, page arXiv:2111.11060, November 2021.

[133] F. D. M. Haldane. Fractional Quantization of the Hall Effect: A Hierarchy of Incompressible Quantum Fluid States. *Phys. Rev. Lett.*, 51(7):605–608, August 1983.

[134] Gregory Moore and Nicholas Read. Nonabelions in the fractional quantum hall effect. *Nuclear Physics B*, 360(2):362–396, 1991.

[135] R. Willett, J. P. Eisenstein, H. L. Störmer, D. C. Tsui, A. C. Gossard, and J. H. English. Observation of an even-denominator quantum number in the fractional quantum hall effect. *Phys. Rev. Lett.*, 59:1776–1779, Oct 1987.

[136] W. Pan, J.-S. Xia, V. Shvarts, D. E. Adams, H. L. Stormer, D. C. Tsui, L. N. Pfeiffer, K. W. Baldwin, and K. W. West. Exact quantization of the even-denominator fractional quantum hall state at $\nu = 5/2$ landau level filling factor. *Phys. Rev. Lett.*, 83:3530–3533, Oct 1999.

[137] J. Falson, D. Maryenko, B. Friess, D. Zhang, Y. Kozuka, A. Tsukazaki, J. H. Smet, and M. Kawasaki. Even-denominator fractional quantum Hall physics in ZnO. *Nature Phys*, 11(4):347–351, April 2015.

[138] A. A. Zibrov, C. Kometter, H. Zhou, E. M. Spanton, T. Taniguchi, K. Watanabe, M. P. Zaletel, and A. F. Young. Tunable interacting composite fermion phases in a half-filled bilayer-graphene Landau level. *Nature*, 549(7672):360–364, September 2017.

[139] J. I. A. Li, C. Tan, S. Chen, Y. Zeng, T. Taniguchi, K. Watanabe, J. Hone, and C. R. Dean. Even-denominator fractional quantum Hall states in bilayer graphene. *Science*, 358(6363):648–652, November 2017.

[140] Qianhui Shi, En-Min Shih, Martin V. Gustafsson, Daniel A. Rhodes, Bumho Kim, Kenji Watanabe, Takashi Taniguchi, Zlatko Papić, James Hone, and Cory R. Dean. Odd- and even-denominator fractional quantum Hall states in monolayer WSe2. *Nat. Nanotechnol.*, 15(7):569–573, July 2020.

[141] Vito W. Scarola, Kwon Park, and J. K. Jain. Cooper instability of composite fermions. *Nature*, 406(6798):863–865, August 2000.

[142] Ken K. W. Ma, Michael R. Peterson, V. W. Scarola, and Kun Yang. Fractional quantum Hall effect at the filling factor ν=5/2, September 2022. arXiv:2208.07908 [cond-mat].

[143] Patrick J. Ledwith, Ashvin Vishwanath, and Daniel E. Parker. Vortexability: A Unifying Criterion for Ideal Fractional Chern Insulators, October 2022. arXiv:2209.15023 [cond-mat].

[144] B. I. Halperin. Theory of the quantized hall conductance. *Helvetica Physica Acta*, 56:75–102, Jun 1983.

[145] Gun Sang Jeon and Jinwu Ye. Trial wave function approach to bilayer quantum hall systems. *Phys. Rev. B*, 71:035348, Jan 2005.

[146] H. A. Fertig. Energy spectrum of a layered system in a strong magnetic field. *Phys. Rev. B*, 40:1087–1095, Jul 1989.

[147] M. Kellogg, I. B. Spielman, J. P. Eisenstein, L. N. Pfeiffer, and K. W. West. Observation of quantized hall drag in a strongly correlated bilayer electron system. *Phys. Rev. Lett.*, 88:126804, Mar 2002.

[148] D. Nandi, A. D. K. Finck, J. P. Eisenstein, L. N. Pfeiffer, and K. W. West. Exciton condensation and perfect Coulomb drag. *Nature*, 488(7412):481–484, August 2012.

[149] Xiaomeng Liu, Kenji Watanabe, Takashi Taniguchi, Bertrand I. Halperin, and Philip Kim. Quantum Hall drag of exciton condensate in graphene. *Nature Physics*, 13(8):746–750, August 2017.

[150] J. I. A. Li, T. Taniguchi, K. Watanabe, J. Hone, and C. R. Dean. Excitonic superfluid phase in double bilayer graphene. *Nature Phys*, 13(8):751–755, August 2017.

[151] Xiaomeng Liu, Zeyu Hao, Kenji Watanabe, Takashi Taniguchi, Bertrand I. Halperin, and Philip Kim. Interlayer fractional quantum Hall effect in a coupled graphene double layer. *Nat. Phys.*, 15(9):893–897, September 2019.

[152] J. I. A. Li, Q. Shi, Y. Zeng, K. Watanabe, T. Taniguchi, J. Hone, and C. R. Dean. Pairing states of composite fermions in double-layer graphene. *Nat. Phys.*, 15(9):898–903, September 2019.

[153] Xiaomeng Liu, J. I. A. Li, Kenji Watanabe, Takashi Taniguchi, James Hone, Bertrand I. Halperin, Philip Kim, and Cory R. Dean. Crossover between strongly coupled and weakly coupled exciton superfluids. *Science*, 375(6577):205–209, January 2022.

[154] Yihang Zeng, Q. Shi, A. Okounkova, Dihao Sun, K. Watanabe, T. Taniguchi, J. Hone, C. R. Dean, and J. I. A. Li. Evidence for a Superfluid-to-solid Transition of Bilayer Excitons, June 2023. arXiv:2306.16995 [cond-mat].

[155] Zheng Zhu, Shao-Kai Jian, and D. N. Sheng. Exciton condensation in quantum hall bilayers at total filling $\nu_T = 5$. *Phys. Rev. B*, 99:201108, May 2019.

[156] Qianhui Shi, En-Min Shih, Daniel Rhodes, Bumho Kim, Katayun Barmak, Kenji Watanabe, Takashi Taniguchi, Zlatko Papić, Dmitry A. Abanin, James Hone, and Cory R. Dean. Bilayer WSe2 as a natural platform for interlayer exciton condensates in the strong coupling limit. *Nat. Nanotechnol.*, 17(6):577–582, June 2022.

[157] Rafi Bistritzer and Allan H. MacDonald. Moiré bands in twisted double-layer graphene. *Proc. Natl. Acad. Sci.*, 108(30):12233–12237, 2011.

[158] Jeil Jung and Allan H. MacDonald. Accurate tight-binding models for the π bands of bilayer graphene. *Phys. Rev. B*, 89:035405, Jan 2014.

[159] Pilkyung Moon and Mikito Koshino. Optical absorption in twisted bilayer graphene. *Phys. Rev. B*, 87:205404, May 2013.

[160] Jong Yeon Lee, Eslam Khalaf, Shang Liu, Xiaomeng Liu, Zeyu Hao, Philip Kim, and Ashvin Vishwanath. Theory of correlated insulating behaviour and spin-triplet superconductivity in twisted double bilayer graphene. *Nature Communications*, 10(1):1–10, dec 2019.

[161] S. S. Saxena, P. Agarwal, K. Ahilan, F. M. Grosche, R. K. W. Haselwimmer, M. J. Steiner, E. Pugh, I. R. Walker, S. R. Julian, P. Monthoux, G. G. Lonzarich, A. Huxley, I. Sheikin, D. Braithwaite, and J. Flouquet. Superconductivity on the border of itinerant-electron ferromagnetism in UGe_2. *Nature*, 406(6796):587–592, August 2000.

[162] Dai Aoki, Andrew Huxley, Eric Ressouche, Daniel Braithwaite, Jacques Flouquet, Jean-Pascal Brison, Elsa Lhotel, and Carley Paulsen. Coexistence of superconductivity and ferromagnetism in URhGe. *Nature*, 413(6856):613–616, October 2001.

[163] N. T. Huy, A. Gasparini, D. E. de Nijs, Y. Huang, J. C. P. Klaasse, T. Gortenmulder, A. de Visser, A. Hamann, T. Görlach, and H. v. Löhneysen. Superconductivity on the Border of Weak Itinerant Ferromagnetism in UCoGe. *Phys. Rev. Lett.*, 99(6):067006, August 2007.

[164] Stephen Julian. Pairing with Spin Fluctuations. *Physics*, 5:17, February 2012. Publisher: American Physical Society.

[165] Xiaomeng Liu, Lei Wang, Kin Chung Fong, Yuanda Gao, Patrick Maher, Kenji Watanabe, Takashi Taniguchi, James Hone, Cory Dean, and Philip Kim. Frictional magneto-coulomb drag in graphene double-layer heterostructures. *Phys. Rev. Lett.*, 119:056802, Aug 2017.

[166] A. F. Hebard and A. T. Fiory. Critical-Exponent Measurements of a Two-Dimensional Superconductor. *Physical Review Letters*, 50(20):1603–1606, May 1983. Publisher: American Physical Society.

[167] Ying Xing, Hui-Min Zhang, Hai-Long Fu, Haiwen Liu, Yi Sun, Jun-Ping Peng, Fa Wang, Xi Lin, Xu-Cun Ma, Qi-Kun Xue, Jian Wang, and X. C. Xie. Quantum Griffiths singularity of superconductor-metal transition in Ga thin films. *Science*, 350(6260):542–545, October 2015. Publisher: American Association for the Advancement of Science.

[168] E. H. Hwang and S. Das Sarma. Dielectric function, screening, and plasmons in two-dimensional graphene. *Physical Review B*, 75(20):205418, May 2007. Publisher: American Physical Society.

[169] Karin Matsumoto, Daisuke Ogura, and Kazuhiko Kuroki. Wide applicability of high-${T}_{c}$ pairing originating from coexisting wide and incipient narrow bands in quasi-one-dimensional systems. *Physical Review B*, 97(1):014516, January 2018. Publisher: American Physical Society.

[170] Kazuhiko Kuroki, Takafumi Higashida, and Ryotaro Arita. High-${T}_{c}$ superconductivity due to coexisting wide and narrow bands: A fluctuation exchange study of the Hubbard ladder as a test case. *Physical Review B*, 72(21):212509, December 2005. Publisher: American Physical Society.

[171] A. Bussmann-Holder, J. Köhler, A. Simon, M. Whangbo, and A. Bianconi. Multigap Superconductivity at Extremely High Temperature: A Model for the Case of Pressurized H2S. *Journal of Superconductivity and Novel Magnetism*, 30(1):151–156, January 2017.

This thesis was typeset using LaTeX, originally developed by Leslie Lamport and based on Donald Knuth's TeX. The body text is set in 11 point Egenolff-Berner Garamond, a revival of Claude Garamont's humanist typeface. The above illustration, "Science Experiment 02", was created by Ben Schlitter and released under CC BY-NC-ND 3.0. A template that can be used to format a PhD thesis with this look and feel has been released under the permissive MIT (X11) license, and can be found online at github.com/suchow/Dissertate or from its author, Jordan Suchow, at suchow@post.harvard.edu.